

Multiscale Computational Methodology Applied to Hydroacoustic Resonance in Cavitating Pipe Flow

THÈSE N° 4778 (2010)

PRÉSENTÉE LE 27 AOÛT 2010

À LA FACULTÉ SCIENCES ET TECHNIQUES DE L'INGÉNIEUR
LABORATOIRE DE MACHINES HYDRAULIQUES
PROGRAMME DOCTORAL EN ENERGIE

ÉCOLE POLYTECHNIQUE FÉDÉRALE DE LAUSANNE

POUR L'OBTENTION DU GRADE DE DOCTEUR ÈS SCIENCES

PAR

Nicolas RUCHONNET

acceptée sur proposition du jury:

Prof. D. Favrat, président du jury
Prof. F. Avellan, directeur de thèse
Dr F. Mazzouji, rapporteur
Dr A. Terrier, rapporteur
Prof. Y. Tsujimoto, rapporteur



ÉCOLE POLYTECHNIQUE
FÉDÉRALE DE LAUSANNE

Suisse
2010

*Whatever you do will be insignificant,
but it is very important that you do it.*

Mahatma Gandhi

Remerciements

Je tiens à exprimer ma gratitude à toutes celles et ceux qui ont contribué à la réalisation de ce travail de thèse.

J'exprime mes sincères remerciements à mon directeur de thèse, Professeur François Avellan, pour m'avoir accordé sa confiance tout au long de ce travail. Je le remercie pour les nombreuses opportunités d'apprentissage, tant sur le plan technique qu'humain, qui m'ont été offertes durant mon travail de doctorat au Laboratoire des Machines Hydrauliques.

Mes remerciements vont également aux membres du Jury, Professeur Daniel Favrat, Dr. Alexandre Terrier, Dr. Farid Mazzouji et Professeur Yoshinobu Tsujimoto qui, par leur correction attentive, ont permis l'amélioration du présent manuscrit.

Ce travail n'aurait pas été possible sans le soutien financier de l'agence de la Confédération pour la promotion de l'innovation et l'entreprise Alstom Hydro. Je tiens à remercier les membres du centre de technologie de Grenoble, Hélène Marin, Michel Couston, Jean-Luc Deniau et Farid Mazzouji pour leurs nombreux conseils.

Ma gratitude va également à mon prédécesseur dans le domaine de l'hydroacoustique, Christophe Nicolet, tout d'abord pour m'avoir fait découvrir le monde passionnant de la recherche scientifique durant mon travail de "master"; puis ensuite pour sa forte implication qui fut cruciale pour le succès du présent travail de thèse. Sa rigueur, son sens de la pédagogie mais aussi son enthousiasme et son amabilité sont un exemple que je m'efforce de suivre au mieux.

Ce travail étant de nature pluridisciplinaire, il a fallu chercher de l'aide auprès de spécialistes. J'ai eu la chance d'en trouver d'éminents parmi mes collègues : Olivier Braun fut d'un grand secours lorsqu'il a fallu faire communiquer les codes de calcul. Je lui en suis très reconnaissant. Je tiens également à remercier Pierre Barmaverain, du bureau d'étude, pour son aide lors de la réalisation du stand d'essai. En ce qui concerne les techniques de mesure et l'instrumentation, ma reconnaissance va à Mohamed Farhat, Philippe Ausoni et Georges Crittin pour leur aide et leurs conseils avisés. Mes remerciements vont également à mon collègue hydro-acousticien, Sébastien Alligné. Nos nombreuses discussions ont permis de clarifier un grand nombre de points essentiels à la réalisation de cette thèse.

Je souhaite aussi remercier l'équipe des mécaniciens du LMH, Louis Bezençon, Raymond Fazan, Christian Sierro, Maxime Raton, Jean-Daniel Niederhauser, Victor Rivas Puentes, Mattias Musco et Jérôme Gruaz, sans qui la partie expérimentale de ce projet n'aurait pas pu être réalisée.

Mes remerciements vont également à l'ensemble du staff du laboratoire, à l'équipe du bureau d'étude et au groupe d'essai sur modèle. Je tiens particulièrement à remercier Philippe Cerruti pour la maintenance du système informatique; Isabelle Stoud-

mann pour sa gestion administrative conviviale et efficace; Philippe Allenbach pour les développements du logiciel SIMSEN indispensable à la réalisation ce travail; Christophe Nicolet, Philippe Ausoni, et Cécile Münch pour leurs "tuyaux"; ainsi que Shadjie Avdulahi pour sa tolérance à l'égard du chenit qui régnait parfois sur mon bureau.

Je ne veux pas oublier toutes les autres personnes avec qui j'ai eu le plaisir de travailler! Je pense notamment aux étudiants avec qui j'ai eu l'opportunité de collaborer: Miénahou, Tchomté, Stefan et Joao. Mais aussi à mes collègues doctorants, post-doctorants et chef de groupes auxquelles je témoigne toute ma sympathie et ma reconnaissance. Les anciens tout d'abord: Mohamed, Youssef, Faïçal, Alexandre, Gabriel, Georgetta, Monica, Lavinia, Jean-Louis, Lluis, Ali, Christophe, Stefan, Olivier Braun et Philippe pour l'agréable ambiance de travail qu'ils ont su créer. Puis ceux qui m'ont rejoint dans l'aventure: Pierre, Cécile, Sebastien, Ran, Francisco, Marco, Amir, Martin, Ebrahim, Martino, Vlad, Steven, Olivier Pacot et Marc qui ont su perpétuer l'esprit "YES PUR"! Je garde de grands souvenirs des moments que nous avons passés ensemble au labo mais aussi à Yokohama avec Ali et Alexandre; sur le terrain de foot avec Youssef, Philipe, Mohamed, Marco, Francisco, Vlad, Amir, Pierre et Marc; en mer avec Olivier Braun; au Caraïbic avec Christophe et consort; dans les montagnes avec Martino et Olivier Pacot; à Piemenson avec Sebastien et Cécile et en camping avec Steven.

Enfin, une pensée spéciale à ma famille et mes pauvres amis de Morges qui m'ont soutenu dans la démarche longue et exigeante de la rédaction.

Résumé

Ce travail est une contribution à l'analyse physique et à la modélisation numérique des fluctuations brusques de pression dans les machines hydrauliques et leurs conduites d'alimentation. Des instabilités hydrodynamiques locales avec cavitation ont tendance à interagir avec l'ensemble de la conduite par la propagation d'ondes acoustiques planes. A la résonance, la superposition des ondes acoustiques génère des ondes stationnaires de grande amplitude sur l'ensemble de la conduite. La fluctuation de vitesse et de pression dans la zone source peut avoir une influence importante sur l'instabilité hydrodynamique. Une technique de modélisation basée sur l'interaction de deux champs est proposée pour la simulation dans le domaine temporel : un modèle hydroacoustique (modèle HA) monodimensionnel est sélectionné pour l'analyse de l'ensemble du champ acoustique, zone source incluse; un modèle hydrodynamique (modèle HD) incompressible et tridimensionnel est utilisé pour décrire l'écoulement dans la zone source. La perturbation acoustique due à l'instabilité est évaluée précisément avec le modèle HD et introduite dans le modèle HA par des sources discrètes. Pour décrire l'interaction complète entre les champs, deux méthodes sont proposées : la rétroaction acoustique est soit complètement modélisée (simulation couplée bidirectionnelle) ou prise en compte à l'aide de paramètres d'interaction (simulation parallèle à couplage unidirectionnel). Avec la première méthode, les conditions limites du modèle HD sont ajustées dynamiquement en utilisant le champ obtenu par le modèle HA et toutes les composantes des sources sont évaluées dans le modèle HD. Dans la seconde méthode, les composantes hydroacoustiques et hydrodynamiques des sources sont considérées comme indépendantes. Les composantes dues au champ hydrodynamique sont évaluées dans le modèle HD en utilisant des conditions aux limites stationnaires puis introduites dans le modèle HA par des sources discrètes. Les composantes des sources dues aux fluctuations acoustiques sont prises en compte avec des paramètres particuliers du modèle HA ; ces paramètres, c'est-à-dire la souplesse de cavitation et le facteur de gain massique, sont évalués à l'aide du modèle HD.

Un cas test de référence a été construit ; des analyses vidéo et des mesures de pressions dynamiques ont été effectuées pour valider les simulations. Le cas test est constitué d'une conduite droite reliant deux réservoirs à pression constante. Un cylindre est placé aux $\frac{3}{4}$ de la conduite. L'instabilité hydrodynamique résultante est caractérisée par le lâché alterné de tourbillon à une fréquence proportionnelle à la vitesse de l'écoulement. Le résonateur hydroacoustique est la conduite elle-même. Les mesures ont été effectuées à la résonance et hors résonance, avec et sans cavitation.

Pour les régimes d'écoulement sans cavitation, la source hydrodynamique est identifiée comme étant une pure source de quantité de mouvement. Les conditions d'écoulement résonantes peuvent être évaluées avec la méthode de couplage bidirectionnel. A la résonance; la distribution, la fréquence et l'amplitude des fluctuations de pression prédites dans la

simulation correspondent aux valeurs mesurées. Pour le cas test sélectionné, la rétroaction acoustique est très faible et n'a pas une influence significative sur la source de quantité de mouvement.

Pour les régimes d'écoulement avec cavitation, deux sources hydrodynamiques ont été identifiées. La source de quantité de mouvement est assimilée à la force de trainée sur le cylindre. La source de masse est assimilée aux fluctuations du volume de vapeur dans la trainée du cylindre. La puissance de la seconde source est largement plus importante que la première ainsi la source de quantité de mouvement peut être négligée. La méthode de couplage unidirectionnel avec mise à jour dynamique des paramètres d'interaction a été mise en oeuvre. Une correspondance acceptable est obtenue entre les mesures et les simulations. L'augmentation des fluctuations observées sous le niveau de cavitation naissante est reproduite. A un niveau de cavitation intermédiaire, l'amplitude des fluctuations et la distribution spectrale d'énergie sont proches des valeurs mesurées. Les modifications des modes propres et des fréquences propres dues à la cavitation sont reproduites de façon satisfaisante avec le paramètre d'interaction appelé souplesse de vapeur.

Mots-clés: Cavitation, hydroacoustique, simulation multi-échelle, écoulement en conduite, fluctuation de pression, résonance.

Abstract

The present work is a contribution to the physical analysis and numerical simulation of the pressure surges in hydraulic machinery and connected conduit systems. Localized hydrodynamic instabilities including cavitation are prone to interact with the entire conduit through the propagation of acoustic plane waves. At resonance, the superimposition of the acoustic waves leads to the formation of large amplitudes standing waves along the entire conduit. The resulting fluctuation of velocity and pressure in the source region may have a significant role on the hydrodynamic instability.

A computational methodology based on two fields is proposed to simulate this interaction in the time domain: a 1D hydroacoustic model (HA model) is selected to analyze the entire acoustic field including the source region, a 3D incompressible hydrodynamic model (HD model) is used to describe the flow in the source region. The acoustic perturbation due to the instability is precisely evaluated with the HD model and injected in the HA model through discrete sources. To describe the complete interaction between the fields, two methods are proposed: the acoustic feedback is either fully modeled (two way coupled simulation) or accounted for using interaction parameters (one way concurrent simulation). In the first method, the boundary conditions of the HD model are adjusted dynamically using the solution field of the HA model and all components of the sources are evaluated in the HD model. In the second method, the acoustics and hydrodynamics components of the sources are considered as independent. The components due to the hydrodynamic field are evaluated in the HD model with steady boundary conditions and injected in HA model through discrete sources. The components of the sources due to the acoustic fluctuations are accounted for with specific parameters of the HA model; those interaction parameters, i.e. cavity compliance and mass flow gain factor, are evaluated with the help of the HD model.

A reference case study has been setup; video analysis and dynamic pressure measurement have been performed to validate the simulations. The case study consists in a straight pipe connecting two constant pressure tanks. A bluff body is placed at 3/4 of the pipe length, the resulting flow instability is characterized by the alternate shedding of vortices at a frequency proportional to the flow velocity. The hydroacoustic resonator is the pipe itself. Measurements have been performed for resonant and non-resonant conditions in cavitating and cavitation free flow regime.

In cavitation free flow regime, the hydrodynamic source is identified as a pure momentum source associated with the drag force on the bluff body. The flow conditions leading to resonance can be evaluated with the two way coupled simulation. At resonance, the distribution, frequency and amplitude of pressure fluctuation predicted in the simulation is in good agreement with the measurement. For the selected case study, the acoustic feedback is very weak and has no significant effect on the momentum source.

In cavitating flow regime, two hydrodynamic sources have been identified, the momentum source and the mass source. The momentum source is associated with the drag force on the bluff body, the mass source is associated with the volume fluctuation of the vapor phase in the wake of the bluff body. The strength of the mass source is orders of magnitude larger and the momentum source can therefore be neglected. One way concurrent simulations using dynamic update of the interaction parameters have been performed. Fair agreement is obtained between the simulations and the measurements. The amplification of the fluctuation observed experimentally below incipient cavitation is reproduced. At intermediate cavitation index, the pressure fluctuation amplitude and the spectral energy distribution is in fair agreement with the experiment. The modifications of the pipe eigenmodes and eigenfrequencies due to cavitation is satisfactorily reproduced with the cavity compliance.

Keywords: Cavitation, hydroacoustic, multiscale simulation, pipe flow, pressure surges, resonance.

Contents

I	Introduction	1
1	Problem overview	3
1.1	Motivation	3
1.2	Previous studies	3
1.3	Case study definition	5
1.4	Description	5
1.4.1	Hydrodynamic instability	5
1.4.2	Acoustic resonator	6
1.4.3	Acoustic feedback	6
1.5	Literature review	7
1.5.1	Source evaluation	7
1.5.2	Propagation of acoustic waves in pipe	8
1.5.3	Coupled systems	8
2	Hydroacoustics	11
2.1	Wave equations	11
2.1.1	Conservation laws and constitutive equations of fluid dynamics	11
2.1.2	Linear acoustics theory	12
2.1.3	Duct acoustic and plane wave propagation	14
2.2	Hydrodynamic sources of sound	15
2.2.1	Lighthill's acoustic analogy	15
2.2.2	Influence of solid body	17
2.2.3	Single bubble noise	18
2.2.4	Dipole sound from cylinder	18
2.2.5	Distinction of the acoustic and turbulent fields	19
3	Cavitation	21
3.1	Cavitation inception	21
3.2	Wake cavitation	21
3.3	Mathematical models	22
4	Problem statement	25
4.1	Objective	25
4.2	Proposed approach	25
4.3	Structure of the document	26

II	Reference case study	29
5	Reference experiment	31
5.1	Setup	31
5.1.1	Installation	31
5.1.2	Instrumentation	31
5.2	Flow conditions	33
5.2.1	Incipient cavitation index	33
5.2.2	Cavitation free conditions	34
5.2.3	Cavitating conditions	35
5.3	Sources of pressure fluctuation	35
5.3.1	Force on bluff body and resulting momentum source	35
5.3.2	Cavity pulsation and resulting mass source	38
5.4	Acoustic pressure fluctuation	38
5.4.1	Eigenfrequency determination	38
5.4.2	Eigenmode shape determination	39
5.4.3	Fluctuation amplitude at resonance	40
6	Hydroacoustic model	49
6.1	Transient pipe flow	49
6.1.1	Conservation laws	49
6.1.2	Constitutive equations	53
6.1.3	Resulting hydroacoustic model	54
6.2	Computational model implementation	56
6.2.1	Space discretization	56
6.2.2	Time discretization	57
6.3	Application to the reference case study	57
6.3.1	Setup	57
6.3.2	Validation and intermediate results	58
7	Interaction	63
7.1	Hydrodynamic source	63
7.1.1	Mass source	64
7.1.2	Momentum source	65
7.2	Acoustic feedback	66
7.2.1	Source without feedback	67
7.2.2	Source with linear feedback	67
7.2.3	Source with nonlinear feedback	72
7.3	Computational model implementation	72
7.3.1	Hydrodynamic source	72
7.3.2	Linearized interaction parameter	73
7.3.3	Nonlinear acoustic feedback	75
7.3.4	Time integration	75
7.3.5	Validation and intermediate results	78

8	Hydrodynamic model	81
8.1	Computational model implementation	81
8.1.1	3D turbulent multiphase flow	81
8.1.2	Space and time discretization	84
8.2	Application to the reference case study	84
8.2.1	Setup	84
8.2.2	Validation and intermediate results	88
8.2.3	Vapor cavity volume evaluation	91
III	Results of the coupled and concurrent simulations	97
9	Cavitation free regime	99
9.1	One-way concurrent simulation	99
9.1.1	Setup	99
9.1.2	Results	100
9.2	Two-way coupled simulation	105
9.2.1	Setup	105
9.2.2	Results	107
10	Cavitating flow regime	111
10.1	One-way concurrent simulation	111
10.1.1	Setup	111
10.1.2	Interaction parameters identification	113
10.1.3	Cavitation model selection	114
10.1.4	Results	114
10.2	Two-way coupled simulation	122
10.2.1	Setup	122
10.2.2	Results	124
IV	Conclusions and perspectives	127
11	Conclusions	129
12	Perspectives	131
	Appendix	135
A	Pipe deformation based on beam theory	135
B	Damping analysis	137
B.1	Damped wave equation	137
B.2	Experimental determination of the pipe viscoelastic response	140
C	Convergent and divergent pipe	143

D Computing resources	145
D.1 Hardware	145
D.2 Software	145
D.3 Communication	146
E Coupling algorithm	147
E.1 One-way	147
E.2 Two-way fully explicit	148
E.3 Two-way staggered	148
E.4 Two-way iterative implicit	149
E.5 Monolithic approach	149
References	153
Curriculum Vitae	162

Notations

Latin

A	Cross section area	[m ²]
C	Flow velocity	[m/s]
D	Bluff body diameter	[m]
E	Young modulus	[Pa]
F	Force	[N]
$F_{x,s}$	Momentum source	[N]
F^{vap}	Vaporization factor	[-]
F^{cond}	Condensation factor	[-]
F_D	Drag force	[N]
H	Pipe height	[m]
K_v	Cavity compliance	[kg·Pa ⁻¹]
L	Length	[m]
L_{TOT}	Total pipe length	[m]
M_G	Mass flow gain factor	[kg·m ⁻¹ ·s]
$\frac{\partial M_s}{\partial t}$	Mass source	[kg·s ⁻¹]
P_{xy}	Cross power spectral density	[E.U. ² /Hz]
P_{xx}	Power spectral density	[E.U. ² /Hz]
\mathbf{P}, P_{ij}	Fluid stress tensor	[Pa]
P	Pipe perimeter	[m]
R	Reflection coefficient	[-]
R	Bubble radius	[m]
S	Surface	[m ²]
S_A	Source inlet	[m ²]
S_B	Source outlet	[m ²]
S_{gl}	Rate of vapor condensation	[kg·m ⁻³ ·s ⁻¹]
S_{lg}	Rate of water vaporization	[kg·m ⁻³ ·s ⁻¹]
T_{xy}	Frequency response function	[-]
T_S	Vortex shedding period	[s]

V	Volume	$[\text{m}^3]$
W	Pipe width	$[\text{m}]$
Z	Acoustic impedance	$[\text{N}\cdot\text{s}\cdot\text{m}^{-3}]$
a_0	Speed of sound in free water	$[\text{m}/\text{s}]$
a_c	Propagation velocity in pipe	$[\text{m}/\text{s}]$
d	Damping coefficient	$[\text{s}^{-1}]$
e	Pipe wall thickness	$[\text{m}]$
f	Frequency	$[\text{Hz}]$
f_n	Natural frequency of the pipe without cavitation	$[\text{Hz}]$
f_s	Frequency of the source	$[\text{Hz}]$
f_{cutoff}	Pipe cut-off frequency	$[\text{Hz}]$
$\underline{f_{x,s}}$	Momentum source per unit length	$[\text{N}\cdot\text{m}^{-1}]$
k	Wave number	$[\text{m}^{-1}]$
k	Turbulent kinetic energy	$[\text{J}\cdot\text{kg}^{-1}]$
\mathbf{k}, k_i	Wave vector	$[\text{m}^{-1}]$
l	Characteristic dimension of the source region	$[\text{m}]$
$\frac{\partial m}{\partial t}$	Mass source per unit length	$[\text{kg}\cdot\text{m}^{-1}\cdot\text{s}^{-1}]$
p	Pressure	$[\text{Pa}]$
p_v	Vaporization pressure	$[\text{Pa}]$
r	Radial distance	$[\text{m}]$
t	Time	$[\text{s}]$
x, y, z	Cartesian coordinates	$[-]$
x, r, θ	Cylindrical coordinates	$[-]$

Greek

α	Volume fraction	$[-]$
α	Pipe taper angle	$[^\circ]$
β	Momentum correction coefficient	$[-]$
δ_{ij}	Kronecker delta	$[-]$
γ	Isentropic expansion factor	$[-]$
λ	Friction factor	$[-]$
λ	Second coefficient of viscosity	$[\text{Pa}\cdot\text{s}]$
λ	Wave length	$[\text{m}]$
μ	Dynamic coefficient of viscosity	$[\text{Pa}\cdot\text{s}]$
μ	Viscoelastic damping	$[\text{Pa}\cdot\text{s}]$
ν	Kinematic coefficient of viscosity	$[\text{m}^2\cdot\text{s}^{-1}]$
ρ	Density	$[\text{kg}/\text{m}^{-3}]$

σ	Cavitation index	[-]
σ_i	Incipient cavitation index	[-]
τ_{ij}	Viscous stress tensor	[Pa·s]
τ_w	Wall shear stress	[Pa·s]
ω	Angular frequency	[s ⁻¹]
ω	Specific dissipation rate, turbulent frequency	[s ⁻¹]

Subscripts

A	Inlet section
B	Outlet section
D	Drag
L	Lift
a	Acoustic quantity
d	Deviation
ext	External element
g	Gaseous phase
l	Liquid phase
n, m	Mode number
nuc	Nuclei
ref	Reference
s	Source
t	Turbulent quantity
v	Vapor
0	Reference state

Mathematic symbol

$\text{std}(O)$	Standard deviation
O'	Fluctuating part
O_0	Reference state
\bar{O}	Time averaged quantity
\tilde{O}	Ensemble averaged quantity
\hat{O}	Amplitude of harmonic oscillation
\underline{O}	Mono dimensional quantity
O^*	Dimensionless quantity
\mathbf{O}, O_i	Vector
\mathbf{O}, O_{ij}	Second order tensor

$\int dx$	Integral
$\int d^2\mathbf{x}$	Surface integral
$\int d^3\mathbf{x}$	Volume integral

Dimensionless Numbers

C_r	Courant number	$C_r = \frac{a_c \Delta t}{\Delta x} [-]$
M	Mach number	$M = \frac{C}{a_0} [-]$
Re	Reynolds number	$Re = \frac{CL}{\nu} [-]$
St	Strouhal number	$St = \frac{fL}{C} [-]$
c_D	Drag coefficient	$c_D = \frac{F_x}{\frac{1}{2}\rho C^2 DL} [-]$
c_L	Lift coefficient	$c_L = \frac{F_y}{\frac{1}{2}\rho C^2 DL} [-]$
c_p	Pressure coefficient	$c_p = \frac{p}{\frac{1}{2}\rho C^2} [-]$
y^+	Boundary layer inner wall distance	$y^+ = \frac{\sqrt{\tau_w} \rho y}{\mu} [-]$
σ	Cavitation number	$\sigma = \frac{p - p_v}{\delta p} [-]$

Acronyms

CFD	Computational Fluid Dynamics
DLL	Dynamic Link Library
EPFL	Ecole Polytechnique Fédérale de Lausanne
FFT	Fast Fourier Transform
HA	HydroAcoustic model
HD	HydroDynamic model
LMH	Laboratoire de Machines Hydrauliques
MPI	Message Passing Interface
PSD	Power Spectral Density
PVC	PolyVinyl Chloride
RANS	Reynolds Averaged Navier Stokes equations
SAS	Scale Adaptive Simulation
SST	Shear Stress Transport
TCPIP	Transmission Control Protocol (TCP), Internet Protocol (IP)

Part I

Introduction

Chapter 1

Problem overview

1.1 Motivation

In Francis turbine, hydrodynamic instabilities in the draft tube are prone to interact with the entire hydraulic circuit through the propagation of plane pressure waves. This phenomenon, known as surge, induces undesired pressure fluctuation and may even compromise the safety of the hydroelectric power plant. To predict the amplitude of the Francis turbine surge at the design stage, innovative simulation method is required. The methodology should include a detailed description of the hydrodynamic instability, a global description of the acoustic system and a careful description of the interaction mechanisms between the acoustic fluctuation and the hydrodynamic instability. Based on these considerations, the present multiscale computational methodology is developed to achieve a reliable prediction of the flow induced pressure fluctuation in hydraulic circuit.

1.2 Previous studies

Part load surge

The flow instability in the draft tube of Francis turbine at part load has been identified for a long time as a problematic source of pressure fluctuation [78, 90, 28]. This type of surge is described as a forced oscillation by Dörfler [29]: An hydrodynamic instability is always present in the draft tube. If the frequency of this flow instability matches the resonance frequency of the acoustic system, large pressure oscillations are expected in the entire system.

The hydrodynamic instability alone can be reproduced using CFD analysis [50, 88, 72, 64]. The frequency and amplitude of the pressure pulsation induced by the precession of the vortex rope is satisfactorily reproduced by the simulation. In a recent publication [50], a cavitation model is included to predict the volume of the gaseous phase in the core of the precessing vortex.

In case of resonance with the hydraulic circuit, such local models fail to predict the amplification of the synchronous part of the fluctuation. To tackle the flow instability/acoustic field interaction, simplified approaches have been proposed:

- The transfer matrix method has been proposed by Dörfler to analyze the half load surge [28, 29]. His simulation includes the impedance of the penstock, the turbine

inertia, the compliance due to the cavitating vortex rope and a momentum source connected with the vortex breakdown. A method is proposed to experimentally determine the compliance and the momentum source from model test.

- A distributed method has been proposed by Couston [77, 21]. The transfer matrix method is also used in his analysis. Instead of a lumped compliance, the rope is described as a distributed modification of the wave speed. The influence of the flow rate fluctuation (mass flow gain factor) is also included in the method.
- Water hammer equations including distributed cavity compliance has been proposed by Nicolet to analyze the acoustic resonance due to the interaction of the cavitating vortex rope with the wall of the draft tube [69, 68]. The compliance due to the cavitating vortex rope is interpreted as a modified wave speed in the draft tube.
- Field partitioning technic has been proposed by Ruprecht to analyze the part load surge [81]. The method of characteristic is employed to describe the acoustic fluctuation in the penstock. The draft tube flow is described using 3D unsteady RANS method. The runner influence is taken into account with a linearized characteristic curve. Constant pressure is imposed at the inlet of the penstock and at the outlet of the draft tube. The velocity and pressure at the interface between the two models is free. The boundary condition for the method of characteristic, pressure at the runner inlet, is updated at each time step using the pressure drop computed with the CFD model and the linearized characteristic curve. The velocity at the interface is evaluated at each time step with the method of characteristic and used as variable boundary condition of the draft tube flow. The two models are properly coupled, but the draft tube flow model is assumed incompressible, the compliance of the vortex rope is not taken into account. Such an incomplete description of the hydroacoustic system leads to an erroneous estimation of the eigenfrequencies.

Full load surge

The flow instability in the draft tube of Francis turbine at full load is due to the interaction of the cavity formed downstream the runner and the acoustic fluctuation in the entire circuit. This full load surge is described as self-induced by Dörfler [29]; the acoustic feedback triggers the instability. The hydrodynamic field alone is stable but the coupled system consisting in the acoustic field and the hydrodynamically generated cavity is unstable for specific flow conditions. Such interaction has been analyzed using simplified 1D model:

- Tsujimoto et al. proposed an analytical mono-dimensional analysis of the full load surge [18]. Three mechanisms are identified for the acoustic feedback on the vapor cavity volume formed in the draft tube.
 1. The pressure in the draft tube has a direct influence on the vapor cavity volume.
 2. The flow velocity upstream modifies the cavity volume through the modification of the velocity triangle at the outlet of the runner resulting in a modification of the swirl inside the draft tube.
 3. The flow velocity downstream influences the cavity volume due to the diffuser effect of the draft tube.
- Water hammer equations has been proposed by Koutnik and Nicolet to simulate the full load instability [52, 38]. 3D flow simulation is used to determine the mass

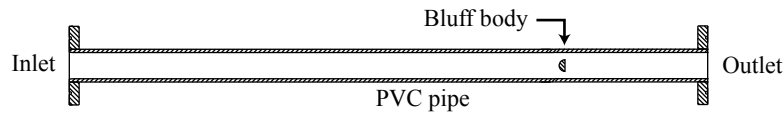


Figure 1.1: Reference case study.

flow gain factor and compliance parameters.

- In [30], Dörfler discusses the methodology to determine the mass flow gain factor. Emphasis is placed on the influence of the location of the acoustic feedback for the stability of the system. The mass flow gain factor can be placed either upstream or downstream the cavitating section in the hydroacoustic model leading to different response of the system.

1.3 Case study definition

The measurement of pressure fluctuation in a reduced scale model including the connected conduit systems is a complex task; moreover, the simulation of the draft tube flow is computationally expensive. For those reasons, a simplified experimental case study has been selected, see Figure 1.1. It consists in a bluff body mounted in a straight PVC pipe of constant cross section. The acoustic resonator is the pipe itself, reflective boundary conditions are imposed using constant pressure tanks at the pipe ends. The vortex shedding in the wake of the bluff body provides the hydrodynamic instability. As cavitation is inherent in hydraulic machinery and is known to interact strongly with the acoustic pressure waves, the measurements have been performed in cavitating and cavitation free flow conditions.

1.4 Description

1.4.1 Hydrodynamic instability

A flow configuration is unstable when small perturbations to it tend to be amplified. Various types of hydrodynamic instability appear in the nature. The most general is the transition to turbulence. Above a critical Reynolds number, the internal mechanisms of energy exchange guaranties the creation and the conservation of a hierarchy of chaotic movement continuously distributed on a large macroscopic scale in the flow [17]. The resulting noise is distributed on a large range of frequencies.

The vortex shedding in the wake of bluff bodies is another type of flow instability. Such instability exists in both laminar and turbulent regime. In laminar regime, the attached eddies are periodically shed from the bluff body to form the Von Kármán vortex street. In such situation the resulting hydrodynamic source is harmonic. In turbulent regime, periodic vortex shedding remains a characteristic of the flow. But the resulting noise is distributed on a large range of frequencies and a dominant frequency is observed among the random fluctuations.

Another type of flow instability is the helicoidal vortex breakdown [44]. This type of instability is observed at part load operation of Francis turbine and is connected with

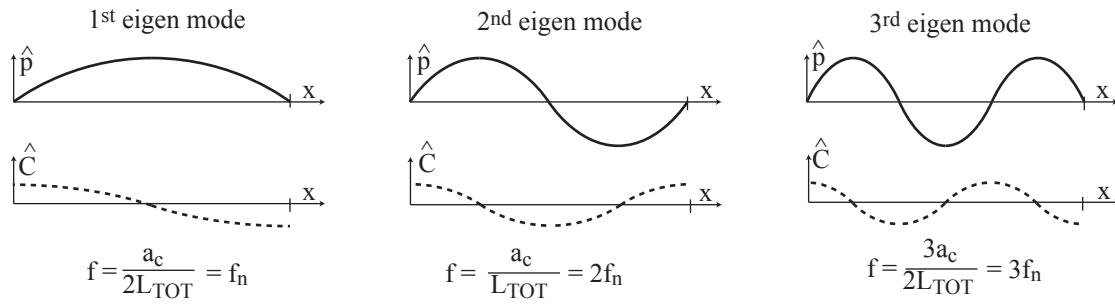


Figure 1.2: Schematic representation of the standing waves mode in a pipe.

the swirl intensity in the draft tube [33]. The resulting noise is also characterized by a dominant frequency.

Those phenomena are purely hydrodynamic, no pressure wave is involved in the generation or in the conservation of the movement. Incompressible flow model is sufficient to analyze such type of instability [44].

1.4.2 Acoustic resonator

A resonator is a system that exhibits resonance at some particular frequency called natural frequency. It can be mechanical, electromagnetic or acoustic. Acoustic resonance is associated with compression waves in fluid.

Below cut-off frequency, the pipe is a particular type of resonator, the degrees of freedom of the system is greatly reduced as only the axial mode of propagation exists for low frequencies, see Subsection 2.1.3. In such system the natural frequency is determined by the impedance conditions at both ends and the propagation velocity of the pressure wave along the pipe axis. At the eigenfrequencies, the interference of the progressive and retrograde waves results in the formation of standing waves. As the system is continuous, an infinity of eigenfrequencies exist. A schematic representation of the 3 first eigenmodes for zero impedance boundary conditions is given in Figure 1.2. For each mode, the maximum amplitude of pressure and velocity is presented with its corresponding fluctuation frequency.

For conservative or lightly damped system, resonance occurs as the source frequency is equal to an eigenfrequency of the system. In such situation, the energy in the system increases at each cycle and maximum amplitude is reached as the power dissipated in the entire system is equal to the source power.

1.4.3 Acoustic feedback

For a source region in an infinite domain, part of the turbulent energy is converted into pressure waves and radiated to the far-field. The flow turbulence is considered as a source of acoustic energy. In an hydraulic circuit, the pipe is acting as a resonator and the acoustic energy remains in the system. Acoustic fluctuation may become important in the entire system including the source region and have a significant effect on the source. This effect is called hydroacoustic feedback, see Figure 1.3. The feedback effect can amplify or damp the fluctuation [7]. At acoustic resonance, three situations are distinguished:

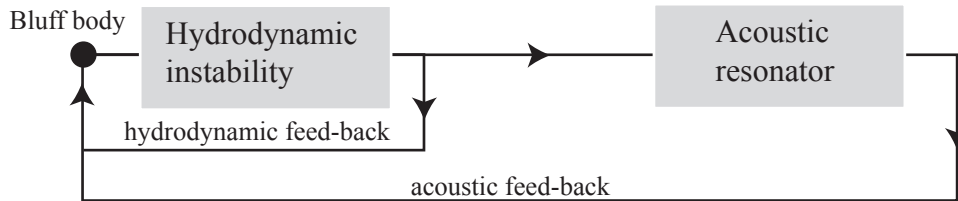


Figure 1.3: Self-sustained oscillation and acoustic feedback; Reprinted from [45].

- Simple hydroacoustic resonance; in such situation the acoustic field is amplified but the hydrodynamic source is weakly influenced by the acoustic field.
- Hydroacoustic resonance with negative feedback; in such situation the acoustic field damps the hydrodynamic source.
- Hydroacoustic resonance with positive feedback, in such situation the acoustic field triggers and even amplifies the hydrodynamic source. This full coupling may lock-in the hydrodynamic instability at the resonance frequency.

1.5 Literature review

1.5.1 Source evaluation

The computation of flow-induced noise and its propagation is known as computational aeroacoustics or hydroacoustics depending on the medium, air or water. Acoustics was originally the study of small pressure waves in air which can be detected by the human ear: sound. The scope of acoustics has been extended to higher and lower frequencies: ultrasound and infrasound. The present study is focused exclusively on hydroacoustic at low frequency (case study: $f_s \sim 100$ Hz, Francis turbine: $f_s \sim 10$ Hz). Two approaches can be distinguished to compute flow-induced noise [94, 20]:

- The direct approach computes the sound together with its fluid dynamic source field by solving the compressible flow equations. Its use is limited to simple flow configurations at low to moderate Reynolds numbers.
- In hybrid approaches, the computation of flow is decoupled from the computation of sound. At low Mach number (case study: $M = 0.015$), incompressible flow simulation are sufficient to compute the space-time history of the flow field in the source region. The far-field sound is obtained in a second step by numerical integration of acoustic analogy equations, see Section 2.2, using the previously computed source field data.

Even for the second approach, Direct Numerical Simulation (DNS) in the source region is necessary to evaluate the entire frequency spectrum of turbulent flow (case study: $Re = 60'000$). Large Eddy Simulation (LES) which resolves only the dynamically important flow scales and models the effects of smaller scales, can also be employed to evaluate the entire frequency spectrum. If the focus is on the low frequency range, it is also possible to use unsteady Reynolds-averaged Navier-Stokes (RANS) methods to compute the noise due to the largest flow features.

In the field of hydraulic machinery, hybrid approach has been proposed to compute the acoustic fluctuation due to rotor stator interaction in 2D centrifugal pump [58, 59]. The discrete vortex method has been chosen to compute the hydrodynamic dipole source corresponding to the force on the impeller blades. Boundary element method was selected for the computation of the acoustic field.

For air-intake parts of automotive engine, hybrid method has been proposed to compute the flow-induced noise due to the quick opening of a throttle valve [82]. Compressible RANS method has been used for the evaluation of the dipole and quadruple source terms. The acoustic fluctuation was computed using tailored Green's functions in the frequency domain.

In hydroacoustic, the cavitation is an important source of noise. The sudden change of density due to the phase change is an "efficient" monopole source. Hybrid methods have been used to compute the noise induced by non-cavitating and cavitating propeller [83, 84]. Larger amplitudes are predicted for the cavitating configuration.

1.5.2 Propagation of acoustic waves in pipe

In pipe flow, the problem of propagation is considerably simplified for sufficiently low frequency (*casestudy* : $f_{cutoff} = 19'000$ Hz). Only one mode of propagation exist, this mono-dimensional mode corresponds to plane waves normal to the pipe axis. In such situation, the source terms can be evaluated directly from the conservation of mass and momentum [45]. For rigid pipe wall, the propagation velocity is equal to the speed of sound. For deformable pipe wall, the propagation velocity decreases and the deformation may even induce none linear effects such as dissipation and dispersion [22, 23, 76]. The other dissipative mechanisms controlling the fluctuation amplitude at resonance are the wall friction [74, 75] and the partial reflection at the pipe ends [74, 89]. Various methods have been proposed to solve the corresponding set of partial differential equations called water hammer equations [41]:

- Implicit finite difference method;
- explicit finite difference method;
- finite volume method;
- method of characteristics.

In the present study, an explicit finite difference method is selected to compute the water hammer equations.

1.5.3 Coupled systems

A fundamental assumption for acoustic analogy-based predictions is the one-way coupling of flow and sound, i.e., the unsteady flow generates sound, but the sound waves do not affect the flow in any significant manner. This assumption is not valid for confined flow such as pipe flow, the acoustic fluctuation may even have an important effect on the source. By example the interaction between the vortex shedding in the wake of a flat plate and the β acoustic mode have been studied experimentally [73, 24, 4], the measurements evidence the two-way coupling mechanism between the acoustic and the hydrodynamic fields.

To integrate the acoustic feedback in the simulation a two-way coupled approach is necessary. The generation of sound by unsteady flow must be taken into account but

also the feedback of the sound waves on the unsteady flow. The coupling mechanism has been extensively studied for the fluid-structure interaction. In such situation the coupled system consists in two physically heterogeneous mechanical components, the fluid and the structure. A coupled system may also consists in two physically homogeneous but computationally heterogeneous components [37], the acoustic field and the unsteady flow field in the present problem of hydroacoustic. Depending on the coupling level, diverse partitioning procedure have been proposed:

- One-way coupling can be used for system with negligible feedback such as flow induced noise in infinite free space [94].
- Two-way explicit coupling is sufficient for loosely coupled system. Examples can be found for aeroelastic coupled system [34].
- Implicit iterative coupling is necessary for strongly coupled system. The interaction of highly deformable blood vessel with incompressible fluid (blood) is a good example of such interaction [39, 55]
- Monolithic approach may be preferable in order to ensure stability and to accelerate the convergence of strongly coupled problems [43].

In addition to these coupled approach, field elimination is used when the effect of one field can be described with a simplified model. In the coupled approach, high accuracy models are used for both fields. But when the interest is focused on one field, the influence of the other field can be accounted for through simple linearized interaction parameters. Such approach has been successfully used to investigate the influence of cavitation on the acoustic field in liquid propulsion system [80], in pumps [15, 16] and in water tunnel [31]. Two parameters have been identified, the cavity compliance and the mass flow gain factor. For the cavity compliance, a quasi-steady linear relation is assumed between the cavity volume and the ambient pressure in the cavitating region. For the mass flow gain factor, a quasi-steady linear relation is assumed between the cavity volume and the flow rate in the cavitating region.

In such linearized approach, the hydrodynamic source due to the cavity volume fluctuation is not treated as an external element of the acoustic field; the hydrodynamic source term is included as a parameter in the acoustic field description. Such approximation allows to describe simply the acoustic field but very sparse information is provided regarding the cavitation dynamics.

Chapter 2

Hydroacoustics

At low Mach number local phenomena such as boundary layer, shear flow instability can be considered as incompressible. Nevertheless, the fluid compressibility plays a crucial role in the propagation of perturbation over large distance and this phenomenon is described by the wave equation. Numerous mathematical tools are available to treat this equation, the most relevant are summarized in Section 2.1, the mathematical developments are based on [61, 13]. In Section 2.2, the mechanism of flow induced sound is introduced. The approach is based on the analogy due to the pioneer work of Lighthill [62, 63]. The most important results are briefly described in Section 2.2, the details of the mathematical development are available in [7, 45, 13].

2.1 Wave equations

2.1.1 Conservation laws and constitutive equations of fluid dynamics

For continuous fluid, the mass and momentum conservation laws take respectively the following differential forms in cartesian coordinate system:

$$\frac{\partial \rho}{\partial t} + \frac{\partial}{\partial x_i} (\rho C_i) = 0 \quad (2.1)$$

$$\frac{\partial}{\partial t} (\rho C_i) + \frac{\partial}{\partial x_j} (P_{ij} + \rho C_j C_i) = 0 \quad (2.2)$$

Where ρ is the fluid density, C_i the flow velocity vector and P_{ji} the fluid stress tensor. This tensor consists in two parts, the pressure, p , and the viscous stress tensor, τ_{ij} . For Newtonian fluid such as water, the viscous stress tensor is linearly related to the rate-of-strain. In full generality, the tensor connecting the rate-of-strain to the stress tensor consist in 81 coefficients of proportionality. Based on symmetry properties and considering isentropic fluid, the number of coefficients is reduced to two elements: μ the dynamic coefficient of viscosity, and λ the second coefficient of viscosity. The resulting fluid stress tensor is:

$$P_{ij} = p\delta_{ij} - \mu \left(\frac{\partial C_i}{\partial x_j} + \frac{\partial C_j}{\partial x_i} \right) + \lambda \frac{\partial C_k}{\partial x_k} \delta_{ij} = p\delta_{ij} - \tau_{ij} \quad (2.3)$$

Depending on the relation between μ and λ , viscous dissipation should be present during volumetric variation:

- For inviscid fluid, both μ and λ are equal to zero. In such fluid, no viscous dissipation is possible.
- For compressible fluids with reversible volumetric variation, the bulk viscosity is null, $\lambda + \frac{2}{3}\mu = 0$ and $\mu > 0$. This condition is known as the Stokes' hypothesis. The viscous dissipation is due to all deformation except volumetric variation.
- For compressible fluids with irreversible volumetric variation, the bulk viscosity is positive, $3\lambda > -2\mu$ and $\mu > 0$. The pure volumetric variation, possible without fluid movement, is also a dissipative process.

For liquid, the pressure is related to the density through the Tait equation [32]. This is a none linear relation with 2 coefficients function of the temperature. However for water, the compressibility is quasi linear from 0 MPa up to 300 MPa. Therefore the speed of sound can be considered as constant over this range of pressure:

$$a^2 = \frac{\partial p}{\partial \rho} ; \text{ for water: } a = 1497 \text{ m/s} \quad (2.4)$$

2.1.2 Linear acoustics theory

In the frame work of the linear acoustic hypothesis, small deviations from a uniform reference state are considered:

$$\begin{aligned} p' &= p - p_0 \\ \rho' &= \rho - \rho_0 \\ C'_i &= C_i - C_{i,0} \end{aligned} \quad (2.5)$$

The transformations are assumed to be adiabatic. The viscous stress tensor is neglected, therefore inviscid fluid is considered. The wave equation is obtained by combining the time derivative of equation (2.1) and the divergence of equation (2.2). The pressure is substituted for density using equation (2.4). As the variations are small, the second order terms can be neglected, the following linear wave equation is obtained:

$$\frac{\partial^2 p'}{\partial t^2} - a^2 \frac{\partial^2 p'}{\partial x_i^2} = 0 \quad (2.6)$$

It describes the propagation of small perturbation in a homentropic fluid at rest. A convenient approach to describe the solution of this type of equation is based on the use of harmonic functions. It is particularly attractive for periodic phenomena. Solutions of the wave equation takes the following form:

$$p'(\mathbf{x}, t) = \hat{p} e^{i\omega t - i\mathbf{k} \cdot \mathbf{x}} \quad (2.7)$$

Introducing this particular solution in equation (2.6) leads to:

$$\frac{\omega}{a_0} = k_0 = |\mathbf{k}| = \frac{2\pi}{\lambda} \quad (2.8)$$

Where ω is the angular frequency, \mathbf{k} is the wave vector, k_0 is the acoustic wave number and λ the wave length.

The following development is restricted to the one dimensional situation. An illustration of the propagation of harmonic oscillation, in the semi infinite domain $0 \leq x < \infty$, is given in Figure 2.1. The pressure field is shown at various instant and location. The relation between the pulsation and the wave length through the speed of sound is clearly enhanced. Using the linear acoustic hypothesis, the momentum equation (2.2) in the x direction reduces to:

$$\rho_0 \frac{\partial C'}{\partial t} = - \frac{\partial p'}{\partial x} \quad (2.9)$$

Considering harmonic oscillation at given pulsation frequency, ω , and amplitude, \hat{p} and \hat{C} , equation (2.9) gives the following result in the frequency domain:

$$\hat{p}(x, \omega) = \rho_0 a_0 \hat{C}(x, \omega) \quad (2.10)$$

This equation relates the acoustic particle velocity to the acoustic pressure. The factor $\rho_0 a_0$ is called the characteristic acoustic impedance of the fluid. It represents the ratio of pressure to velocity amplitude. Now we consider the infinite domain, $-\infty < x < \infty$. An interface is located at $x = 0$ between two fluids or a fluid and a solid. An harmonic wave is traveling from the negative x toward the positive x , at the interface part of the wave is transmitted and the other part is reflected. Considering the acoustic field for $x < 0$, the

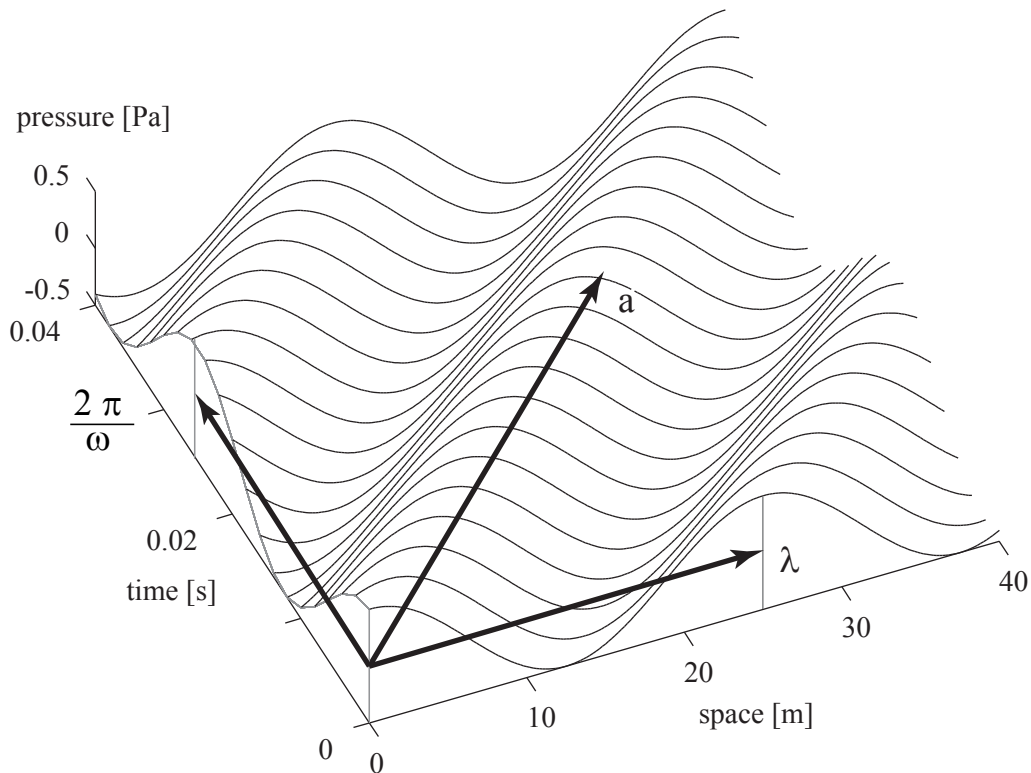


Figure 2.1: Propagation of acoustic wave from harmonic pressure fluctuation at $x = 0$.

pressure can be split in two components. One is propagating in the positive x direction, the other in the negative direction:

$$p'(x, t) = \hat{p}(x)e^{i\omega t} = p^+e^{i\omega t - ikx} + p^-e^{i\omega t + ikx} \quad (2.11)$$

It follows for $x = 0$ the interface between the two mediums:

$$p'(0, t) = \hat{p}(0)e^{i\omega t} = p^+e^{i\omega t} + p^-e^{i\omega t} \quad (2.12)$$

Where p^+ is the amplitude of the incident wave and p^- is the amplitude of the reflected wave. The impedance at the interface is defined as:

$$Z(0, \omega) = \frac{p'(0, t)}{C'(0, t)} = \frac{\hat{p}}{\hat{C}} \quad (2.13)$$

From the linear momentum equation (2.9), the velocity is given by:

$$\hat{C}(x) = \frac{1}{\rho_0 a_0} (p^+e^{-ikx} - p^-e^{ikx}) \quad (2.14)$$

Substituting equation (2.14) in the definition of the impedance at the interface (2.13) gives the following relation:

$$\frac{Z}{\rho_0 a_0} = \frac{p^+ + p^-}{p^+ - p^-} \quad (2.15)$$

The ratio on the left is a dimensionless number called specific impedance. Introducing the reflection coefficient R defined as $R = p^-/p^+$, equation (2.15) is written:

$$\frac{Z}{\rho_0 a_0} = \frac{1 + R}{1 - R} \quad (2.16)$$

The specific impedance can be used to characterize the reflection at the interface between two mediums:

- For $Z = \infty$, the wave is fully reflected, $R = 1$ and $p^- = p^+$. This condition is verified if the velocity fluctuation is null at the interface, $\hat{C}(x, \omega) = 0$;
- For $Z = 0$, the wave is fully reflected with a change of sign $R = -1$ and $p^- = -p^+$. This condition corresponds to a constant pressure at the interface $\hat{p}(x, \omega) = 0$;
- For $Z = \rho_0 a_0$, the wave is fully transmitted. $R = 0$ and $p^- = 0$. This condition is verified if both mediums share the same characteristic impedance.

2.1.3 Duct acoustic and plane wave propagation

In the previous Subsection, the analysis has been focused on the propagation of acoustic waves in infinite mediums. In case of acoustic waves in a confined domain such as a pipe, the reflection at the pipe wall has to be taken into account. For a rigid-walled pipe, the fluid velocity is equal to zero at the wall. In a pipe of rectangular cross section defined as $0 < y < W$ and $0 < z < H$, the wall boundary conditions are represented by:

$$\rho \frac{\partial C'_2}{\partial t} = -\frac{\partial p'}{\partial y} = 0, \text{ at } y = 0 \text{ and } y = W \quad (2.17)$$

$$\rho \frac{\partial C'_3}{\partial t} = -\frac{\partial p'}{\partial z} = 0, \text{ at } z = 0 \text{ and } z = H \quad (2.18)$$

A solution of the form (2.7) is assumed. In the y direction, the second component of the wave vector, k_n , takes the following form to respect the boundary conditions:

$$k_n = k_2 = \frac{n\pi}{W}, \quad n = 0, 1, 2, \dots \quad (2.19)$$

Similarly for the z direction, we have:

$$k_m = k_3 = \frac{m\pi}{H}, \quad m = 0, 1, 2, \dots \quad (2.20)$$

No boundary condition is imposed for the x direction and the general solution for the acoustic pressure field in a rectangular pipe is:

$$p'(x, y, z) = \sum_{n=0}^{\infty} \sum_{m=0}^{\infty} \cos\left(\frac{n\pi}{W}y\right) \cos\left(\frac{m\pi}{H}z\right) (A_{nm}e^{-ik_1x} + B_{nm}e^{ik_1x}) \quad (2.21)$$

Nevertheless to respect the wave equation (2.6), the following condition has to be verified:

$$k_1^2 + k_2^2 + k_3^2 = k_0^2 \quad (2.22)$$

As long as $k_{mn} = \sqrt{k_n^2 + k_m^2}$ is less than k_0 , the wave number k_1 is real and the wave propagates. But for k_0 smaller than k_{mn} , k_1 is imaginary and the wave is evanescent. This is a very important result for the present study. There is no propagation for a given mode below the cut-off frequency:

$$f_{cutoff,nm} = a_0 \left(\frac{n}{2W} + \frac{m}{2H} \right) \quad (2.23)$$

The mode $n = m = 0$ is particular as no cut-off frequency is defined. It corresponds to plane wave propagation along the pipe axis x . As shown in equation (2.23), the cut-off frequency is proportional to the speed of sound and inversely proportional to the height or width of the pipe. Below the cutoff frequency ($f_{cutoff} = 19'000$ Hz, in the present case study), only the mono-dimensional mode of propagation exists. The present study is focused on low frequency as the HA model describes only the plane wave propagation mode.

2.2 Hydrodynamic sources of sound

2.2.1 Lighthill's acoustic analogy

The Lighthill analogy describes the mechanism of sound generation by flow. The analogy is based on the representation of the complex fluid dynamic process of sound generation by an acoustically equivalent source term. The Lighthill's equation is derived without approximation from the Navier-Stokes equations. Similarly to (2.6), the time derivative of the mass conservation (2.1) and the divergence of the momentum conservation (2.2) are combined. The following equation is obtained:

$$\frac{\partial^2 p}{\partial x_i^2} = \frac{\partial^2 \rho}{\partial t^2} + \frac{\partial^2}{\partial x_i \partial x_j} (\tau_{ij} - \rho C_i C_j) \quad (2.24)$$

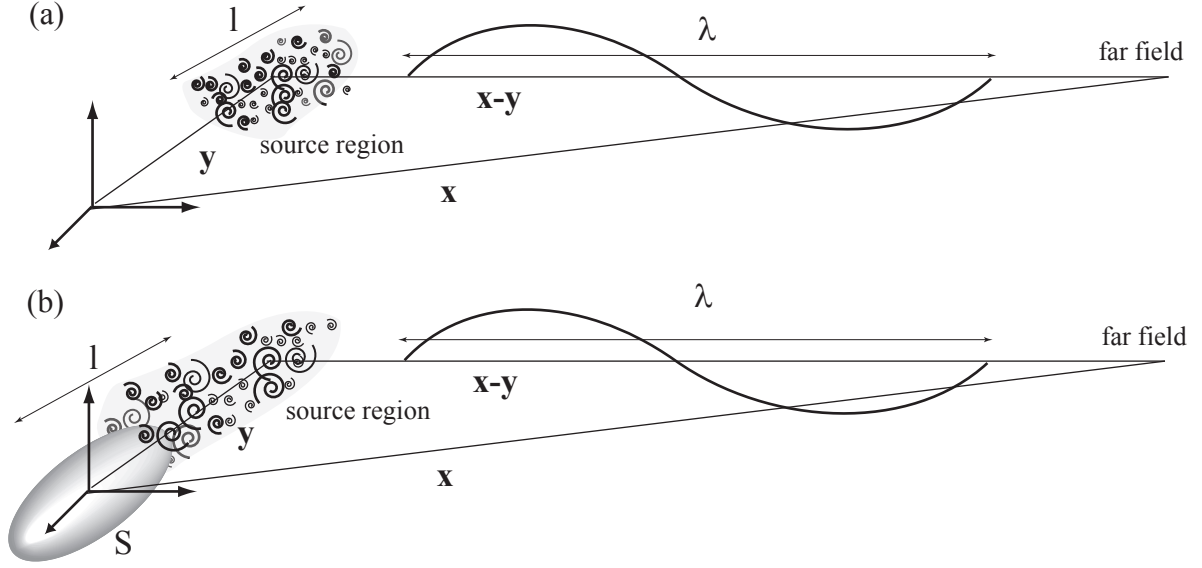


Figure 2.2: Noise induced by turbulence in free field (a); in the presence of a solid body (b).

The viscous stress tensor τ_{ij} is defined as:

$$\tau_{ij} = \mu \left(\frac{\partial C_i}{\partial x_j} + \frac{\partial C_j}{\partial x_i} \right) - \lambda \frac{\partial C_k}{\partial x_k} \delta_{ij} \quad (2.25)$$

Small deviations from a uniform field with reference pressure p_0 and reference density ρ_0 are considered. Subtracting $a_0^{-2} \frac{\partial^2 p'}{\partial t^2}$ in equation (2.24) gives the Lighthill equation (2.26) with the pressure as acoustic variable:

$$\frac{1}{a_0^2} \frac{\partial^2 p'}{\partial t^2} - \frac{\partial^2 p'}{\partial x_i^2} = \frac{\partial^2}{\partial x_i \partial x_j} (\rho C_i C_j - \tau_{ij}) + \frac{\partial^2}{\partial t^2} \left(\frac{p'}{a_0^2} - \rho' \right) \quad (2.26)$$

In this form, the equation is exact but can not be conveniently solved. The concept of the Lighthill analogy consists in separating the space in two regions, the source region and the far field. The sound or acoustic perturbation is assumed to be generated only in a localized region where hydrodynamic fluctuations are intense. If this source region is small with respect to the wave length of interest ($l \ll \lambda$), the source is compact and can be approximated as a point source, see Figure 2.2 (a). In the far field, the fluid is assumed to be at rest and small perturbations are considered. The fluid properties are described by the linear acoustic theory with perturbations emanating from the point sources. The left hand side of equation (2.26) describes the propagation of acoustic perturbation and the right hand side the generation of sound by hydrodynamic fluctuation.

Two types of sources are distinguished:

- The sources due to the non-linear convective forces $\rho C_i C_j$ and the viscous forces τ_{ij} ;
- The sources due to the deviation from a uniform sound velocity a_0 or the deviation from an isentropic behavior.

For low Mach number, M , and high Reynolds number, Re , and no phase change, $\rho C_i C_j \approx \rho_0 C_i C_j$, the viscous stress τ_{ij} and the second term on the right of equation (2.26) are

negligible. Using free space Green's function, the solution of (2.26) is given by:

$$p'(\mathbf{x}, t) \approx \frac{\partial^2}{\partial x_i \partial x_j} \int_{V_0} \frac{\rho_0 C_i C_j(\mathbf{y}, t - |\mathbf{x} - \mathbf{y}|/a_0)}{4\pi |\mathbf{x} - \mathbf{y}|} d^3 \mathbf{y} \quad (2.27)$$

Where V_0 is the source region, \mathbf{y} the position of the point source and \mathbf{x} the position of the listener in the far field, $|\mathbf{x} - \mathbf{y}| > \lambda$. The integrand is evaluated at the retarded time $t - |\mathbf{x} - \mathbf{y}|/a_0$. This formulation is valid for sound generated aerodynamically by low Mach number turbulence in a medium which is at rest at infinity and has uniform density.

2.2.2 Influence of solid body

In the presence of a solid body in the flow, Curle (2.28) identified an additional sound source due to the body [25]. For a compact body ($l \ll \lambda$) bounded by the surface, S , located at the origin and surrounded by a compact turbulent source region ($\mathbf{y} \ll \lambda$), see Figure 2.2 (b), the solution of (2.24) using free space Green's function is the given by:

$$p'(\mathbf{x}, t) \approx \frac{x_i x_j}{4\pi a_0^2 |\mathbf{x}|^3} \frac{\partial^2}{\partial t^2} \int_{V_0} [\rho C_i C_j] d^3 \mathbf{y} - \frac{1}{4\pi |\mathbf{x}|} \frac{\partial}{\partial t} \int_S [\rho C_i n_i] d^2 \mathbf{y} - \frac{x_j}{4\pi a_0 |\mathbf{x}|^2} \frac{\partial}{\partial t} \int_S [(P_{ij} + \rho C_i C_j) n_i] d^2 \mathbf{y} \quad (2.28)$$

The square brackets denotes evaluation at the retarded time. The first term of (2.28) is the pressure fluctuation due to turbulence similarly to equation (2.27). The second term is due to the normal velocity of the body surface. The last term is connected with the momentum flux through the surface and the fluid stress tensor at the surface. For rigid body with no slip condition, the velocity is equal to zero on the surface. Therefore, the second term of (2.28) and the Reynolds stress tensor in the third term are vanishing. Consequently the integral of the third term is equal to the force applied by the fluid on the body.

Dimensional analysis helps to emphasize the relative importance of the different terms of (2.28). The characteristic time scale of the flow is determined by the Strouhal number $St = \frac{fl}{C_0}$. As St is quasi constant for a given obstacle, we have $\partial/\partial t \sim C_0/l$. The volume and surface integral scales respectively with l^3 and l^2 . The Reynolds stress is of order $\rho_0 C_0^2$. Based on the definition of the drag coefficient $c_D = F_D/0.5\rho_0 C_0^2 l^2$, we have $F_D \sim \rho_0 C_0^2 l^2$. From equation (2.28), the order of magnitude of the pressure fluctuation in the far field is estimated as:

$$p' \sim \frac{1}{|\mathbf{x}| a_0^2} \left(\frac{C_0}{l}\right)^2 (\rho_0 C_0^2) l^3 - \frac{1}{|\mathbf{x}|} \left(\frac{C_0}{l}\right) (\rho_0 C_0) l^2 - \frac{1}{a_0 |\mathbf{x}|} \left(\frac{C_0}{l}\right) (\rho_0 C_0^2 + \rho_0 C_0^2) l^2 \quad (2.29)$$

Introducing M , the first term due to the turbulence scales as:

$$p' \sim \frac{l \rho_0 C_0^2}{|\mathbf{x}|} M^2 \quad (2.30)$$

The second term due to the fluctuation of the body's volume scales as:

$$p' \sim \frac{l\rho_0 C_0^2}{|\mathbf{x}|} \quad (2.31)$$

And the last term due to the momentum flux through the surface and the force on the body surface scales as:

$$p' \sim \frac{l\rho_0 C_0^2}{|\mathbf{x}|} M \quad (2.32)$$

For solid body, the volume fluctuation and the momentum flux is null. It follows for low Mach number flow that the third term is predominant with respect to the first term; and the direct turbulence noise can be neglected. Therefore, the acoustic perturbation in the far field can be predicted from the time history of the force acting on an immersed solid body:

$$p'(\mathbf{x}, t) \approx \frac{x_i}{4\pi a_0 |\mathbf{x}|^2} \frac{\partial F_i}{\partial t} (t - |\mathbf{x}|/a_0) \quad (2.33)$$

2.2.3 Single bubble noise

According to the dimensional analysis, see equation (2.29), the second term of (2.28) is predominant for low Mach number flow. Consequently, the pressure fluctuation in the far field induced by small oscillation of a spherical bubble takes the following form in the spherical coordinate system [13]:

$$p'(r, t) = \frac{\rho_0 \frac{\partial^2 V}{\partial t^2} (t - (r - R_0)/a_0)}{4\pi r} \quad (2.34)$$

where $p(r, t)$ is the pressure at time t and at a distance r from the bubble center. $\frac{\partial^2 V}{\partial t^2}$ is the volumetric acceleration of the bubble. $(t - (r - R_0)/a_0)$ account for the travel time of the wave from the bubble surface to position r . If the mass transfer at the gas/liquid interface is neglected, this development is also valid for vapor cavity.

2.2.4 Dipole sound from cylinder

Vortex shedding in the wake of cylinder is a well documented case of flow instability leading to acoustic perturbation [11, 97]. The formation of a wake results in a force in opposite direction to the flow. For flow parallel to the x axis, the mean drag coefficient is introduced as:

$$\bar{c}_D = \frac{\bar{F}_x}{\frac{1}{2}\rho C^2 DL} \quad (2.35)$$

Where F_x is the drag force, C is the flow velocity, D the cylinder diameter and L is its length. At high Reynolds number, the dimension of the separation zone is function of the Reynolds number, the drag coefficient is Re dependant.

The flow past a bluff body is characterized by the formation of two shear layer of opposite vorticity on each side of the body. At high Reynolds number, the interaction

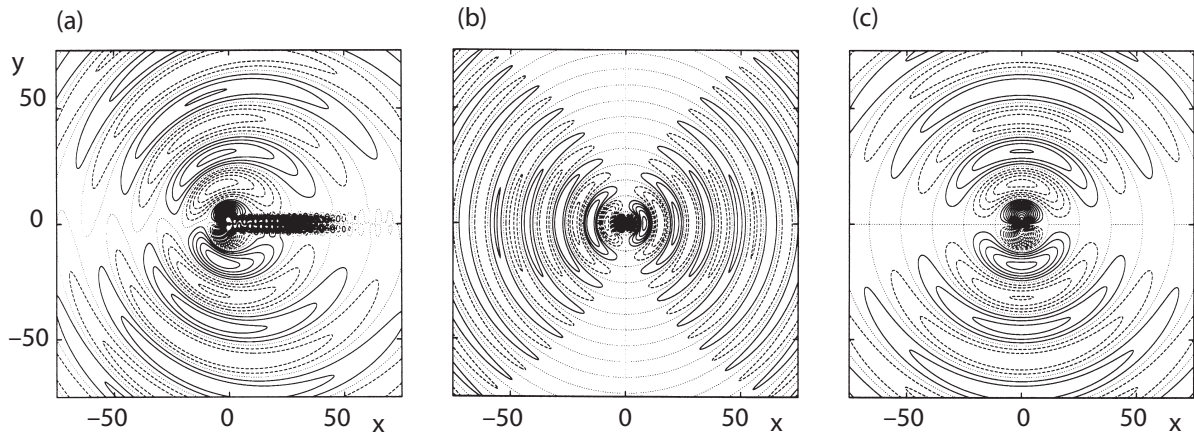


Figure 2.3: Pressure field of flow past a cylinder for $M = 0.2$ and $Re = 150$ from DNS (a), using Curle's solution for drag force F_x (b) and lift force F_y (c). The contour plot increment is equal to $0.0025M^{2.5}$ for (a),(c) and $0.00025M^{2.5}$ for (b); Reprinted from [48].

of the shear layers in the wake becomes absolutely unstable and results in the alternate shedding of vortices of opposite sign. The shedding frequency is given by the Strouhal number $St = fD/C$ which is also function of Re . The lift force is proportional to the resulting circulation around the bluff body and its frequency is equal to the vortex shedding frequency. As two alternate vortices are shed in each period, the fluctuating part of the drag force has a frequency equal to twice the vortex shedding frequency.

It is important to notice that the phase of the vortex shedding varies along the axis of the cylinder especially for turbulent flow regime. The resulting drag force is distributed over a given frequency range; the fluctuation is never purely harmonic for turbulent flow.

In the far field, the pressure field can be estimated using Curle's equation (2.33). The component parallel to the main flow corresponds to the fluctuating part of the drag force. The component perpendicular to the main flow corresponds to the lift force. In Figure 2.3, the pressure field resulting from the vortex shedding past a circular cylinder at low Mach and low Reynolds number has been computed using compressible DNS (a). The fluctuation computed using the Curle's equation from the drag (b) and lift force(c) are compared with the exact solution (a). This direct numerical simulation of the two-dimensional compressible Navier-Stokes equation for low M has been performed by O. Inoue and N. Hatakeyama [48] Due to the low Re , the fluctuation is harmonic. The directivity of the acoustic source in the y direction is clearly visible in (a). The amplitude in the x direction (b) is much smaller than in the y direction (c) and the frequency in the x direction is twice the frequency in the y direction.

2.2.5 Distinction of the acoustic and turbulent fields

Following Ribner's developments, the pressure fluctuations may be split into two components [79]:

$$p' = p'_t + p'_a \quad (2.36)$$

the pseudo-sound p'_t is associated with the convective motions of the fluid and the acoustic pressure p'_a with propagation of compression waves. Neglecting the viscous force and the

non-isentropic effects in (2.26), the pseudo-sound is defined as:

$$\frac{\partial^2 p'_t}{\partial x_j^2} = -\rho_0 \frac{\partial}{\partial x_i \partial x_j} (C_i C_j) \quad (2.37)$$

And the acoustic pressure is defined as:

$$\frac{1}{a_0^2} \frac{\partial^2 p'_a}{\partial t^2} - \frac{\partial^2 p'_a}{\partial x_j^2} = -\frac{1}{a_0^2} \frac{\partial^2 p'_t}{\partial t^2} \quad (2.38)$$

for the case of vortex shedding presented in Figure 2.3. In the turbulent region of the wake, the pressure is dominated by the pseudo-sound which is accounted for in Figure 2.3 (a) only. In the far-field, the pressure is dominated by the acoustic pressure therefore the exact solution (a) and the solution based on Curle's equation (b) and (c) are equivalent.

Chapter 3

Cavitation

3.1 Cavitation inception

Cavitation describes the transition from liquid to gaseous phase at quasi constant temperature. For water at ambient temperature, cavitation occurs at vapor pressure, $p_v = 2338$ Pa. In a steady flow field, the pressure decreases in region with high velocity. The minimum pressure in a hydraulic system depends on the characteristic pressure drop due to an obstacle, δp , and the reference pressure in the far field, p . The cavitation level in the system is therefore defined using the cavitation index σ :

$$\sigma = \frac{p - p_v}{\delta p} \quad (3.1)$$

Below a given σ , defined as incipient cavitation number, σ_i , cavitation is expected in the system. The value of σ_i depends mostly on the geometry of the obstacle. However, surface tension inhibits the transition from liquid to gas. For this reason, transition occurs only at cavitation nuclei with sufficiently low surface tension. This blocking action of the surface tension is strongly dependant on the size of the nuclei. Additionally, in flow at high Reynolds number, the turbulence induces fluctuation of pressure. Therefore the incipient cavitation number at a given temperature is triggered by the ambient pressure and the characteristic pressure drop, the turbulence level and the cavitation nuclei size and population in the flow.

3.2 Wake cavitation

Various types of cavitation may occur depending on the flow. In the present study, the focus is on the turbulent wake cavitation, see Figure 3.1. This type of flow has been analyzed by Belahadji [10]. The flow is characterized by an intense shear and a high level of turbulence. His observation are restricted to wedge induced wakes. Nevertheless his results are qualitatively applicable to wakes induced by any thick obstacles [40]. Cavitation appears in 3 different structures:

- Large quasi 2D vortices parallel to the cylinder generator called primary vortices;
- Small 2D vortices in the shear layer;
- 3D vortex filaments appearing in the streamwise direction called secondary vortices.



Figure 3.1: Cavitating vortices in the separated wake of a lifting flat plate with a flap; the flow is from the right to the left; Reprinted from [14].

At incipient cavitation number, the cavitation appears primary in the 3D vortex filaments due to the high level of vorticity in this region.

Those cavitation structures are strongly related with the structure of the flow field. The wake is essentially structured in 3 zones:

- The near wake close to the obstacle is a dead zone bounded by two shear layers of intense vorticity;
- The intermediate transition region, in this region the successive pairing of vortices results in the formation of the primary and probably secondary vortices;
- The far wake where primary and secondary vortices are convected by the mean flow.

The shedding frequency of the primary vortices is normalized using the Strouhal number. For cavitation index above σ_i , the Strouhal number is independent of σ and weakly dependant on the Reynolds number. For lower cavitation level, the flow is weakly influenced by the cavitation and St remains constant. Further decrease of σ , corresponding to a more intense cavitation, leads first to an increase of the Strouhal number up to a maximum value of more then 20 percent its non cavitating value. It is followed by a decrease of the shedding frequency [10, 47, 8]. For very low σ , a fully developed cavity is observed in the wake and the periodicity of the phenomenon is lost.

3.3 Mathematical models

The cavitation models used in CFD code can be divided in 3 families [93, 1]:

- Single-phase interface tracking model;
- Multi-phase state equation based model;
- Multi-phase transport equation based model.

In inhomogeneous multi-phase models, the flow fields of the gaseous phase and liquid phase are distinct. In homogeneous multi-phase models, single-fluid modeling approach is employed for both phases.

In the single-phase interface tracking model, the computation is done only in the liquid phase region [19, 46]. The cavity is assumed to have a constant pressure equal to the vapor pressure. The liquid-vapor interface is tracked based on this assumption and the cavity

is excluded from the computational domain. Such model is not adequate for detached cavitation. [93].

In the multi-phase state equation based model; Various methodology have been proposed to compute the density field:

- An energy or enthalpy equation is added to the Navier-Stokes equations [92].
- An arbitrary barotropic equation of state is employed [27].
- The time dependant Rayleigh-Plesset equation is coupled to the flow solver and the void fraction is based on the bubble radius [56].

In multi-phase transport equation based model an additional transport equation for the gaseous phase is added to the Navier-Stokes equations [85, 57]. The vapor volume/mass fraction is regulated by a source term dependant on the pressure. Empirical factors must be introduced to regulate the mass transfer. These factors have a significant influence on the dynamic of cavity volume.

Chapter 4

Problem statement

4.1 Objective

The objective of the present work is to predict the conditions leading to flow induced acoustic resonance in cavitating pipe flow and to evaluate the resulting pressure fluctuation amplitude. To achieve this purpose, the methodology is developed in order to forecast on the spatial distribution, the frequency and the amplitude of the pressure fluctuations in the entire system based on the identification of the acoustic resonance frequencies, the precise evaluation of sources of acoustic perturbation and the complete description of the acoustic feedback on the sources.

4.2 Proposed approach

To model the interaction of localized hydrodynamic instabilities with the acoustic field, a computational methodology consisting in the coupling of two models is proposed:

- A local hydrodynamic (HD) model is used to describe the hydrodynamic instability and the formation of vapor in the source region. The incompressible unsteady Reynolds Averaged Navier-Stokes equations are solved using the most suitable turbulence model. A cavitation model is also included to predict the volume of gaseous phase.
- A global hydroacoustic (HA) model is used to analyze the propagation of acoustic plane waves in the entire pipe including the source region. This model is mono-dimensional and a viscoelastic relation is included in the model to account for the pipe wall deformation and its influence on the propagation of acoustic waves.

For cavitation free flow conditions, a two-way coupled approach is proposed. The interaction between the HA and the HD model is presented in Figure 4.1 (a). The difference between the solution of the HD model and the HA model in the source region is used to adjust the correction terms of the HA model, the mass and the momentum source. To account for the acoustic feedback, the boundary conditions of the HD model are adjusted with the state variables of the HA model, the pressure and the velocity in the source region.

For cavitating flow conditions a different method is proposed. A compromise between fully coupled approach and field elimination technique is proposed, see Figure 4.1 (b). The sources are decomposed in two components assumed to be independent. The component

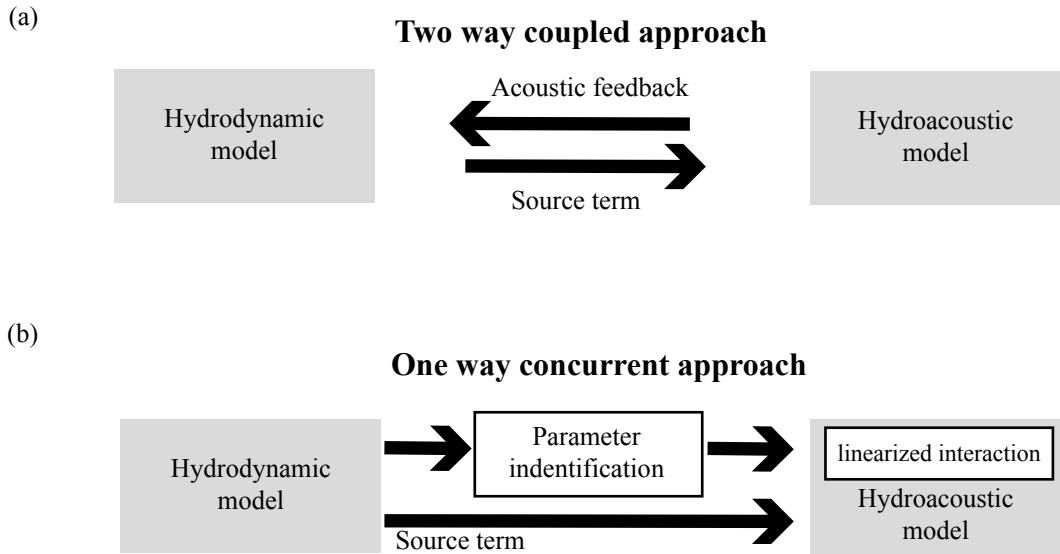


Figure 4.1: Modeling methodology for cavitation free (a) and cavitating regime (b).

due to the hydrodynamic fluctuation and the component due to the acoustic fluctuation. The time dependant mass and momentum source due to the hydrodynamic component are computed in a first step using the HD model. From the computed results of the HD model, linearized interaction parameters are identified to account for the acoustic component of the sources. Those parameters are then employed in the HA model in combination with the hydrodynamic sources of mass and momentum.

4.3 Structure of the document

In part I, the principal concepts necessary for the understanding of the present work are introduced. In Chapter 1, the motivation and the context of the study are presented. Chapter 2 introduces the hydroacoustic approach, its advantage and limitations. In Chapter 3, the cavitation and its mathematical description are briefly presented. The objective and the proposed approach are stated in Chapter 4.

In part II, the computational methodology and its application to the reference case study is presented in details. Chapter 5 presents the experimental setup and the measurements results. In Chapter 6, the propagation of pressure wave in pipe is described. Starting from the conservation laws, a mono-dimensional description of the phenomenon is given. This description is used to construct a mathematical model of the acoustic resonator called HA model, this model is applied to the reference case study. In Chapter 7 the deviation of this mono-dimensional model from its exact 3D counterpart in the perturbed region is identified as a mass and a momentum source. A method is proposed to compute the source terms using the HD model. Two methods are proposed to describe the mechanism of acoustic feedback on the hydrodynamic sources. In Chapter 8 the incompressible 3D model used to describe the source source region is presented and the evaluation of the sources is validated.

In part III, the results of the computational methodology are presented for the refer-

ence case study. In Chapter 9, setups and results are presented for one-way and two-way simulation in cavitation free flow regime. In Chapter 10, the setup and results are presented for the one-way concurrent simulation in cavitating flow regime. The two-way coupled simulation is unstable for cavitating flow regime.

In part IV, the conclusions regarding the application of the method to the reference case study are drawn in chapter 11. Finally in chapter 12, the perspectives of application of the method to Francis turbine surge are presented.

Part II

Reference case study

Chapter 5

Reference experiment

5.1 Setup

5.1.1 Installation

To validate the computational strategy, a specific experimental setup has been installed at the EPFL, Laboratory for Hydraulic Machines. The purpose of the experiment is to study the hydroacoustic resonance in a pipe induced by flow perturbation. The hydroacoustic resonator is a square-cross-sectional PVC pipe (length: 1050 mm, inner dimension: 40 mm \times 40 mm, wall thickness: 2 mm) connecting two tanks. The perturbation is induced by a semi circular bluff body (diameter: 20 mm) located at $\frac{3}{4}$ of the pipe length. The bluff body is mounted perpendicular to the flow and is embedded on both sides in a purposely designed Plexiglas support. The rounded side faces upstream and the flat side downstream. The flow velocity in the pipe is controlled by a variable speed pump, see Figure 5.1 and the hydrostatic pressure is adjusted using a vacuum pump connected to the downstream tank. The water used in the experiment is air saturated tap water. During all experiments, the water temperature is kept constant at 293 ± 3 K. The reflection of plane waves at the pipe ends is achieved using tanks with free surface. The influence of the free surface level on the resonance frequency has been verified, no significant effect has been measured. In order to have a stable flow at the pipe inlet, the upstream tank is equipped with a convergent (1/25 cross section ratio); after settling in the upstream tank, the flow goes first through a honeycomb (5 mm hexagon mesh), a screen (10 mm holes for 1/4 open area ratio) and the convergent before entering the pipe. The outlet of the pipe consists in an abrupt change of cross section (cross sectional area ratio 2.4). No end correction is introduced as this error can be neglected with respect to the uncertainty regarding the determination of the propagation velocity.

5.1.2 Instrumentation

The flow velocity is monitored with a vortex flow meter (range: 0 – 70 m³/h) placed between the circulating pump and the upstream tank. High speed camera (resolution: 640 \times 512 pixels, acquisition rate: 3000 frames/sec, exposure time: 80 μ s) is used for the visualization of the wake cavitation. To achieve proper visual access, the bluff body support is made of Plexiglas elements (total length: 70 mm, inner dimensions: 40 mm \times 40 mm, wall thickness: 40 mm).

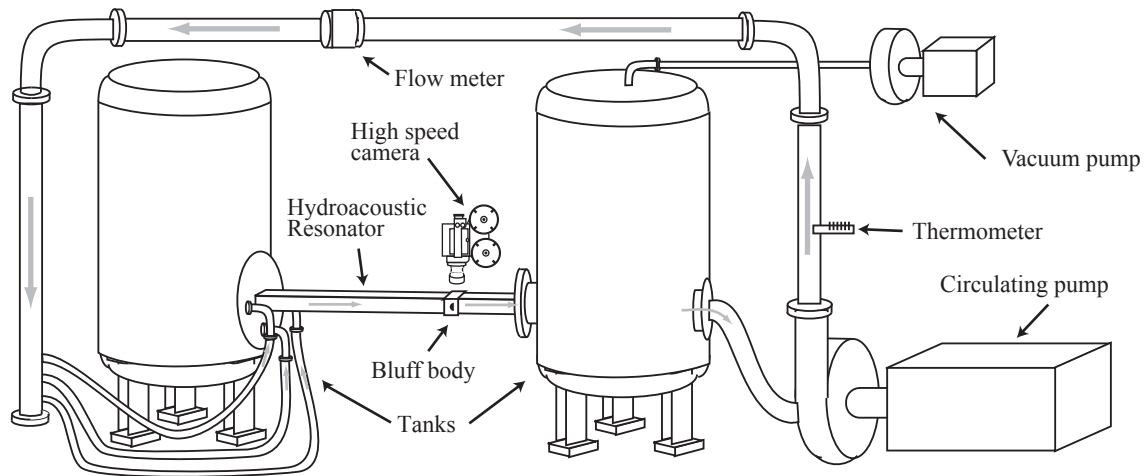


Figure 5.1: Experimental setup.

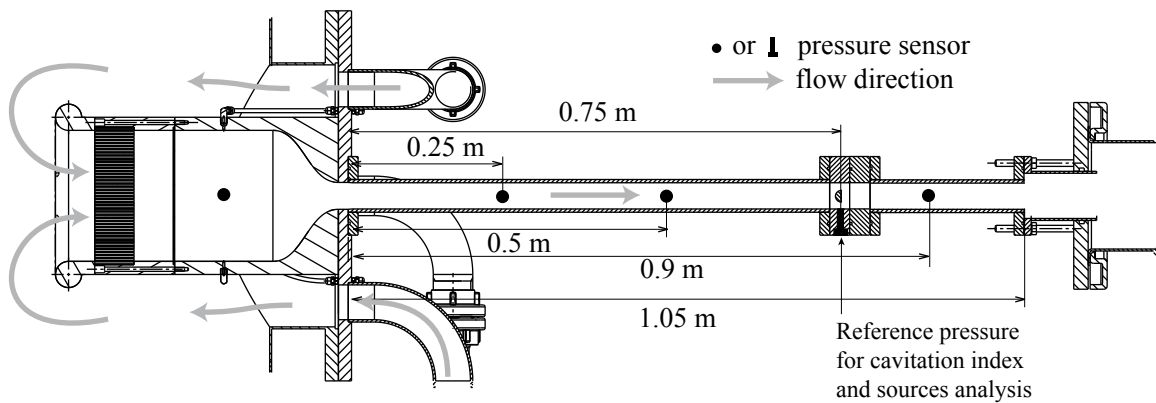


Figure 5.2: Pressure sensors positions.

Dynamic and static pressure measurement

Acoustic eigenfrequencies and eigenmodes shapes are measured with flush mounted piezoresistive pressure sensors distributed along the hydroacoustic resonator; positions are given in Figure 5.2. The sensor located in the downstream tank is not indicated in the figure. The sensor located below the mid-span trailing edge of the bluff body is also employed to determine the vortex shedding frequency. Static calibration of all sensors has been performed for absolute pressures ranging from 0.2 to 1.8 bar. The dynamic response has been validated in a previous experimentation by Farhat et al [35].

The pressure is simultaneously recorded at all locations. After amplification, all signals are digitalized synchronously with a NI DAQ6221 (sampling frequency: 1000 Hz, nb. of channels: 5). In the frequency domain, Welch method is used for the averaging [95]; the parameters for the averaging are given in Table 5.1.

Table 5.1: Welch's method parameters.

Parameter	Value
Sampling frequency	1000 Hz
Time signal duration	66 s
Spectral resolution	0.98 Hz
Window size	2^{10} samples
Window overlap	2^8 samples
Window type	Hamming

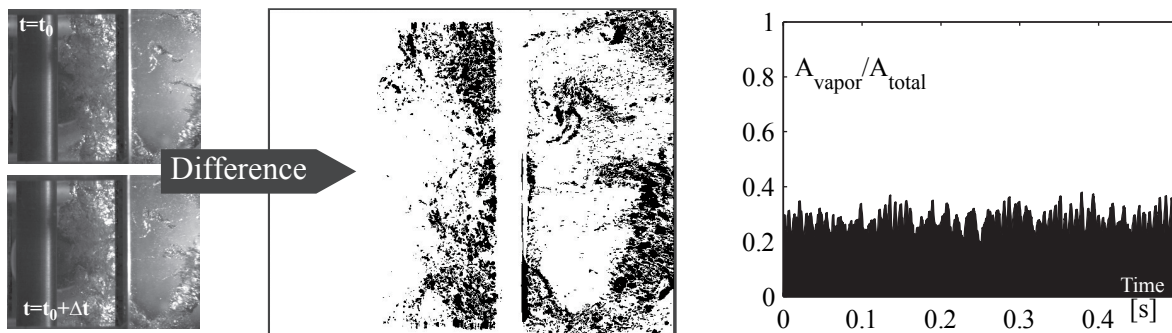


Figure 5.3: Video analysis of the vapor fraction in the wake of the bluff body.

Video analysis

The volume of vapor is estimated with video analysis. To identify the gaseous phase, a motion detection algorithm has been used, see Figure 5.3. The method is based on the comparison of two successive images. As the liquid phase is transparent and the gaseous phase is visible, the cavity is identified as the moving part of the image. The volume of vapor is estimated from the time history of moving area fraction. This method is sufficient to measure the fluctuation frequency but the error on the absolute volume is large as the information is only two-dimensional.

5.2 Flow conditions

5.2.1 Incipient cavitation index

The cavitation index is calculated using the method introduced in Chapter 3. As the cavitation appears in the wake of the bluff body, the characteristic pressure drop is based on the flow velocity in the pipe and the ambient pressure is measured with the closest sensor from the bluff body. The cavitation index is given by:

$$\sigma = \frac{p - p_v}{\frac{1}{2}\rho C^2} \quad (5.1)$$

where p is the absolute pressure measured below the bluff body, see Figure 5.2 for the pressure sensor location. $p_v = 2338$ Pa is the water vaporization pressure at 293 K and C is

the flow velocity in the pipe. To determine the incipient cavitation index, visual inspection of the flow at various flow velocity and cavitation level have been performed. No significant influence of Re on the incipient cavitation index has been observed over the investigated range of flow velocity ($5 \cdot 10^4 < Re < 1.15 \cdot 10^5$). The incipient cavitation is observed in intermittent filament structures appearing near the pipe wall at approximately $1D$ downstream the bluff body for:

$$\sigma < \sigma_i \simeq 9 \quad (5.2)$$

5.2.2 Cavitation free conditions

In cavitation free conditions measurements have been performed at constant flow velocity, the flow conditions have been modified by steps of 0.25 m/s for velocity ranging from 1.25 m/s to 3.5 m/s, corresponding to $f_s/f_n = 0.5$ and $f_s/f_n = 1.41$ respectively. Where f_s is the source frequency proportional to the flow velocity and f_n is the natural frequency of the system for cavitation free flow conditions. The measurements have been repeated for various water levels in the upstream and down stream tanks. No significant influence of the water level on the pressure fluctuation amplitude and frequency have been detected. The investigated flow conditions are summarized in Table 5.2.

Table 5.2: Investigated flow conditions.

Cavitation free flow conditions										
Flow velocity [m/s]	1.25	1.50	1.75	2.00	2.25	2.50	2.75	3.00	3.25	3.50

Cavitating flow conditions, variable σ						
Flow velocity [m/s]	2.50	3.00	3.50	4.00	4.50	5.00

Cavitating flow conditions, variable C			
Cavitation index [-]	9.90	6.50	5.50

The dimensionless numbers characterizing the flow are:

$$Re = \frac{CD}{\nu} \simeq \frac{3 \cdot 0.02}{10^{-6}} = 60'000 \quad (5.3)$$

$$M = \frac{C}{a_c} \simeq \frac{3}{202.65} = 0.015 \quad (5.4)$$

The Reynolds number is based on an average flow velocity of $C = 3$ m/s; the bluff body diameter, $D = 0.02$ m; and the kinematic viscosity of water at 293 K, $\nu = 10^{-6} \text{ m}^2 \cdot \text{s}^{-1}$. The Reynolds number is sufficiently high to guaranty a fully turbulent flow. The Mach number is based on the average flow velocity, $C = 3$ m/s; and the average propagation velocity in the pipe based on the natural frequency of the pipe, $2L_{TOT}f_n = a_c = 202.65$ m/s. The small Mach number indicates a weak influence of the compressibility.

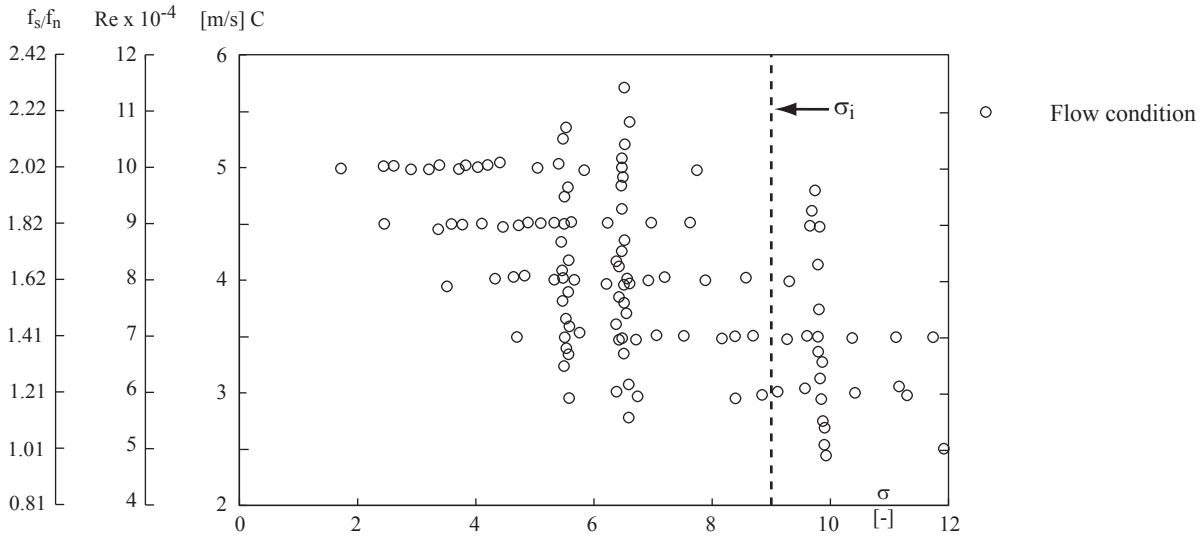


Figure 5.4: Investigated flow conditions in cavitating regime; flow velocity vs. cavitation index.

5.2.3 Cavitating conditions

In cavitating conditions, two methods have been used to perform the measurements:

- At constant flow velocity, the hydrostatic pressure in the pipe has been changed by step of 2000 Pa from atmospheric pressure to minimum pressure reachable using the vacuum pump. The process has been repeated for $C = 2.5$ m/s to $C = 5$ m/s by step of 0.5 m/s.
- At constant cavitation index, the velocity have been changed by step of 0.1 m/s. At each step the hydrostatic pressure has been adjusted to maintain the cavitation index. The process has been repeated for $\sigma/\sigma_i = 1.1$, $\sigma/\sigma_i = 0.73$ and $\sigma/\sigma_i = 0.62$.

The investigated flow conditions in cavitating regime are summarized in Table 5.2 and in Figure 5.4.

5.3 Sources of pressure fluctuation

5.3.1 Force on bluff body and resulting momentum source

The flow instability in the wake of the bluff body is the main source of the pressure fluctuation in the pipe. This type of flow is well described as a pair of dipole sources, see Subsection 2.2.4. One is parallel to the pipe axis and connected to the drag force, the other is perpendicular and connected to the lift force. The source inducing plane wave corresponds to the drag force. For this reason, the source frequency, f_s , is equal to twice the lift frequency, f_L :

$$f_s = f_D = 2f_L = \frac{2St}{D}C \quad (5.5)$$

To describe the source, the sensor located below the bluff body has been used, see

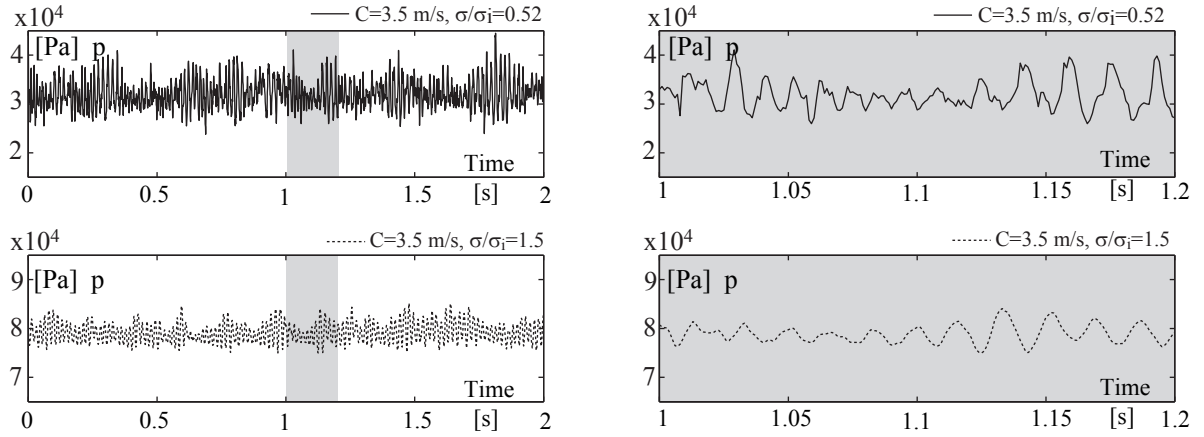


Figure 5.5: Example of pressure history below the bluff body, in cavitation, $\sigma/\sigma_i = 0.52$ and cavitation free regime $\sigma/\sigma_i = 1.5$.

Subsection 5.1.2. The pressure history is characterized by a periodic fluctuation with an unsteady low frequency modulation. Typical pressure history are presented in Figure 5.5 for cavitation and cavitation free regime.

Frequency and amplitude

In Figure 5.6, the pressure fluctuation below the bluff body is presented for various flow velocity values in cavitation free regime. Near the bluff body, the hydrodynamic fluctuation connected with the lift is much larger than the acoustic fluctuation connected with the acoustic fluctuation, the acoustic resonance is therefore not visible. The waterfall spectrum (a) of pressure fluctuation is plotted for flow velocity ranging from 2.5 m/s to 4.8 m/s. The acoustic resonance is hardly visible as the acoustic fluctuation is much smaller than the hydrodynamic fluctuation. The frequency value with maximum amplitude corresponding to the lift frequency is reported in (b). The lift frequency is linearly proportional to the flow velocity. The standard deviation of the pressure coefficient is presented in (c). The fluctuation amplitude of the pressure coefficient is constant with respect to the flow velocity. The momentum source frequency is therefore proportional to the flow velocity and the momentum source amplitude is proportional to the square of the flow velocity.

The vortex shedding frequency is known to vary with the cavitation index and Reynolds number. To investigate the influence of σ on the momentum source frequency, measurements of f_s have been performed for various σ values. The lift frequency ($f_s = 2f_L$) is presented in Figure 5.7 (a) for cavitation and cavitation free regime. Using linear regression, see Figure 5.7 (a), the mean value and standard deviation of the Strouhal number have been calculated (68% confidence bound):

$$St = \frac{f_L D}{C} = 0.39 \pm 0.006 \quad (5.6)$$

This particularly high value of St is due to the confinement $D/H = 0.5$ [71].

In Figure 5.7 (b), the Strouhal number is presented versus the cavitation index. For the selected range of cavitation index, $\sigma/\sigma_i > 0.5$, the cavitation has no influence on the

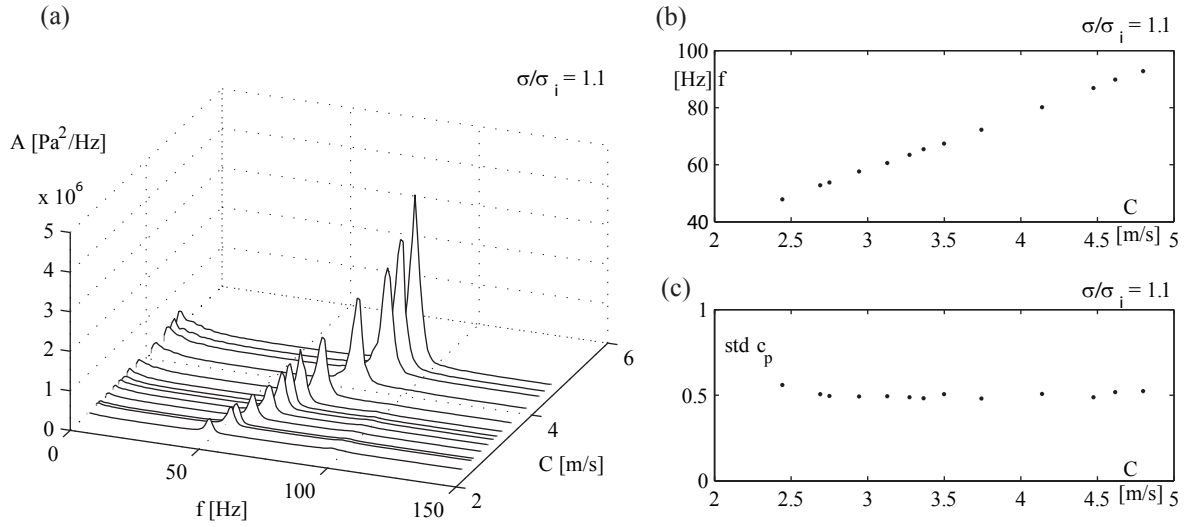


Figure 5.6: Lift frequency versus flow velocity for $\sigma/\sigma_i = 1.1$; (a) waterfall spectrum of pressure fluctuation below the bluff body; (b) lift frequency; (c) fluctuation amplitude of pressure coefficient.

vortex shedding frequency; St increases solely for very low σ . Similar behavior has been described in the literature, see Chapter 3. No significant variation of St is observed over the explored range of flow velocities, see Figure 5.7 (c). The momentum source frequency is therefore directly proportional to the flow velocity and no corrective coefficient is needed for the selected range of flow velocity ($0.5 \cdot 10^5 < Re < 1.15 \cdot 10^5$).

Mean value

To determine the mean drag force on the bluff body, indirect method has been used. The force is measured using the pressure difference between the sensors located upstream and downstream the bluff body, positions $L/L_{TOT} = 0.5$ and $L/L_{TOT} = 0.9$ respectively. The pressure difference is due to the force on the bluff body and the wall friction. As the wall friction is assumed constant along the pipe, the pressure difference between two sensors located upstream the bluff body, $L/L_{TOT} = 0.25$ and $L/L_{TOT} = 0.5$, has been used to evaluate the part due to the pipe wall friction. The pressure difference is normalized by the distance to obtain a pressure drop per unit length. Finally, the drag force is given by:

$$c_D = \frac{\overline{F_D}}{\frac{1}{2}\rho C^2 DL} = (\overline{p_{0.5}} - \overline{p_{0.9}})A - (\overline{p_{0.25}} - \overline{p_{0.5}})A \frac{0.9 - 0.5}{0.5 - 0.25} \quad (5.7)$$

Where \overline{p} is the time averaged pressure at the position indicated by the subscript and A the pipe cross section. The measured drag coefficient is:

$$c_D = 3.53 \pm 0.06 \quad (5.8)$$

The estimation is based on 53 samples of flow conditions ranging from $C = 1.5$ m/s to $C = 3.5$ m/s in cavitation free regime.

5.3.2 Cavity pulsation and resulting mass source

Cavitation structures

The incipient cavitation is observed in filament structures located near the pipe wall at $1D$ downstream the bluff body. Below σ_i , cavitation is observed in the wake of the bluff body. Snapshots of the wake are presented for 3 cavitation levels in Figure 5.8. The flow is from the left to the right. The picture is taken from above, see Subsection 5.1.2. Large variation of cavity volume is observed for all σ ; an increase of mean cavity volume is correlated with the decrease of σ . The spatial distribution of the cavitation is weakly influenced by σ . From video analysis it can be stated that cavitation is confined between $0.5D$ and $4D$ downstream the bluff body except for very low cavitation index ($\sigma/\sigma_i < 0.5$). This region corresponds probably to the transition region as described in Section 3.2.

Amplitude

The time evolution of the cavity volume generates pressure pulsation, see Subsection 2.2.3. Its frequency is related to hydrodynamic fluctuation in the wake of the bluff body. The standard deviation of c_p below the bluff body is presented in Figure 5.9. Above σ_i , the fluctuation is proportional to the square of the flow velocity and the pressure coefficient is therefore constant. Below σ_i , the cavity pulsation generates additional pressure fluctuation. Maximum amplitude is measured for intermediate cavitation index ($0.5 < \sigma/\sigma_i < 0.7$). The important dispersion at this cavitation level is suspected to originate from the acoustic resonance.

Frequency

The frequency of the cavity pulsation is presented in Figure 5.10. The waterfall diagram of power spectral density (PSD) is presented in (a) for the range of frequency corresponding to the drag frequency. The pressure fluctuation below the bluff body is given for various flow velocity at $\sigma/\sigma_i = 0.62$. The result of the pressure measurement is compared with the cavity pulsation frequency determined using video analysis in (b), see Section 5.1.2. The direct determination of the cavity pulsation frequency confirms the analysis based on the measurement of the pressure field. The cavity pulsation is due to the hydrodynamic instability in the wake of the bluff body and its frequency is equal to twice the vortex shedding frequency. For $\sigma/\sigma_i > 0.5$, the gaseous phase has no influence on the vortex shedding frequency, see Figure 5.7 (b). Therefore the mass source frequency is directly proportional to the flow velocity.

5.4 Acoustic pressure fluctuation

5.4.1 Eigenfrequency determination

Above σ_i the natural frequency of the system remains constant. Below σ_i , the developed cavitation in the wake of the bluff body decreases the eigenfrequency of the system consisting in the pipe and the vapor cavity. Two methods have been used to determine

the eigenfrequencies of the system. Both are based on the spectral analysis of the pressure fluctuation. The first method is based on broad band noise excitation, the second on acoustic resonance.

Broad band excitation

The broad band noise due to the low frequency modulation of the bluff body vortex shedding is exploited to detect the eigenfrequencies of the system. In Figure 5.11 (a), an example of the PSD of pressure fluctuation at the mid-length of the pipe is presented. The position is chosen as it corresponds to a pressure antinode for the 3 first eigenfrequencies, see Subsection 5.4.2. In this spectrum, the source main frequency and the system eigenfrequencies are visible. In 5.11 (b), numerous flow conditions ($0.25 < \sigma/\sigma_i < 1.5$ and $3 \text{ m/s} < C < 6 \text{ m/s}$) have been investigated. For each flow condition, the frequencies with maximum amplitude are reported for 3 ranges of frequency corresponding to the first, second and third eigenfrequency; the eigenfrequency is identified as the frequency with maximum amplitude. Below σ_i , the first eigenfrequency decreases strongly with the cavitation index, this behavior is in good agreement with the measurement performed by Hassis [42]. The frequency peak due to the source is disturbing the identification of 2nd eigenfrequency; Therefore, another method is necessary to measure the second eigenfrequency. The 3rd eigenfrequency decreases slightly with σ .

In Figure 5.11 (c), the frequency with maximum amplitude is reported for cavitation free conditions. Above σ_i the natural frequency is constant. The average and standard deviation of the natural frequency of the pipe in cavitation free conditions is:

$$f_n = 96.5 \text{ Hz} \pm 1 \quad (5.9)$$

This value will be used as a reference frequency to normalize the source frequency and the resonance frequencies.

Resonance

In Figure 5.12, resonance is used to measure the influence of the cavitation on the second eigenfrequency. For constant cavitation index, measurements are performed for various flow velocities and corresponding source frequencies according to equation (5.5), see Figure 5.12 (a). The source frequency inducing maximum fluctuation is identified as the eigenfrequency at the given cavitation index. Similar methodology is applied using constant flow velocity and variable cavitation indexes in Figure 5.12 (b). The resonant flow conditions are summarized in Table 5.3 and in Figure 5.12(c), relative large dispersion in the prediction of the eigenfrequency is observed.

5.4.2 Eigenmode shape determination

The eigenmode shapes are also influenced by the cavitation index. In Figure 5.13, the three first eigenmode shapes are plotted for $\sigma/\sigma_i > 1$, $\sigma/\sigma_i = 0.81$, $\sigma/\sigma_i = 0.73$ and $\sigma/\sigma_i = 0.62$. The frequency response function for $L/L_{TOT} = 0$, $L/L_{TOT} = 0.5$, $L/L_{TOT} = 0.75$ and $L/L_{TOT} = 1$ with sensor $L/L_{TOT} = 0.25$ (filled circle) as reference is employed to determine the mode shapes of pressure fluctuation [89]. The frequency

Table 5.3: 2nd eigenfrequency at various cavitation index.

	constant C	constant σ
σ/σ_i	f/f_n	
0.62	1.42	1.48
0.64	1.52	
0.69	1.62	
0.73		1.55
0.76	1.72	
0.81		1.7

response function, T_{xy} , is estimated with the cross power spectral density normalized by the power spectral density at the reference position:

$$T_{xy}(f) = \frac{P_{xy}(f)}{P_{xx}(f)} \quad (5.10)$$

For each cavitation index, the frequency response function has been calculated for various flow velocities in resonant and in non-resonant conditions, the mean values and the standard deviations of the frequency response function are indicated in Figure 5.13. The lines are computed using the HA model, see Subsection 7.3.5. The discontinuity produced by the cavity compliance is clearly visible for low cavitation index. The antinode of the 1st eigenmode is shifted from the middle of the pipe to the vapor cavity location with the decrease of σ . For the 2nd eigenmode, the vapor cavity tends to behave as a node of pressure with the increase of vapor compliance. Similar behavior is observed for the 3rd eigenmode.

5.4.3 Fluctuation amplitude at resonance

The amplitude of fluctuation in the acoustic resonator depends mainly on two parameters:

- the strength of the source;
 - the difference between the source frequency and the eigenfrequency of the system.
- Maximum amplitude is expected at resonance as the source frequency is equal to an eigenfrequency of the system.

In Figure 5.14, the power distribution between the first, second and third eigenfrequency (f_1 , f_2 , f_3) is given for 3 cavitation indexes and various flow velocities. The location $L/L_{TOT} = 0.25$ is chosen in order to avoid any pressure node in the selected range of frequency, see Subsection 5.4.2. To distinguish the power distribution over the 3 first eigenfrequencies, the power spectrum is divided in 3 parts. The power density is integrated over each part of the PSD to obtain the total power in the frequency range. As the eigenfrequencies decrease with σ , the PSD is divided in order to distinguish the eigenfrequencies independently of the cavitation index (0-120 Hz for f_1 in (a), 120-240 Hz for f_2 in (b) and 240-360 Hz for f_3 in (c)).

In cavitation free regime, f_1 is equal to the natural frequency of the pipe. In the range of the explored source frequency ($0.47 - 1.93f_n$), the maximum is reached for $f_{source} = 1f_n$,

see Figure 5.14 (a).

In cavitation regime, the values of the eigenfrequencies decrease with the cavitation index, see Subsection 5.4.1. The maximum amplitude is reached at resonance, as $f_s = f_2$, see Figure 5.14 (b). Resonance at f_1 and f_3 is not possible as the explored range of source frequency ($1.1 - 2.2f_n$) matches only f_2 ($f_2/f_n = 1.55$ for $\sigma/\sigma_i = 0.73$ and $f_2/f_n = 1.48$ for $\sigma/\sigma_i = 0.62$). In cavitation regime, the amplitude at resonance is orders of magnitude larger than for the cavitation free regime. This difference highlights the predominance of the mass source over the momentum source.

In Figure 5.15, the standard deviation of pressure fluctuation at $L/L_{TOT} = 0.5$ is shown for various cavitation indexes ($0.5 < \sigma/\sigma_i < 1.1$) and source frequencies ($1f_n < f_{source} < 2.2f_n$). Using Delaunay triangulation and linear interpolation, a surface based on the measured amplitude of fluctuation (points) is computed in order to plot the iso-amplitude curves (lines). For all σ , the maximum amplitude is reached at resonance. The resonance amplitude and frequency vary with σ . Maximum amplitude is reached for intermediate cavitation index ($0.5 < \sigma/\sigma_i < 0.7$).

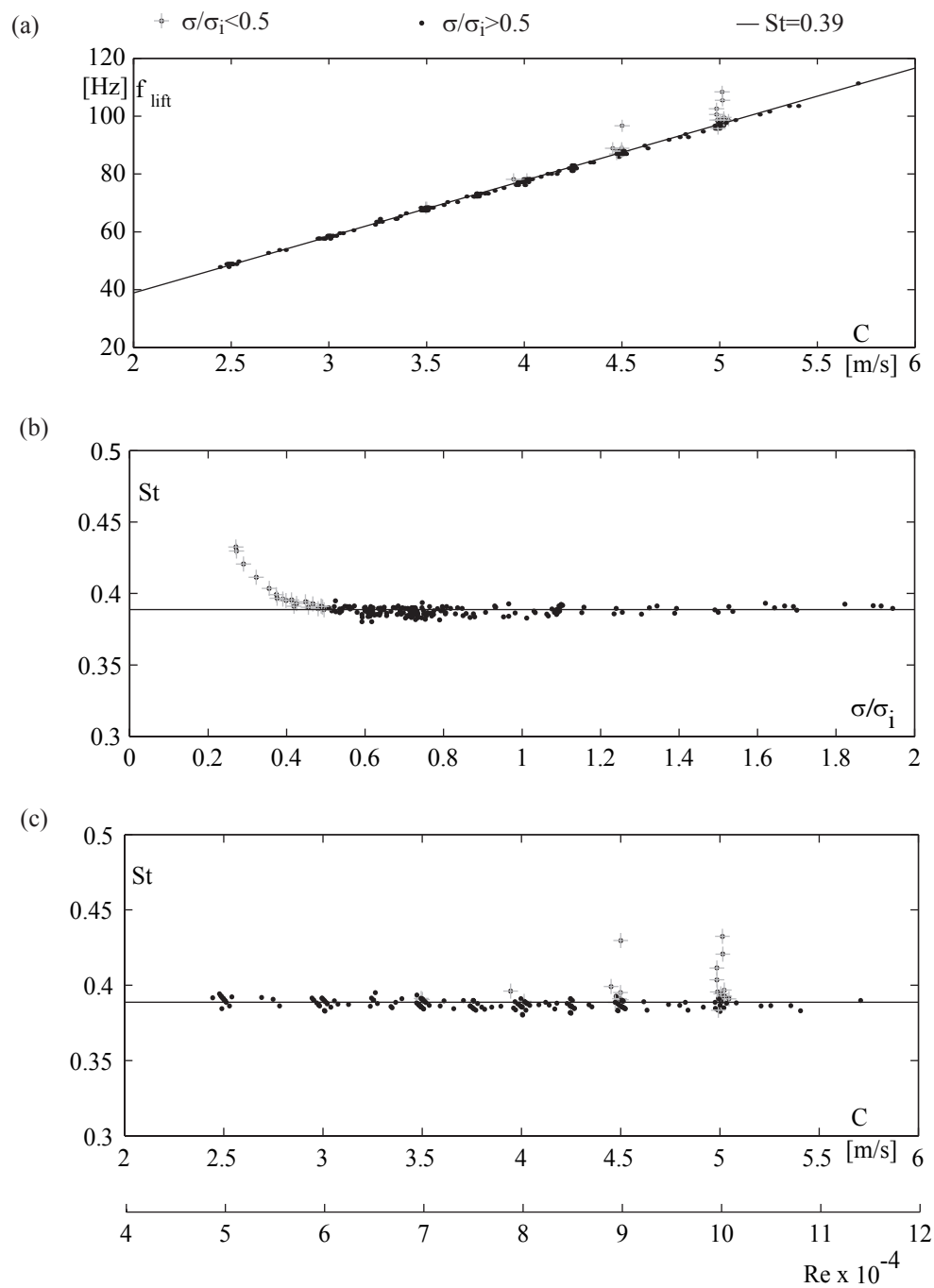


Figure 5.7: (a) Lift frequency versus flow velocity; (b) Strouhal number versus cavitation index; (c) Strouhal number versus flow velocity.

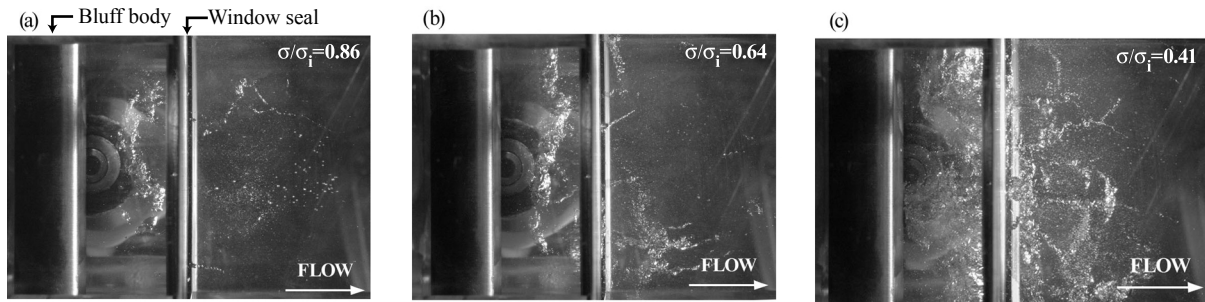


Figure 5.8: Snapshot of the cavitation structure in the wake of the bluff body.

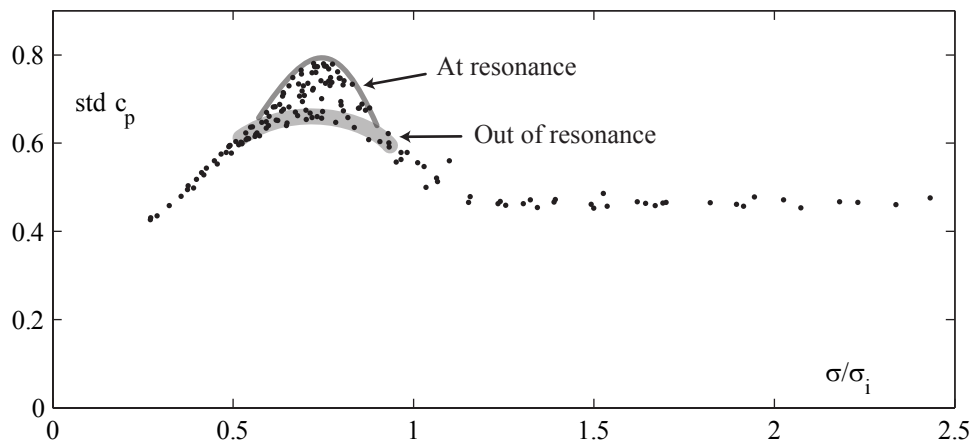


Figure 5.9: Standard deviation of pressure below the bluff body for various cavitation index.

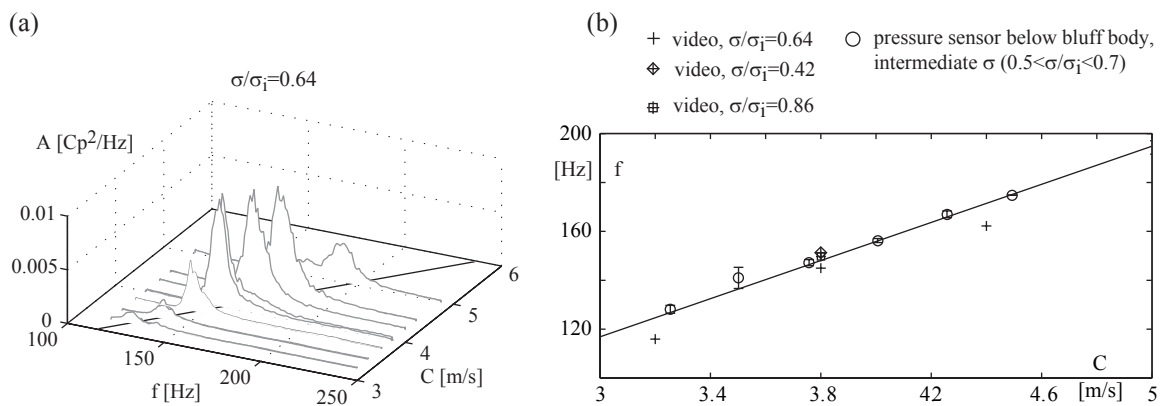


Figure 5.10: Mass source frequency versus flow velocity ; (a) Waterfall spectrum of pressure pulsation for various flow velocity and (b) cavity pulsation frequency from video and pressure signal.

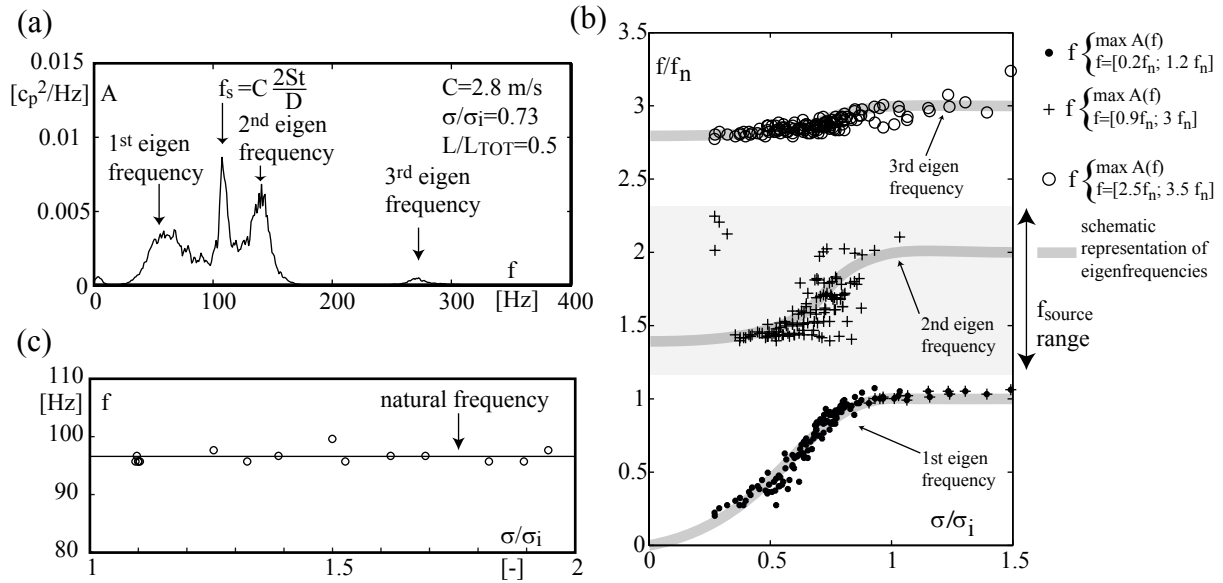


Figure 5.11: Cavitation influence on eigenfrequency values; (a) typical power spectrum of pressure coefficient at the middle of the pipe; (b) maximum amplitude frequencies for various cavitation indexes; (c) natural frequency determination using maximum amplitude frequency for $\sigma > \sigma_i$.

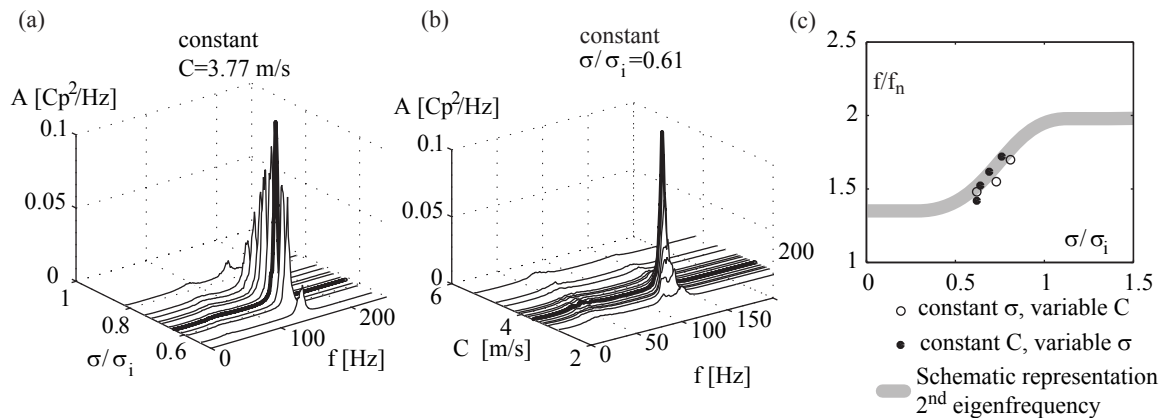


Figure 5.12: 2nd eigenfrequency values obtained from resonance frequency, measured at $L/L_{TOT} = 0.25$; (a) Waterfall spectrum at constant flow velocity and variable cavitation index; (b) Waterfall spectrum at constant cavitation index and variable flow velocity; (c) resonance frequency versus cavitation index.

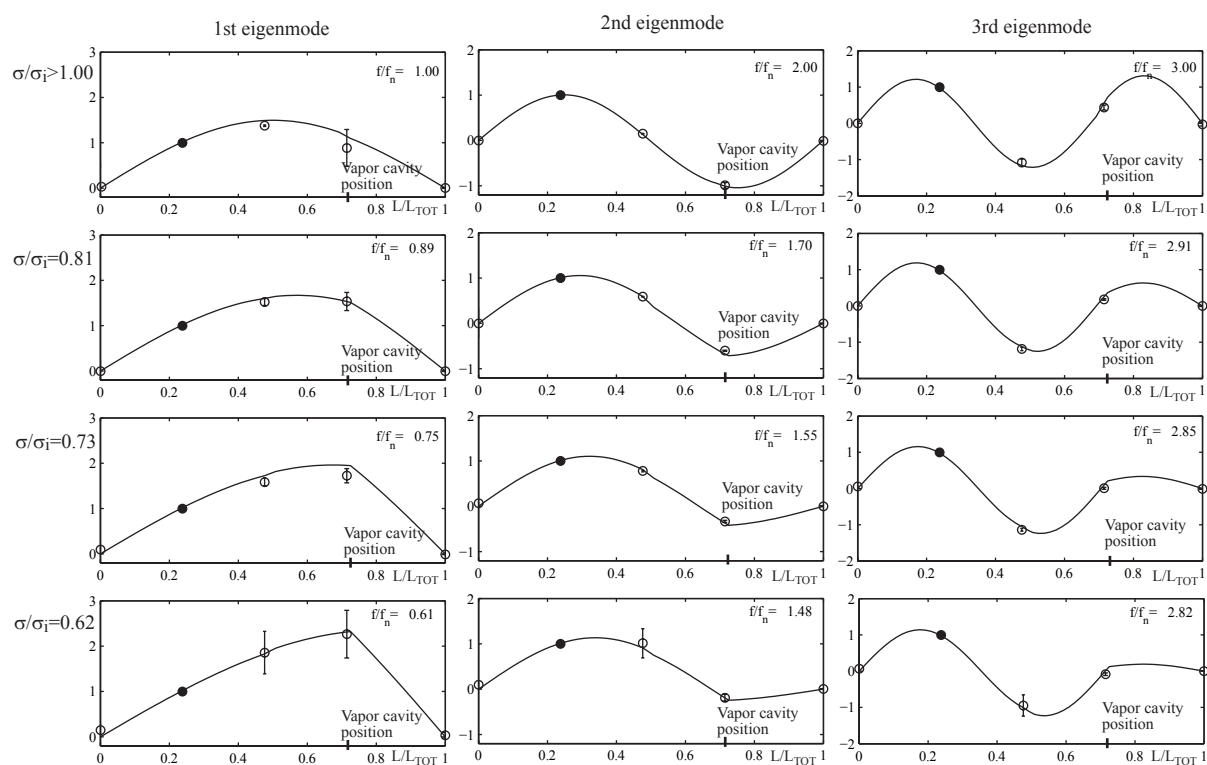


Figure 5.13: 1st, 2nd and 3rd pressure eigenmode shapes for various cavitation indexes. Black point: reference amplitude at $L/L_{TOT} = 0.25$; error bar: mean value and standard deviation of the frequency response function at $L/L_{TOT} = 0, 0.5, 0.75, 1$; Lines: mathematical model.

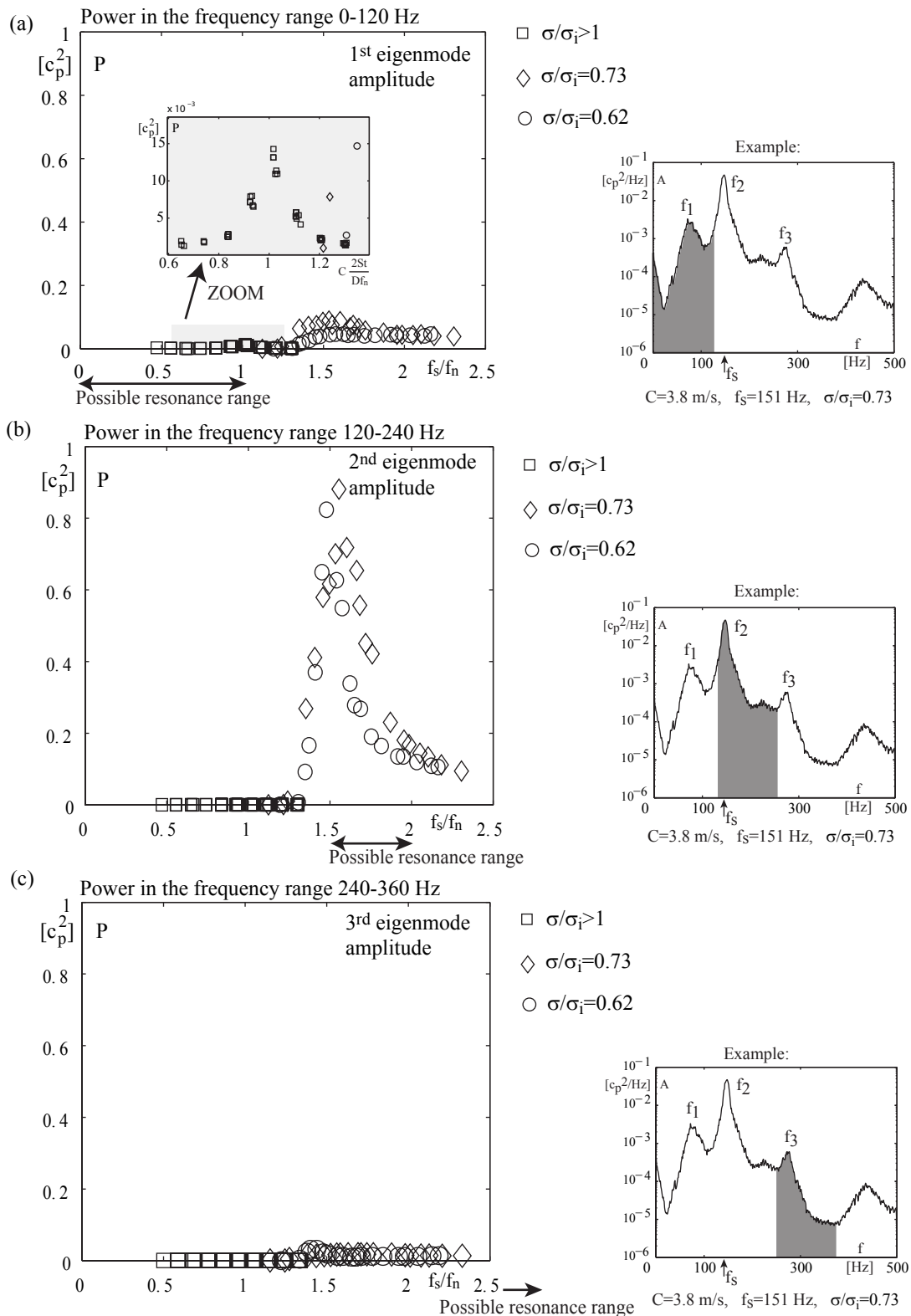


Figure 5.14: Integration of the power spectral density for 3 cavitation indexes at and at various source frequency, pressure fluctuation at $L/L_{TOT} = 0.25$; the frequency range corresponding to f_1 (a), f_2 (b) and f_3 (c) are shown in a typical PSD.

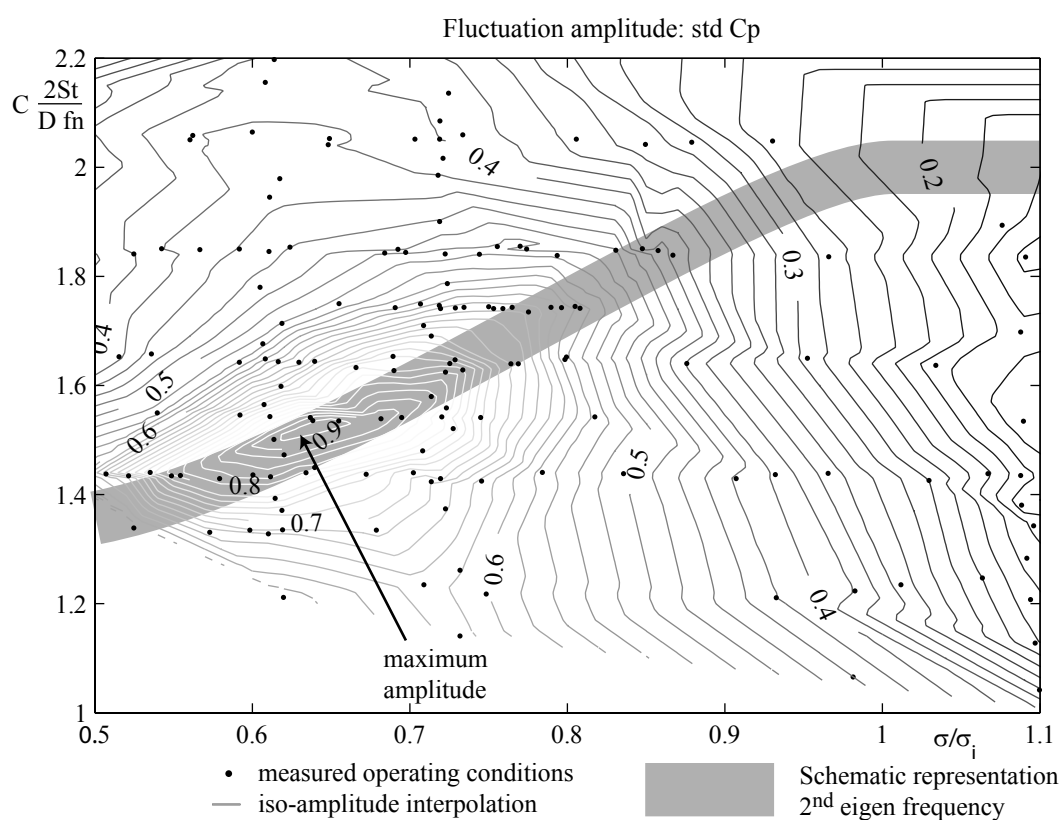


Figure 5.15: fluctuation amplitude for various cavitation indexes and source frequency. Standard deviation of c_p at $L/L_{TOT} = 0.5$; measured flow conditions (points) and interpolated values (lines).

Chapter 6

Hydroacoustic model

The hydroacoustic fluctuation is generalized to transient flow. The fluid in the pipe is considered as weakly compressible; the density and the cross section are quasi steady: $\rho' \ll \rho_0$ and $A' \ll A_0$, see Subsection 2.1.2. But the pressure and the discharge velocity, \underline{p} and \underline{C} , are variables. The hydroacoustic model describes the acoustic fluctuation but also the low frequency variations of \underline{p} and \underline{C} due to the change of flow conditions. Therefore the acoustic feedback of the H \bar{A} model includes the acoustic fluctuations and the time evolution of the flow conditions. The acoustic fluctuation is triggered by the resonance of the pipe and is usually a relatively high frequency phenomenon. The time evolution of the operating condition is a low frequency phenomenon connected with the modulation of the hydrodynamic instability. Either one or both variations may be large in the source region and have a significant effect on the source.

6.1 Transient pipe flow

In pipe flow the axial flux of mass and momentum are far greater than their radial counterparts. A 1D approach is therefore sufficient to model most of the physic involved in pipe flow dynamic. In the followings developments, we consider a transient flow in a horizontal deformable straight pipe, see Figure 6.1.

6.1.1 Conservation laws

The mass (6.1) and momentum (6.2) conservation laws for a time dependant control volume are written hereafter:

$$\frac{d}{dt} \int_V \rho d^3\mathbf{x} + \int_S \rho C_i \cdot n_i d^2\mathbf{x} = 0 \quad (6.1)$$

$$\frac{d}{dt} \int_V \rho C_i d^3\mathbf{x} + \int_S (p\delta_{ij} - \tau_{ij} + \rho C_i C_j) n_j d^2\mathbf{x} = \int_V f_i d^3\mathbf{x} \quad (6.2)$$

Considering a horizontal deformable straight pipe, for a section of infinitesimal length δx , the following boundary conditions are imposed:

- Open inlet at plane S_A , the plane is normal to the x axis, $\mathbf{n} = [-1 \ 0 \ 0]$;
- Open outlet at plane S_B , $\mathbf{n} = [1 \ 0 \ 0]$;

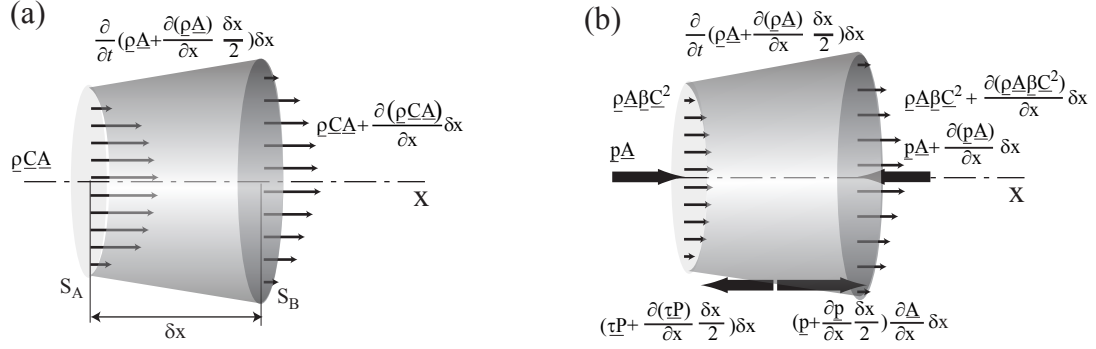


Figure 6.1: The mass (a) and momentum (b) conservation law applied to the section of a horizontal straight pipe.

- None porous wall and zero velocity at the pipe wall, S_{AB} .

The conservation of mass (6.3) and momentum (6.4) along the x axis reduces to:

$$\frac{d}{dt} \int_V \rho d^3 \mathbf{x} - \int_{S_A} \rho C_1 d^2 \mathbf{x} + \int_{S_B} \rho C_1 d^2 \mathbf{x} = 0 \quad (6.3)$$

$$\begin{aligned} & \frac{d}{dt} \int_V \rho C_1 d^3 \mathbf{x} + \int_{S_{AB}} (p \delta_{1j} - \tau_{1j}) n_j d^2 \mathbf{x} \\ & - \int_{S_A} (p - \tau_{11} + \rho C_1^2) d^2 \mathbf{x} + \int_{S_B} (p - \tau_{11} + \rho C_1^2) d^2 \mathbf{x} = 0 \end{aligned} \quad (6.4)$$

To simplify the problem, mono dimensional variables are introduced. The mono dimensional variables are underlined to distinguish them from the usual variables. The pressure is assumed uniform in a cross section:

$$p(x, y, z, t) = \underline{p}(x, t) \quad (6.5)$$

Based on the Tait relation, see Section 2.1, the density is proportional to the pressure. Therefore the density is also uniform in a cross section:

$$\rho(x, y, z, t) = \underline{\rho}(x, t) \quad (6.6)$$

The cross sectional area is by definition function of x (and t for deformable pipe):

$$\underline{A}(x, t) \quad (6.7)$$

The discharge velocity $\underline{C}(x, t)$ is defined as :

$$\underline{C} = \int_A C_1 d^2 \mathbf{x} / \underline{A} \quad (6.8)$$

Due to the boundary layer, the x component of the velocity, C_1 , is never uniform in a cross section. For this reason the momentum correction coefficient is introduced:

$$\underline{\beta} = \int_A C_1^2 d^2 \mathbf{x} / (\underline{C}^2 \underline{A}) \quad (6.9)$$

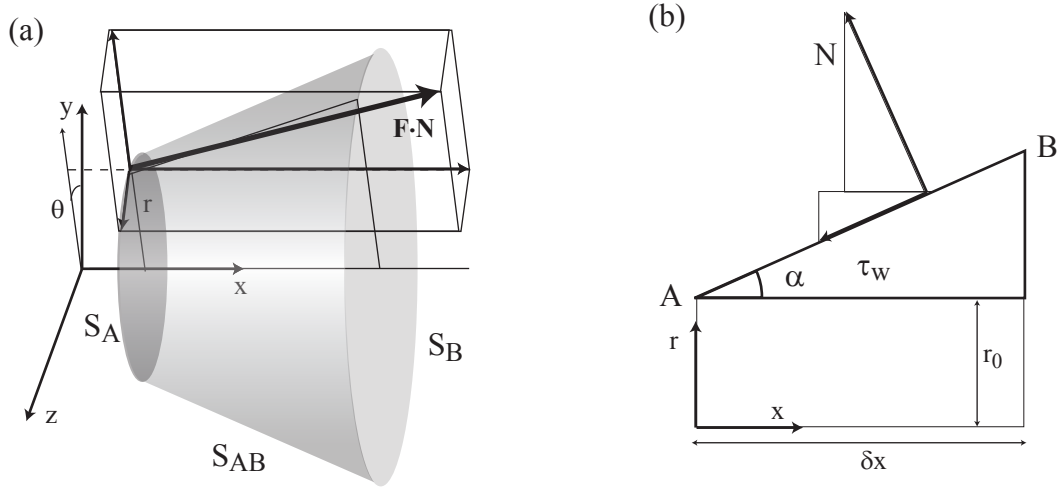


Figure 6.2: The components of the stresses at the wall are given in cylindrical coordinate system (x, r, θ) (a), including the decomposition of the pressure (b) and the wall shear stress (c).

For compressible fluid with reversible volumetric variation, the term τ_{11} is equal to zero, see Section 2.1. As the volumetric dissipation is usually very small this term can also be neglected for fluid with irreversible volumetric variation.

We consider a circular divergent pipe in cylindrical coordinate system (x, r, θ) , see Figure 6.2 (a). The pipe taper angle, α , is defined as $\tan \alpha = \frac{\partial r}{\partial x}$. A parametric representation of the pipe wall surface is given by the inequalities $0 \leq u \leq \delta x$, $0 \leq v \leq 2\pi$ and:

$$\mathbf{r} = \begin{cases} x & u \\ r & = r_0 + u \tan \alpha \\ \theta & v \end{cases}$$

For a given tensor \mathbf{P} , the surface integral over S in cylindrical coordinate is defined as [54]:

$$\int_S (P_{ij} n_i) d^2 \mathbf{x} = \int \int \mathbf{P} \cdot \mathbf{N}(u, v) r du dv \quad (6.10)$$

Where the infinitesimal surface is given by:

$$\mathbf{N}(u, v) r du dv = \left(\frac{\partial \mathbf{r}}{\partial v} \times \frac{\partial \mathbf{r}}{\partial u} \right) r du dv = [-\tan \alpha \ 1 \ 0]^T (r_0 + u \tan \alpha) du dv$$

And the stress tensor at the wall is written:

$$\mathbf{P} = \begin{bmatrix} p & -\tau_{xr} & -\tau_{x\theta} \\ -\tau_{rx} & p & -\tau_{r\theta} \\ -\tau_{\theta x} & -\tau_{\theta r} & p \end{bmatrix}$$

The x component of the second term of (6.4) is equal to:

$$\int_{S_{AB}} (p\delta_{1j} - \tau_{1j}) n_j d^2\mathbf{x} = \int_A^B \int_0^{2\pi} (-p \tan \alpha - \tau_{xr}) (r_0 + u \tan \alpha) dv du \quad (6.11)$$

The projection of the wall shear stress on the xr plane is defined as:

$$\tau_{\mathbf{w}} = [\cos \alpha \tau_{xr} \quad \sin \alpha \tau_{rx} \quad 0]^T$$

Assuming a uniform wall shear stress on the perimeter \underline{P} , the one dimensional scalar wall shear stress, τ_w , is introduced as:

$$\tau_w = -sgn(\tau_{xr}) |\tau_{\mathbf{w}}| = -\tau_{xr} \quad (6.12)$$

For cylindrical pipe, we have $2\pi(r_0 + u \tan \alpha) = \underline{P}$. Consequently the surface integral (6.11) is equivalent to the one dimensional integral:

$$\int_{S_{AB}} (p\delta_{1j} - \tau_{1j}) n_j d^2\mathbf{x} = \int_A^B (-\underline{p} \tan \alpha + \tau_w) \underline{P} dx \quad (6.13)$$

Using the previous definitions and generalizing (6.13) for arbitrary cross sectional shape, equation (6.1) and (6.2) can be reformulated in the one dimensional form:

$$\frac{d}{dt} \int_A^B \underline{\rho A} dx + (\underline{\rho AC})_B - (\underline{\rho AC})_A = 0 \quad (6.14)$$

$$\begin{aligned} \frac{d}{dt} \int_A^B \underline{\rho AC} dx - \int_A^B \underline{P p} \tan \alpha dx + \int_A^B \underline{P \tau_w} dx \\ + (\underline{pA} + \underline{\beta \rho AC^2})_B - (\underline{pA} + \underline{\beta \rho AC^2})_A = 0 \end{aligned} \quad (6.15)$$

The integral equations (6.14), (6.15) are applied to a section of infinitesimal length δx as shown in Figure 6.1. At the limit, as δx tends to zero, the differential form of mass conservation (6.14) is:

$$\frac{\partial (\underline{\rho A})}{\partial t} + \frac{\partial (\underline{\rho AC})}{\partial x} = 0 \quad (6.16)$$

And for the momentum equation (6.15), we have:

$$\frac{\partial (\underline{\rho AC})}{\partial t} - \underline{p} \frac{\partial \underline{A}}{\partial x} + \tau_w \underline{P} + \frac{\partial}{\partial x} (\underline{pA} + \underline{\beta \rho AC^2}) = 0 \quad (6.17)$$

Reformulating (6.16) and (6.17), the integral form of the conservation of mass (6.14) and momentum (6.15) along the axial direction x corresponds to the following system of partial differential equation:

$$\frac{\partial (\underline{\rho A})}{\partial t} + \underline{C} \frac{\partial (\underline{\rho A})}{\partial x} + \underline{\rho A} \frac{\partial \underline{C}}{\partial x} = 0 \quad (6.18)$$

$$\underline{\rho A} \frac{\partial \underline{C}}{\partial t} + \underline{C} \underline{\rho A} \frac{\partial \underline{C}}{\partial x} + \frac{\partial (\underline{\beta - 1}) \underline{\rho AC^2}}{\partial x} + \underline{A} \frac{\partial \underline{p}}{\partial x} + \tau_w \underline{P} = 0 \quad (6.19)$$

The third term of equation (6.19) accounting for the spatial variation of the velocity profile is usually neglected. The system is open as there are 6 unknowns for 2 equations, additional relations are necessary.

6.1.2 Constitutive equations

Elastic pipe

In elastic divergent or convergent pipe, the pipe cross section is function of the pipe cross section at rest and the deformation due to internal pressure, $\underline{A}(x, t) = A_0(x) + \underline{A}'(x, t)$. The differential form of the mass conservation law (6.18) is rewritten for an elastic pipe as:

$$\frac{\partial \underline{\rho}}{\partial t} + \underline{C} \frac{\partial \underline{\rho}}{\partial x} + \frac{\underline{\rho}}{\underline{A}} \left(\frac{\partial \underline{A}'}{\partial t} + \underline{C} \frac{\partial \underline{A}'}{\partial x} \right) + \underline{C} \frac{\underline{\rho}}{\underline{A}} \frac{\partial A_0}{\partial x} + \underline{\rho} \frac{\partial \underline{C}}{\partial x} = 0 \quad (6.20)$$

For long wavelength, λ , the pipe can be approximated as a serie of massless rings expanding and contracting in accordance with the internal fluid pressure, \underline{p} . For elastic pipe, the cross sectional area variation \underline{A}' is linearly proportional to the internal pressure, see appendix A. The propagation velocity, a_c , is therefore depended on the characteristic of the fluid and the pipe:

- For compressible fluid in rigid pipe, we have $a_c^{-2} = a_0^{-2} = d\underline{\rho}/d\underline{p}$;
- For incompressible fluid in elastic pipe, we have $a_c^{-2} = (\rho_0/A_0)d\underline{A}'/d\underline{p}$;
- For compressible fluid in elastic pipe, we have $a_c^{-2} = d\underline{\rho}/d\underline{p} + (\rho/A_0)d\underline{A}'/d\underline{p}$.

The last two relations are valid for small deformation of the pipe, $\underline{A}' \ll A_0$. For curved pipe, the axial motion of the pipe may be influenced by the fluid transient. Similarly for shorter wavelength, the axial stresses can't be neglected. In such situations, the fluid-structure interaction is complex and additional differential equation must be introduced to describe the structural deformation [91]. But such analysis is out of the scope of the present investigation.

Viscoelastic pipe

The behavior of PVC pipe is not purely elastic, viscous dissipation is associated with the deformation of the material. Similar behavior is expected from the fluid. A Kelvin-Voigt constitutive relation is assumed between the pressure and the mass per unit length contained in the pipe [98]:

$$\underline{p} = \frac{a_c^2}{A_0} \underline{\rho} A + \frac{\mu}{\rho_0 A_0} \frac{\partial \underline{\rho} A}{\partial t} \quad (6.21)$$

Where a_c^2 is the propagation velocity of plane waves in the pipe and μ is the viscosity associated with the pipe deformation and fluid compression. The introduction of (6.21) into (6.19) and (6.18) leads to a specific type of equation. The propagation of plane wave in pipes is described by a damped wave equation with a damping term function of the fluctuation frequency. The details of the derivation are given in appendix B.

Geometrical relation

The relation between the cross section \underline{A} and perimeter \underline{P} is straight forward for simple geometries:

- $\underline{P} = 2\pi \underline{R}$ and $\underline{A} = \pi \underline{R}^2$ for circular cross section, where \underline{R} is the radius;
- $\underline{P} = 4\underline{H}$ and $\underline{A} = \underline{H}^2$ for square cross section, where \underline{H} is the height and width.

For more complex geometries and small pipe deformation, the ratio r between the perimeter and the cross sectional area can be determined a fortiori, $\underline{r}(x, t) = \frac{\underline{P}(x, t)}{\underline{A}(x, t)} \simeq \frac{\underline{P}_0(x)}{\underline{A}_0(x)}$.

Wall shear stress

On one side, the wall shear stress $\underline{\tau}_w$ for steady flow is driven by the mean flow velocity \underline{C} . For laminar flow regime, the relation between head losses and mean flow velocity is linear. For turbulent flow, the relation is quadratic with an influence of the Reynolds number.

On the other side, for acoustic fluctuation in a mean turbulent flow, the damping of the acoustic fluctuation, depends on the ratio between the acoustic boundary layer, $\delta_a \simeq \sqrt{2\nu/\omega}$, and the laminar sublayer of the turbulent main flow, $\delta_{sub} \simeq 15\nu/\sqrt{\tau_w\rho}$. In the present configuration the acoustic boundary layer is orders of magnitude larger than the viscous sublayer. With $C_0 = 3$ m/s, $\lambda = 0.02$ and $\omega = 600$ [rad/s], we have $\delta_a \simeq 5 \cdot 10^{-5}$ and $\delta_{sub} \simeq 1 \cdot 10^{-7}$. In such situation a quasi steady relation for turbulent flow can be used for the damping of the acoustic fluctuation and the head losses due to the mean flow [74]:

$$\underline{\tau}_w = \lambda\rho|\underline{C}|\underline{C}/8 \quad (6.22)$$

Weakly compressible fluid

For weakly compressible fluid, we have $\underline{\rho} \simeq \rho_0$ and $\underline{a} \simeq a_0$ [87]. The density and speed of sound can be assumed as constant in the zero order terms. This assumption is valid for liquid such as water over a large range of pressure, see Section 2.1. In standard applications, the elastic deformations of the pipe is small, $\underline{A}' \ll A_0$, and the cross sectional area can also be approximated, $\underline{A} \simeq A_0$, in the zero order derivative terms.

6.1.3 Resulting hydroacoustic model

Elastic pipe

Neglecting the third term in (6.19) and introducing the acoustic wave speed for weakly compressible fluid in elastic pipe, $a_c^{-2} = d\underline{\rho}/d\underline{p} + (\rho_0/A_0)d\underline{A}'/d\underline{p}$ in equation (6.20) and the quasi steady wall shear stress for rectangular pipe in (6.19), the following system of differential equation is obtained:

$$\frac{1}{\rho_0 a_c^2} \left(\frac{\partial \underline{p}}{\partial t} + \underline{C} \frac{\partial \underline{p}}{\partial x} \right) + \frac{\underline{C}}{A_0} \frac{\partial A_0}{\partial x} + \frac{\partial \underline{C}}{\partial x} = 0 \quad (6.23)$$

$$\frac{\partial \underline{C}}{\partial t} + \underline{C} \frac{\partial \underline{C}}{\partial x} + \frac{1}{\rho_0} \frac{\partial \underline{p}}{\partial x} + \frac{\lambda |\underline{C}| \underline{C}}{2\sqrt{A_0}} = 0 \quad (6.24)$$

The system of partial differential equation (6.23), (6.24) describes the global dynamic behavior of the flow in the pipe. It is valid for large variation of \underline{C} and \underline{p} . As it describes plane waves, this model is valid only for slow variation of pressure and velocity with respect to the cutoff frequency, see Subsection 2.1.3. The spatial discretization of (6.23) and (6.24) is presented in appendix C.

Viscoelastic pipe

For low Mach number flow, the convective terms can be neglected. Let us consider equation (6.23) and (6.24). We can compare the importance of the different terms by

performing an order of magnitude analysis. The pressure scale as $p \simeq \rho_0 a_0 C_0$, and the relation between the time scale and the spatial scale for the various eigenmode number is given by, see Section 1.4:

$$t_0 = \frac{1}{n} \frac{2l_0}{a_0}, \text{ with } n = 1, 2, \dots \quad (6.25)$$

where n is the eigenmode number. For constant pipe cross section, the third term of (6.23) is equal to zero and the normalized form of equation (6.23) and (6.24) is given by:

$$\frac{1}{\rho^* a^{*2}} \left(\frac{\partial p^*}{\partial t^*} + \frac{2M}{n} C^* \frac{\partial p^*}{\partial x^*} \right) + \frac{2}{n} \frac{\partial C^*}{\partial x^*} = 0 \quad (6.26)$$

$$\frac{\partial C^*}{\partial t^*} + \frac{2M}{n} C^* \frac{\partial C^*}{\partial x^*} + \frac{2}{n} \frac{\partial p^*}{\partial x^*} + M \frac{l_0 \lambda}{\sqrt{A_0} n} \tau_w^* = 0 \quad (6.27)$$

$$(6.28)$$

where the star indicates dimensionless values. The convective terms scales with M over n and are therefore negligible for low Mach number flows and small eigenmode number. The friction term scales also with M . But for high friction factor and large length/section ratio this term can not be neglected.

For a constant cross section rectangular pipe, low Mach number flow, quasi steady friction losses, negligible velocity profile variation and considering a viscoelastic response for the mass/pressure relation, the following system of partial differential equation is obtained from (6.18), (6.19) and (6.21):

$$\frac{\partial(\underline{\rho A})}{\partial t} + \rho_0 A_0 \frac{\partial \underline{C}}{\partial x} = 0 \quad (6.29)$$

$$\rho_0 A_0 \frac{\partial \underline{C}}{\partial t} + A_0 \frac{\partial \underline{p}}{\partial x} + \frac{\lambda \rho_0 \sqrt{A_0} |\underline{C}| \underline{C}}{2} = 0 \quad (6.30)$$

$$\frac{a_c^2}{A_0} \underline{\rho A} + \frac{\mu}{\rho_0 A_0} \frac{\partial \underline{\rho A}}{\partial t} = \underline{p} \quad (6.31)$$

Multiplying (6.31) and (6.29) by $\frac{\partial}{\partial x}$, combining and introducing the result into (6.30), we obtain:

$$\frac{\partial(\underline{\rho A})}{\partial t} + \rho_0 A_0 \frac{\partial \underline{C}}{\partial x} = 0 \quad (6.32)$$

$$\frac{\partial \underline{C}}{\partial t} + \frac{a_c^2}{\rho_0 A_0} \frac{\partial(\underline{\rho A})}{\partial x} - \frac{\mu}{\rho_0} \frac{\partial^2 \underline{C}}{\partial x^2} + \frac{\lambda |\underline{C}| \underline{C}}{2\sqrt{A_0}} = 0 \quad (6.33)$$

$$\frac{a_c^2}{A_0} \underline{\rho A} + \frac{\mu}{\rho_0 A_0} \frac{\partial \underline{\rho A}}{\partial t} = \underline{p} \quad (6.34)$$

For sufficiently low fluctuation frequency, equation (6.34) can be approximated as $\underline{p} \simeq \frac{a_c^2}{A_0} \underline{\rho A}$. Using this approximation, the mass term, $\underline{\rho A}$, can be replaced by the pressure in (6.32) and (6.33) to lead to the final form of the set of partial differential equations:

$$\frac{1}{\rho_0 a_c^2} \frac{\partial \underline{p}}{\partial t} + \frac{\partial \underline{C}}{\partial x} \simeq 0 \quad (6.35)$$

$$\frac{\partial \underline{C}}{\partial t} + \frac{1}{\rho_0} \frac{\partial \underline{p}}{\partial x} - \frac{\mu}{\rho_0} \frac{\partial^2 \underline{C}}{\partial x^2} + \frac{\lambda |\underline{C}| \underline{C}}{2\sqrt{A_0}} \simeq 0 \quad (6.36)$$

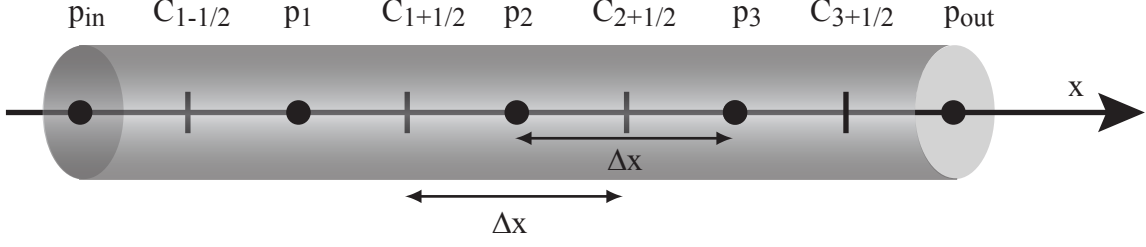


Figure 6.3: Staggered grid for spatial discretization.

The introduction of a viscoelastic damping results in an additional term in (6.36). This damping term is a second derivative of the velocity with respect to space. Detailed analysis of the damping is given in appendix B.

6.2 Computational model implementation

6.2.1 Space discretization

PVC pipe features viscoelastic response, therefore equations (6.35) and (6.36) apply:

$$\frac{1}{\rho_0 a_c^2} \frac{\partial p}{\partial t} + \frac{\partial C}{\partial x} = 0 \quad (6.37)$$

$$\frac{\partial C}{\partial t} + \frac{1}{\rho_0} \frac{\partial p}{\partial x} - \frac{\mu}{\rho_0} \frac{\partial^2 C}{\partial x^2} + \frac{\lambda |C| C}{2\sqrt{A_0}} = 0 \quad (6.38)$$

The spatial discretization is performed on a staggered grid. For stability purpose, the velocity and pressure are evaluated at different positions as shown in Figure 6.3. The discretized form of (6.37) and (6.38) using centered finite difference scheme is respectively (6.39) and (6.40):

$$\frac{1}{\rho_0 a_{ci}^2} \frac{dp_i}{dt} + \frac{C_{i+1/2} - C_{i-1/2}}{\Delta x} = 0 \quad (6.39)$$

$$\rho_0 \frac{dC_{i+1/2}}{dt} + \frac{p_{i+1} - p_i}{\Delta x} - \mu \frac{C_{i+3/2} - 2C_{i+1/2} + C_{i-1/2}}{\Delta x^2} + \frac{\lambda \rho_0 |C_{i+1/2}|}{2\sqrt{A_{0i+1/2}}} C_{i+1/2} = 0 \quad (6.40)$$

The system is quasi linear except for the friction term (fourth term in (6.40)). The following system of linear differential equation is obtained:

$$\mathbf{A} \frac{d\mathbf{x}}{dt} = \mathbf{B}\mathbf{x} + \mathbf{s} \quad (6.41)$$

The following notations are introduced to describe the elements of \mathbf{A} , \mathbf{B} and \mathbf{s} :

$$k_i = \frac{\Delta x}{\rho_0 a_{ci}^2} \quad d_i = \frac{\mu_i}{\Delta x}$$

$$l_{i+1/2} = \rho_0 \Delta x \quad r_{i+1/2} = \frac{\lambda \rho_0 \Delta x |C_{i+1/2}|}{2\sqrt{A_{0i+1/2}}}$$

Where k is the compliance due to the liquid compressibility and pipe elasticity. The viscoelasticity is accounted for through the damping term, d . The term l is the fluid inertance and r is the friction term. As the friction is non-linear, the time dependant velocity, C , is also included in the coefficient matrix \mathbf{B} . In equation (6.41), the state variable vector, \mathbf{x} , corresponding to the pipe shown in Figure 6.3 is:

$$\mathbf{x} = [C_{1-1/2} \ p_1 \ C_{1+1/2} \ p_2 \ C_{2+1/2} \ p_3 \ C_{3+1/2}]^T$$

The source vector contains the boundary conditions, constant pressure at inlet and outlet:

$$\mathbf{s} = [p_{in} \ 0 \ 0 \ 0 \ 0 \ 0 \ -p_{out}]^T$$

The coefficient matrix \mathbf{A} is diagonal and the elements on the diagonal are the compliance and the inertance:

$$\mathbf{A} = \text{diag}(l_{1-1/2} , k_1 , l_{1+1/2} , k_2 , l_{2+1/2} , k_3 , l_{3+1/2})$$

Finally the coefficient matrix $[B]$ includes the damping and friction terms:

$$\mathbf{B} = \begin{bmatrix} -r_{1-1/2} & -1 & 0 & 0 & 0 & 0 & 0 & 0 \\ 1 & 0 & -1 & 0 & 0 & 0 & 0 & 0 \\ d_{1+1/2} & 1 & -r_{1+1/2} - 2d_{1+1/2} & -1 & d_{1+1/2} & 0 & 0 & 0 \\ 0 & 0 & 1 & 0 & -1 & 0 & 0 & 0 \\ 0 & 0 & d_{2+1/2} & 1 & -r_{2+1/2} - 2d_{2+1/2} & -1 & d_{2+1/2} & 0 \\ 0 & 0 & 0 & 0 & 1 & 0 & 0 & -1 \\ 0 & 0 & 0 & 0 & 0 & 0 & 1 & -r_{3+1/2} \end{bmatrix}$$

6.2.2 Time discretization

Equation (6.41) has to be conditioned for solving the system in the time domain. For this reason, the diagonal matrix $[A]$ is inverted. This operation is straight forward as the matrix is diagonal and the following linear system of differential equation is obtained:

$$\frac{d\mathbf{x}}{dt} = \mathbf{A}^{-1}\mathbf{B}\mathbf{x} + \mathbf{A}^{-1}\mathbf{s} \quad (6.42)$$

The Runge Kutta time marching method is selected to solve (6.42). This is an explicit method, 4th order accurate. Its stability region includes a portion of the imaginary axis, consequently this method is adapted for non-stiff problems, see [68]. For explicit methods and pure wave equation, the maximal time step is limited by the CFL criteria defined by:

$$C_r = \frac{a_c \Delta t}{\Delta x} < 1 \quad (6.43)$$

6.3 Application to the reference case study

6.3.1 Setup

The HA model is limited to the section of the pipe with constant cross section, the convergent and the divergent are not included in the model. Zero impedance is assumed

at the inlet and outlet of the model. The total length of the pipe, $L_{TOT} = 1050$ mm is subdivided in 40 elements of length, $dx = 1050/40$ mm. The time step is selected in agreement with the CFL criteria, $dt = 0.00002$ s, see Subsection 6.2.2. The cross section corresponds to the experimental setup, $A = 40 \times 40 = 1600$ mm². The wave speed including the effect of the wall elasticity is selected in order to fit the natural frequency of the pipe determined experimentally, $a = 2L_{TOT}f_n = 202.65$ m/s. This value differs, 30% and 11% error respectively, from the estimated value based on beam theory, see Appendix A and preliminary experiment, see Appendix B. The error is mainly due to the pipe inhomogeneities, the actual propagation velocity varies along the pipe. The Young modulus and the thickness of the bluff body support differs from the PVC pipe resulting in a different pipe elasticity. Similarly, the inlet and outlet supports are different. Nevertheless those local inhomogeneities have a negligible effect on the global behavior of the acoustic system and the average wave speed is sufficient to model the acoustic resonance, see Subsection 5.4.2 for comparison between the mathematical model and the experimental results. The wall shear stress has a small importance, it influences marginally the damping of the acoustic fluctuation, see appendix B; the friction factor corresponding to a turbulent flow at high Reynolds number is selected, $\lambda = 0.02$. The damping due to the viscoelastic response of the pipe wall has been determined experimentally, $\mu = 3685$ Pa·s, see annexe B. The momentum source position corresponds to the bluff body position in the experimental setup, $L/L_{TOT} \simeq 0.75$. According to the notation introduced in Figure 6.3, with $i = 0$ at the inlet and $i=40$ at the outlet, the momentum source is located at node number $i = 29 + 1/2$. The mass source is located at $i = 30$, this location corresponds to the wake downstream the bluff body. The parameters of the HA model used in the one-way and two-way simulations are summarized in Table 6.1.

Table 6.1: Parameters of the HA model.

Name	Description	Value	Unit
L_{TOT}	Pipe length	1.05	m
A	Cross section	$1.6 \cdot 10^{-3}$	m ²
i	Number of elements	40	-
$i = 29 + 1/2$	Momentum source position	$0.7375L/L_{TOT}$	-
$i = 30$	Mass source position	$0.75L/L_{TOT}$	-
a_c	Wave speed	202.65	m/s
μ	Viscoelastic damping	3685	Pa·s
λ	Friction factor	0.02	-
dt	Time step	0.00002	s
t_{total}	Simulation time	2.2	s

6.3.2 Validation and intermediate results

Harmonic fluctuation

In order to validate the HA model, harmonic source located at $L/L_{TOT} = 0.75$ with adjustable frequency has been used, see Figure 6.4. The procedure is the following:

1. Short transient simulation (total simulation time: 0.2 s) is performed using the HA model and the parameters given in Table 6.1 for a given type of source (momentum source in the present situation) and a given harmonic source frequency of unit amplitude, $F_s(t) = \hat{F}_s \sin(2\pi f_s t)$.
2. After a transition of 0.16 s, maximum fluctuation amplitude is reached and the peak to peak amplitude of pressure fluctuation is recorded for each location along the pipe, see Figure 6.4 (a). Half peak to peak amplitude is reported for each location along the pipe, see Figure 6.4 (b). The sign is employed to highlight the phase of the fluctuation. The position $L/L_{TOT} = 0.025$ is selected as reference, fluctuations in phase are represented with positive values, fluctuations in phase opposition are represented with negative values.
3. Another simulation is performed with a shift in the source frequency value. The operation is repeated from $f_s = 5$ to $f_s = 200$ Hz by step of 5 Hz. A surface representing the amplitudes of the fluctuations as a function of the position along the pipe and the frequency of the source is obtained, see Figure 6.4 (c). The position $L/L_{TOT} = 0$ corresponds to the pipe inlet and $L/L_{TOT} = 1$ corresponds to the pipe outlet. The amplitude of fluctuation is normalized using the source amplitude.

The step situated at the source position corresponds to the source amplitude. For non-resonant conditions, the fluctuations are in phase opposition on each side of the source and the size of the step is equal to the source amplitude. The important amplitude of the standing wave at $f_s = 96.5$ Hz and $f_s = 193$ Hz corresponds respectively to the resonance at the first and second eigenfrequency of the system. The first pressure mode has one antinode at the center of the pipe and two nodes at both ends of the pipe. The second mode has two antinodes in phase opposition at $L/L_{TOT} = 0.25$, $L/L_{TOT} = 0.75$ and three nodes at $L/L_{TOT} = 0$, $L/L_{TOT} = 0.5$ and $L/L_{TOT} = 1$. The resonance frequencies are in good agreement with the experimental results. For $f_s \simeq f_n = 96.5$ Hz, the amplitude is maximal as the source frequency is equal to the natural frequency of the pipe. For $f_s \simeq 2f_n$, the second resonance is observed. For both resonance frequency, the shapes of the pressure standing waves are similar to the eigenmodes measured experimentally in Subsection 5.4.2 for the cavitation free conditions at equivalent frequencies.

Viscoelastic damping

The influence of the viscoelastic damping on the amplification factor is presented in Figure 6.5. Pressure fluctuation is generated by a momentum source located at $L/L_{TOT} = 0.75$ according to the methodology presented in Figure 6.4. But the source frequency is kept constant at $f_s = f_n$ in (b) and $f_s = 3f_n$ in (c). And the simulations are performed for viscoelastic damping ranging from $\mu = 0$ Pa·s to $\mu = 4000$ Pa·s by step of 100 Pa·s. The spatial distribution of fluctuation amplitude along the pipe is presented for $f_s = f_n$ in Figure 6.5 (b) and for $f_s = 3f_n$ in Figure 6.5 (c). The fluctuation amplitude is normalized by the harmonic momentum source amplitude. The maximum amplitude of pressure fluctuation is plotted versus the viscoelastic damping for $f_s = f_n$ and $f_s = 3f_n$ in Figure 6.5 (a). Without viscoelastic damping, larger fluctuation are expected for the highest frequency, $f = 3f_n$. With viscoelastic damping the highest frequencies are strongly damped, see annexe B. For the measured viscoelastic damping, $\mu = 3685$ kg/ms, the amplification factor is larger for $f_s = f_n$ than for $f_s = 3f_n$. Consequently the highest

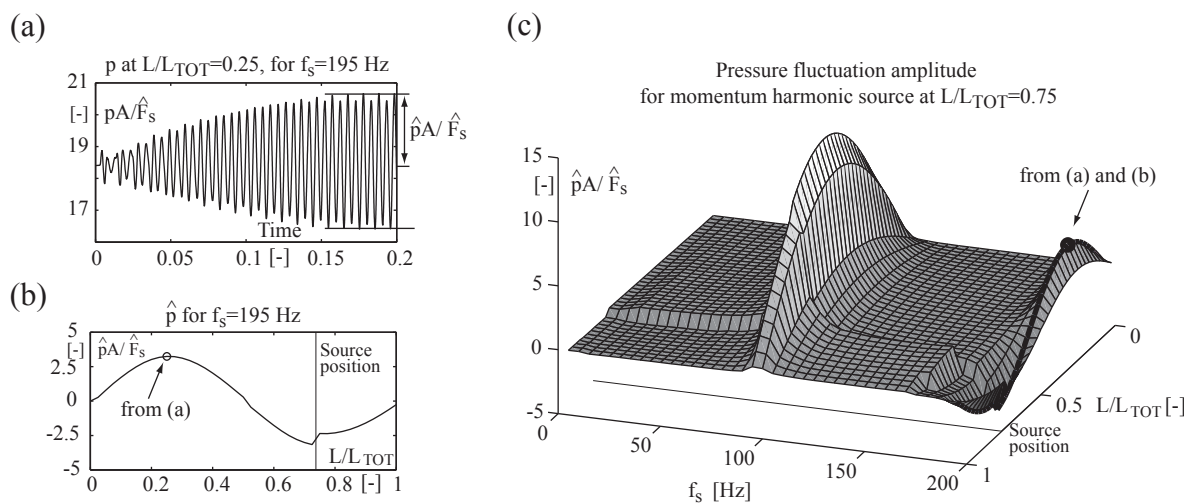


Figure 6.4: Amplitude of pressure fluctuation due to an harmonic momentum source located at $L/L_{TOT} = 0.75$; (a) Time history of pressure at $L/L_{TOT} = 0.25$ for $f_s = 195$ Hz; (b) amplitude along the pipe for $f_s = 195$ Hz; (c) Surface representation of the pressure fluctuation as a function of the position and the source frequency.

frequencies are strongly damped in the simulations.

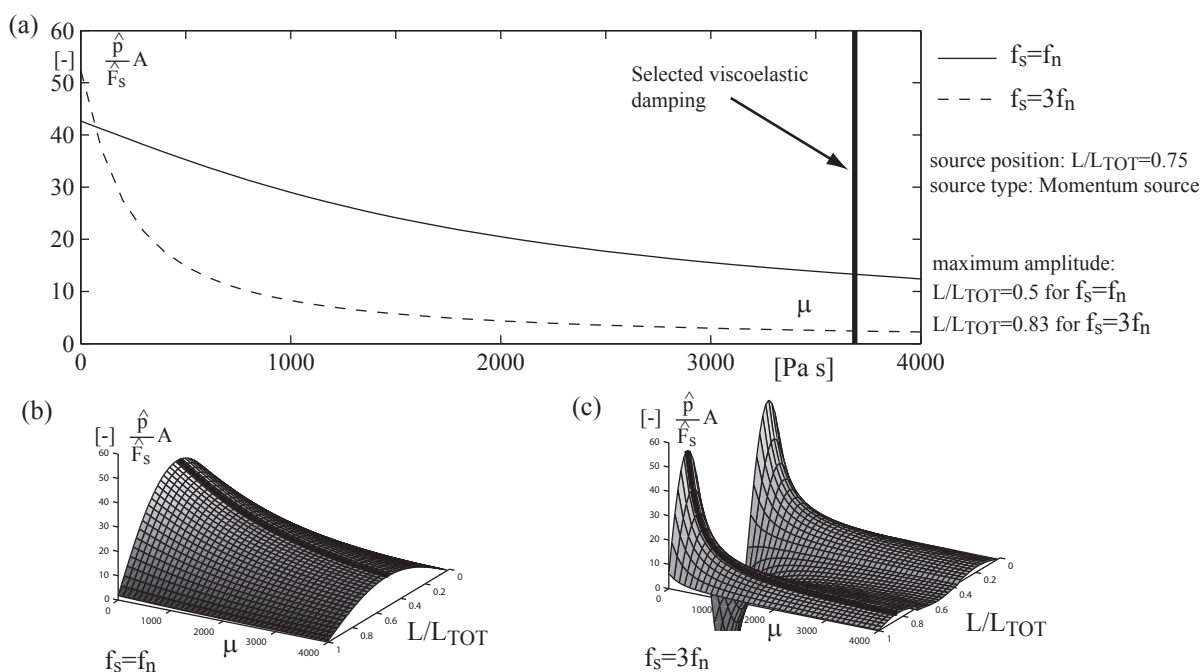


Figure 6.5: Maximum amplitude of pressure fluctuation (a) due to harmonic momentum source at frequency $f_s = f_n$ (b) and $f_s = 3f_n$ (c) vs. viscoelastic damping.

Chapter 7

Interaction

7.1 Hydrodynamic source

The methodology, presented in Section 2.2, is applied to the specific situation of pipe flow transient at low frequency (below cut off frequency). In the present approach the acoustic system is one dimensional; only mass source and momentum sources are evaluated. In the Lighthill analogy, see equation (2.26), the source term is associated with a deviation from the linear acoustic approximation of the fluid dynamic. In the present modeling strategy, the source term is associated with a deviation from the 1D HA model. The HA model, see Section 6.1 is not sufficient to describe complex processes such as flow separation, cavitation, etc. In such situation, see Figure 7.1, source terms are included in the differential equation (6.18), (6.19) to correct the 1D model. In equation (7.1), the mass source, $\frac{\partial m}{\partial t}$, corresponds to an external mass injection per unit length and per unit time. It includes all complex processes neglected in the one dimensional formulation of the continuity equation such as phase change, fluid injection, elastomer expansion joint, etc. In equation (7.2), the momentum source term, f_x , is an external force per unit length. It includes all complex processes neglected in the one dimensional formulation of the momentum conservation law such as flow separation and body forces. Specific model is necessary to evaluate the values of the source terms. This model, called HD model, is 3D and covers the entire source region.

$$\frac{\partial(\rho A)}{\partial t} + \frac{\partial(\rho AC)}{\partial x} = \frac{\partial m}{\partial t} \quad (7.1)$$

$$\frac{\partial(\rho AC)}{\partial t} + \frac{\partial(\beta \rho AC^2)}{\partial x} + \frac{\partial(pA)}{\partial x} - \underline{p} \frac{\partial A}{\partial x} + \underline{\tau}_w \underline{P} = f_x \quad (7.2)$$

The source term equivalence is valid as long as the source region is compact with respect to the wave length ($l \ll \lambda$). In such situation, the variation of emission time over the source region can be neglected, see Section 2.2. As the source region is compact, the fluid can be approximated as a quasi incompressible fluid, $\rho(x, t) = \rho(x, y, z, t) \simeq \rho_s$, and the wall movement can also be neglected, $A \simeq A_0$. This can be proven using dimensional analysis. The variables of equation (6.35) are normalized, $p^* = \underline{p}/\rho C_0^2$, $C^* = \underline{C}/C_0$, etc. The result is the following dimensionless conservation of mass, where the star indicates the dimensionless quantities:

$$\frac{1}{\rho^* a^{*2}} M \frac{l_0}{a_0 t_0} \frac{\partial p^*}{\partial t^*} + \frac{\partial C^*}{\partial x^*} = 0 \quad (7.3)$$

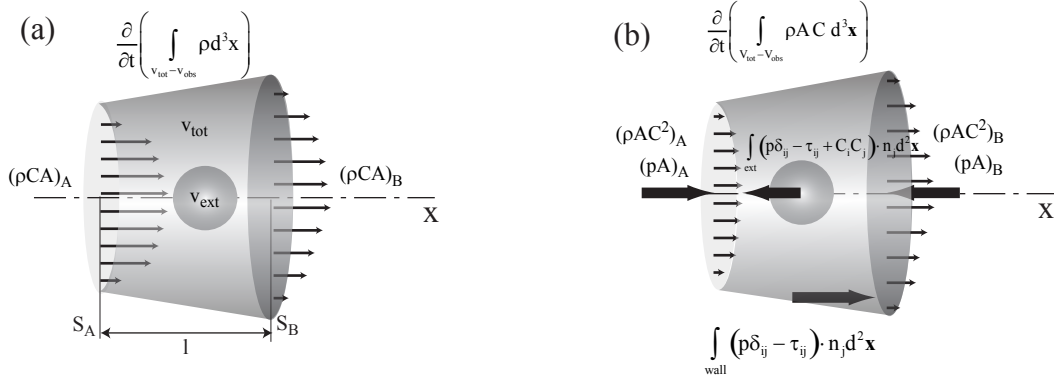


Figure 7.1: Mass (a) and momentum (b) conservation law applied to the section of pipe with an external element.

In typical pipe flow, the length scale l_0 is large compared to the wave length $\lambda_0 = a_{c0}t_0$. But for a compact region $l_0 \ll \lambda_0$ and the first term of (7.3) can be neglected. For small length scale, the continuity equation (6.23) reduces to:

$$\frac{\partial C}{\partial x} = 0 \quad (7.4)$$

which corresponds to the mass conservation of incompressible fluid in a constant diameter pipe. Consequently, the HD model used to evaluate the sources values is incompressible and the pipe wall deformation is neglected.

7.1.1 Mass source

The integration of (7.1) over the source region yields to

$$\int_0^L \frac{\partial \rho A}{\partial t} dx + (\rho AC)_B - (\rho AC)_A = \int_0^L \frac{\partial m}{\partial t} dx \quad (7.5)$$

The left hand side of (7.5) is an approximation of the continuity equation based on the HA model. The right hand side is a corrective term called mass source. As the propagation time is neglected, the source term can be replaced by its mean value over the source region m_s and equation (7.5) reduces to:

$$\int_0^L \frac{\partial \rho A}{\partial t} dx + (\rho AC)_B - (\rho AC)_A = L \frac{dm_s}{dt} = \frac{dM_s}{dt} \quad (7.6)$$

where $\frac{dM_s}{dt}$ is the integral of the mass sources over the source region.

The integration of (6.1) over the control volume consisting in the section of the pipe, external volume excluded, ($V = V_{tot} - V_{ext}$, see Figure 7.1 (a)) provides the exact solution in the source region:

$$\frac{d}{dt} \int_{V=V_{tot}-V_{ext}} \rho d^3\mathbf{x} + \int_{ext} \rho C_i \cdot n_i d^2\mathbf{x} + \int_B \rho AC d^2\mathbf{x} - \int_A \rho AC d^2\mathbf{x} = 0 \quad (7.7)$$

As the propagation time can be neglected in the source region, the liquid density can be considered as uniform. The first term of (7.7) is rewritten:

$$\frac{d}{dt} \int_{V=V_{tot}-V_{ext}} \rho d^3\mathbf{x} = \frac{d}{dt} \rho_s \int_{V_{tot}} d^3\mathbf{x} - \frac{d}{dt} \rho_s \int_{V_{ext}} d^3\mathbf{x} \quad (7.8)$$

At the inlet and outlet of the source region, the hypothesis for 1D pipe flow, see Section 6.1, are valid therefore $\int \rho AC d^2\mathbf{x} = \underline{\rho AC}$ on surface S_A and S_B . No transfer of mass is considered between the fluid domain and the external domain, $\int_{ext} \rho C_i \cdot n_i d^2\mathbf{x} = 0$. The fluid is considered as quasi incompressible, $\rho_s \simeq \rho_0$ and (7.7) reduces to:

$$\rho_s \frac{dV_{tot}}{dt} - \rho_s \frac{dV_{ext}}{dt} + (\underline{\rho AC})_B - (\underline{\rho AC})_A = 0 \quad (7.9)$$

Where ρ_s is the density of the fluid in the source region. The 1D approximation corresponding to the left hand side of (7.6) is compared with the volume integral (7.9), the difference is included in the source term of (7.6):

$$\left(\rho_s \int_0^L \frac{\partial A}{\partial t} dx - \rho_s \frac{dV_{tot}}{dt} \right) + \rho_s \frac{dV_{ext}}{dt} = \rho_s \frac{dV_{ext}}{dt} = L \frac{dm_s}{dt} = \frac{dM_s}{dt} \quad (7.10)$$

The first terms in the parenthesis cancels each other, the two terms are equivalent in the exact solution and in the 1D approximation. The mass source corresponds to the variation of volume of external element such as gas bubble or vapor cavity if the mass transfer due to vaporization/condensation is neglected.

7.1.2 Momentum source

The integration of (7.2) over the source region yields to:

$$\int_0^L \frac{\partial (\underline{\rho AC})}{\partial t} dx + (\underline{\beta \rho AC^2} + \underline{pA})_B - (\underline{\beta \rho AC^2} + \underline{pA})_A - \int_0^L \left(\underline{p} \frac{\partial A}{\partial x} - \underline{\tau_w P} \right) dx = \int_0^L \underline{f_x} dx \quad (7.11)$$

The left hand side of equation (7.11) is an approximation of the momentum conservation in the source region based on one dimensional variables. The momentum source on the right hand side is a corrective term to account for the exact flow dynamic in the source region. As the fluid is quasi incompressible and the pipe wall is considered as rigid in the source region, equation (7.11) reduces to:

$$\rho_s \int_0^L A_0 \frac{\partial C}{\partial t} dx + (\underline{\beta \rho AC^2} + \underline{pA})_B - (\underline{\beta \rho AC^2} + \underline{pA})_A - \int_0^L \left(\underline{p} \frac{\partial A_0}{\partial x} - \underline{\tau_w P} \right) dx = L \underline{f_{x,s}} = F_{x,s} \quad (7.12)$$

At the inlet and outlet of the source region, the hypothesis for standard pipe flow, see Section 6.1, are valid therefore the 1D approximation of the momentum flux is exact,

$\int (p\delta_{1j} - \tau_{1j} + \rho C_1 C_j) n_j d^2 \mathbf{x} = (\beta \rho A C^2 + pA)$. The integration of (6.2) over the control volume ($V = V_{tot} - V_{ext}$) as shown in Figure 7.1 (b) provides the exact solution in the source region:

$$\begin{aligned} & \frac{d}{dt} \int_{V=V_{tot}-V_{ext}} \rho C_1 d^3 \mathbf{x} + (\beta \rho A C^2 + pA)_B - (\beta \rho A C^2 + pA)_A \\ & + \int_{wall} (p\delta_{1j} - \tau_{1j}) n_j d^2 \mathbf{x} + \int_{ext} (p\delta_{1j} - \tau_{1j} + \rho C_1 C_j) n_j d^2 \mathbf{x} = 0 \end{aligned} \quad (7.13)$$

In equation (7.13), the subscript *wall* refers to the pipe wall and *ext* refers to the external element surface. The 1D approximation corresponding to the left hand side of (7.12) is compared with the volume integral (7.13), the difference is included in the source term of (7.12):

$$\begin{aligned} & \rho_s \left(\int_0^L A_0 \frac{\partial C}{\partial t} dx - \frac{d}{dt} \int_{V=V_{tot}-V_{ext}} C_1 d^3 \mathbf{x} \right) \\ & - \left(\int_0^L \left(p \frac{\partial A_0}{\partial x} + \tau_w P \right) dx - \int_{wall} (p\delta_{1j} - \tau_{1j}) n_j d^2 \mathbf{x} \right) \\ & - \left(\int_{ext} (p\delta_{1j} - \tau_{1j} + \rho C_1 C_j) n_j d^2 \mathbf{x} \right) \\ & = L \underline{f}_{x,s} = F_{x,s} \end{aligned} \quad (7.14)$$

The momentum source term is governed by 3 corrective terms:

- The first term is the difference between the exact fluid momentum in the source region and the 1D approximation;
- the second term is the difference between the approximate and the exact force acting on the pipe wall;
- the third term is the force acting on the external element.

7.2 Acoustic feedback

In full generality four different types of feedback, i.e. pressure or velocity on mass or momentum source, may be observed. Depending on the flow configuration, two different methods are proposed to model the acoustic feedback on hydrodynamic instabilities:

- The two-way coupled simulation, see Figure 7.2 (a); the interaction is complex and the relation between the acoustic feedback and the source is nonlinear.
- The one way concurrent method; the source is assumed to consist in two independent components, the acoustic and the hydrodynamic. Linear relation is assumed between the acoustic component and the acoustic fluctuation in the source region. In such situation, the feedback of the acoustic fluctuation can be accounted for in the HA model only with a linearized interaction parameter, see Figure 7.2 (b).

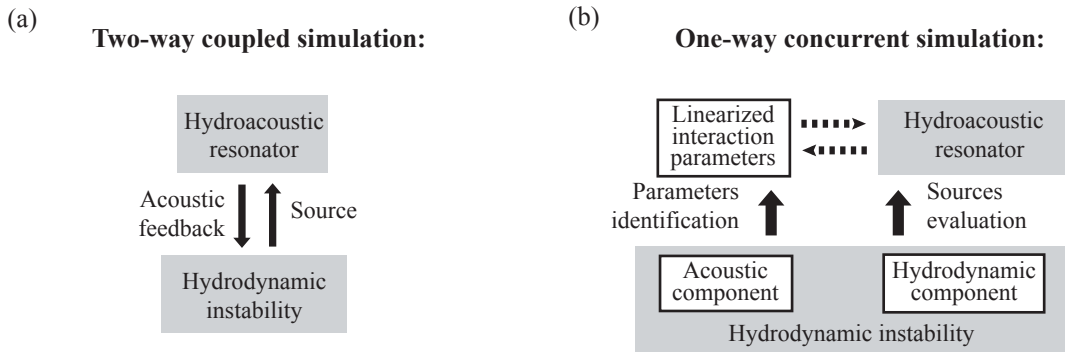


Figure 7.2: (a) Simulated action of the source and feedback of the acoustic resonator in the two-way coupling methodology; (b) Simulated and modeled action and feedback in the one way concurrent methodology.

The choice of modeling strategy for the feedback mechanisms depends on the flow configuration. The first method is general but may be difficult to implement; the second method is restricted to particular cases. A non-exhaustive presentation of acoustic feedback mechanisms is introduced in the next sections. Some examples are proposed to illustrate the linear and non-linear interactions.

7.2.1 Source without feedback

For quasi steady flow conditions, small deviations from a reference state are considered in the HA model :

$$\begin{aligned} \underline{p} &= p_0 + p' \\ \underline{C} &= C_0 + C' \end{aligned} \quad (7.15)$$

For sufficiently small deviations, the hydrodynamic source is not influenced by p' and C' . The solution of the HD model is therefore independent of the HA model. In such situation, the hydrodynamic source is evaluated independently. The boundary conditions of the HD model are given by the reference state, p_0 and C_0 . Once the temporal evolutions of the sources, $F_{x,s}(t)$ and/or $\frac{dM_s}{dt}(t)$, have been computed; the solutions are injected in the HA model.

7.2.2 Source with linear feedback

In numerous configurations, the time constants of the physical phenomena in the source region are much shorter than the time constant of the hydroacoustic system. By example, the natural frequency of a gas bubble is orders of magnitude higher than the resonance frequency of a penstock. Due to the difference of time scale, the dynamic effects in the source region can be neglected and quasi-static relations are considered between the acoustic field and the source. In such situation the acoustic feedback is linear for quasi-steady flow conditions with small fluctuation, equation (7.15). The source

terms, $\frac{dM_s}{dt}$ and/or $F_{x,s}$, are linearly proportional to one or both state variables of the HA model, \underline{p} or \underline{C} . To account for the interaction, linearized parameters are introduced in the HA model. The source term is not an independent source, but can be interpreted as part of the hydroacoustic system. The source/acoustic field interaction can modify the eigenfrequencies of the system [42], stabilize the system or make the system unstable [18]. Using small perturbation approach, the stability of such linearly coupled system can be assessed [2].

Pressure feedback on the momentum source

The acoustic pressure can not have any feedback effect on a compact momentum source. For pure momentum source, the two integrals of the first element of equation (7.14) cancel each other. As the source is compact, the pressure field in the source region can be written:

$$p(x, y, z, t) = p_d(x, y, z, t) + \underline{p}_B(t) \quad (7.16)$$

where $\underline{p}_B(t)$, the pressure at the outlet cross section, is considered as the reference pressure and p_d is the deviation from this reference pressure. The deviation from the reference pressure, p_d , is connected with the local hydrodynamic field and is independent of the acoustic field. On the contrary, the outlet pressure, p_B , depends on the acoustic field only. Using this notation, the last two terms of equation (7.14) are given by:

$$\begin{aligned} & - \left(\underline{p}_B \int_0^L \frac{\partial A_0}{\partial x} dx - \underline{p}_B \int_{wall} \delta_{1j} n_j d^2 \mathbf{x} \right) \\ & \quad - \underline{p}_B \int_{ext} \delta_{1j} n_j d^2 \mathbf{x} \\ & - \left(\int_0^L \underline{\tau}_w P dx - \int_{wall} (p_d \delta_{1j} - \tau_{1j}) n_j d^2 \mathbf{x} \right) - \left(\int_{ext} (p_d \delta_{1j} - \tau_{1j} + \rho C_1 C_j) n_j d^2 \mathbf{x} \right) \\ & \quad = L \underline{f}_{x,s} = F_{x,s} \quad (7.17) \end{aligned}$$

The two elements of the first line cancels each other. The element of the second line is equal to zero as the surface S_{ext} is closed and \underline{p}_B , the acoustic pressure, is uniform in the source region. The third line is not dependant on the acoustic pressure. Alternatively, the pressure at the inlet cross section can be chosen as the reference pressure. In any case, the momentum source, $F_{x,s}$, is independent of the acoustic pressure and no feedback is possible.

Velocity feedback on the momentum source

We consider a compact source region in a pipe of constant cross section. A solid sphere is attached at the center of the region, see Figure 7.1. Invoking the conservation of the mass flow for incompressible fluid in stationary control volume, the two integrals of the first element of (7.14) cancels each others. For constant cross section, the taper term, $\frac{\partial A_0}{\partial x} = 0$, and the pressure on the wall, $p \delta_{1j} n_j = 0$, are equal to zero. For external element

sufficiently distant from the pipe wall, its influence on the shear stress at the pipe wall can be neglected, $\int_A^B \underline{\tau}_w \underline{P} dx \simeq \int_{wall} \tau_{1j} n_j d^2 \mathbf{x}$. Finally equation (7.14) reduces to:

$$- \int_{ext} (p \delta_{1j} - \tau_{1j}) n_j d^2 \mathbf{x} = L \underline{f}_{x,s} = F_{x,s} \quad (7.18)$$

For instance at low Reynolds number flow past a sphere, the integral on the left hand side of equation (7.18) is proportional to the flow velocity, $F = -6\pi\mu r C$. Where r is the sphere radius. If the confinement effect is neglected ($\pi r^2 \ll A_0$), the momentum source is given by:

$$F_{x,s} = \frac{F_{x,s}}{C} C = -6\pi\mu r C = L \underline{f}_{x,s} \quad (7.19)$$

In such situation, the momentum source is linearly proportional to the flow velocity.

Pressure feedback on the mass source or compliance

We consider an external element in a compact source region, its volume is sensitive to pressure, see Figure 7.1. For example, a small gas bubble in a liquid. The volume of the bubble is connected to its internal pressure through the polytropic relation $\frac{dV_g}{dp_g} = -\frac{\gamma V_{g,0}}{p_{g,0}}$. Assuming an internal pressure in the bubble equal to the ambient pressure (no surface tension), $p_g = p_s$, the mass source is linearly proportional to the ambient pressure in the source region, $p_s(t)$:

$$\frac{dM_s}{dt} \simeq \rho_l \frac{dV_g}{dt} = \rho_l \frac{dV_g}{dp_s} \frac{dp_s}{dt} = -\rho_l \frac{\gamma V_{g,0}}{p_{g,0}} \frac{dp_s}{dt} = -K_v \frac{dp_s}{dt} \quad (7.20)$$

The proportionality constant $K_v = -\rho_l \frac{dV_g}{dp_s}$ is called cavity compliance in the literature when the bubble contains vapor [80, 15, 16, 77]. The mass transfer at the gas/liquid interface is neglected and quasi-static relation is assumed between the vapor volume and the ambient pressure. The cavity compliance modifies the eigenfrequencies and eigenmodes of the acoustic system [42, 68]. The coupled system consisting in the acoustic resonator and the vapor cavity has specific eigenfrequencies strongly dependent on the cavity volume.

Velocity feedback on the mass source or mass flow gain factor

Let us consider an external element in a compact source region, its volume is dependant on the flow velocity. In Figure 7.3, the external element is modeled by a cylinder containing a gas ($\frac{dp_{ext}}{p_{ext}} = -\frac{1}{\gamma} \frac{dV_{ext}}{V_{ext,0}}$). The cylinder is equipped with a piston ($p_{ext} A_c = F_p$, with A_c the cylinder cross section, F_p the force on the piston). The piston is connected to a flat plate mounted perpendicular to the flow ($\overline{F}_p = \frac{1}{2} \rho_s \overline{C}^2 A_{fp} c_D$, with A_{fp} the flat plate surface, c_D the drag coefficient and C the free stream velocity). The pressure applied by the liquid on the external face of the piston is neglected, $p_s A_c \ll F_p$ and the confinement effect of the velocity field near the flat plate is neglected, $A_{fp} \ll A_0$. Using chain rule derivation the volume of the external element is connected to the free stream velocity through the following relation:

$$\frac{dM_s}{dt} = \rho_l \frac{dV_{ext}}{dt} = \rho_l \frac{dV_{ext}}{dC} \frac{dC}{dt} = -2\rho_l \gamma \frac{V_{ext,0}}{C_0} \frac{dC}{dt} = M_G \frac{dC}{dt} \quad (7.21)$$

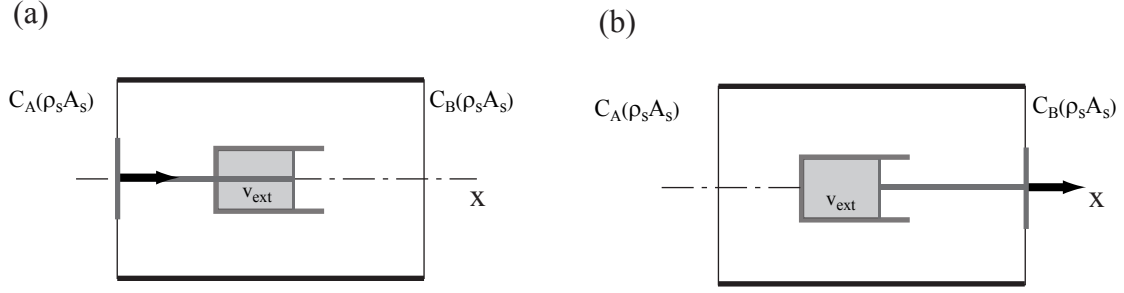


Figure 7.3: Linear feed-back of velocity on the mass source or mass flow gain factor.

The term $M_G = \rho_l \frac{dV_{ext}}{dC}$ is called mass flow gain factor. It has been used to study the dynamic stability of pumping system and Francis turbine at full load operation [16, 18, 53].

C is the velocity in the section corresponding to the flat plate location. If the flat plate is located upstream on surface A, $C = \underline{C}_A$. If the flat plate is located downstream the cylinder, $C = \underline{C}_B$. The flat plate location has a strong effect on the stability of the coupled system. The difference between \underline{C}_A and \underline{C}_B is given by equation (7.10).

For the flat plat located upstream:

$$\frac{dM_s}{dt} = M_G \frac{dC_A}{dt} = 2\gamma \frac{V_{ext}\rho_s}{\underline{C}_A} \frac{dC_A}{dt} \quad (7.22)$$

For the flat plat located downstream:

$$\frac{dM_s}{dt} = M_G \frac{dC_B}{dt} = 2\gamma \frac{V_{ext}\rho_s}{\underline{C}_B} \frac{dC_B}{dt} \quad (7.23)$$

Source with quasi linear feedback

For large fluctuation, the acoustic field/source relation is in general not linear but the relation can be piecewise linearized. Let's assume the arbitrary relation between the downstream pressure \underline{p}_B and the time averaged external volume \bar{V}_{ext} given in Figure 7.4. It is the typical behavior for attached cavitation on a profile at low incidence. In cavitation free regime, the external volume corresponds to the obstacle volume. Below a threshold ambient pressure, the cavity volume increases in a non-linear manner. At constant velocity, the mass source is defined by:

$$\frac{1}{\rho_s} \frac{dM_s}{dt} = \frac{\partial \underline{p}_B}{\partial t} \frac{d\bar{V}_{ext}}{d\underline{p}_B} \quad (7.24)$$

In such situation, if we assume $\frac{dV_{ext}}{dp_B} \simeq \frac{d\bar{V}_{ext}}{dp_B}$, the HD model can be used to evaluate the relation, $\frac{d\bar{V}_{ext}}{d\underline{p}_B}$, for various flow conditions. Afterwards, the relation is used to evaluate the acoustic feedback on the mass source, $\frac{dM_s}{dt}$, see Figure 7.2. The interaction parameter $\frac{\partial V_{ext}}{\partial p_B}$ is updated dynamically as a function of V_{ext} . As shown in Figure 7.4, the slope of the curve corresponding to the interaction parameter depends on V_{ext} .

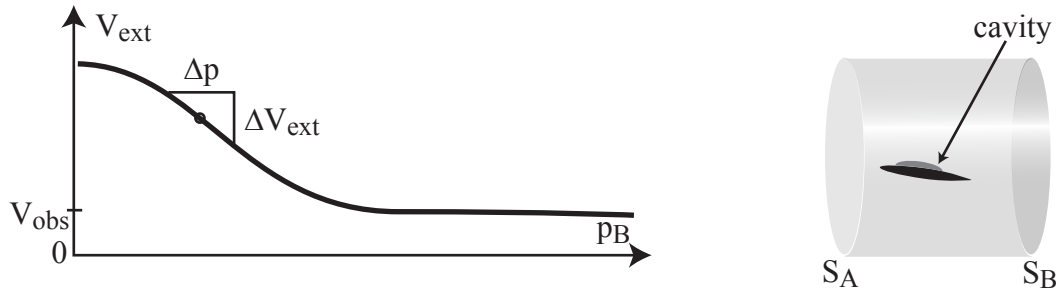


Figure 7.4: Non linear relation between the pressure and the volume of external elements.

Source component with linear feedback

As shown in Subsection 2.2.5, the pressure and velocity field in the source region may be split into a turbulent part and an acoustic part. Therefore we can assume that the source is also split into an hydrodynamic and an acoustic component:

$$F_{x,s} = F_a + F_t \quad (7.25)$$

$$\frac{dM_s}{dt} = \frac{dM_a}{dt} + \frac{dM_t}{dt} \quad (7.26)$$

The hydrodynamic component of the source is due to the unsteady pressure and velocity field induced by the hydrodynamic instability. The acoustic component of the source is due to the fluctuation of pressure and velocity induced by the superimposition of the acoustic waves in the source region. For compact source region, the acoustic field is uniform or stepwise uniform (two uniform fields separated by a step corresponding to the source amplitude).

Let's consider the vortex cavitation in the wake of a bluff body, see Section 3.2. For sufficiently low frequency of acoustic fluctuations, the cavitating part of the wake can be considered as a compact source region. The mass source is given by the fluctuation of the total volume of gaseous phase, from equation (7.10):

$$\frac{dM_s}{dt} = \rho_l \frac{dV_g}{dt} \quad (7.27)$$

Where V_g is the volume of gaseous phase in the source region and $\rho_l = \rho_s$ is the density of the liquid phase in the source region. The contribution of the pressure fluctuation on the cavity volume is split into two parts $\frac{dV_g}{dt} \approx \frac{dV_{g,t}}{dt} + \frac{dV_{g,a}}{dt}$. For sufficiently small acoustic fluctuation, the relation between $\underline{p_s}$ and the vapor volume can be linearized; and the mass source approximated as:

$$\frac{dM_s}{dt} \simeq \rho_l \left(\frac{dV_{g,t}}{dt} + \frac{dV_{g,a}}{dp_s} \frac{dp_s}{dt} \right) \quad (7.28)$$

The term $\kappa_v = -\rho_l \frac{dV_{g,a}}{dp_s}$ corresponds to the cavity compliance; the term $\rho_l \frac{dV_{g,t}}{dt}$ account for the hydrodynamically induced cavity pulsation [6, 84]. Depending on the flow configuration, similar approach can be used to treat the acoustic feedback of velocity on the mass or momentum source. In such situation, the HD model can be used to evaluate the linearized interaction parameter and the hydrodynamic component of the source.

7.2.3 Source with nonlinear feedback

As introduced in Subsection 2.2.4, the flow instability in the wake of a bluff body induces a fluctuating lift and drag force. Applying equation (7.14) to a bluff body installed in a constant diameter pipe gives the following relation between the momentum source and the drag force:

$$F_D(t) = F_{x,s} \quad (7.29)$$

The time averaged drag force is proportional to the square of the flow velocity through the well known relation ($\overline{F_D} = \frac{1}{2}\rho_s \overline{C}^2 A c_D$). But for the time dependent quantity, the relation between C and F_D is complex. The time constant of the flow instability is not negligible with respect to the time constant of the acoustic resonator. Small oscillations of C can alter the vortex shedding dramatically [9]. The oscillation can even take control of the instability mechanism that leads to vortex shedding. This phenomenon, called lock-in, occurs for flow oscillation, f_C , close to twice the vortex shedding frequency, $f_C = \frac{2StC}{D}$.

Using oscillating flow, Barnes and al. shown that a perturbation, $C'/C_0 = 0.008$, is sufficient to lock-in the vortex shedding; the lock-in range depends on the bluff body shape [5]. In such situation, a two-way coupled simulation is necessary to capture the complex interaction between the momentum source and the acoustic feedback of velocity.

7.3 Computational model implementation

7.3.1 Hydrodynamic source

The mass and momentum source terms are included on the right hand side of equation (6.35) and (6.36) to correct the 1D approximation in the source regions, see equation (7.1) and (7.2).

$$\frac{1}{\rho_0 a_c^2} \frac{\partial p}{\partial t} + \frac{\partial C}{\partial x} = \frac{1}{\rho_0 A_0} \frac{dm_s}{dt} \quad (7.30)$$

$$\frac{\partial C}{\partial t} + \frac{1}{\rho_0} \frac{\partial p}{\partial x} - \frac{\mu}{\rho_0} \frac{\partial^2 C}{\partial x^2} + \frac{\lambda |C| C}{2\sqrt{A_0}} = \frac{1}{\rho_0 A_0} f_{x,s} \quad (7.31)$$

The spatial discretization is performed on a staggered grid using centered finite difference scheme:

$$\frac{1}{\rho_0 a_{ci}^2} \frac{dp_i}{dt} + \frac{C_{i+1/2} - C_{i-1/2}}{\Delta x} = \frac{1}{\rho_0 A_{0i}} \frac{dm_{si}}{dt} \quad (7.32)$$

$$\rho_0 \frac{dC_{i+1/2}}{dt} + \frac{p_{i+1} - p_i}{\Delta x} - \mu \frac{C_{i+3/2} - 2C_{i+1/2} + C_{i-1/2}}{\Delta x^2} + \frac{\lambda \rho_0 |C_{i+1/2}|}{2\sqrt{A_{0i+1/2}}} C_{i+1/2} = \frac{1}{A_{0i+1/2}} f_{xsi+1/2} \quad (7.33)$$

The system has a form equivalent to equation (6.39) and (6.40):

$$\mathbf{A} \frac{d\mathbf{x}}{dt} = \mathbf{B}\mathbf{x} + \mathbf{s} \quad (7.34)$$

The matrices \mathbf{A} and \mathbf{B} are equal, the matrix \mathbf{s} contains additional elements for the sources. For the sake of clarity, the source terms per unit length are replaced by the integral of the sources over the element corresponding to the source region:

$$s_{Ai} = \frac{\Delta x}{\rho_0 A_{0i}} \frac{dm_{si}}{dt} = \frac{1}{\rho_0 A_{0i}} \frac{dM_{si}}{dt} \quad (7.35)$$

$$s_{Bi+1/2} = \frac{\Delta x}{A_{0i+1/2}} f_{xsi+1/2} = \frac{1}{A_{0i+1/2}} F_{xsi+1/2} \quad (7.36)$$

The source vector, for the example given in Figure 6.3, is defined as:

$$\mathbf{s} = \left[p_{in} \quad s_{A1} \quad s_{B1+1/2} \quad s_{A2} \quad s_{B2+1/2} \quad s_{A3} \quad -p_{out} \right]^T$$

7.3.2 Linearized interaction parameter

Velocity feedback on momentum source

As described in Subsection 7.2.2, we consider by example a solid sphere in a laminar flow at position $i = 2 + 1/2$. The momentum source is defined as, $F_{x,s} = -6\pi\mu r \underline{C}$, the equation (7.32) for position $i = 2 + 1/2$ is modified as follow:

$$\rho_0 \frac{dC_{2+1/2}}{dt} + \frac{p_3 - p_2}{\Delta x} - \mu \frac{C_{3+1/2} - 2C_{2+1/2} + C_{1+1/2}}{\Delta x^2} + \frac{\lambda \rho_0}{2\sqrt{A_0}} C_{2+1/2} = -\frac{1}{A_0 \Delta x} 6\pi\mu r C_{2+1/2} \quad (7.37)$$

As the momentum source/velocity interaction is linearized, the source term can be moved on the left of equation (7.37). The element \mathbf{B}_{55} of the linear system of differential equation (7.34) is written:

$$r_{2+1/2} = \frac{\lambda \rho_0 \Delta x}{2\sqrt{A_0}} + \frac{1}{A_0} 6\pi\mu r \quad (7.38)$$

And the element $\mathbf{s}_{2+1/2}$ is simply:

$$s_{B2+1/2} = 0 \quad (7.39)$$

The friction due to the external element is added to the skin friction at the pipe wall. Such approach is valid only for flow at low Re without flow instability.

Pressure feedback on mass source or compliance

We assume a vapor cavity at position $i = 2$ dependant on the ambient pressure p_2 . As described in Subsection 7.2.2, the mass source is defined as, $\frac{1}{\Delta x} \frac{dM_s}{dt} \simeq -\frac{K_v}{\Delta x} \frac{dp_s}{dt}$. The equation (7.32) for position $i = 2$ is modified as follow:

$$\frac{1}{\rho_0 a_c^2} \frac{dp_2}{dt} + \frac{C_{2+1/2} - C_{2-1/2}}{\Delta x} = \frac{1}{\rho_0 A_0} \frac{-K_v}{\Delta x} \frac{dp_2}{dt} \quad (7.40)$$

As the mass source/pressure interaction is linearized, the source term can be moved on the left of equation (7.40). The element \mathbf{A}_{44} of the linear system of differential equation (7.34) is written:

$$k_2 = \frac{\Delta x}{\rho_0 a_c^2} + \frac{K_v}{\rho_0 A_{02}} \quad (7.41)$$

And the element s_2 is simply:

$$s_{A2} = 0 \quad (7.42)$$

It is also important to modify the terms $d_{2+1/2}$, $d_{2-1/2}$ in matrix \mathbf{B} . As shown in appendix B, the viscoelastic and the compliance are coupled. In the presence of vapor, the compliance and dissipation are governed by the vapor volume variation. The dissipation is neglected in the cavitating region and we assume:

$$d_{2+1/2} = d_{2-1/2} = 0 \quad (7.43)$$

The cavitation modifies the propagation velocity locally, based on equation (7.41), we can write:

$$\frac{1}{a_{mod}^2} = \frac{\rho_0 k}{\Delta x} = \frac{1}{a_c^2} + \frac{K_v}{\Delta x A_0} \quad (7.44)$$

Where a_{mod} is the locally modified propagation velocity; a_c is the normal propagation velocity and K_v is the cavity compliance.

Flow velocity feedback on mass source or mass flow gain factor

We consider the external element described in Subsection 7.2.2 with the flat plat located upstream at position $i = 2$, the external volume depends on the upstream velocity $C_{2-1/2}$. The mass source is defined as, $\frac{1}{\Delta x} \frac{dM_s}{dt} \simeq \frac{M_G}{\Delta x} \frac{dC_s}{dt}$. The equation (7.32) for position $i = 2$ is modified as follow:

$$\frac{1}{\rho_0 a_c^2} \frac{dp_2}{dt} + \frac{C_{2+1/2} - C_{2-1/2}}{\Delta x} = \frac{1}{\rho_0 A_0} \frac{M_G}{\Delta x} \frac{dC_{2-1/2}}{dt} \quad (7.45)$$

As the mass source/flow velocity interaction is linearized, the source term can be moved on the left of equation (7.45). The matrix \mathbf{A} of the linear system of differential equation (7.34) is written:

$$\mathbf{A} = \begin{bmatrix} l_{1-1/2} & 0 & 0 & 0 & 0 & 0 & 0 \\ 0 & k_1 & 0 & 0 & 0 & 0 & 0 \\ 0 & 0 & l_{1+1/2} & 0 & 0 & 0 & 0 \\ 0 & 0 & -\frac{M_G}{\rho_0 A_0} & k_2 & 0 & 0 & 0 \\ 0 & 0 & 0 & 0 & l_{2+1/2} & 0 & 0 \\ 0 & 0 & 0 & 0 & 0 & k_3 & 0 \\ 0 & 0 & 0 & 0 & 0 & 0 & l_{3+1/2} \end{bmatrix}$$

In such situation, the matrix \mathbf{A} is no longer diagonal and specific inversion algorithm is necessary to obtain the formulation (6.42) necessary for the time integration. The element s_2 is simply:

$$s_{A2} = 0 \quad (7.46)$$

7.3.3 Nonlinear acoustic feedback

space interaction

If no simplification is possible to describe the acoustic feedback, a two-way coupling approach is necessary. The mass and momentum source of the HA model are evaluated using the HD model. The acoustic feedback is integrated in the HD model using adjustable boundary conditions.

The HA model covers the entire acoustic resonator including the source region. The HD model covers the source region; and for computational accuracy, the HD model has actually to extent beyond the source region, see Figure 7.5. The total velocity fluctuation in a given cross section is the sum of the turbulent fluctuation C_d and the acoustic fluctuation, C_a at the cross section. As the HD model is incompressible, the mean flow velocity is considered as constant along the entire domain for momentum source in pipe with constant cross section. But the HD model may have the order of magnitude of the wavelength, therefore the acoustic fluctuation in the region corresponding to the inlet of the HD model, \underline{C}_{inlet} , may differ from the fluctuation in the source region, \underline{C}_s . For mass source, the mean flow velocity differs between the inlet and the outlet of the source region, this difference is given by the source term, $\rho A(\underline{C}_B - \underline{C}_A) \simeq \frac{dM_s}{dt}$. As the flow rate in the HD model is set at the inlet boundary, \underline{C}_{inlet} , the acoustic feedback given by the HA model has to be obtained from the inlet of the source region, \underline{C}_A , in order to approximate accurately the acoustic fluctuation in the source region.

Similar development is done for the pressure fluctuation. The pressure gradient out of the source region can be neglected, see Section 8.2. The pressure difference between the inlet, \underline{p}_A , and the outlet, \underline{p}_B , of the source region is governed by the momentum source:

$$(\underline{p}_B - \underline{p}_A) A \simeq F_{x,s} \quad (7.47)$$

As the pressure is set at the outlet boundary of HD model, \underline{p}_{outlet} . The pressure in a mass or momentum source region is given by the acoustic pressure at the outlet of the source region, \underline{p}_B .

For the selected boundary conditions in the HD model (imposed flow velocity at the inlet and imposed pressure at the outlet), only one field combination is valid to estimate the acoustic feedback on the mass and momentum source, see Figure 7.5:

- The acoustic velocity at the inlet of source region, \underline{C}_A , is introduced at the inlet of the HD model, \underline{C}_{inlet} .
- The acoustic pressure at the outlet of source region, \underline{p}_B , is introduced at the outlet of the HD model, \underline{p}_{outlet} .

7.3.4 Time integration

The time step size and time marching method is different for the HD and HA model:

- an implicit method with large time step is used to integrate the HD model;
- an explicit method with small time steps is used to integrate the HA model.

Consequently, a subcycling technique is employed for the coupled simulations. At t_0 , the beginning of a time interval, Δt , the source terms and boundary conditions are exchanged between the HA and HD model using the procedure presented in appendix D. The HD model is advanced by one time step, $dt_{HD} = \Delta t$. Meanwhile the HA model is advanced

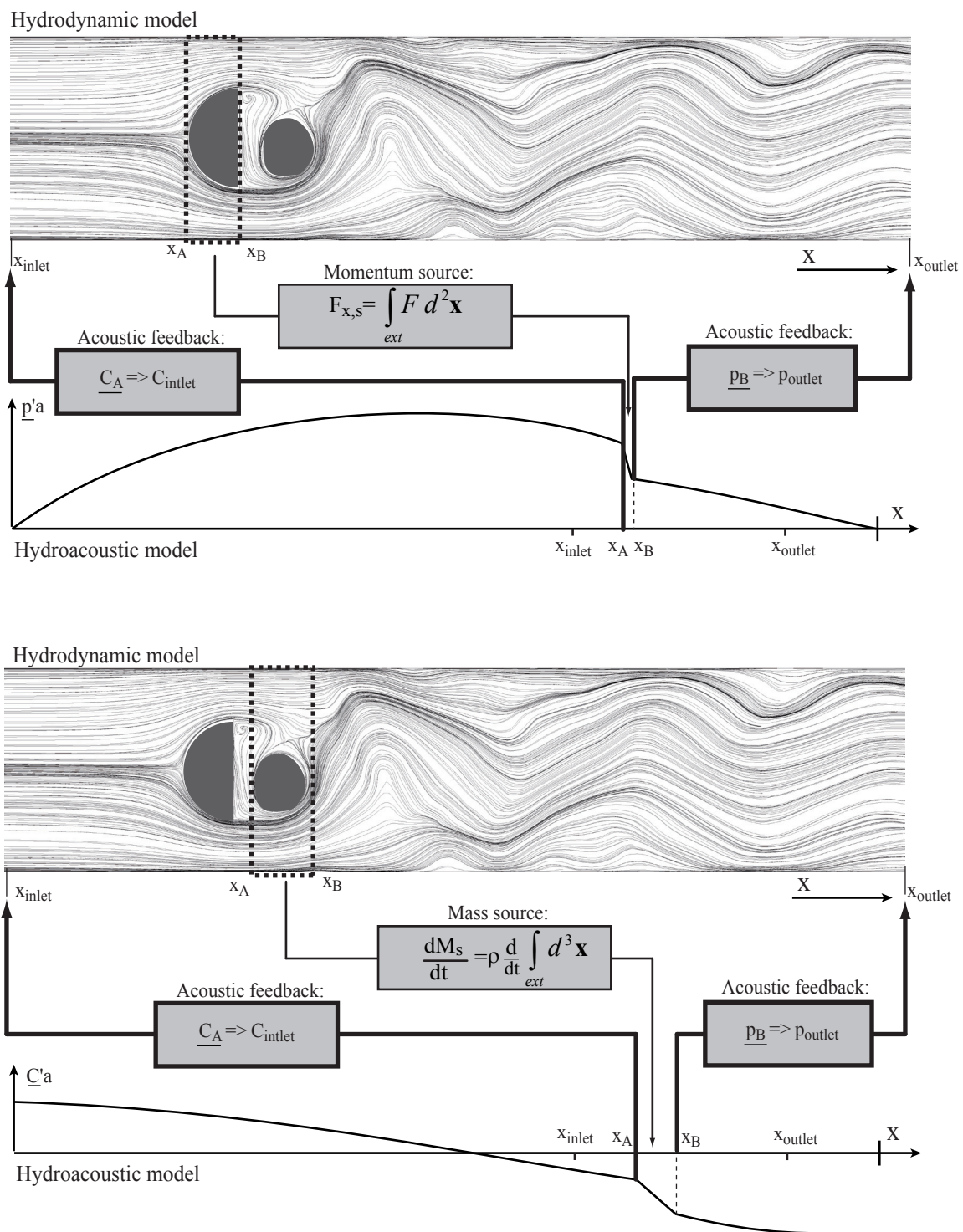


Figure 7.5: Acoustic feedback on momentum and mass source.

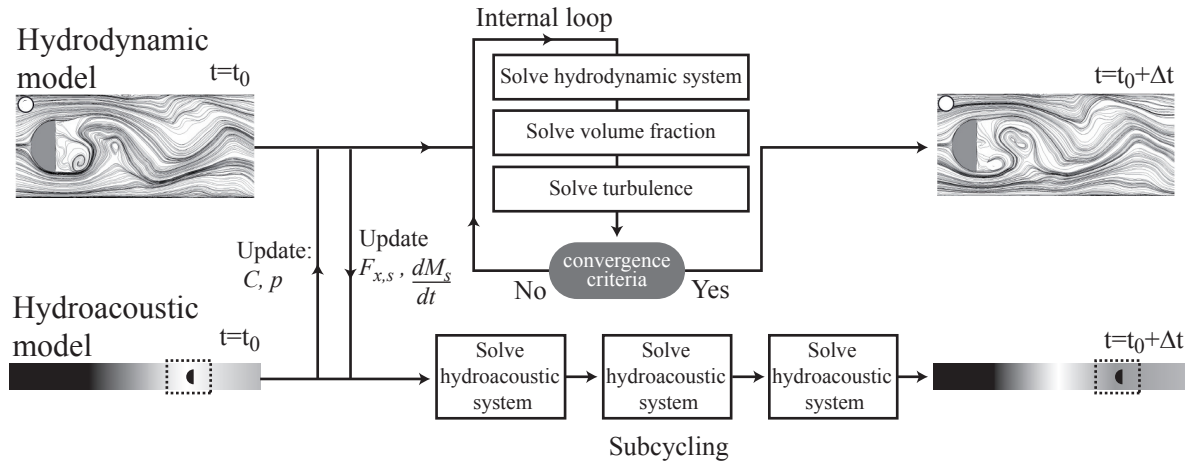


Figure 7.6: Time discretization and data exchange for two-way coupled simulation.

of 10 time steps of size $dt_{HA} = \Delta t/10$. The source terms are assumed constant during the time interval, Δt . Using the notation introduced in appendix E, with x representing the state vector of the HD model and y the state vector of the HA model, the coupling algorithm is written:

$$\mathbf{x}^{t+1} = \mathbf{x}^t + dt(\mathbf{B}_{11}\mathbf{x}^{t+1} + \mathbf{B}_{21}\mathbf{y}^t) \quad (7.48)$$

$$\mathbf{y}^{t+1} = \mathbf{y}^t + dt(\mathbf{B}_{22}\mathbf{y}^t + \mathbf{B}_{12}\mathbf{x}^t) \quad (7.49)$$

Where $\mathbf{B}_{21}\mathbf{y}^t$ is the coupling matrix containing the modification of the boundary conditions of the HD model by the HA model. This matrix is empty except for the lines corresponding to the inlet and outlet boundary regions. $\mathbf{B}_{12}\mathbf{x}^t$ is the coupling matrix containing the source terms. This matrix is empty except for the lines corresponding to the source region. The notation in (7.48) and (7.49) is simplified: The euler implicit stands also for second orders method. The euler explicit stands for the RK4 method including the subcycles. The detailed algorithms for each partition are given in Subsection 6.2.2 and 8.1.2. The overview of the time marching method used for the coupling is given in Figure 7.6.

To simulate 0.4 s, corresponding to 2000 time steps for the HD model and 20'000 time steps for the HA model, the total elapsed time is:

- 20'200+11 s, for the one way concurrent simulation. The models are run sequentially, but the elapsed time for the HA model run, 11 s, is very small with respect to the total simulation time. The HD model is run in parallel mode on 8 processors, see appendix D.
- 27'000 s, for the two-way coupled simulation. The difference with respect to the one way simulation is due to the communication time between the HD and the HA model.

7.3.5 Validation and intermediate results

Mass and momentum source comparison

According to the methodology introduced in Subsection 6.3.2 and the HA model parameter given in Table 6.1 various acoustic fluctuations are plotted in Figure 7.7; the pressure (a),(b) and velocity (c), (d) fluctuations are compared for unit amplitude mass source (b), (d) and momentum source (a), (c). The amplitudes are normalized to obtain a dimensionless amplification factor.

On one side, the momentum source introduces a step in the pressure amplitude for out of resonance flow conditions. On the other side the mass source introduces a step in the velocity amplitude. This can be understood through the analysis of equation (7.1) and (7.2). The momentum source is a discontinuity in the momentum conservation law (7.2) and the mass source is a discontinuity in the mass conservation law (7.1). The step observed for out of resonance conditions is due to this discontinuity. At resonance this step is hardly visible as the discontinuity due to the source is hidden by the large amplitude standing wave.

The amplitude of the first standing wave, $f_s = f_n$, is larger than the second standing wave, $f_s = 2f_n$ for the momentum source. The opposite is observed for the mass source. This is due to the position of the source in the pipe. For the momentum source, the amplification is maximum if the momentum source is on a velocity antinode and minimum if the momentum source is on a velocity node. Similarly, the amplification is maximum if the mass source is on a pressure antinode and minimum if the mass source is on a pressure node. In the present situation, the source is located at $L/L_{TOT} = 0.75$. This position corresponds to the mid distance between node and antinode for the first eigenmode. Therefore the amplification factor is medium for both the momentum and mass source at this frequency and source position. For the second eigenmode, the position $L/L_{TOT} = 0.75$ corresponds to a velocity node and a pressure antinode. Therefore the amplification factor, is maximum for the mass source and minimum for the momentum source. Consequently the relative amplitude of the standing waves corresponding to the first and second eigenfrequency are different for the mass and momentum source.

Cavity compliance influence

For cavitating conditions, the approach developed for source component with linear feedback is employed, see Subsection 7.2.2. The acoustic component of the mass source located at $L/L_{TOT} = 0.75$ is accounted for with a cavity compliance, K_v . Due to this linearized interaction parameter, the eigenfrequencies and eigenmode shapes of the system are modified.

In Figure 7.8, the amplification factor is presented for a harmonic mass source (hydrodynamic component) located also at $L/L_{TOT} = 0.75$. In (a) the amplitudes of pressure fluctuations are presented for various cavity compliance corresponding to the cavitation indexes analyzed in Subsection 5.4.2, the cavity compliance have been adjusted to fit the resonance frequencies. $K_v = 0$ kg/Pa corresponds to non cavitating conditions; $K_v = 8.25 \cdot 10^{-9}$ kg/Pa corresponds to $\sigma/\sigma_i = 0.81$; $K_v = 2.1 \cdot 10^{-8}$ kg/Pa corresponds to $\sigma/\sigma_i = 0.73$ and $K_v = 4.02 \cdot 10^{-8}$ kg/Pa corresponds to $\sigma/\sigma_i = 0.62$. The amplitudes of pressure fluctuations are presented as a function of the position along the pipe and the source frequency according to the method presented in Figure 6.4. At resonance, the

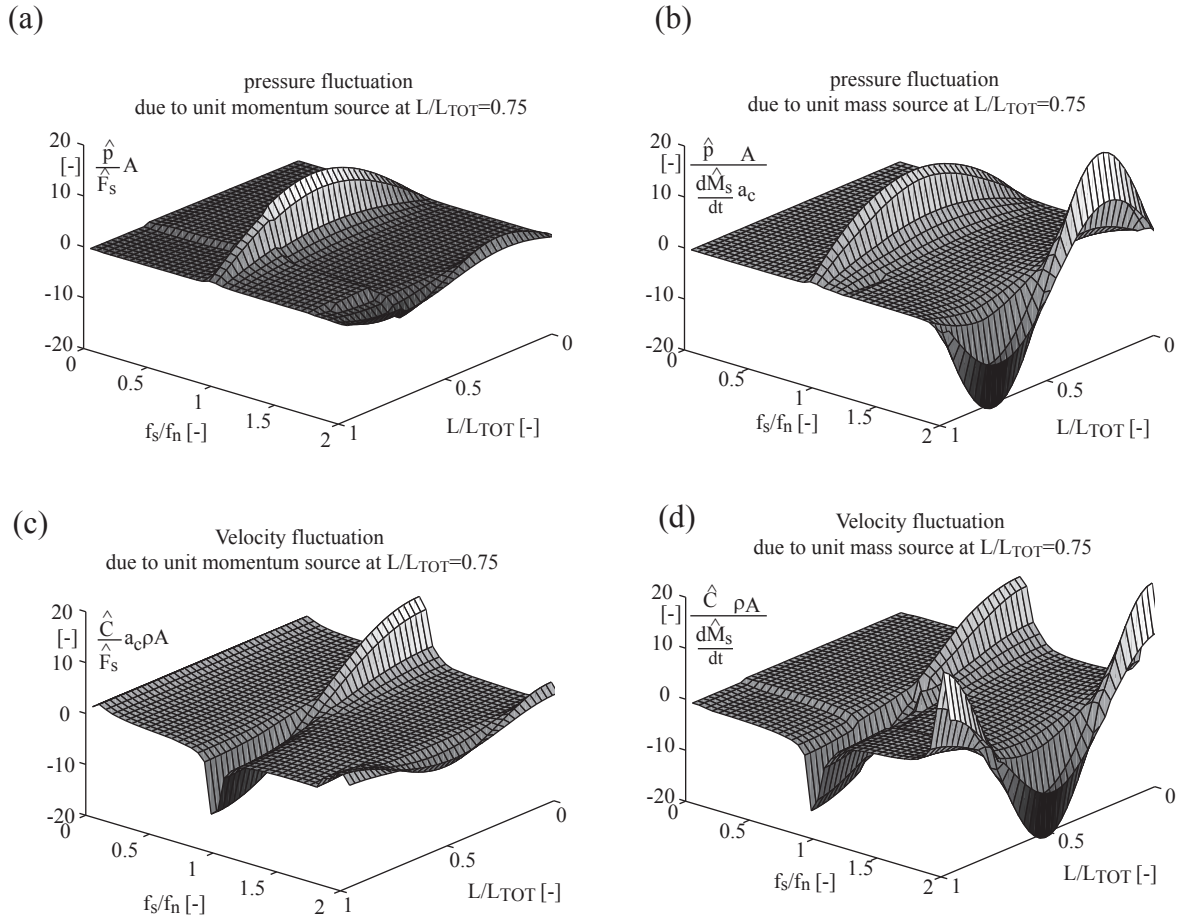


Figure 7.7: Amplitude of pressure (a,b) and velocity (c,d) fluctuation due to harmonic momentum (a, c) or mass (b, d) source located at $L/L_{TOT} = 0.75$ for source frequency varying from 5 to 200 Hz.

shapes of the standing waves are in good agreement with the measured eigenmodes, see Figure 5.13.

In Figure 7.8 (b), the amplification factor is presented for $L/L_{TOT} = 0.25$, $L/L_{TOT} = 0.5$ and $L/L_{TOT} = 0.75$. The resonance frequencies are inversely proportional to the cavity compliance. The amplification factor is strongly influenced by the shape of the standing wave. For $L/L_{TOT} = 0.5$ and $K_v = 0$ kg/Pa the pressure fluctuation for $f_s = 2f_n$ is small because the position corresponds to a pressure node. With a small increase of cavity compliance, $K_v = 8.25 \cdot 10^{-9}$ kg/Pa, the standing wave is modified and the pressure node is shifted from the middle of the pipe toward the cavity. As a result, the position $L/L_{TOT} = 0.5$ is close to a pressure antinode and the amplitude of pressure fluctuation is strongly increased for this location.

Using harmonic sources in the HA model, it is possible to compute the eigenfrequencies for various compliance. The first and second eigenfrequency are plotted as a function of the compliance in Figure 7.8 (c).

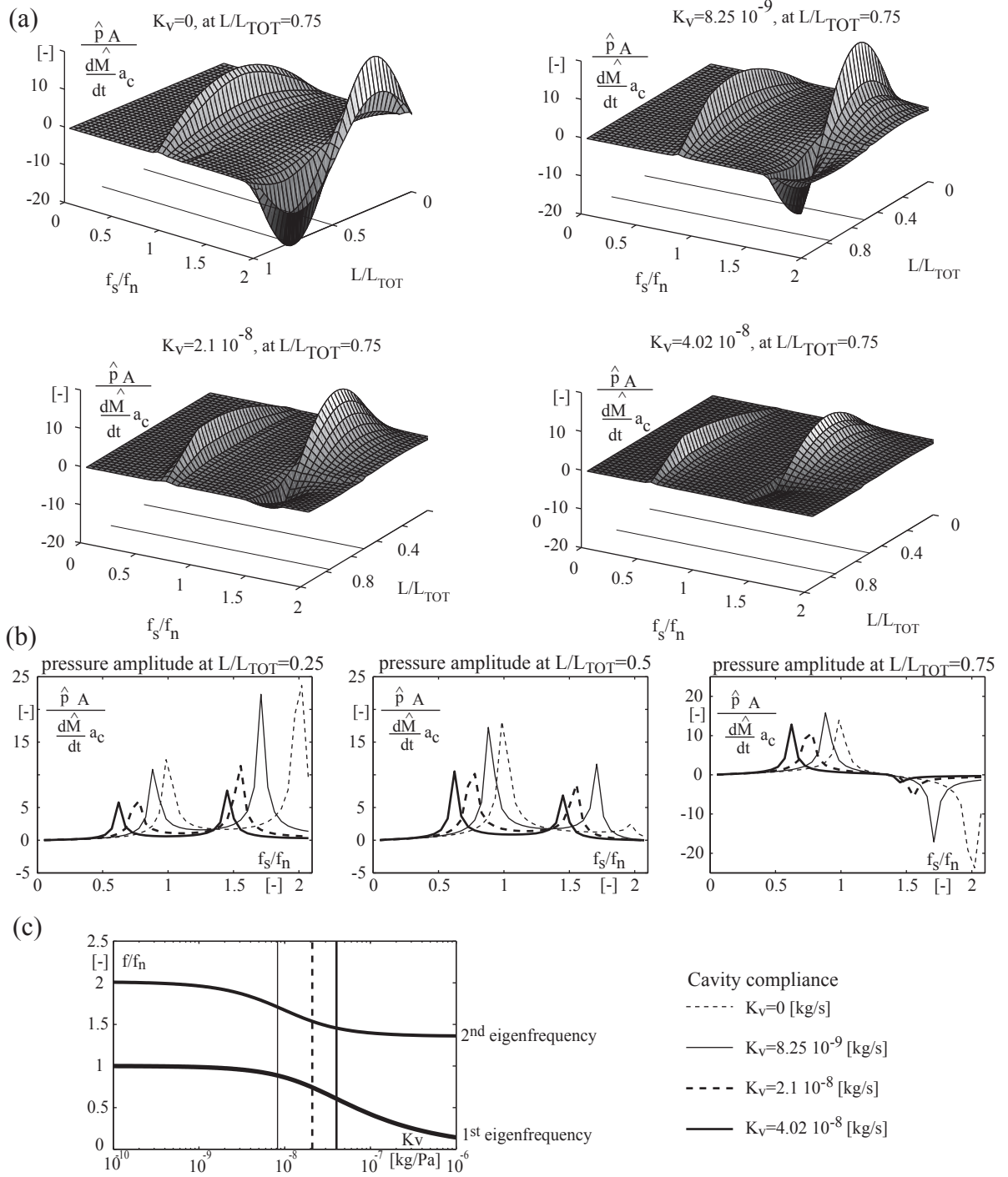


Figure 7.8: Influence of a cavity compliance located at $L/L_{TOT} = 0.75$ on the resonance frequencies and standing waves due to an harmonic mass source located at $L/L_{TOT} = 0.75$; (a) standing wave for different cavity compliance; (b) amplification factor at $L/L_{TOT} = 0.5$ and $L/L_{TOT} = 0.75$ for source frequency varying from 5 to 200 Hz and various cavity compliance; (c) eigen frequency versus cavity compliance.

Chapter 8

Hydrodynamic model

8.1 Computational model implementation

8.1.1 3D turbulent multiphase flow

In the cavitating region, the flow is multiphase, turbulent and highly three dimensional. The objective of the HD model, see appendix D for the software details, is to compute the mass and momentum source resulting from this complex flow. As the source region is compact, the liquid is assumed incompressible. The sources are integrated values and the detailed description of the flow is therefore of minor importance. For this reason, an homogenous multiphase approach is chosen to model the cavitating flow. For the same reason, the turbulence is not analyzed in details. A turbulence model is introduced to take into account the influence of the turbulence on the mean flow. The homogenous assumption leads to the following formulation for the pressure (8.1), velocity (8.2) and density (8.3) of the mixture:

$$p = p_g = p_l \quad (8.1)$$

$$\mathbf{C} = \mathbf{C}_g = \mathbf{C}_l \quad (8.2)$$

$$\rho = \alpha_g \rho_g + \alpha_l \rho_l \quad (8.3)$$

$$1 = \alpha_g + \alpha_l \quad (8.4)$$

The indices g refer to the gaseous phase, l refer to the liquid phase. By convenience, the indices are omitted for the mixture variables. In equation (8.3), the mixture density is given in term of volume fraction α . The mass transfer between the phases is accounted for through a source term in the transport equation of one phase:

$$\frac{\partial}{\partial t} (\alpha_l \rho_l) + \frac{\partial}{\partial x_i} (\alpha_l \rho_l C_{li}) = S_{gl} \quad (8.5)$$

$$S_{gl} = -S_{lg} \quad (8.6)$$

The source term S_{gl} , is the mass rate of condensing vapor/vaporizing water per unit volume. This term is positive during the condensation process and negative during the vaporization process. As the mass is conserved, S_{lg} is equal with an opposite sign.

As the mixture is considered as homogenous, the mass (8.7) and momentum (8.8)

conservation laws of the mixture are introduced as follow:

$$\frac{\partial \rho}{\partial t} + \frac{\partial}{\partial x_i} (\rho C_i) = 0 \quad (8.7)$$

$$\frac{\partial}{\partial t} (\rho C_i) + \frac{\partial}{\partial x_j} (P_{ji} + \rho C_j C_i) = 0 \quad (8.8)$$

The variables are decomposed in a fluctuating part (x') and an average part (\tilde{x}):

$$C_i = \tilde{C}_i + C'_i \quad (8.9)$$

$$p = \tilde{p} + p' \quad (8.10)$$

As the simulation is unsteady and the density is variable, particular ensemble-average method must be used [67, 36]. After some calculation, the averaged mass (8.11) and momentum (8.12) equations are obtained. In the averaged equation the Reynolds stress tensor ($\rho C'_i C'_j$) has been approximated using the Boussinesq hypothesis. Consequently, the turbulent viscosity μ_t is added to the fluid viscosity and the turbulent kinetic energy k is added to the pressure [17]. This formulation is known as the unsteady Reynolds Averaged Navier Stokes (RANS) equations:

$$\frac{\partial \rho}{\partial t} + \frac{\partial}{\partial x_i} (\rho \tilde{C}_i) = 0 \quad (8.11)$$

$$\rho \left[\frac{\partial \tilde{C}_i}{\partial t} + \tilde{C}_j \frac{\partial \tilde{C}_i}{\partial x_j} \right] = \frac{\partial}{\partial x_j} \left[\left[\tilde{p} + \frac{2}{3} k \right] \delta_{ij} + (\mu + \mu_t) \left[\frac{\partial \tilde{C}_i}{\partial x_j} + \frac{\partial \tilde{C}_j}{\partial x_i} - \frac{2}{3} \frac{\partial \tilde{C}_k}{\partial x_k} \delta_{ij} \right] \right] \quad (8.12)$$

The system is open as μ_t and k are unknown. To close the system, two additional transport equation are introduced to evaluate the turbulent viscosity and the turbulent kinetic energy, see SAS-SST turbulence model for the details. To estimate the source term, S_{lg} , in the transport equation (8.5), an algebraic relation is introduced in the cavitation model.

SAS-SST turbulence model

Turbulent flows at high Reynolds number span a large range of length and time scales. It is therefore difficult to solve directly all those scales. Nevertheless it is possible to estimate the global behavior of the flow by taking into account the influence of the small scales using appropriate turbulence model. The selected model, the SAS-SST model is a first order two equations turbulence model developed by Menter et al. [66, 65]. The particularity of this model is to include a term with the second derivative of the velocity field in the length scale transport equation. This term allows the model to react dynamically to the resolved length scale. Series of blending functions and limiters are included in the SAS-SST model to obtain the behavior of the $k - \omega$ model in the steady region. The $k - \omega$ model leads to stable numerical solution and allows to resolve the boundary layer consistently using mesh resolutions down to the viscous sublayer [96]. However, this will require a near wall grid resolution of at least $y^+ < 2$. For coarser mesh, a wall function is employed to connect the wall shear stress to the tangential near wall velocity [60].

Cavitation model

The cavitation model is based on a simplified form of the Rayleigh-Plesset equation. The nucleation sites are assumed to be gas bubbles homogeneously distributed. For spherical bubbles in infinite domain of liquid, the size of the bubbles is related to the ambient pressure through the Rayleigh equation. Its linearized form is introduced as:

$$\frac{dR}{dt} \simeq \sqrt{\frac{2}{3} \frac{|p_v - p|}{\rho_l}} \operatorname{sgn}(p_v - p) \quad (8.13)$$

where R is the bubble radius, p_v the vaporization pressure and p the ambient pressure. For small variation of the bubble size, the time derivative of the volume is proportional to the time derivative of radius:

$$\frac{dV}{dt} \simeq 4\pi R_0^2 \frac{dR}{dt} \quad (8.14)$$

where the initial radius is written R_0 . Introducing (8.13) into (8.14) and noticing that $m_g = \rho_g V$, the mass source term, $S_{lg} = \frac{dm_g}{dt}$, is related to the pressure through the following relation:

$$S_{lg} = N \rho_g 4\pi R_0^2 \sqrt{\frac{2}{3} \frac{|p_v - p|}{\rho_l}} \operatorname{sgn}(p_v - p) \quad (8.15)$$

where N is the number of cavitation nuclei per unit volume in the liquid. Assuming a constant population of nuclei in the mixture with a given radius R_0 , the number of active nuclei for the vaporization process (in the liquid phase) is related to the volume fraction of nuclei by:

$$N^{vap} = \frac{3\alpha_{nuc}\alpha_l}{4\pi R_0^3} \quad (8.16)$$

For the condensation process, the number of site is proportional to the vapor fraction:

$$N^{cond} = \frac{3\alpha_g}{4\pi R_0^3} \quad (8.17)$$

In practice, the vaporization and condensation processes have different time scales. Empirical constants, F^{cond} and F^{vap} are introduced and the mass source of equation (8.5) is finally written as:

$$S_{gl} = S_{gl}^{vap} + S_{gl}^{cond} \quad (8.18)$$

With

$$S_{gl}^{vap} = -F^{vap} \frac{3\rho_g \alpha_{nuc} \alpha_l}{R_0} \sqrt{\frac{2}{3} \max\left(\frac{p_v - p}{\rho_l}, 0\right)} \quad (8.19)$$

$$S_{gl}^{cond} = F^{cond} \frac{3\rho_g \alpha_g}{R_0} \sqrt{\frac{2}{3} \max\left(\frac{p - p_v}{\rho_l}, 0\right)} \quad (8.20)$$

In the present study, standard constants have been used. The nuclei volume fraction is 10^{-5} and the radius of nuclei is $R_0 = 10^{-6}$ m. The vaporization is a quick process, the constant is set to $F^{vap} = 50$, the condensation is slower, $F^{cond} = 0.01$.

8.1.2 Space and time discretization

The space discretization is based on finite volume method. The governing equations (8.5), (8.11), (8.12) and two additional transport equations for the turbulence are integrated over each control volume. Gauss' divergence theorem is applied to transform the volume integral into surface integrals. The time evolution of each variable in a volume is given by the summation of the flux through the surfaces. In the solver, non staggered grid is used to evaluate the fluxes and finite element shape functions are employed to approximate the variables and the derivatives at specific location on the surface called integration points. 3 systems of partial differential equation are obtained. One for the hydrodynamic field, one for the turbulence model and one for the volume fraction equation.

Second order backward euler scheme is used to advance the hydrodynamic system and the transport equation of the volume fraction in time. First order backward euler is used for the turbulence model. These methods are robust, implicit and conservative in time. It leads to 3 linearized system of the form:

$$\mathbf{Ax} = \mathbf{s} \quad (8.21)$$

where \mathbf{A} is the coefficient matrix, \mathbf{x} is the solution vector consisting in C_1 , C_2 , C_3 and p for the hydrodynamic system and \mathbf{s} the right hand side. A multigrid accelerated lower upper factorization technique is used to solve each system, the method is iterative and the residuals are normalized to obtain a convergence criteria. To couple implicitly the hydrodynamic equation with the turbulence transport equation and the volume fraction transport equation, all systems are solved incrementally in an internal loop according to Figure 7.6. Using this iterative technique, the interaction between the systems is taken into account in an implicit manner, see appendix E.

8.2 Application to the reference case study

8.2.1 Setup

Computational domain

In the presence of a bluff body, the flow field in the pipe is strongly perturbed especially downstream the bluff body. Therefore the computational domain of the HD model would have to extend far downstream the bluff body in order to have a uniform pressure field at the outlet. But according to Section 2.2, the force on the external element is predominant with respect to the non-uniformity of the flow field, a compact bluff body is therefore sufficient to respect the compact source assumption ($D \ll \lambda$). Even if the wake length is the same order of magnitude as the wave length, the compact source approximation is still valid. The computational domain of the HD model is presented in Figure 8.1. A distance of $x/D = 4$ was selected for the inlet boundary condition and $x/D = 10$ for the outlet boundary condition. The other dimensions are chosen to fit the experimental setup presented in Section 5.1.

The grid consists in block structured hexahedral mesh using geometric law for the refinement near the solid surfaces. High mesh density is selected in the region of vortex formation, the overview of the nodes distribution is shown in Figure 8.1.

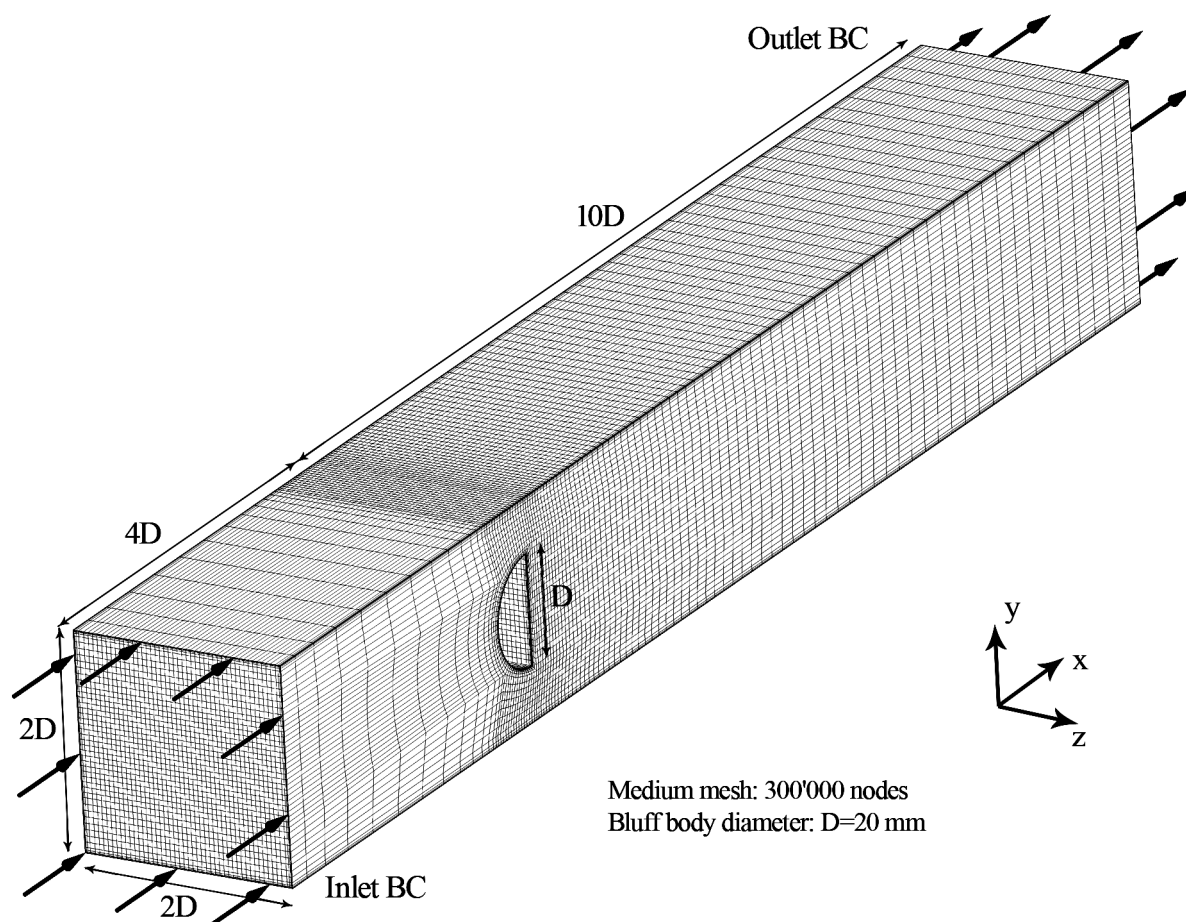


Figure 8.1: Domain dimensions for the HD model.

Simulation time

For each flow condition, after a transition period of 0.2 s, a relevant simulation time of 2 s is performed. Such long simulation time is necessary to perform a consistent analysis of the statistical quantities. As the vortex shedding period T_S depends on the flow velocity, the simulation time corresponds to $85 T_S$ for $C = 2$ m/s and $170 T_S$ for $C = 4$ m/s.

The parameters of the HD model selected to perform the one way and two-way simulations are given in Table 8.1.

Table 8.1: Parameters of the HD model.

Name	Description	Value	Unit
dt	Time step	0.0002	s
T_{total}	Simulation time	2.2	s
medium	Mesh	300'000	node
SAS-SST	Turbulence model	-	-

Boundary conditions

The imposed inlet boundary conditions are velocity, water mass fraction and turbulence profiles. No slip condition is imposed on the solid surfaces. For the outlet boundary, the area averaged pressure is imposed. The HA model provides the area averaged velocity \underline{C} and pressure \underline{p} . Consequently, the velocity profile including the turbulent part at the inlet have to be estimated from the mean flow velocity, \underline{C} . For this purpose, the profiles for a reference flow velocity, $C_{ref} = 3m/s$, have been computed in advance for a fully developed turbulent pipe flow, see Figure 8.2. The profiles are assumed to depend only on the mean flow velocity and to vary linearly with it over the studied range of velocity:

$$\begin{aligned} C_i(y, z) &= C_{i,ref}(y, z) \frac{\underline{C}}{C_{ref}} \\ k(y, z) &= k_{ref}(y, z) \frac{\underline{C}}{C_{ref}} \\ \omega(y, z) &= \omega_{ref}(y, z) \frac{\underline{C}}{C_{ref}} \end{aligned} \quad (8.22)$$

Using those linear relations (8.22), the inlet profiles can be adjusted. For one way concurrent simulation, stationary flow velocity is imposed. For two-way coupled simulation, the inlet velocity is adjusted dynamically at each time step. In all simulations, pure liquid is assumed at the inlet, $\alpha_l = 1$.

The relation between the average pressure of the HD model and the pressure as defined in the HA model is straightforward:

$$\frac{\int_{out} p d^2\mathbf{x}}{\int_{out} d^2\mathbf{x}} = \underline{p}_{outlet} \quad (8.23)$$

In the one-way concurrent simulation, the outlet pressure is kept constant; in the coupled simulation for cavitation free flow conditions the outlet pressure is adjusted at each time step at the post-processing stage. For the cavitating flow conditions, the outlet pressure is adjusted at each time step during the coupled simulation.

Time step size and mesh refinement

For unsteady phenomena such as vortex shedding, strict criteria of mesh and time step independence of the solution is not feasible. The main reason is that the SAS-SST turbulence model adjusts itself dynamically. Two simulations on different grids or using different time step are not comparable by asymptotic expansion, as they are based on different levels of eddy viscosity and consequently on a different resolution of the turbulent scales [3]. Additionally, the HD model is used for various flow velocity in cavitation and cavitation free conditions leading to different vortex shedding frequency. Nevertheless a sensitivity study to mesh refinement and time step has been performed for a reference velocity in cavitation free conditions:

$$C_{ref} = 3m/s \quad (8.24)$$

The summary of the investigated configurations is given in Table 8.2. The cavitation model is not activated. As the direct comparison of the force acting on the bluff body

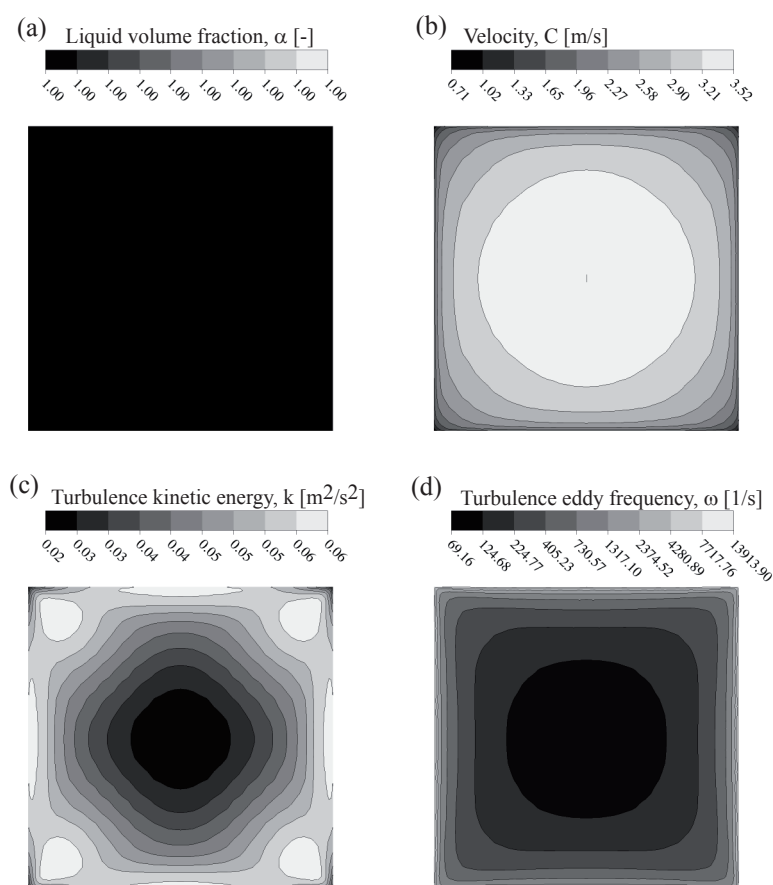


Figure 8.2: Inlet boundary conditions for an average velocity of 3 m/s; (a) volume fraction of liquid; (b) velocity m/s; (c) turbulence kinetic energy; (d) turbulence eddy frequency.

with experimental data is not possible, the target quantities for the convergence of the result are the shedding frequency and the time averaged drag coefficient, see Figure 8.3 and 8.4.

To evaluate the influence of the mesh refinement on the target quantities, the results for a coarse, medium and fine mesh, see Table 8.2 cases 1-3, are compared in Figure 8.3. The mean y^+ on the bluff body for the coarse mesh is $y^+ = 32$ and for the medium mesh $y^+ = 4$. Therefore wall function has been used to compute the boundary layer. Even for fine mesh, $y^+ = 2.3$, the mesh resolution is not sufficient to solve directly the viscous sublayer. The drag coefficient is weakly influenced by the grid refinement. On the other side, the vortex shedding frequency is underestimated for the coarse grid and overestimated for the medium and fine grid. As the low frequency modulation of the drag force is well predicted using the fine and medium mesh while quasi harmonic fluctuation is obtained with the coarse mesh, the medium grid is chosen. Using this mesh, the dynamic behavior of the momentum source is well reproduced for an acceptable computational cost.

To evaluate the influence of the time step value, the time is normalized by the period of vortex shedding, $T_S = 0.017\text{s}$ for $C = 3\text{m/s}$. As shown in Figure 8.4, the target

Table 8.2: Sensitivity study for the HD model.

Case	C [m/s]	Turb. model	Nb. nodes	Δt [s]	y^+	C_D	St
1	3	SAS-SST	26'000	0.0002	36	3	0.36
2	3	SAS-SST	300'000	0.0002	4	3	0.42
3	3	SAS-SST	750'000	0.0002	2.3	2.9	0.42
4	3	SAS-SST	300'000	0.0064	4	2.8	0.21
5	3	SAS-SST	300'000	0.0032	4	3.4	0.29
6	3	SAS-SST	300'000	0.0016	4	3.8	0.36
7	3	SAS-SST	300'000	0.0008	4	3.3	0.4
8	3	SAS-SST	300'000	0.0004	4	2.9	0.42
9	3	SAS-SST	300'000	0.0001	4	2.9	0.42
10	3	SAS-SST	300'000	0.00005	4	3	0.42

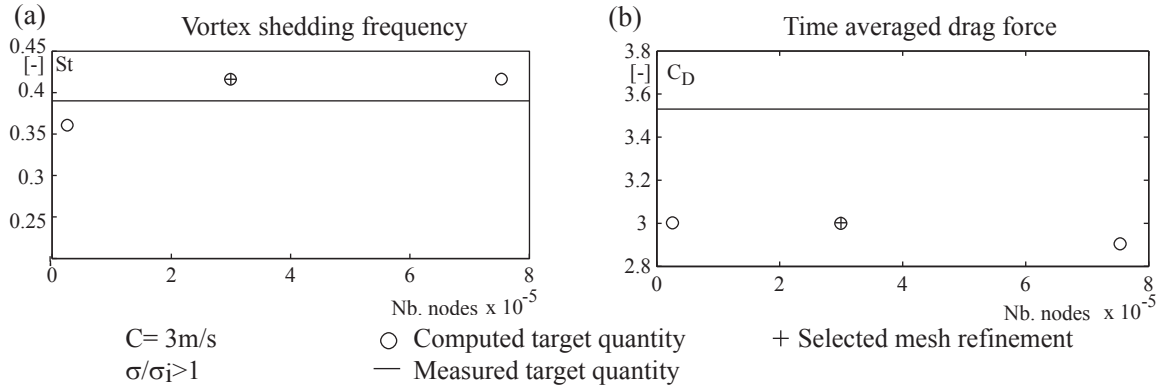


Figure 8.3: Influence of mesh size on the vortex shedding frequency (a) and time averaged drag coefficient (b).

quantities are converging toward a finite value for low time step. Above approximately 50 time steps per period of vortex shedding, the result is weakly dependent on the time step value. Consequently, a constant time step size of $\Delta t = 0.0002 \text{ s}$ is sufficient to cover the entire flow velocity range.

8.2.2 Validation and intermediate results

Vortex shedding and resulting source frequency

As introduced in Subsection 2.2.4, the force on the bluff body is driven by the dynamic of the near wake. The fluctuation of the drag and lift force are presented in Figure 8.5 (a) for $C = 3 \text{ m/s}$. The details of the fluctuation during a period of large fluctuation are given in (b) for the lift force and (c) for the drag force. The streamlines on the symmetry plane XY are plotted at various instant during the corresponding period in (d). The relation between the alternate formation of vortices and the force acting on the bluff body is clearly visible. The intermittent nature of the fluctuation observed experimentally, see

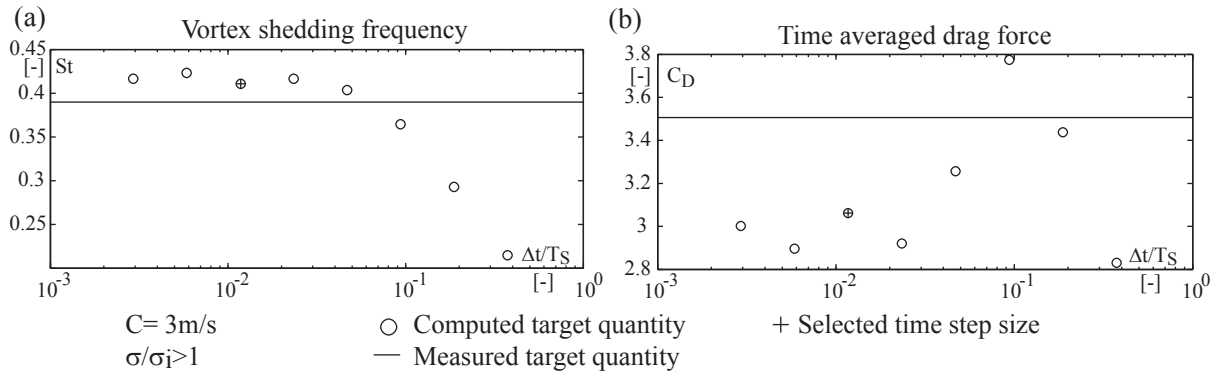


Figure 8.4: Influence of the time step size on the vortex shedding frequency (a) and the time averaged drag coefficient (b).

Figure 5.5, is well reproduced by the HD model.

As shown in Section 5.3, the vortex shedding frequency is proportional to the flow velocity and the drag force is proportional to the square of the flow velocity. In Figure 8.6 (a) the Strouhal numbers computed for various flow velocities, see Table 8.3, are compared with the experimental results. The vortex shedding frequency is overestimated over the entire velocity range by a factor of approximately 7%. Similarly, the drag coefficient is underestimated by a factor of 15%. Consequently, the source frequency is systematically overestimated in the simulation by this factor of 7%, see equation (5.5).

Table 8.3: Flow velocity for the HD model.

C [m/s]	1.75	2	2.25	2.5	2.75	3	3.5	4
c_D [-]	3.01	2.98	3.05	3.03	2.98	3.1	3.1	3.18
St [-]	0.413	0.42	0.414	0.414	0.408	0.419	0.418	0.416

Momentum source approximation

The source identification method is based on the assumption that the 1D pipe flow approximation is valid at the inlet and outlet of the source region, see Chapter 8. This can be validated with the help of the HD model. A reference simulation has been performed for a constant inlet flow velocity, $C = 4$ m/s. As the flow rate is constant at the inlet, the cross section is constant and the model is incompressible, equation (7.13) reduces to:

$$\underbrace{\left(\underbrace{\beta_{out} - \beta_{in}}_{0.54\%} \right) \rho A C_0^2}_{\text{momentum flux}} + \underbrace{\left(p_{out} - p_{in} \right) A}_{99.46\%} + \int_{wall} (-\tau_{1j}) n_j d^2 \mathbf{x} + \int_{ext} (p \delta_{1j} - \tau_{1j}) n_j d^2 \mathbf{x} = 0 \quad (8.25)$$

At the inlet of the domain, the momentum correction coefficient is imposed by the velocity profile, $\beta_{inlet} = 0.9775$. At 10D downstream the bluff body, the correction coefficient

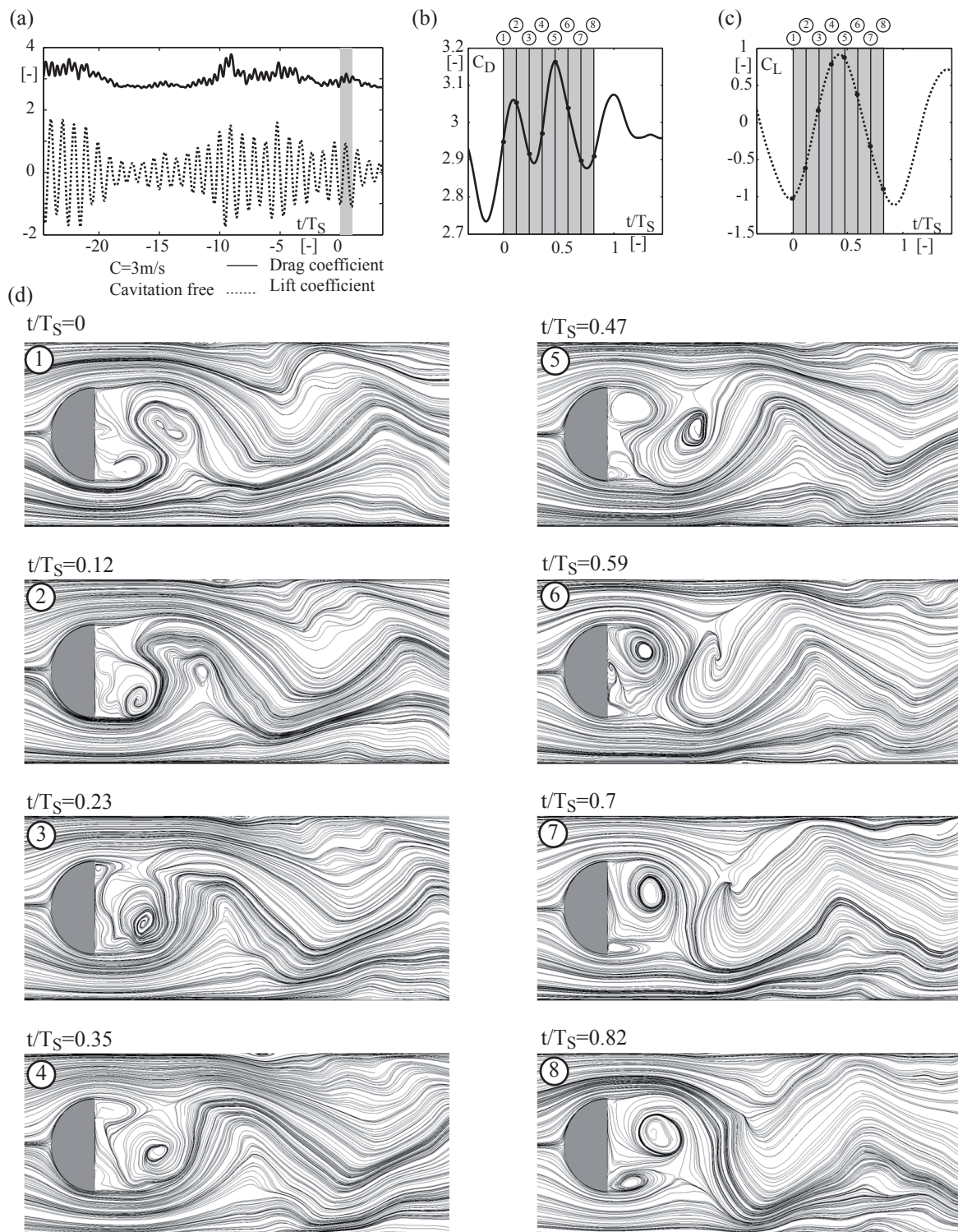


Figure 8.5: Relation between the flow structures and the forces acting on the bluff body; (a) drag and lift fluctuations; details of the drag force (b) and lift force (c) lift; corresponding streamlines on the symmetry plane XY (d).

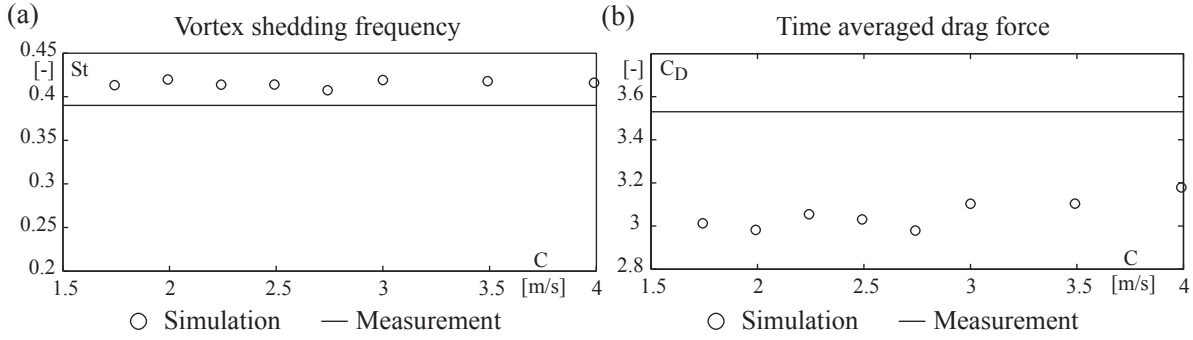


Figure 8.6: Computed vortex shedding frequency (a) and time averaged drag coefficient (b) for different reference flow velocity using medium grid refinement.

fluctuates with the passage of the vortices, $\beta_{10D} = 0.9688 \pm 0.0085$. Far downstream the bluff body, the fluctuations decrease as the vortices are dissipated, $\beta_{50D} = 0.9854 \pm 0.0011$. The hypothesis to neglect β in the HA model, see Section 6.1, is validated through the evaluation of the different terms of (8.25). The first and second terms represent the flux of momentum through the source region. The difference of momentum between the inlet and the outlet of the HD model is governed by the pressure difference, the part due to the non-uniformity of the flow field is less than 0.54%. Therefore the 1D approximation is valid at the inlet and outlet of the HD model and the momentum source (7.14) can be reduced to:

$$\int_0^L \frac{\lambda \rho C |C| P}{8} dx - \int_{wall} -\tau_{1j} n_j d^2 \mathbf{x} - \int_{ext} (p \delta_{1j} - \tau_{1j}) n_j d^2 \mathbf{x} = F_{x,s} \quad (8.26)$$

Based on the parameters of the HA model, the force on the wall is $\int_0^L \frac{\lambda \rho C |C| P}{8} dx = 1.78$ N. In the HD model, the force on the wall is given by, $\int_{wall} -\tau_{1j} n_j d^2 \mathbf{x} = 1.68$ N. The error due to the wall shear stress can be neglected with respect to the force on the bluff body, $\int_{ext} (p \delta_{1j} - \tau_{1j}) n_j d^2 \mathbf{x} = 20.31$ N:

$$\frac{- \int_0^L \frac{\lambda \rho C |C| P}{8} dx - \int_{wall} -\tau_{1j} n_j d^2 \mathbf{x}}{- \int_{ext} (p \delta_{1j} - \tau_{1j}) n_j d^2 \mathbf{x}} = 0.56\% \quad (8.27)$$

Therefore the momentum source is evaluated using the integral of the force on the external element. In the present situation, the external element is defined as the bluff body; the momentum source is equal to the drag force on the bluff body.

8.2.3 Vapor cavity volume evaluation

Two methods are compared to evaluate the volume of vapor in the wake of the bluff body. The first is a simple approximation of the cavitating region based on iso-pressure surface; the second is based on the multi-phase homogenous model, see Section 3.3. In the first method, the change of density is neglected in the HD model and the mass conservation

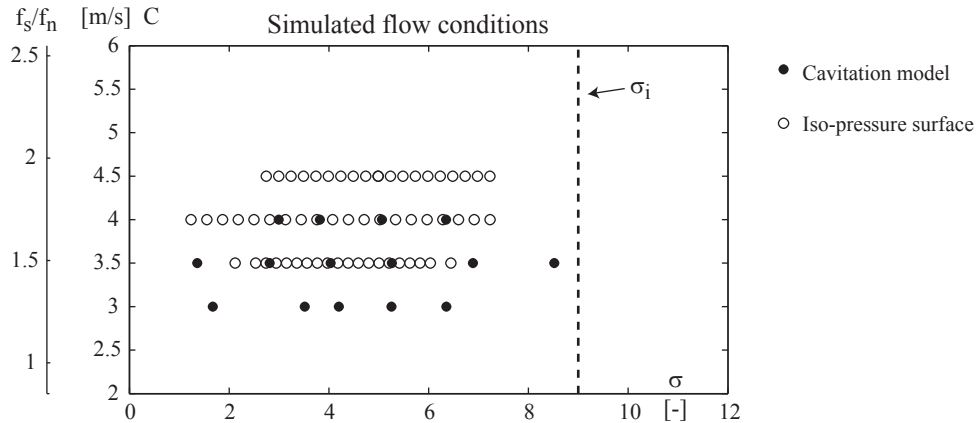


Figure 8.7: Simulated flow conditions using cavitation model and iso-pressure surface.

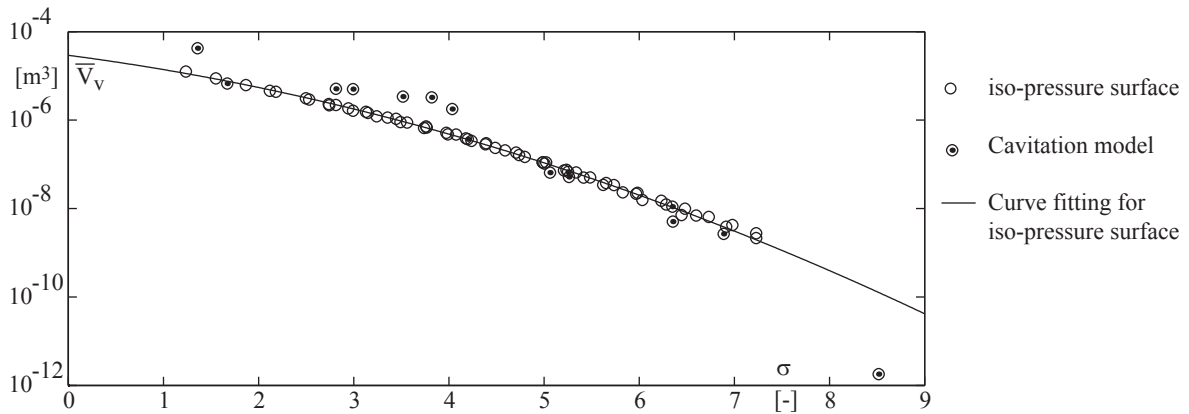


Figure 8.8: Relation between cavitation index and volume of vapor using iso-pressure surface.

law is verified in the HA model only. With the second method, the change of density is taken into account in the HD model; the exact mass and momentum conservation laws are evaluated in the HD model and used to evaluate the mass and momentum source for the HA model.

Iso-pressure surface

The cavitation volume is determined at the post-processing stage using the iso-surface of vaporization pressure, p_v . The volume of fluid contained inside the surface is assimilated with vapor. As the reference pressure has no influence on the solution field, the reference pressure is shifted by step of 2500 Pa to determine the volume of vapor for different cavitation indexes. Using a single solution field for a given flow velocity, the volume of vapor is evaluated for up to 10 cavitation indexes in the present study. Using the parameters given in Table 8.1, 6 simulations (2 per flow velocity) have been performed for $C = 3.5$ m/s, $C = 4$ m/s and $C = 4.5$ m/s, see Figure 8.7. The time averaged volume of vapor using iso-pressure surface is presented in Figure 8.8.

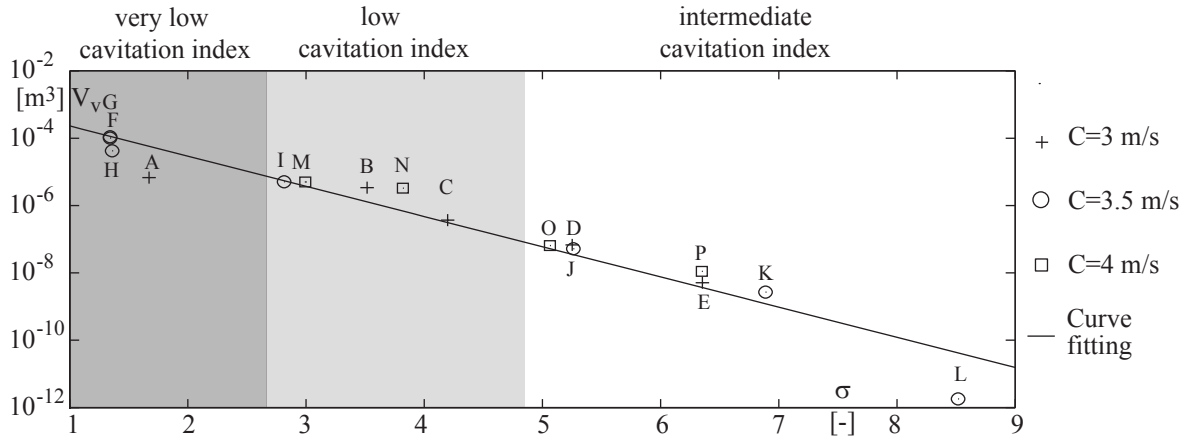


Figure 8.9: Relation between cavitation index and volume of vapor using cavitation model.

Multi-phase model

Table 8.4: Validation of the cavitation model.

Case	C [m/s]	p_{Out} [Pa]	σ	St	\bar{V}_v [m ³]
A	3	15'000	1.67	0.41	$3.02 \cdot 10^{-9}$
B	3	20'000	3.52	0.43	$1.52 \cdot 10^{-9}$
C	3	25'000	4.2	0.41	$1.66 \cdot 10^{-10}$
D	3	30'000	5.25	0.42	$3.02 \cdot 10^{-11}$
E	3	35'000	6.35	0.42	$2.27 \cdot 10^{-12}$
F	3.5	10'000	1.34	-	$4.93 \cdot 10^{-8}$
G	3.5	12'000	1.34	-	$4.52 \cdot 10^{-8}$
H	3.5	16'000	1.36	-	$1.89 \cdot 10^{-8}$
I	3.5	23'000	2.81	0.48	$2.28 \cdot 10^{-9}$
J	3.5	40'000	5.26	0.41	$2.32 \cdot 10^{-11}$
K	3.5	50'000	6.89	0.42	$1.2 \cdot 10^{-12}$
L	3.5	60'000	8.52	0.42	$8.06 \cdot 10^{-16}$
M	4	30'000	3	0.48	$2.24 \cdot 10^{-9}$
N	4	35'000	3.81	0.48	$1.47 \cdot 10^{-9}$
O	4	50'000	5.06	0.41	$2.91 \cdot 10^{-11}$
P	4	60'000	6.35	0.42	$4.95 \cdot 10^{-12}$

Simulations with the multi-phase cavitation model (Section 8.1) have been performed for inlet velocities of 3 m/s, 3.5 m/s and 4 m/s with outlet average pressure ranging from 10'000 Pa to 60'000 Pa. The details of the simulations are given in Table 8.4. The reference pressure location to calculate the cavitation index is the same in the simulation and in the experiment, see Subsection 5.2.1. The mesh and time step size selected in cavitation free conditions are adopted, $Nb.nodes = 300'000$ and $\Delta t = 0.0002$ s. The time averaged volume of vapor obtained from the integration of the vapor fraction, \bar{V}_v , are presented for different cavitation indexes in Figure 8.9. Three regimes of cavitation can

be distinguished:

- At intermediate cavitation level, $5 < \sigma$, the onset of cavitation is intermittent. Small cavities appear in the near wake at approximately $0.5D$ from the trailing edge of the bluff body. The volume of vapor is small enough to have no influence on the vortex shedding dynamics; the Strouhal number, $St \simeq 0.42$, remains constant in this regime.
- At low cavitation level, $3 > \sigma > 5$, the presence of cavitation is permanent in the wake of the bluff body. The vortex shedding frequency increases in this regime.
- At very low cavitation index, $\sigma < 3$, a pocket of vapor is formed in the wake of the bluff body and the periodicity of the phenomenon is lost.

The simulation results are compared with the experimental data in Figure 8.10. In (c), the simulation is given in terms of volume, V_v , and the experiment in terms of visible surface, A_v . In Figure 8.10 (a) and (b), snapshots of the cavitation figure are presented for the simulation and for the experiment with equivalent flow conditions. Both images are taken from above in the negative y direction, see Figure 5.1 for the camera position and Figure 8.1 for the coordinate system. The shape of the cavities provided by the numerical simulation corresponds to the observed cavities. At low cavitation index, the volume of vapor seems similar in the simulation and in the experiment, see Figure 8.10 B and β . But the high frequency pulsation corresponding to the vortex shedding is inaccurately predicted in the simulation. Independently of the flow velocity, case B, I, M and N, a frequency peak is predicted at $1.9 f_n$. Such behavior hasn't been observed in the experiment. It is therefore suspected to be a numerical artefact. At intermediate cavitation level, see Figure 8.10 D and δ , intermittent cavitation is predicted in the simulation and permanent cavitation has been observed in the experiment for equivalent cavitation index. For higher cavitation index close to σ_i , see Figure 8.10 K and κ , the volume of vapor is underestimated in the the simulation. In the experiment, the vapor is quasi continuously observed in the wake of the bluff body. On the contrary, small cavitating structures burst randomly during the simulation.

The time history of vapor volume using cavitation model and iso-pressure surface are compared for intermediate and low cavitation level in Figure 8.11. At intermediate cavitation index (a), $\sigma \simeq 7$, intermittent cavitation is predicted using both methods. The fluctuation frequency is equivalent for both models but the amplitude is larger for the iso-pressure method. At low cavitation index (b), $\sigma \simeq 3$, no correlation is observed between the flow velocity and the cavity pulsation frequency with the cavitation model. On the contrary, using iso-pressure surface, the cavity pulsation frequency is proportional to the flow velocity and equal to twice the vortex shedding frequency according to the experiment, see 5.3.2. With the iso-pressure method, the volume of vapor but also the fluctuation amplitude increases at low cavitation.

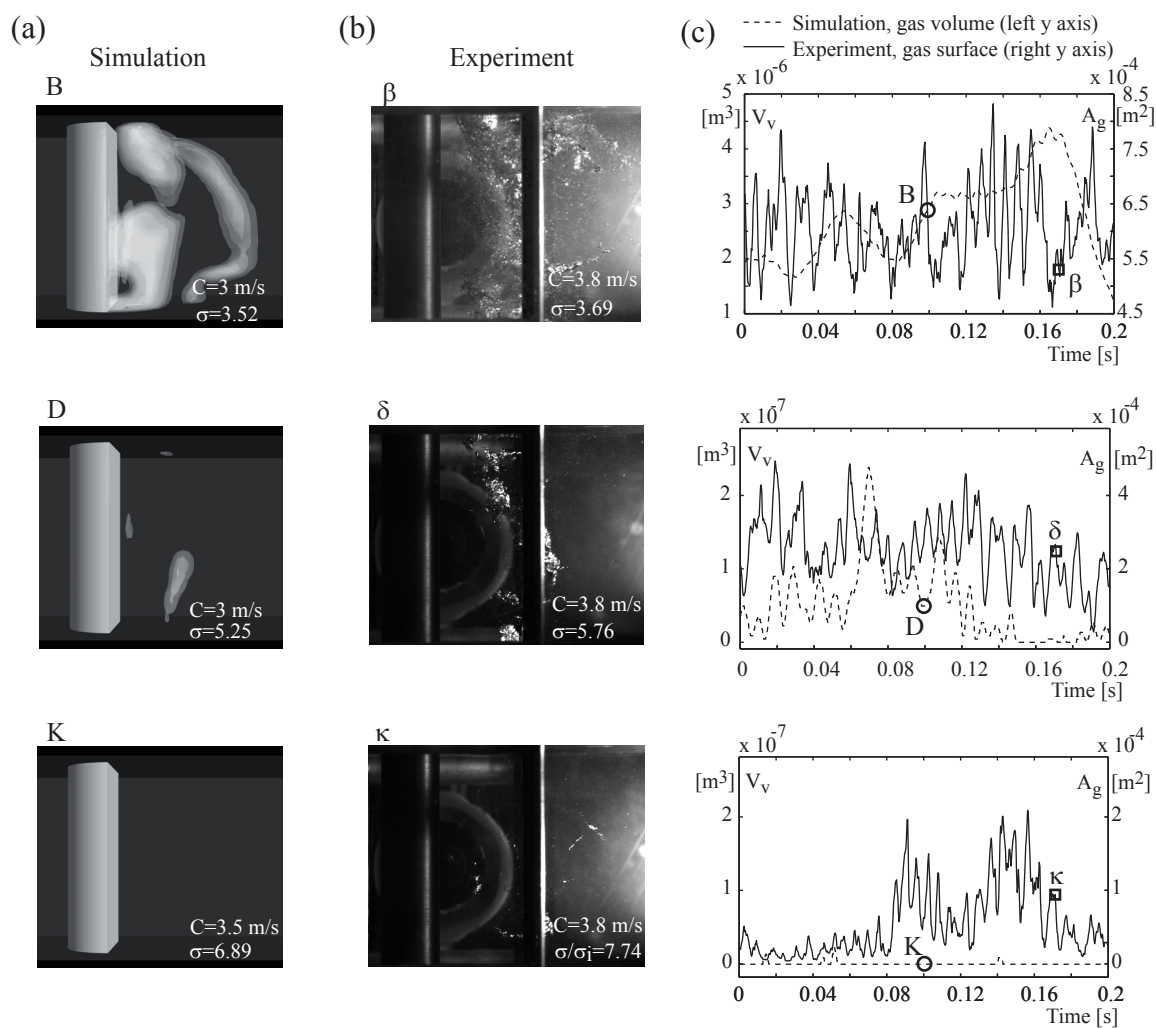


Figure 8.10: Comparison of the predicted and measured cavitation volume; snapshots of the simulation (a), snapshot of the experiment (b) and time history of the vapor volume fraction (c).

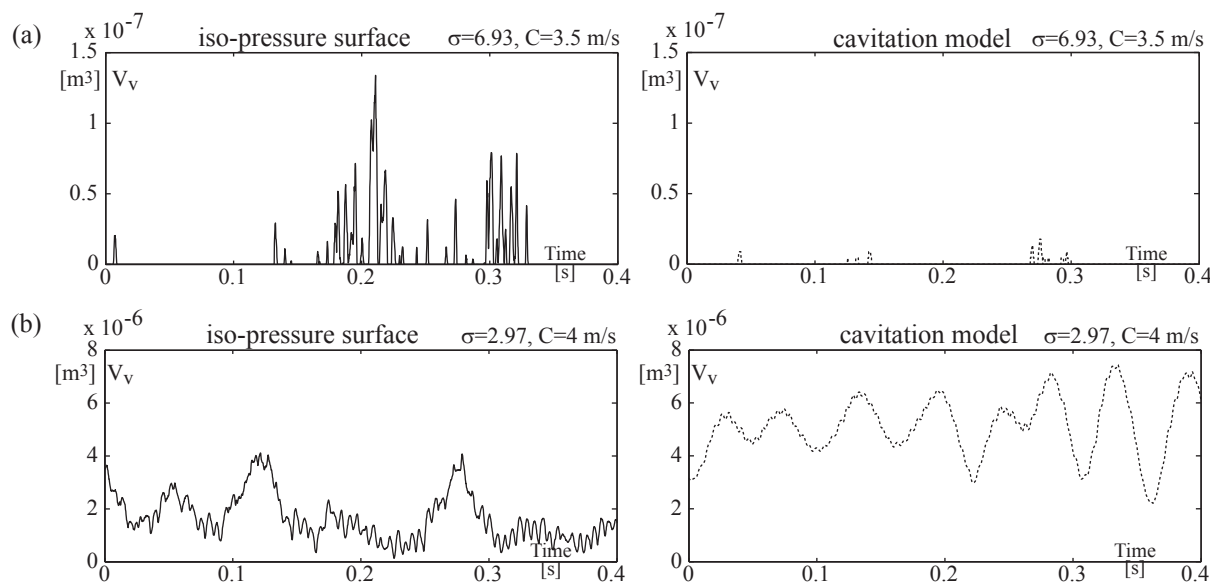


Figure 8.11: Comparison of the time history of cavity volume using cavitation model and iso-pressure surfaces for intermediate (a) and low cavitation level (b).

Part III

Results of the coupled and concurrent simulations

Chapter 9

Cavitation free regime

9.1 One-way concurrent simulation

9.1.1 Setup

No mass source is considered, the momentum source, F_s , is estimated using the force acting on the bluff body, $\int_{ext} F_x d^2x$, according to the developments presented in Subsection 7.1.2 and the simplification for the present case study, see Subsection 8.2.2. The acoustic feedback of pressure is null and the acoustic feedback of velocity is assumed to be negligible, see Subsection 7.2.1. The data exchange between the models is summarized in Figure 9.1

Flow conditions

In cavitation free conditions, the resonance frequency is $f_n = 96.5$ Hz. The investigated velocity range is selected in order to have the source frequency below, at and above the resonance frequency. The investigated flow conditions are summarized in Table 9.1.

Table 9.1: Flow conditions for the one-way concurrent simulation.

C [m/s]	1.75	2	2.125	2.25	2.375	2.5	2.625	2.75	3	3.5	4
f_s/f_n [-]	0.75	0.87	0.9	0.96	1.01	1.07	1.1	1.16	1.3	1.51	1.72
Δp [kPa]	4.9	6.5	7.3	8	9	9.8	10.1	12	14.5	20	26

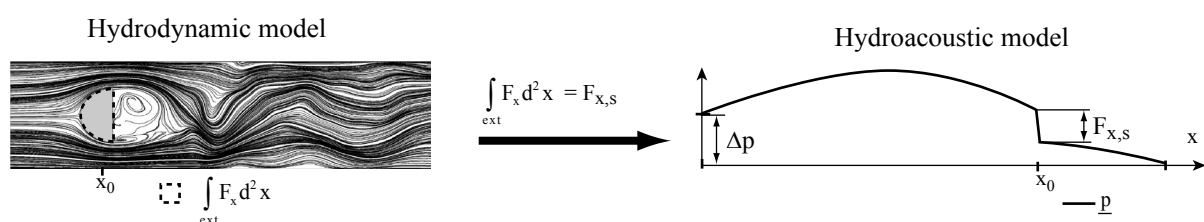


Figure 9.1: One-way concurrent simulation data exchange.

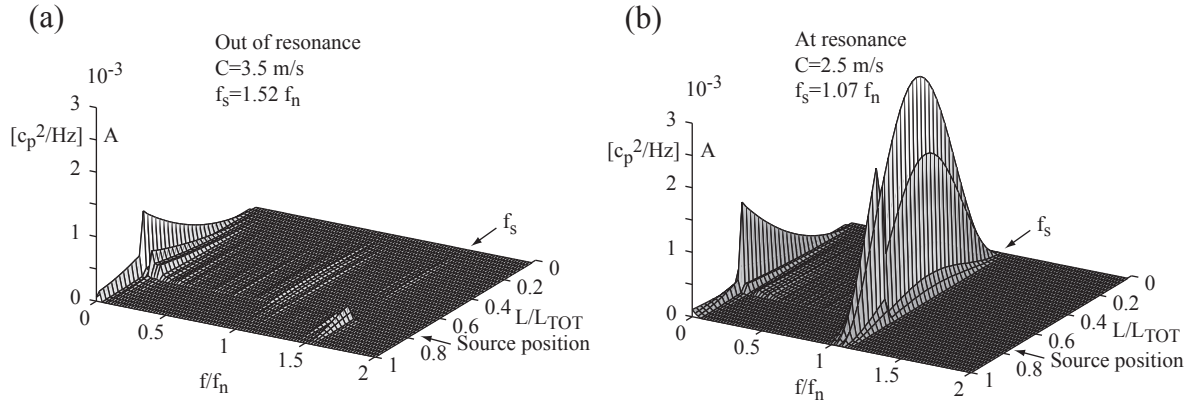


Figure 9.2: PSD of pressure fluctuation along the pipe for resonant (a) and non-resonant conditions (b).

The source frequency, f_s , is calculated using the results given in Table 8.3. Δp is the pressure difference between the inlet and outlet boundary of the HA model.

Simulation procedure

In a first step, The time evolution of the momentum source is computed with the HD model using the parameters given in Table 8.1. Constant velocity and turbulence is imposed at the inlet, constant pressure is imposed at the outlet. The cavitation model is switched off.

In a second step, the time evolution of the force acting on the bluff body is introduced as a momentum source in the HA model, the parameters of the HA model are given in Table 6.1. The position of the source in the HA model corresponds to the bluff body position, $L/L_{TOT} \simeq 0.75$. As the time steps of the HA model are smaller, the force between two time step is estimated using spline interpolation.

Finally, in order to compare the simulation results with the measurement data in the spectral domain, the simulation data are resampled at the experimental sampling frequency of 1000 [Hz]. For measurement and simulation, the same parameters, given in Table 5.1, have been used for the spectral analysis except for the time signal duration.

The mean flow velocity in the HA model depends on the momentum source and the pressure difference between the inlet and outlet of the pipe. Therefore the boundary conditions of the HA model (inlet and outlet pressure) have to be adjusted for each operating condition in order to fit the flow velocity imposed in the HD model: the boundary conditions of the HA model are evaluated at the beginning of each simulation using the time averaged momentum source.

9.1.2 Results

Distribution of acoustic pressure fluctuation

Two flow conditions are selected for detailed analysis, $C = 2.5$ m/s and $C = 3.5$ m/s.

- For $C = 2.5$ m/s, the source frequency is close to the natural frequency, $f_s = 1.07 f_n$.

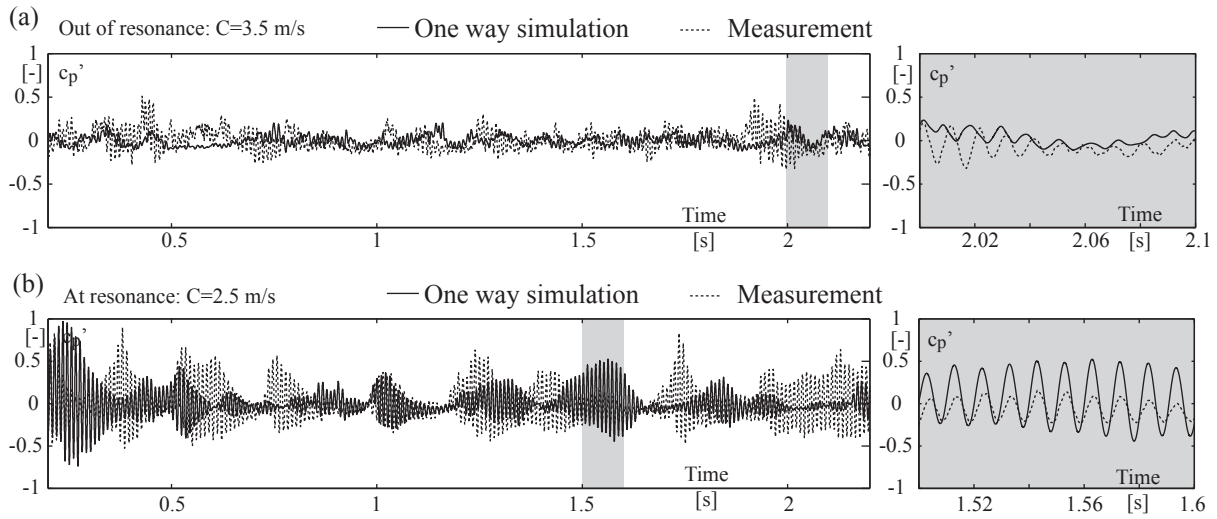


Figure 9.3: Time history of the pressure fluctuation at $L/L_{TOT} = 0.5$ for non-resonant (a) and resonant (b) conditions.

– For $C = 3.5$ m/s, the source frequency is far from the natural frequency, $f_s = 1.51f_n$. In Figure 9.2, the amplitude of the pressure fluctuation is presented for the non-resonant condition (a) and for the resonant condition (b). The PSD of the pressure coefficient is plotted for each node of the HA model. Pressure fluctuations are observed at the source frequency and at the natural frequency of the pipe for both conditions:

- For $f_s = 1.07f_n$ (b), The source frequency is slightly higher than the natural frequency. Large fluctuation with equivalent amplitudes are observed at both frequencies. The distribution of pressure at the natural frequency corresponds to the eigenmode shape. The distribution of pressure at the source frequency is similar but a discontinuity is observed at the source position.
- For $f_s = 1.51f_n$ (a), The source frequency is far from the natural frequency. Due to the broad band noise of the source, small fluctuation is observed at the natural frequency. At this frequency, the pressure distribution corresponds to the first eigenmode. At the source frequency, small fluctuation is observed especially in the downstream part of the pipe.

The relatively large fluctuation observed at low frequency is due to the low frequency modulation of the momentum source. The effect is observed in both conditions. At higher frequencies, very small fluctuation is observed at the second and third eigenfrequencies. The distribution of pressure fluctuation at the eigenfrequencies is in good agreement with the measurement, see Figure 5.13.

Time history of acoustic pressure fluctuation

The pressure fluctuations at $L/L_{TOT} = 0.5$ are presented in Figure 9.3 for non-resonant (a) and resonant conditions (b). The position corresponds to a pressure antinode and maximum amplitude is expected at this location. The modulated nature of the fluctuation observed during the experiment is reproduced in the simulation for both flow conditions.

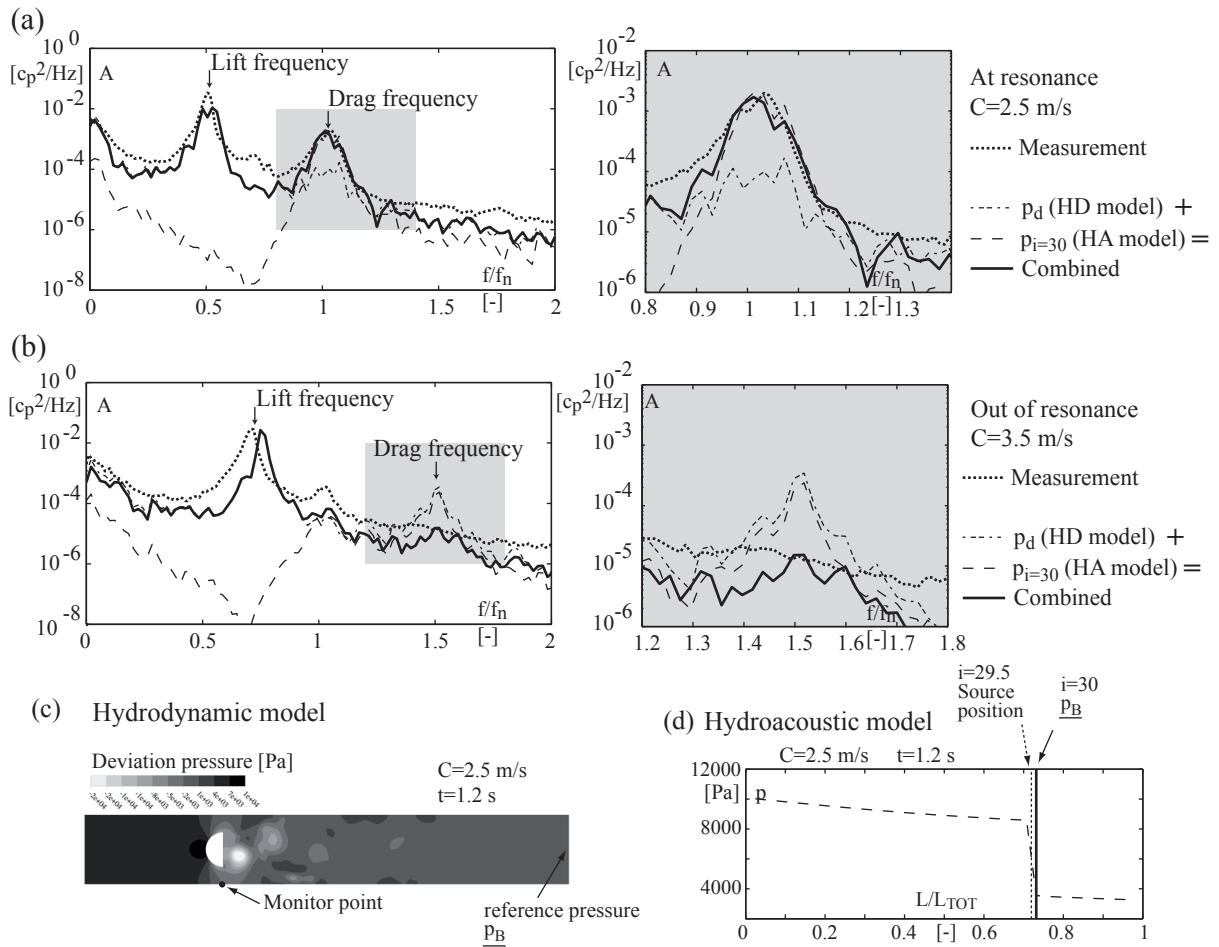


Figure 9.4: PSD of pressure fluctuation below the bluff body (monitor point) for resonant (a) and non-resonant conditions (b); Snapshot of the solution field of the HD model (c) and HA model (d).

Pressure fluctuation in the source region

In Figure 9.4, the PSD of pressure fluctuation below the bluff body (the exact monitoring position is given in (c)) are presented for resonant (a) and non-resonant condition (b). The fluctuation amplitude of the pressure coefficient is given in logarithmic scale. The measurement is compared with the solution of the HD model alone, the solution of the HA model alone and the combination of both solution. The pressure field in the source region is decomposed as follow:

$$p(x, y, z, t) = p_d(x, y, z, t) + \underline{p}_B(t) \quad (9.1)$$

where $\underline{p}_B(t)$ is the surface averaged pressure at the outlet of the source region and p_d is the deviation from this average pressure, see Figure 9.5. The outlet of the source region is defined as follow:

- In the HA model, \underline{p}_B corresponds to the pressure node located downstream the source, $p_{i=30}$;
- In the HD model, \underline{p}_B corresponds to the outlet average pressure, \underline{p}_{outlet} .

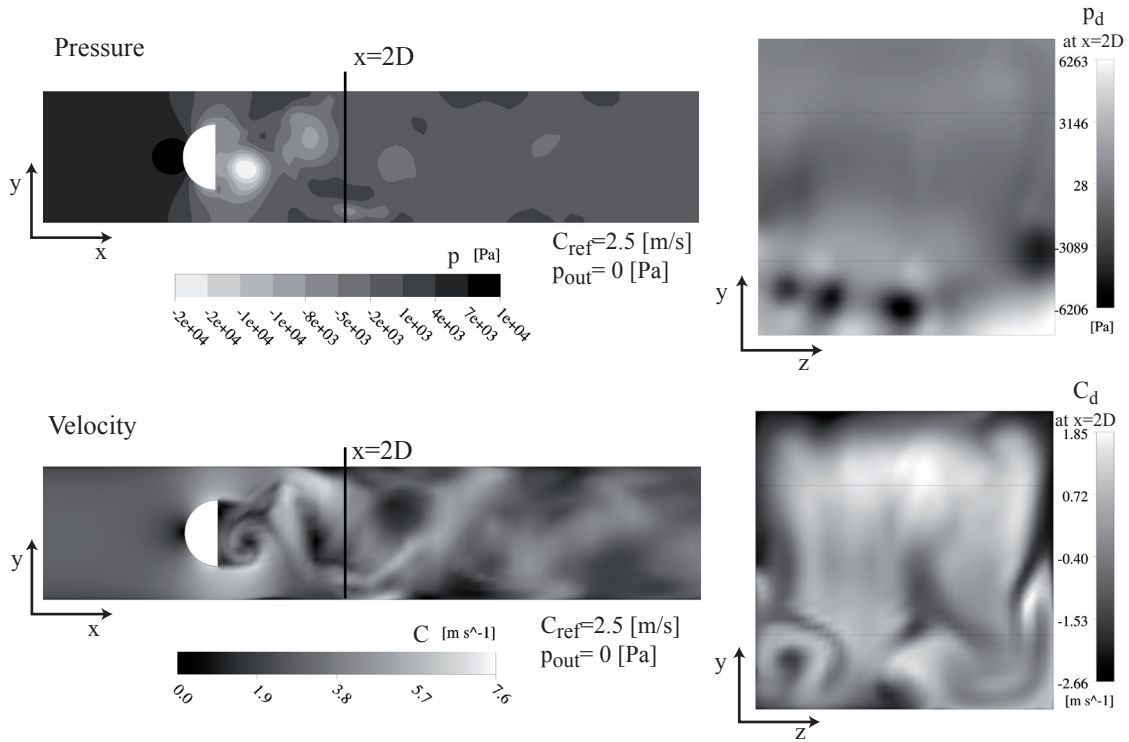


Figure 9.5: Decomposition of the 3D field in a 1D variable and a deviation field.

The combined solution field of the concurrent simulation in the source region is therefore defined as:

$$p(x, y, z, t) = p_d(x, y, z, t) + \underline{p_{i=30}}(t) \quad (9.2)$$

where p_d is the deviation from the reference outlet pressure given by the HD model and $\underline{p_{i=30}}$ is the reference pressure given by the HA model at the node downstream the source position.

The frequency range with maximum energy corresponds to the pressure fluctuation associated with the lift force, see Subsection 2.2.4; for $C = 3.5 \text{ m/s}$, $f_L \simeq 0.7 f_n$; for $C = 2.5 \text{ m/s}$, $f_L \simeq 0.5 f_n$. The height of this peak is well predicted in both cases, Figure 9.4 (a) and (b), by the HD model. This fluctuation is due to the inhomogeneity of the flow field at the obstacle position. The frequency shift observed between the measurement and the simulation is due to the overestimation of the source frequency in the simulation, see Section 8.2.

The frequency range associated with the drag force corresponds to $f_D \simeq 1.5 f_n$ for $C = 3.5 \text{ m/s}$ and $f_D \simeq f_n$ for $C = 2.5 \text{ m/s}$. The amplitude of this peak is well predicted by the combined solution in both cases. For the resonant condition, $C = 2.5 \text{ m/s}$, the amplitude at this frequency is underestimated by the HD model. On the other hand, the amplitude is well estimated by the HA model. At resonance, the fluctuations are amplified by the acoustic resonance, this effect is taken into account only by the HA model. For non-resonant conditions, the HD model overestimates the amplitude of the fluctuation, but the HA model compensates this error (the fluctuations are in phase opposition) and the combined solution is in good agreement with the measurement at this frequency.

In the source region, the pressure fluctuations associated with 3D dynamic are well predicted using the HD model alone. But for phenomena associated with axial dynamics, the combined solution is better in resonant and non-resonant conditions. In resonant conditions the acoustic amplification is taken into account only by the HA model. More surprisingly, in non-resonant situation the combined solution is improved with respect to the solution of the HD model alone. The reason is the following: in the HD model, the imposed boundary conditions, fixed velocity at inlet and fixed average pressure at outlet, are not realistic. On the contrary, the boundary conditions of the HA model are more realistic, constant pressure at inlet and outlet of the pipe. For this reason, the combined solution is in better agreement with the measurement even in non-resonant situation.

Amplitude of the acoustic pressure fluctuation

At resonance, the maximum amplitude of pressure fluctuation is located at the pressure antinode, $L/L_{TOT} = 0.5$. In Figure 9.6, the amplitude of pressure fluctuation at this location is presented for different flow conditions, see Table 9.1. As shown in Section 8.2, the source frequency is systematically overestimated by 7% in the simulation. To avoid this offset, the amplitude are presented in function of the source frequency instead of the flow velocity. In Figure 9.6 (a), the waterfall PSD of pressure coefficient is plotted for the simulated flow conditions given in Table 9.1. The results are compared with measurement performed at equivalent source frequencies. Good agreement is found between the measurements and the simulations:

- Maximum amplitude is observed at resonance as the source frequency is equal to the natural frequency of the pipe.
- In non-resonant conditions, two peaks are visible, one at the source frequency, the other at the natural frequency of the pipe.
- The low frequency modulation is present at all flow conditions.

In Figure 9.6 (b), the standard deviation of the pressure coefficient is employed to compare the fluctuation amplitudes for different source frequencies. For the measurements, the mean value and 95% confidence bound are presented. The statistic is obtained from 32 samples of 2 s each. At resonance ($f_s \simeq f_n$), relatively good agreement is found between the simulation and the measurement. Out of resonance, the amplitude is underestimated in the simulation by a factor of approximatively 50%. A possible explanation is the presence of additional sources in the system which are not taken into account in the simulation; the abrupt cross sectional variation at the outlet of the pipe is suspected to generate the additional pressure fluctuation observed in the experiment for non-resonant conditions.

Influence of the viscoelastic damping

As shown in appendix B and in Section 6.3, the viscoelastic damping has an influence on the amplitude of the fluctuation but no effect on the resonant frequency and spatial distribution of the pressure fluctuation. In Figure 9.7, the standard deviation of pressure at $L/L_{TOT} = 0.5$ for resonant condition, $f_s = 0.96f_n$, is presented for various viscoelastic damping. The amplitude is compared with the measured value at equivalent flow conditions, $f_s = 0.97f_n$. Mean value and 95% confidence bound are determined using 32 samples of 2 s each. The result obtained from the viscoelastic damping determined experimentally, see appendix B, is inside this confidence bound. Both results are

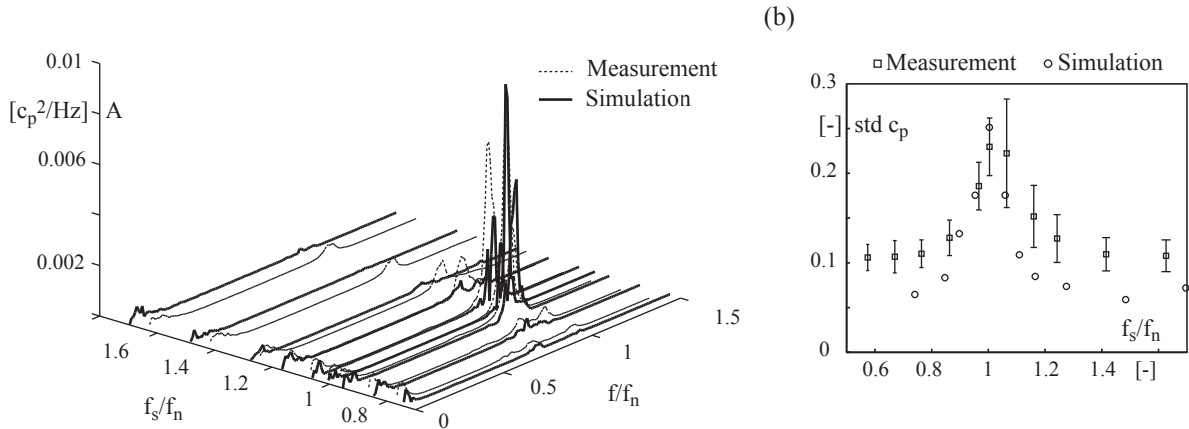


Figure 9.6: Amplitude of pressure fluctuation at $L/L_{TOT} = 0.5$ versus source frequency; waterfall diagram of PSD (a) and standard deviation of c_p (b).

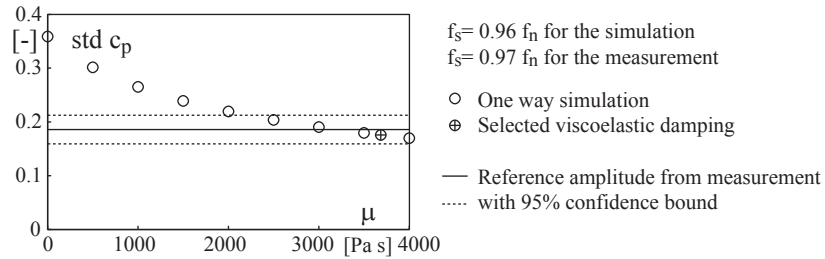


Figure 9.7: Amplitude of pressure fluctuation in resonant conditions at $L/L_{TOT} = 0.5$ versus viscoelastic damping.

coherent, similar order of magnitude is estimated for the viscoelastic damping in both configurations:

- Based on impulse response (experiment presented in appendix B), the viscoelastic damping is estimated at $\mu = 3685$ Pa·s.
- Based on response of quasi harmonic forcing function (resonance simulated using one-way simulation), the viscoelastic damping is estimated at $\mu \simeq 3000$ Pa·s.

9.2 Two-way coupled simulation

9.2.1 Setup

No mass source is considered, the momentum source, F_s , is estimated using the force acting on the bluff body, $\int F_x d^2\mathbf{x}$, according to Subsection 7.1.2. In the two-way coupled simulation, the acoustic feedback of the flow velocity on the momentum source is fully modeled, see Subsection 7.2.3. The inlet boundary condition of the HD model, C_{inlet} , is updated using the flow velocity obtained in the HA model at the source location, $C_{i=29+1/2}$. The exchange is performed according to the methodology presented in Subsection 7.3.3, the corresponding data flux between the software is described in appendix D.

The pressure has no feedback effect on the momentum source, see Subsection 7.2.2,

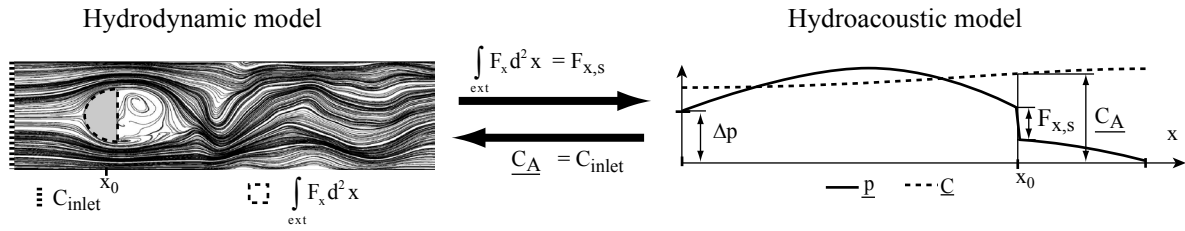


Figure 9.8: Two-way concurrent simulation data exchange.

therefore the outlet pressure of the HD model is not updated during the simulation. Nevertheless, the pressure field in the source region can be corrected during the post-processing stage. The pressure downstream the momentum source, $p_{i=30}$ is added to the outlet pressure of the HD model, p_{outlet} to account for the acoustic fluctuation of pressure in the source region. The data exchange between the models is summarized in Figure 9.8.

Operating condition

Three flow conditions at resonant and non-resonant condition are selected to compare the one-way concurrent simulation with the two-way coupled simulation, see Table 9.1 and Table 9.2. Strong acoustic feedback is expected at the resonant frequency.

Table 9.2: Flow conditions for the two-way coupled simulation.

C [m/s]	2.25	2.5	3
f_s/f_n [-]	0.96	1.05	1.27
Δp [Pa]	8'000	9'800	14'500

Simulation procedure

To set the initial conditions of the simulation the models are initialized separately:

- In a first step, the inlet velocity of the HD model is set to the desired flow condition and a preliminary simulation is performed. The time averaged momentum source for the selected flow condition is estimated from this preliminary simulation.
- In a second step, the time averaged momentum source is injected in the HA model. The boundary conditions of the HA model are adjusted recursively in order to obtain the selected flow velocity in the source region.

The resulting fields are used as initial conditions for the coupled simulation.

The total simulation time is 2.4 s. At the beginning of the simulation, the mean value of the exchanged data, the flow velocity and the drag force, are at equilibrium, but the phase and amplitude of the fluctuations can not be synchronized. A transition period is necessary to reach a realistic regime. Consequently, the first 0.4 s of simulation are not considered in the result analysis. Finally, for the post-processing, the simulation data are resampled at 1000 [Hz]. Except for the time signal duration, the parameters given in Table 5.1 are used for the spectral analysis.

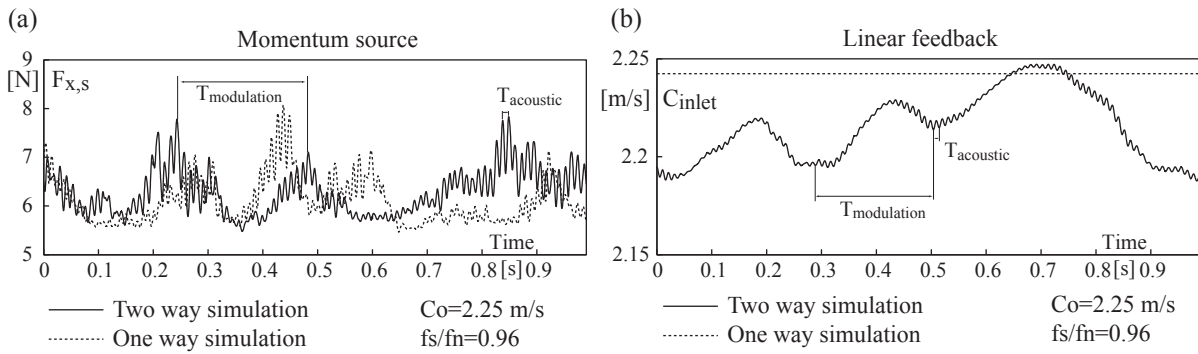


Figure 9.9: Comparison between the one-way and two-way simulation for the evaluation of momentum source (a) and feedback (b).

9.2.2 Results

Momentum source and feedback

The momentum source and the acoustic feedback is shown in Figure 9.9 for $C = 2.25$ m/s. The one and two-way simulation are compared. In Figure 9.9 (a), the time history of momentum sources are plotted. No significant difference is visible. In Figure 9.9 (b), the feedback of the HA model is shown. As the feedback effect is not taken into account in the one-way simulation, the inlet velocity is constant. On the contrary, the flow velocity in the HD model is adjusted at each time step in the two-way simulation. Fluctuations at the acoustic resonance are observed, the amplitude of these fluctuations is very small, $C''/C < 0.001$. But the low frequency modulation of the momentum source induces relatively large amplitude of velocity fluctuation in the local domain, 11%. As described in Section 6.1, the HA model includes the acoustic effects; and the low frequency dynamic of the pipe connected with the head losses along the circuit. In the present situation, the low frequency modulation is suspected to have a stronger effect on the momentum source than the acoustic feedback.

As described in Subsection 9.2.1, the flow velocity in the HD model is a result and can not be set precisely. Consequently, \bar{C} is slightly lower than 2.25 m/s, 1.3%.

Acoustic fluctuation amplitude and frequency

In Figure 9.10, the fluctuation of pressure at the middle of the pipe are presented for $f/f_s = 0.96$, $f/f_s = 1.05$ and $f/f_s = 1.27$. In Figure 9.10 (a), (b) and (c), the PSD and the time history of the one-way and two-way simulation are compared. At resonance, the distribution of energy is similar with both methods. The energy is concentrated on a small frequency band which coincides with the natural frequency of the pipe. Low frequency fluctuation with the same order of magnitude is observed. At non-resonant condition, the amplitude is much smaller with both methods.

Given the uncertainty related to the averaging technique (with the significant simulation time of 2 s, only two samples are used for the Welch's averaging), the differences observed in the frequency domain between the two methods are not significant.

In Figure 9.10 (d), the amplitude of the pressure fluctuation is plotted as a function of the source frequency. For one-way and two-way simulation, the computed amplitude

is within the measured uncertainty at resonant condition and slightly below for out of resonance condition.

The results using both methods are similar and the acoustic feedback can therefore be considered as negligible for cavitation free conditions. Even at resonance, the acoustic fluctuation of velocity in the source region is not sufficient to modify significantly the momentum source.

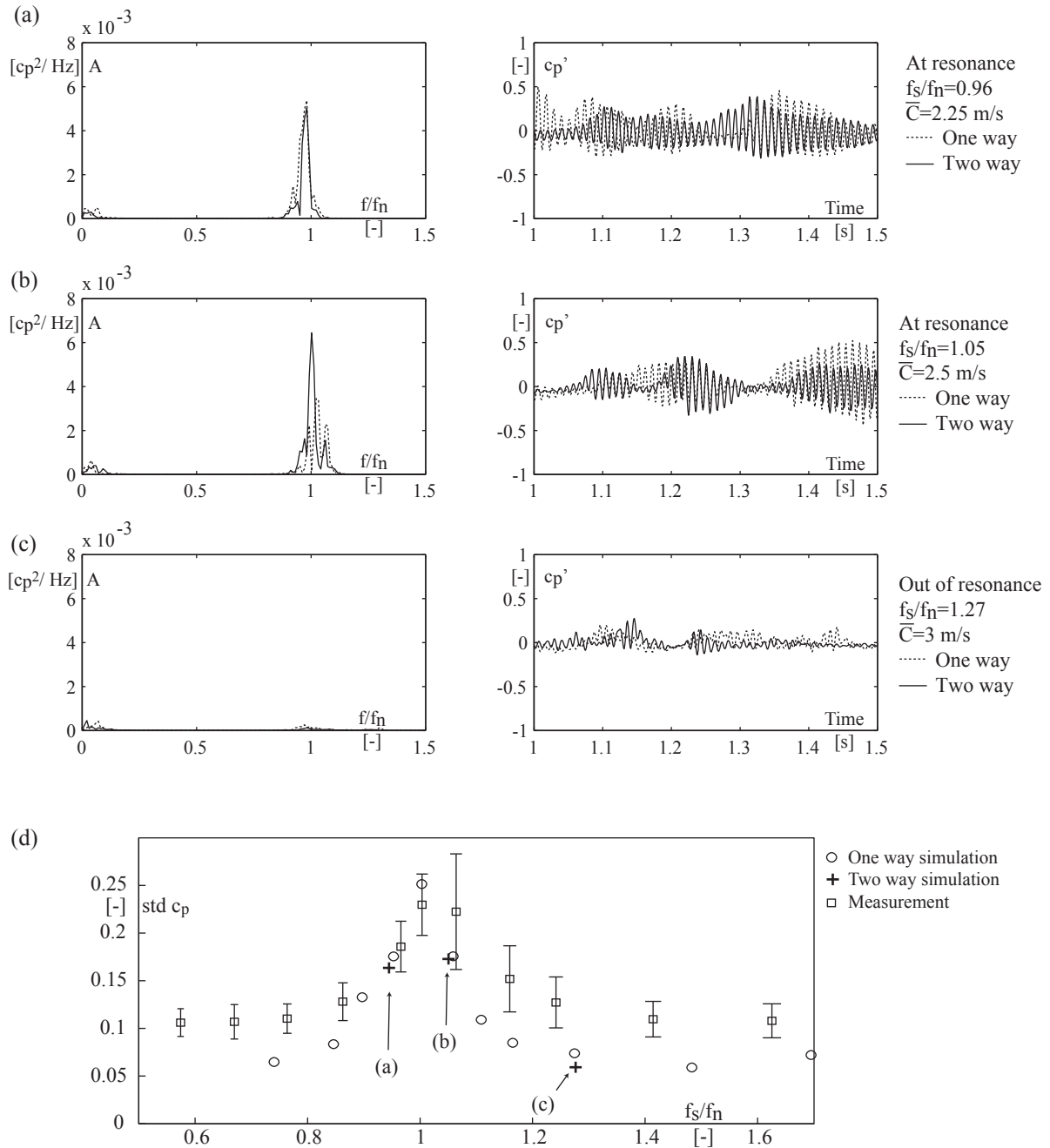


Figure 9.10: Comparison between the one-way and two-way simulation, acoustic fluctuation at $L/L_{TOT} = 0.5$; PSD and time history (a), (b) and (c); Standard deviation (d),

Chapter 10

Cavitating flow regime

10.1 One-way concurrent simulation

10.1.1 Setup

In cavitating conditions, the hydrodynamic component of the mass and momentum source are evaluated with the HD model, see Figure 10.1. The mass source is evaluated using the time history of vapor volume, $\rho_s \frac{dV_v}{dt} = \frac{dM_s}{dt}$. The mass transfer at the liquid-vapor interface is neglected and the vapor is considered as an external element, see Subsection 7.1.1. The momentum source is estimated using the force acting on the bluff body, $\int F_x d^2\mathbf{x}$, according to the developments presented in Subsection 7.1.2. As the time steps of the HA model are smaller, the force and the vapor volume between two time steps are estimated using linear interpolation.

The acoustic feedback of the velocity on the momentum source is neglected. But the acoustic feedback on the mass source is accounted for. The two linearized interaction parameters of the mass source, K_v and M_G , are evaluated a priori, see Subsection 7.2.2. To account for the low frequency variation of the vapor volume, the parameters are adjusted dynamically using moving average of the cavity volume in the HD model with a subset length of 1000 samples corresponding to 0.02 s, see Figure 10.2. The averaging is crucial to filter the acoustic fluctuation. Without filtering, the fluctuation of the interaction parameters at the acoustic frequency generates unrealistic fluctuation in the HA model.

The mass flow gain factor and the cavity compliance are introduced in the source vector; consequently, the mass source is decomposed in a hydrodynamic and an acoustic part, see Subsection 7.2.2:

$$s = \frac{1}{\rho_0 A_0 \Delta x} \frac{dM}{dt} = \frac{1}{\rho_0 A_0 \Delta x} \left(\rho_0 \frac{\partial V_t}{\partial t} + \rho_0 \frac{\partial V_a}{\partial t} \right) = \frac{1}{\rho_0 A_0 \Delta x} \left(\rho_0 \frac{\partial V_t}{\partial t} + M_G \frac{\partial C}{\partial t} - K_v \frac{\partial p}{\partial t} \right) \quad (10.1)$$

Where $\rho_0 \frac{\partial V_t}{\partial t}$ is the mass source estimated from the time history of vapor volume in the HD model. M_G is the mass flow gain factor and K_v is the cavity compliance. p is the pressure at the mass source position, $i = 30$; C is the flow velocity upstream the mass source position, $i = 29 + \frac{1}{2}$. The upstream velocity is chosen as the acoustic feedback on the volume is due to the bluff body located upstream the mass source, see Subsection 7.2.2 for details.

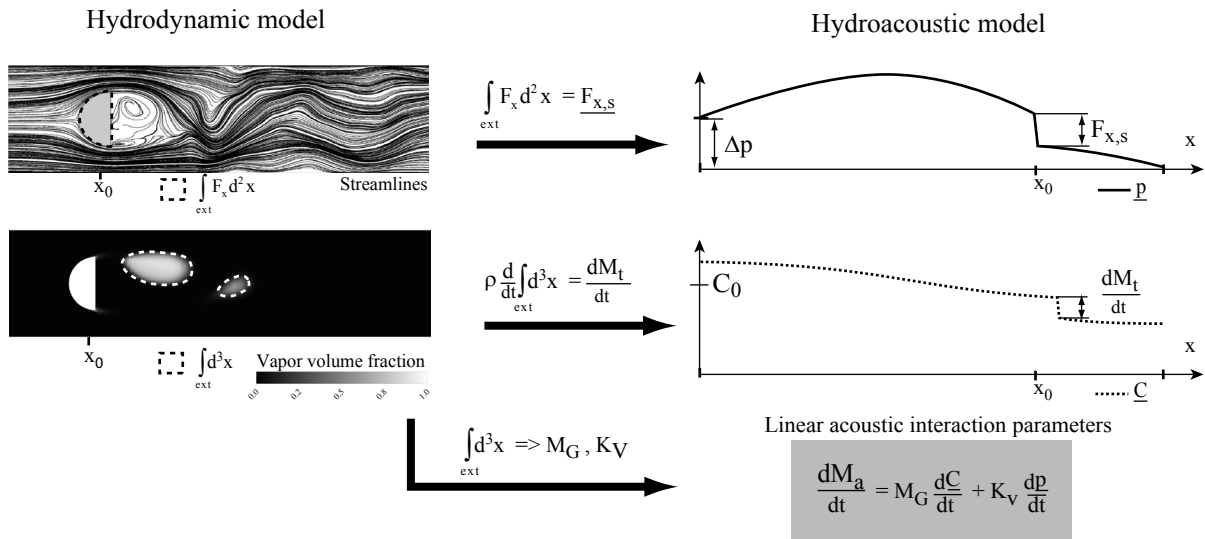


Figure 10.1: One-way concurrent simulation in cavitating conditions.

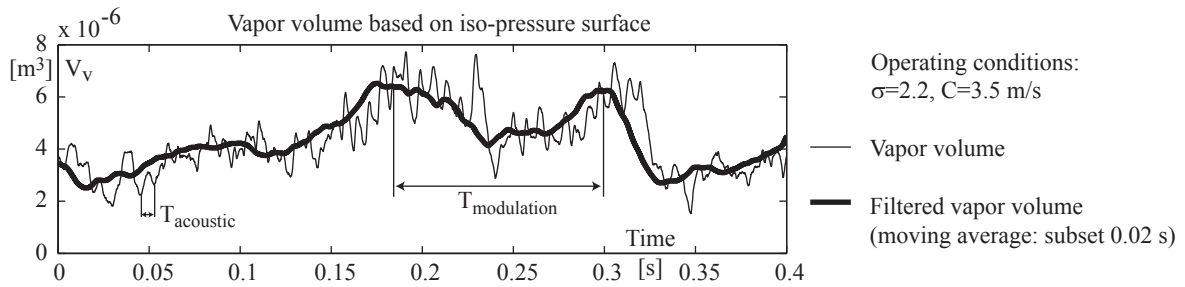


Figure 10.2: Moving average of the vapor volume to compute dynamically K_v and M_G .

The compliance and mass flow gain factor are introduced in the matrix A at the mass source position $i = 30$, see Section 7.3. The other parameters of the HA model remain unchanged and are given in Table 6.1.

Simulation procedure

In a first step, the time evolution of the force and vapor volume is computed for various flow velocities and cavitation indexes, see Figure 8.7, with the HD model using the parameters given in Table 8.1.

In a second step, the time averaged volume of vapor is computed. Using the cavitation model, see Figure 8.9 or using iso-pressure surface, see Figure 8.8. The mass flow gain factor and cavity compliance are evaluated from the time averaged volume of vapor.

In a third step, the vapor volume and force are introduced as mass and momentum sources in the HA model. The parameters of the HA model are modified to account for the acoustic interaction.

Finally, in order to compare the simulation results with the measurement data in the spectral domain, the simulation data are resampled at the experimental sampling frequency of 1000 [Hz]. For measurement and simulation, the same parameters, given in

Table 5.1, have been used for the spectral analysis except for the time signal duration.

The boundary conditions of the HA model (inlet and outlet pressure) are adjusted for each operating condition according to the procedure presented in Subsection 9.1.1.

10.1.2 Interaction parameters identification

K_v and M_G determination using cavitation model

For the cavitation model, see Figure 8.9, the volume of vapor appears to vary exponentially with the cavitation index. Using curve fitting, the following relation is established between the cavitation index and the time averaged volume of gaseous phase:

$$\bar{V}_g = e^{C_1\sigma+C_2}, \text{ with } C_1 = -1.37 \text{ and } C_2 = -9.24 \quad (10.2)$$

This relation is based on the multi-phase cavitation model using a wide range of reference pressure and flow velocity, see Table 8.4. Based on the definition of the cavitation index (5.1), we have for the compliance:

$$K_v = -\rho \frac{\partial V_g}{\partial p} = -\rho \frac{\partial V_g}{\partial \sigma} \frac{\partial \sigma}{\partial p} = -C_1 e^{C_1\sigma+C_2} \frac{1}{\frac{1}{2}C^2} \quad (10.3)$$

Similarly for the mass flow gain factor, we have:

$$M_G = \rho \frac{\partial V_g}{\partial C} = \rho \frac{\partial V_g}{\partial \sigma} \frac{\partial \sigma}{\partial C} = -\rho \frac{2C_1 e^{C_1\sigma+C_2} \sigma}{C} \quad (10.4)$$

The linearized interaction parameters are presented in Figure 10.3. The effect of pressure (a) and flow rate (b) on the mass source is presented versus the cavitation index. The cavity compliance, K_v and the mass flow gain factor, M_G , are plotted for two reference flow velocities using relation (10.3) and (10.4).

K_v and M_G determination using iso-pressure surface

For the iso-pressure method, the relation between the cavitation index and the volume of vapor is sufficiently precise and non-linear to use a quadratic curve fitting, see Figure 8.8. The following relation is established between the cavitation index and the time averaged volume of gaseous phase:

$$\bar{V}_g = e^{C_1\sigma^2+C_2\sigma+C_3}, \text{ with } C_1 = -0.094, C_2 = -0.65 \text{ and } C_3 = -10.4 \quad (10.5)$$

This relation is based on the simulations performed for flow velocities of 3.5 m/s, 4 m/s and 4.5 m/s, see Figure 8.7. Based on the definition of the cavitation index (5.1), we can derive the compliance:

$$K_v = -\rho \frac{\partial V_g}{\partial p} = -\frac{V_g}{\frac{1}{2}C^2} (2\sigma C_1 + C_2) \quad (10.6)$$

Similarly for the mass flow gain factor, we have:

$$M_G = \rho \frac{\partial V_g}{\partial C} = -\rho \frac{2V_g\sigma}{C} (2\sigma C_1 + C_2) \quad (10.7)$$

The interaction parameters based on iso-pressure and multi-phase cavitation model are compared in Figure 10.3. Both methods provides similar parameters.

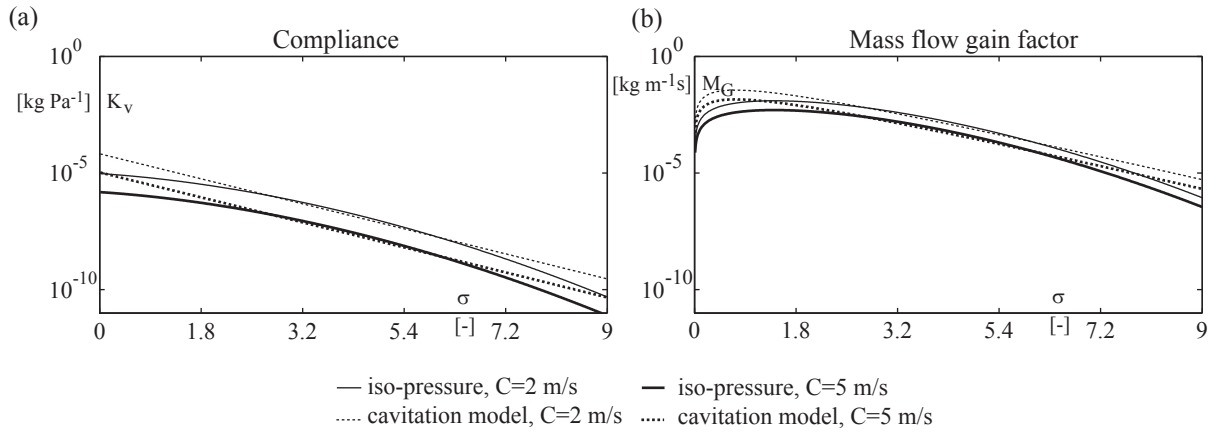


Figure 10.3: Interaction parameters estimated from HD model; (a) cavity compliance; (b) mass flow gain factor.

10.1.3 Cavitation model selection

At incipient cavitation level, the acoustic fluctuation induced by the mass source computed with the multi-phase cavitation model and the iso-surface method are similar.

For intermediate cavitation level and non-resonant conditions, the results using the cavitation model and the iso-pressure method are compared with measurements in Figure 10.4. The amplitudes are larger compared to incipient cavitation level. The pressure fluctuation at $L/L_{TOT} = 0.5$ is chosen for the comparison. The fluctuation predicted using the cavitation model is overestimated, see (a). But the amplitude and frequency of fluctuation is well predicted using iso-pressure method, see (a) and (b). The inaccurate PSD of acoustic fluctuation obtained with the cavitation model is caused by the erroneous evaluation of the cavity volume fluctuation, see Subsection 8.2.3. Therefore iso-pressure method is selected for further investigation.

10.1.4 Results

Eigenfrequencies

As shown in Subsection 5.4.1, the cavitation index has a strong influence on the eigenfrequencies of the acoustic resonator. This effect can be modeled with the cavity compliance, see Subsection 7.2.2.

In Figure 10.5 (a), the second eigenfrequency and the corresponding cavity compliance are presented as a function of the cavitation index. Using the method presented in Subsection 7.3.5, the eigenfrequencies are estimated for a given cavity compliance and vice versa. The measured values can therefore be compared with the simulation results. The measured second eigenfrequencies are determined using resonance, see Subsection 5.4.1. The simulated values are based on the time averaged cavity compliance computed using relation (10.3) or (10.6). For a given cavitation index, the cavity volume is systematically underestimated in the HD model, see Subsection 8.2.3, leading to an erroneous estimation of the cavity compliance and corresponding eigenfrequency. This may be connected with the evaluation of the pressure drop due to the bluff body. As the pressure drop is underestimated by the HD model, see Subsection 8.2.2, the average pressure in the wake

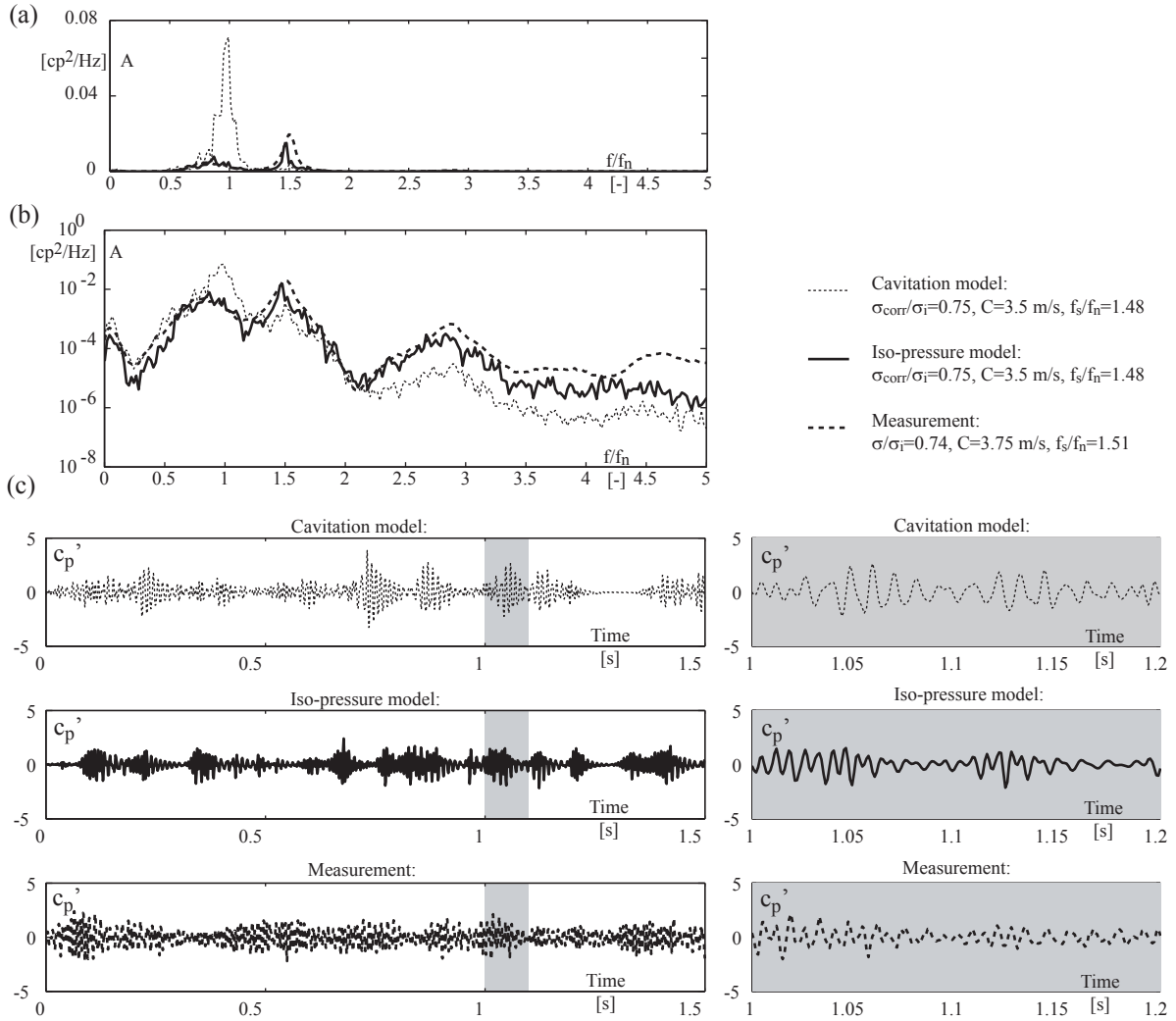


Figure 10.4: Pressure fluctuation at $L/L_{TOT}=0.5$ for intermediate cavitation index; Comparison between cavitation model and iso-pressure method in the frequency domain (a), using logarithmic scale (b); and in the time domain (c).

is overestimated leading to a poor estimation of the mean cavity volume. To compensate this error, a correction factor is introduced to shift the cavitation index of the simulation:

$$\sigma_{corr} = \sigma \frac{\sigma_i^{sim}}{\sigma_i^{mes}} = \sigma \cdot 1.28 \quad (10.8)$$

The factor is chosen in order to fit the compliance and corresponding eigenfrequency with the available experimental data. The corrected incipient cavitation index is $\sigma_i^{sim} = 7$. In Figure 10.5 (b), the corrected simulation data fits well with the experimental results for intermediate cavitation index.

Acoustic fluctuation at incipient cavitation

At incipient cavitation, the amplitude of the pressure fluctuation increases with respect to cavitation free flow. In Figure 10.6, the simulation results are compared with the

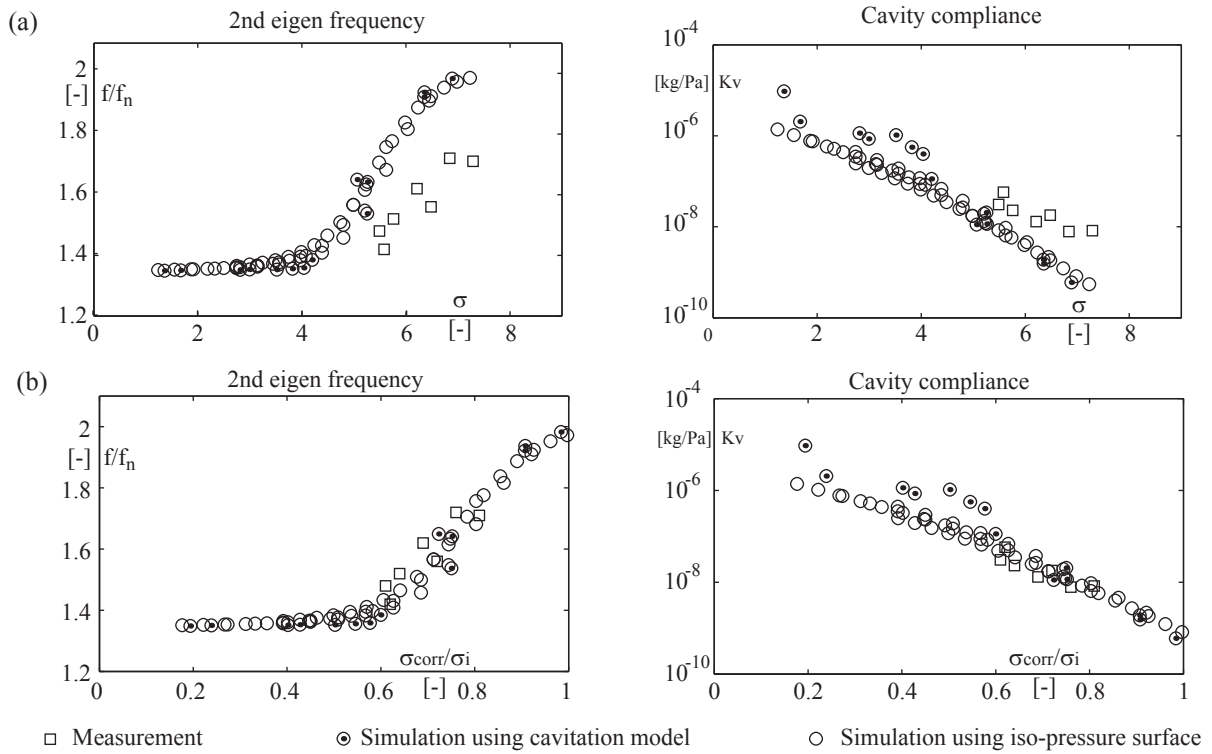


Figure 10.5: Eigenfrequency and corresponding cavity compliance versus cavitation index, original cavitation index (a) and corrected cavitation index (b).

measurements for non-resonant conditions in cavitation free and at incipient cavitation. In (a), the PSD of pressure fluctuation at $L/L_{TOT} = 0.5$ and corresponding time history of pressure coefficient are presented for cavitation free regime. In Figure 10.6 (b), the PSD and time history are presented for incipient cavitation regime. The comparison of the time history of vapor volume and pressure fluctuation of the simulation shows that the pressure fluctuation burst (at $t = 0.7$ s; $t = 1.3$ s) observed at incipient cavitation corresponds to the apparition of vapor. The measured flow conditions, with similar intermittent burst of fluctuation is slightly above σ_i . Consequently, unnoticed bubbles are suspected to be present in the experiment even for cavitation index above σ_i .

The amplification of the pressure fluctuation at incipient cavitation is predicted in the simulation. But the pressure level for incipient cavitation is underestimated in the simulation. The correction factor based on the resonant frequency at intermediate cavitation index, see Subsection 10.1.4, is not sufficient to correct the incipient cavitation.

Pressure distribution

In Figure 10.7, the PSD has been computed for each node of the HA model. the pressure fluctuation distribution is presented as a function of the frequency for three simulations using iso-pressure surface. The fluctuations in phase opposition are represented with negative amplitudes.

Resonant conditions at low cavitation level is presented in (a). The source frequency is equal to the second eigenfrequency of the pipe. As expected, the eigenmodes and eigenfrequencies are modified by the cavity compliance, see Subsection 7.3.5 and Figure

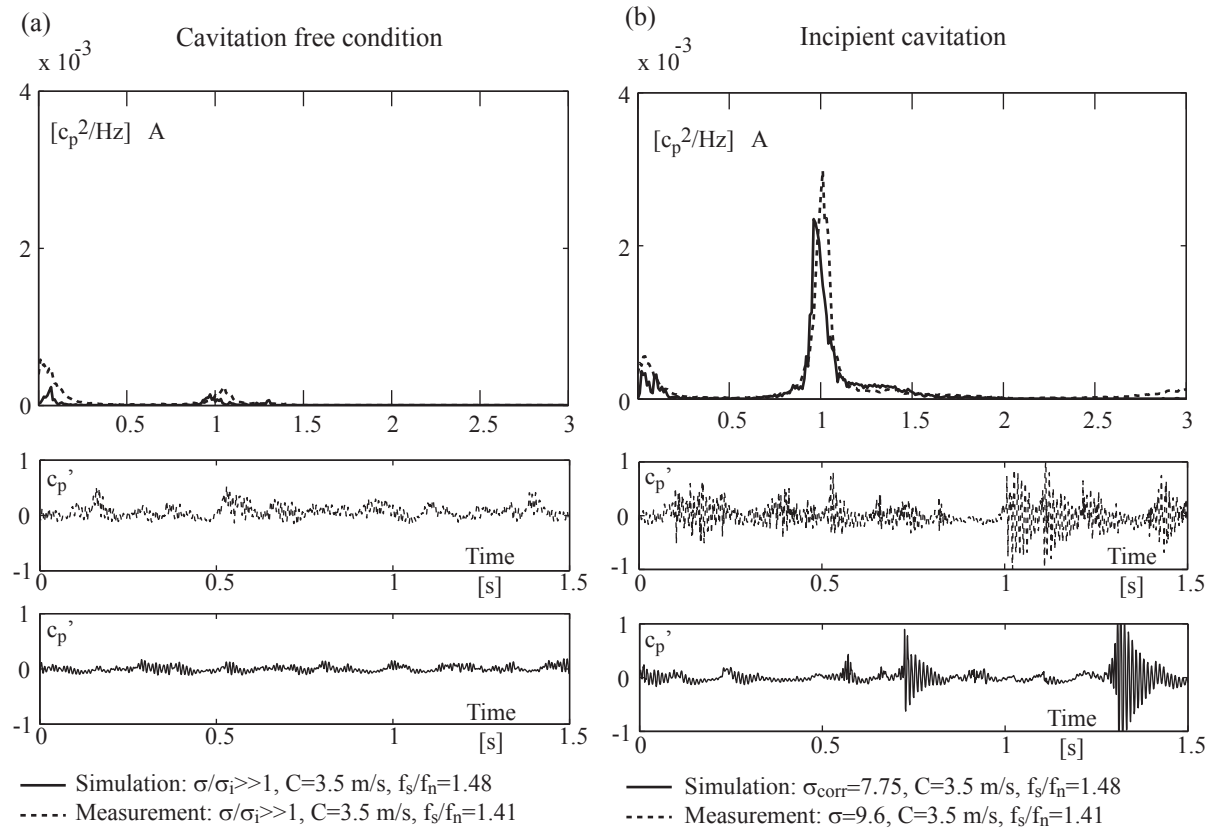


Figure 10.6: Comparison in the frequency and time domain of the pressure fluctuation at $L/L_{TOT}=0.5$ for cavitation free conditions (a) and incipient cavitation (b). Simulations and measurements are compared in the frequency domain (a) and the time domain (b).

10.5.

Figure 10.7 (b), corresponds to non-resonant condition at intermediate cavitation index. The eigenfrequencies are lower than in cavitation free conditions according to Figure 10.5. As the source frequency is between the first and second eigenfrequency, no resonance is observed.

In Figure 10.7 (c), the pressure fluctuation amplitude is presented for incipient cavitation, the cavity compliance is not sufficient to modify the eigenfrequency of the pipe. The first eigenfrequency corresponds to the natural frequency of the pipe without cavitation.

Resonance amplitude

In Figure 10.8 and 10.9, the simulated pressure fluctuation at respectively $L/L_{TOT} = 0.5$ and $L/L_{TOT} = 0.25$ are compared with the measurements for $f_s/f_n \sim 1.5$ (a), $f_s/f_n \sim 1.7$ (b) and $f_s/f_n \sim 1.9$ (c). For each flow velocity, the PSD of pressure coefficient is presented in waterfall diagram for various cavitation indexes. Resonance occurs as the second eigenfrequency of the pipe is equal to the source frequency. As shown in Subsection 5.4.1, the eigenfrequency of the system is modified in the presence of vapor. The eigenfrequency decreases for lower cavitation index as the volume of vapor and corresponding compliance increases. As the mass source strength increases also at low cavitation index, larger amplitude, especially at resonance, are observed for lower cavitation index. The

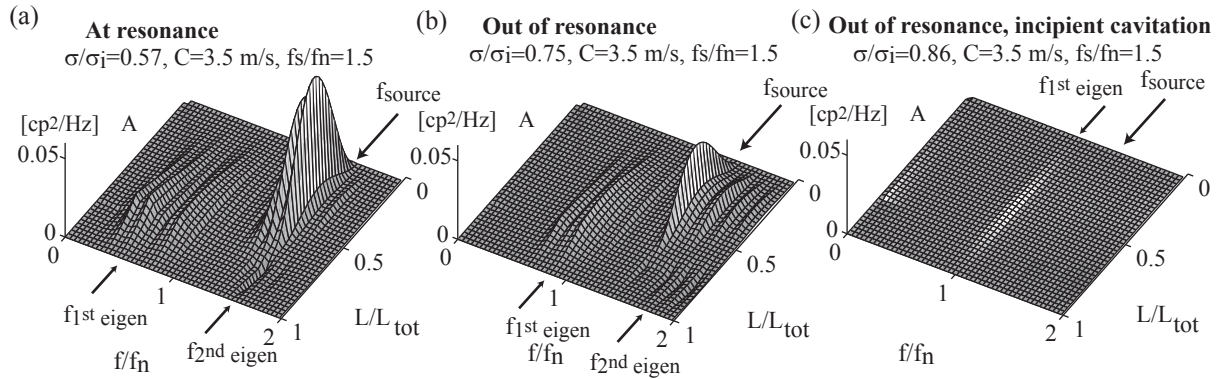


Figure 10.7: Distribution of pressure fluctuation along the pipe for (a) resonant, (b) non-resonant conditions at intermediate cavitation level and (c) incipient cavitation; simulations are performed using iso-pressure method.

difference in amplitude between the two locations (Figure 10.9 and 10.8) is due to the shape of the eigenmodes, see Subsection 7.3.5.

For the source with low frequency, the amplitude, frequency and cavitation index at resonance is accurately predicted, see (a). For higher source frequency, (b) and (c), the amplitude is in fair agreement with the measurement, but the cavitation index at resonance is underestimated.

The overall fluctuation amplitudes and frequencies are fairly predicted in the simulations. By example, in Figure 10.8 (a), the decrease of the first eigenfrequency observed in the measurement at low cavitation index ($f_1 \simeq 1$ for $\sigma/\sigma_i > 0.8$ and $f_1 \simeq 0.4$ for $\sigma/\sigma_i = 0.5$) is also predicted in the simulation. However, the noise in the power spectrum of the simulated data makes precise comparison difficult.

In Figure 10.10, the standard deviation of pressure fluctuation at $L/L_{TOT} = 0.5$ (a) and $L/L_{TOT} = 0.25$ (b) are presented, the amplitude is plotted versus the cavitation index. Simulations have been performed for $f_s/f_n = 1.49$, $f_s/f_n = 1.7$ and $f_s/f_n = 1.9$ using iso-pressure method. The simulations are compared with the measurement performed for $f_s/f_n = 1.51$, $f_s/f_n = 1.71$ and $f_s/f_n = 1.81$.

At $L/L_{TOT} = 0.5$, the amplitude at resonance is accurately reproduced for all source frequencies. At $L/L_{TOT} = 0.25$, the amplitude is systematically underestimated; but the dependance of the fluctuation amplitude on the source frequency is captured: the amplitude at resonance increases for lower source frequency. The resonant cavitation index is predicted accurately for $f_s/f_n \sim 1.5$ but is underestimated for $f_s/f_n \sim 1.7$ and $f_s/f_n \sim 1.9$. As resonance is expected at higher cavitation index for higher source frequency, we can conclude that the correction factor estimated in Subsection 10.1.4, is not adapted for cavitation index close to σ_i .

Influence of the sources and interaction parameters

In order to compare the importance of the mass and momentum source on one side, the compliance and the mass flow gain factor on the other side. One operating point with intermediate cavitation index, $\sigma_{corr}/\sigma_i = 0.75$, in non-resonant conditions, $f_s/f_n = 1.48$ has been selected, see Figure 10.10. Different cases are evaluated. In each case, one parameter or source is neglected in order to evaluate its influence:

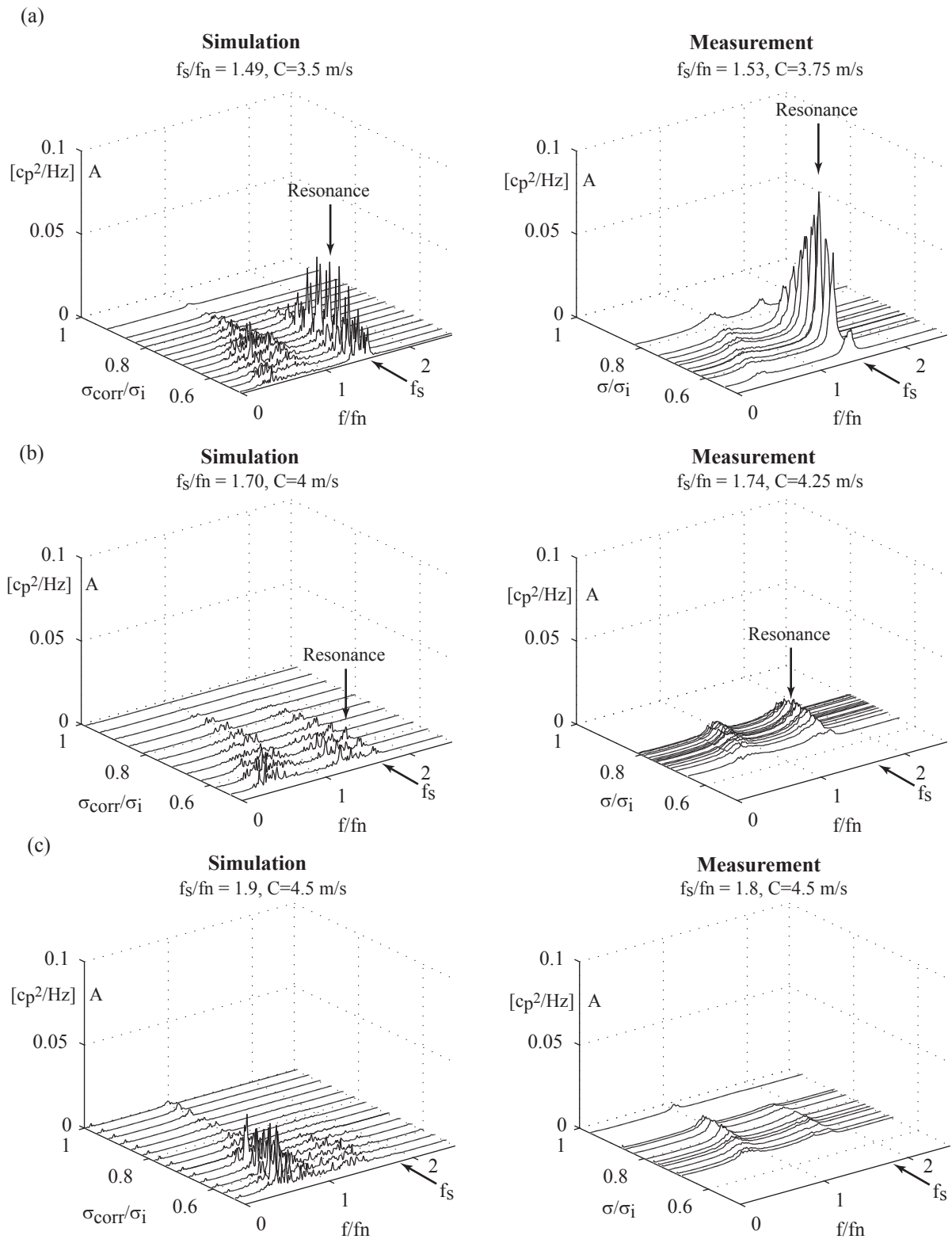


Figure 10.8: Comparison of pressure fluctuation at $L/L_{TOT} = 0.5$ between simulation and measurement; Waterfall of the PSD for $f_s/f_n \sim 1.5$ (a), $f_s/f_n \sim 1.7$ (b), $f_s/f_n \sim 1.9$ (c) and variable cavitation indexes.

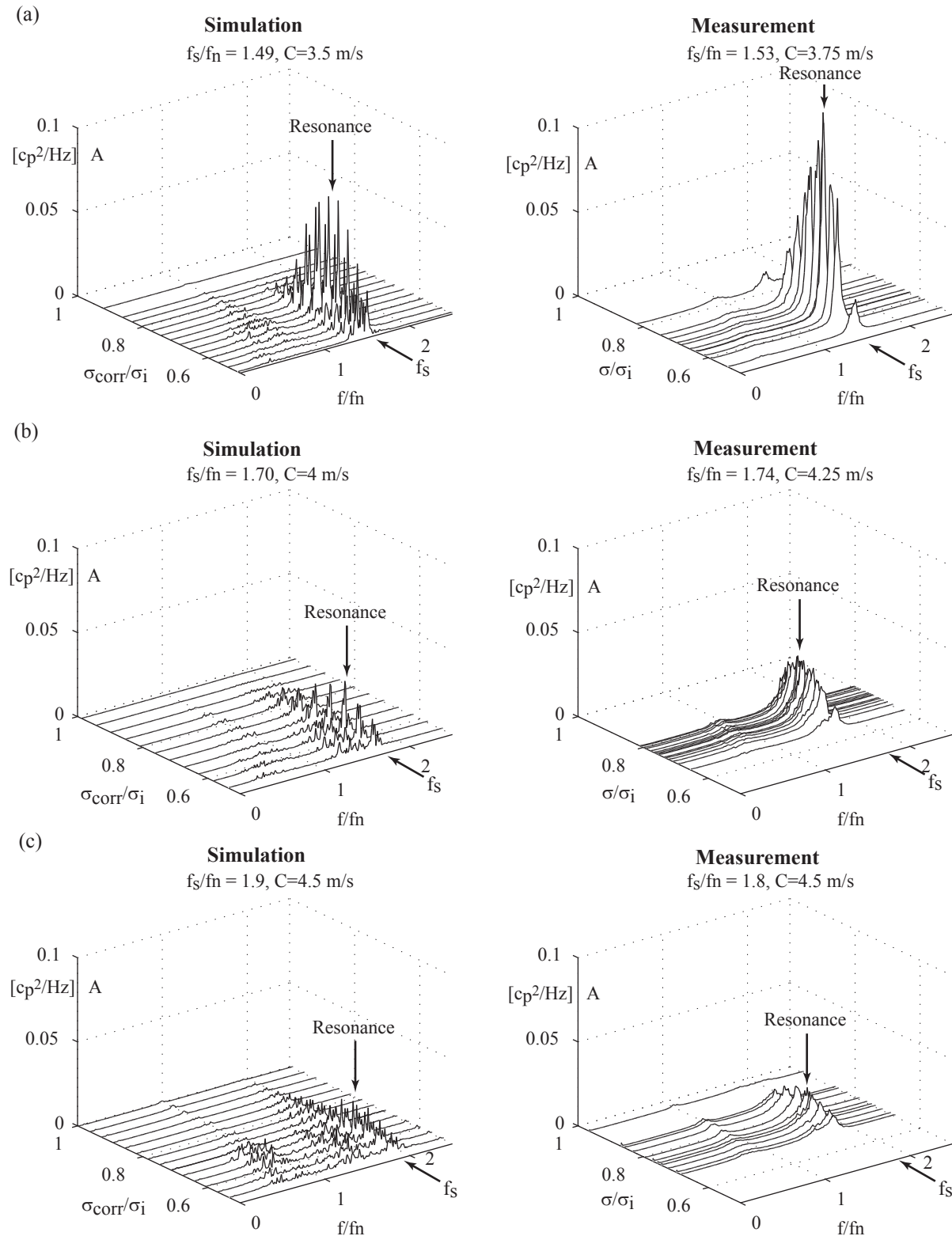


Figure 10.9: Comparison of pressure fluctuation at $L/L_{TOT} = 0.25$ between simulation and measurement; Waterfall of the PSD for $f_s/f_n \sim 1.5$ (a), $f_s/f_n \sim 1.7$ (b), $f_s/f_n \sim 1.9$ (c) and variable cavitation indexes.

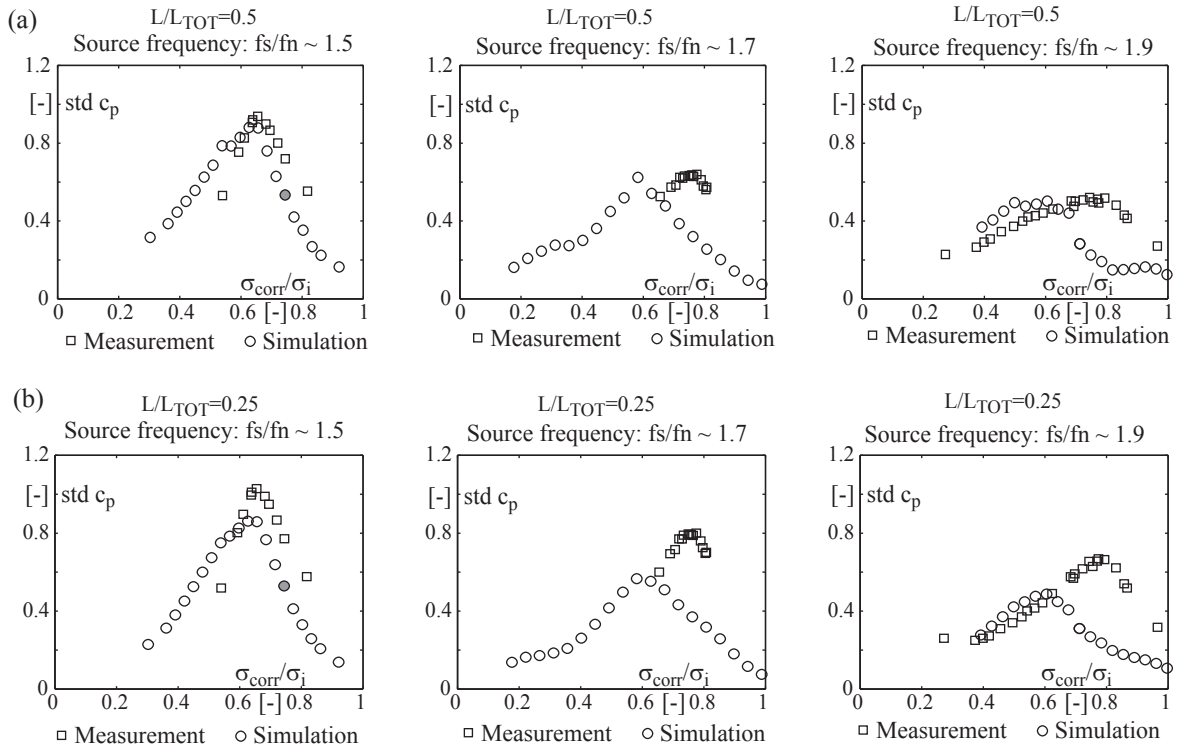


Figure 10.10: Comparison of pressure fluctuation at $L/L_{TOT} = 0.5$ (a) and $L/L_{TOT} = 0.25$ (b) between simulation and measurement; standard deviation at variable cavitation indexes for $f_s/f_n \sim 1.5$, $f_s/f_n \sim 1.7$, $f_s/f_n \sim 1.9$.

- The momentum source, F_s , is neglected, the parameters of the HA model are unchanged.
- The mass source, $\frac{dM_s}{dt}$, is neglected.
- All the parameters of the HA model are unchanged.
- The acoustic feedback of the velocity on the mass source (mass flow gain factor) is neglected, $M_G = 0$.
- The compliance, K_v , is kept constant and computed using the time averaged volume of vapor.

The standard deviation of c_p at $L/L_{TOT} = 0.25$ and $L/L_{TOT} = 0.5$ are presented in Table 10.1. The amplitudes and distributions of pressure fluctuations are presented in Figure 10.11. The PSD of c_p is computed for each node of the HA model. The time history of pressure fluctuation at $L/L_{TOT} = 0.5$ is presented in Figure 10.11 (f). The following effects are observed:

- In (a) the momentum source is neglected. The predicted amplitude of pressure fluctuation decreases slightly, important diminution is observed for the second eigenfrequency. Therefore the momentum source contributes marginally to the excitation of the acoustic resonator.
- In (b) the mass source is neglected. The amplitude decreases dramatically, small fluctuation remains only at the source frequency. Therefore the mass source is the main source of fluctuation in cavitating conditions.

Table 10.1: Sources and feedback parameters influence on pressure fluctuation.

	std(c_p)	std(c_p)
	$L/L_{TOT}=0.5$	$L/L_{TOT}=0.25$
a) no F_x	0.52	0.49
b) no $\frac{dM}{dt}$	0.11	0.11
c) normal	0.57	0.56
d) no M_G	0.75	0.83
e) constant K_v	0.76	0.71

- In (d) the mass flow gain factor is neglected. The amplitude increases, therefore the mass flow gain factor has a damping effect in the present configuration.
- In (e) the compliance is not updated dynamically but a constant value has been used. Consequently, the resonance frequency is precisely defined and the energy content in the resonator is concentrated on a narrow band of frequency.

In cavitating conditions, the principle source of fluctuation is the mass source but the momentum source contributes also to the generation of acoustic plane waves, see (a), (b) and (c). Their relative importance depends on the cavitation index. The momentum source is quasi independent of the vapor volume and the mass source is proportional to the vapor volume, see Subsection 8.2.3. The mass flow gain factor contributes to the damping of the acoustic fluctuation. The damping effect is due to the phase shift between the vapor volume and the flow velocity. Therefore, the velocity amplitude and phase in the source region is the key parameter for this damping mechanism.

10.2 Two-way coupled simulation

10.2.1 Setup

According to Subsection 7.1.1 and 7.1.2, the momentum source, F_s , is estimated using the force acting on the bluff body, $\int F_x d^2\mathbf{x}$. The mass source, $\frac{dM_s}{dt}$, is estimated using the fluctuation of vapor volume fraction, $\rho \frac{d}{dt} \int_{ext} d^3\mathbf{x}$. The acoustic feedback of the flow velocity and pressure are modeled. The inlet boundary condition of the HD model, C_{inlet} , is updated using the flow velocity obtained in the HA model at $C_{i=29+1/2}$. The outlet boundary condition of the HD model, p_{outlet} is updated using the pressure obtained in the HA model at $p_{i=31}$. The data exchange between the models is summarized in Figure 10.12.

Operating condition

One flow condition out of resonance is selected, see Table 10.2. Strong acoustic feedback is expected for all flow conditions in cavitating flow regime. The outlet pressure in the HD model as a strong influence on the vapor cavity volume even for non-resonant condition.

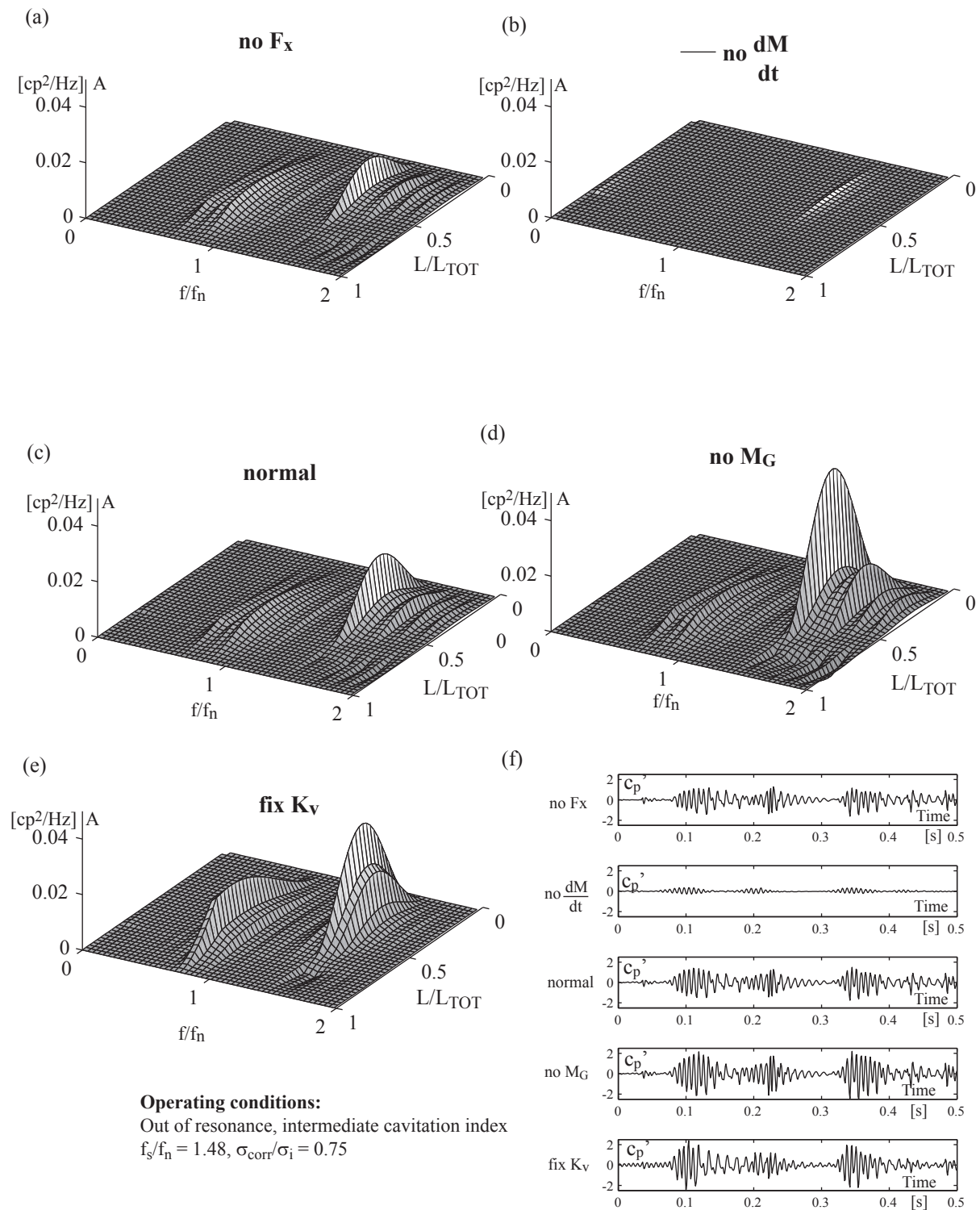


Figure 10.11: Influence of the sources and feedback parameters on the pressure fluctuation amplitude in the frequency and time domain; simulation without momentum source (a), without mass source (b); reference simulation (c); simulation without mass flow gain factor (d); simulation with constant compliance (e); corresponding pressure fluctuation at $L/L_{TOT} = 0.5$ in the time domain (f).

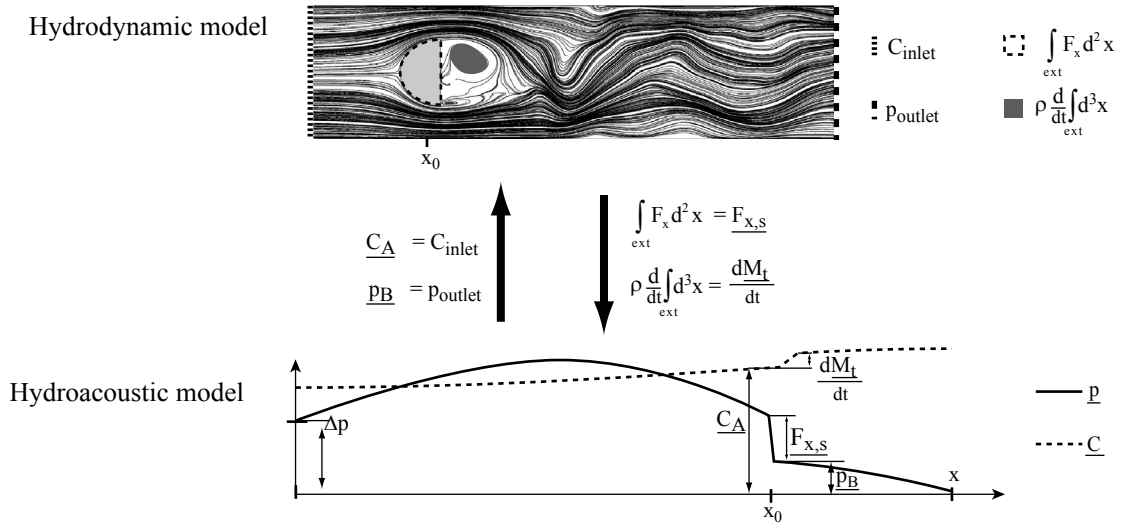


Figure 10.12: Two-way concurrent simulation data exchange.

Table 10.2: Operating condition for the two-way concurrent simulation.

C [m/s]	3
f_s/f_n [-]	1.27
p_{inlet} [Pa]	32760
p_{outlet} [Pa]	24700

Simulation procedure

To set the initial conditions of the simulation the models are initialized separately:

- In a first step, the inlet velocity and outlet pressure of the HD model are set to the desired operating condition and a preliminary simulation is performed. The time averaged momentum source for the selected operating condition is estimated from this preliminary simulation.
- In a second step, the time averaged momentum source is injected in the HA model. The boundary conditions of the HA model, p_{inlet} and p_{outlet} in Table 10.2, are adjusted recursively in order to obtain the selected flow velocity and pressure in the source region.

The field obtained at the end of the initialization for the HA and HD model are used as initial conditions for the coupled simulation.

10.2.2 Results

The coupled simulation diverges immediately. In Figure 10.13, the volume of vapor computed in the HD model, the resulting mass source and the pressure computed in the HA model are presented for the first time steps. The interaction is schematized using arrows. The stepwise allure of the mass source is due to the subcycling. One time step in the HD model corresponds to 10 time steps in the HA model. The mass source term is overestimated in the HD model after the first coupling leading to nonphysical injection

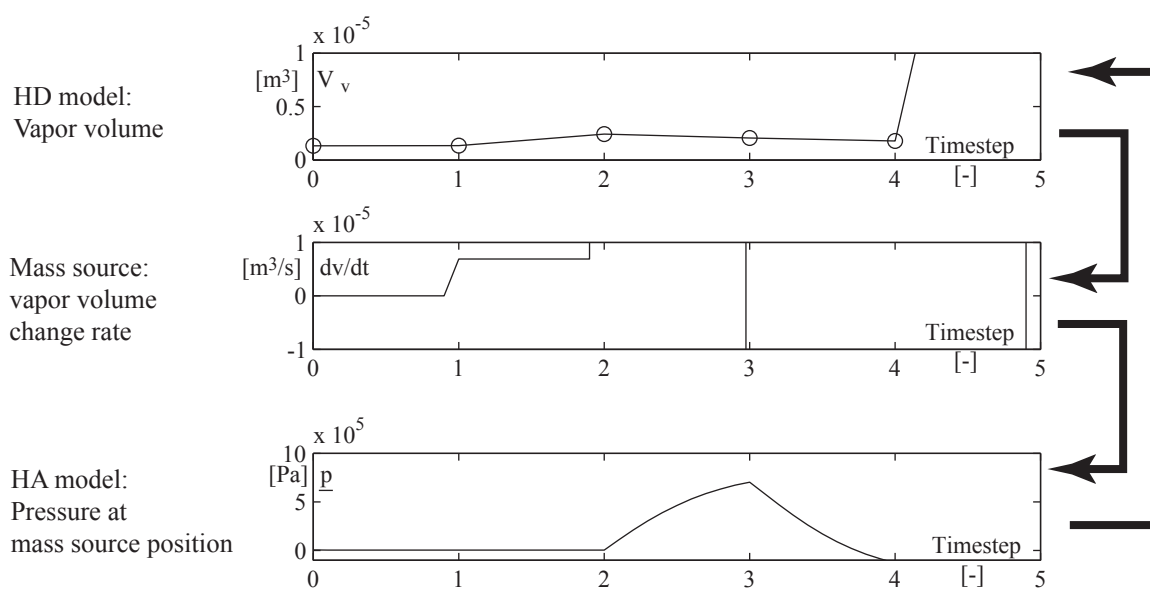


Figure 10.13: First steps of the coupled simulation.

of mass in the HA model at the second coupling step. The amplitude of the oscillation increases in a dramatic manner after few time steps. The coupling is too strong for the selected explicit coupling method. To avoid such numerical instability, implicit coupling method is necessary, see appendix E.

Part IV

Conclusions and perspectives

Chapter 11

Conclusions

A computational methodology based on two models is proposed to investigate flow induced hydroacoustic resonance in hydraulic system. A mono-dimensional model describes the acoustic field and a detailed 3D model is used for the local hydrodynamic instability. Based on a rigorous development of the water-hammer equations, the sources in the hydroacoustic model can be interpreted as corrective terms. The sources are identified as the difference between the exact solution of the integral form of the conservation of mass and momentum (HD model) and its simplified mono-dimensional counterparts (HA model). The momentum source is equal to the force applied on an external element. The mass source is associated with the volume fluctuation of external elements.

The acoustic feedback on the source has been analyzed systematically. Two methods are proposed to model the feedback. The feedback is either fully modeled in the framework of a two way coupled simulation, or accounted for using a linearized interaction parameter in the hydroacoustic model. The widely used, cavity compliance and mass flow gain factor are classified as a linearized form of interaction parameter. A new method is proposed to adjust dynamically the interaction parameters during the simulation. For the feedback on the mass source, a moving average is applied on the volume of vapor prior to the evaluation of the feedback parameter. The filtering effect of the moving average annihilate the parasite fluctuation of the feedback parameter at the acoustic frequency.

To validate the methodology, a reference case study as been setup for cavitating and cavitation free flows. In cavitation free conditions, the hydrodynamic source is identified as a pure momentum source. One way and two way coupling have been considered for the modeling. The comparison of the time history of pressure with the measurement is satisfactory considering the high unsteadiness of the selected case study. The evaluation of the momentum source based on integrated force has been validated. The resonance amplitude at the natural frequency of the pipe is accurately predicted by both methods. The flow velocity at resonance is underestimated by 7%. This shift is due to the hydrodynamic model, the vortex shedding frequency is overestimated by the same factor. Improvement in the modeling of the turbulence is therefore necessary to predict more precisely the resonant flow conditions.

The comparison of the one way and two way coupled simulation shows a negligible effect of the acoustic feedback. The pressure fluctuation has no effect on the momentum source. In the selected configuration, the velocity fluctuation due to the acoustic standing wave is too small to influence significantly the hydrodynamic instability, no look-in has been observed.

In cavitating conditions, two hydrodynamic sources have been identified. The momentum source is associated with the fluctuating force on the bluff body. The mass source is associated with the volume fluctuation of the vapor cavity in the wake of the bluff body. The strength of the mass source is orders of magnitude larger than the momentum source and the second can therefore be neglected. One way coupling using linearized interaction parameters has been performed. Two way coupled simulation was also investigated but due to the strong coupling between the acoustic pressure and the mass source, the simulation is unstable. An implicit coupling method is therefore necessary for such simulation in cavitating conditions. The implementation of such coupling method is out of the scope of the present study.

The one way coupled simulation provides satisfactory results. The amplification of the fluctuation observed experimentally below σ_i is reproduced. At intermediate cavitation index, the amplitude and spectral energy distribution is in fair agreement with the experiment. As shown in previous works, the cavity compliance model is sufficient to predict the modification of the eigenmodes and corresponding resonance frequencies. The predicted distribution of pressure fluctuation along the pipe fits with the measurements. The present coupled method goes one step further, the amplitude can also be predicted. The dependence of the resonance amplitude to the cavitation index can be reproduced at least qualitatively.

Unfortunately, the volume of vapor is underestimated in the simulation and a correction factor on the cavitation index is necessary. The time averaged vapor volume predicted using the cavitation model or iso-pressure surfaces are equivalent. But the iso-pressure surface provides better results regarding the dynamic of the cavity.

On account of the dynamic update of the interaction parameter, the spectral energy distribution is satisfactory. The energy is distributed on a broad range of frequency as the eigenfrequency of the pipe changes during the simulation.

Chapter 12

Perspectives

The application of the developed methods to hydraulic machinery is the next step. The precise identification of the coupling mechanism between the global hydroacoustic fluctuation and localized hydrodynamic instability opens new perspectives for the analysis and the numerical simulation of such phenomena:

Full load surge

Considering the full load surge frequency, the vapor cavity causing the surge can be considered as a compact region. This consideration is also supported by experimental evidence. Consequently, the localized source approach is consistent for the problem in consideration.

Two way simulation with a mixed approach is proposed. As pointed out, the source of the numerical instability is the acoustic feedback of pressure on the mass source. But the feedback of velocity has been identified as the root cause for the full load surge. The proposed methodology consists in modeling completely the interaction between the mass source and the acoustic velocity and to use a linearized interaction parameter (compliance) for the feedback of acoustic pressure.

For incompressible hydrodynamic model the standard set of boundary conditions dissociate the velocity (imposed at the inlet) and the pressure (imposed at the outlet). The acoustic feedback can therefore be split in two parts. The acoustic feedback of velocity is modeled by adjusting dynamically the inlet boundary. The velocity fluctuation at this location is obtained from the hydroacoustic model. The outlet pressure is kept constant and the acoustic feedback of pressure is therefore not modeled. Nevertheless, the feedback of pressure is accounted for in the hydroacoustic model using the cavity compliance.

Such method is precise as the driving interaction is fully modeled. All the non-linear effect neglected with the mass flow gain factor approach are naturally integrated in the method. The two way simulation guarantee to capture the interaction in details. Only the marginal interaction due the pressure is linearized to avoid numerical instability.

Part load surge

At part load, Important acoustic fluctuations may span over a large range of frequency. For the highest frequencies, the compact source assumption is questionable; the source region cover a large part of the draft tube and the acoustic wavelength may scope the

same dimensions. Consequently, compressible hydrodynamic model is a must to model such large source region. Due to the large dimensions of the hydraulic circuit, a mono-dimensional hydroacoustic model is still necessary to model the rest of the installation. Thus an implicit method is compulsory to couple the two models.

The cavitation model offers the desired compressibility effect for the hydrodynamic model; the draft tube as a whole becomes compressible if the cavitation model is activated. The global pressure/density relation is governed by the cavitation model. Further investigation is necessary to evaluate the capability of the cavitation models to capture the propagation of acoustic waves in cavitating flow.

Appendix

Appendix A

Pipe deformation based on beam theory

For long wavelength, λ , the pipe can be approximated as a series of massless rings expanding and contracting in accordance with the internal fluid pressure, p . The propagation velocity depends on the characteristic of the fluid and the pipe. For purely elastic behavior, the wave speed is given by:

$$a_c^{-2} = \frac{\rho'}{p'} + \frac{\rho_0 A'}{A_0 p'} \quad (\text{A.1})$$

For pipes of square cross section (used for the reference experiment), the second part of (A.1) can be estimated using beam theory. Based on the symmetry of the problem each side can be treated individually, see Figure A.1. The cross section variation under internal pressure is due to the deflection (a) and the elongation (b). Due to the symmetry, both ends are considered as fully embedded for the deflection. Neglecting the shear stresses, the deformation is given by [26]:

$$y = \frac{p'}{3Ee^3}(x^4 + H^2x^2 - 2Hx^3) \quad (\text{A.2})$$

Where y is the deflection at position x , p' the internal pressure, e the pipe wall thickness, H the pipe height and E the young modulus of the pipe material. The variation of section is given by the integration of (A.2):

$$A'_d = \int_0^H y dx = \frac{p'H^5}{60Ee^3} \quad (\text{A.3})$$

The elongation of the pipe wall due to internal pressure is:

$$A'_e = \frac{p'H^3}{4Ee} \quad (\text{A.4})$$

Noticing that $A_0 = H^2$, the total deformation for the pipe, 4 sides, is therefore:

$$A' = 4(A'_e + A'_d) = \frac{A_0 p' H}{Ee} \left(1 + \frac{H^2}{15e^2} \right) \quad (\text{A.5})$$

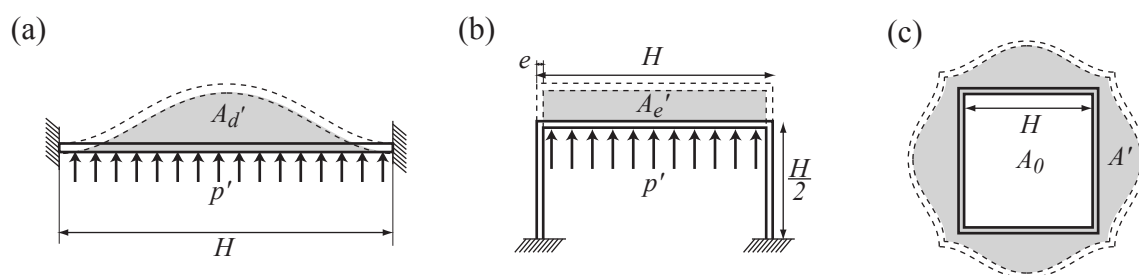


Figure A.1: Pipe deformation under internal pressure (c) due to deflection (a) and elongation (b).

Using the numerical data corresponding to the experimental setup given in Table A.1, the propagation velocity of plane wave along the pipe axis is estimated at:

$$a_c^2 = 262.9 \text{ m/s} \quad (\text{A.6})$$

Table A.1: Numerical data corresponding to the experimental setup.

Name	Description	Value	Unit
H	Pipe height	0.04	m
A_0	Pipe cross section	$1.6 \cdot 10^{-3}$	m^2
e	Pipe wall thickness	$5 \cdot 10^{-3}$	m
E	PVC Young modulus	$3 \cdot 10^9$	Pa
$\sqrt{\frac{p'}{\rho'}}$	Speed of sound in pure water	1485	m/s

Appendix B

Damping analysis

B.1 Damped wave equation

We consider the mass (6.18) and momentum (6.19) conservation laws applied to a pipe of constant cross section. The spatial variation of the velocity profile and the convective terms are neglected [41]. For small deformation, the density and pipe cross section can be approximated by the reference quantities in the zero order terms, see subsection 6.1.2. Finally, quasi steady friction for a pipe of square cross section is considered. The following system of equation is obtained:

$$\frac{\partial(\rho A)}{\partial t} + \rho_0 A_0 \frac{\partial C}{\partial x} = 0 \quad (\text{B.1})$$

$$\rho_0 A_0 \frac{\partial C}{\partial t} + A_0 \frac{\partial p}{\partial x} + \frac{\lambda \rho_0 \sqrt{A_0} |C| C}{2} = 0 \quad (\text{B.2})$$

The behavior of PVC pipe is not purely elastic, viscous dissipation is associated with the deformation of the material. To relate the deformation of the pipe with the pressure in the pipe, various models with different level of accuracy are proposed in the literature [91]:

- The simplest model consists in a modified wave speed to account for the elastic deformation of the pipe [51], see Figure B.1 (a).
- A generalized Kelvin-Voigt model is proposed by Covas to describe the stress-strain relation of the pipe material [22, 23, 86]. Such method is very precise to predict the exponential decay during water-hammer transient, but the identification of the creep function of the material is a challenging task. It is difficult to distinguish the influence of the unsteady friction from the viscoelasticity of the pipe wall, see Figure B.1 (c).

In the present study a Kelvin-Voigt constitutive relation is assumed between the pressure and the mass per unit length contained in the pipe [98]:

$$\underline{p} = \frac{a_c^2}{A_0} \underline{\rho A} + \frac{\mu}{\rho_0 A_0} \frac{\partial \underline{\rho A}}{\partial t} \quad (\text{B.3})$$

Where a_c is the propagation velocity in the pipe due to the pipe and fluid elasticity and μ is the viscosity associated with the pipe deformation and fluid compression, see Figure

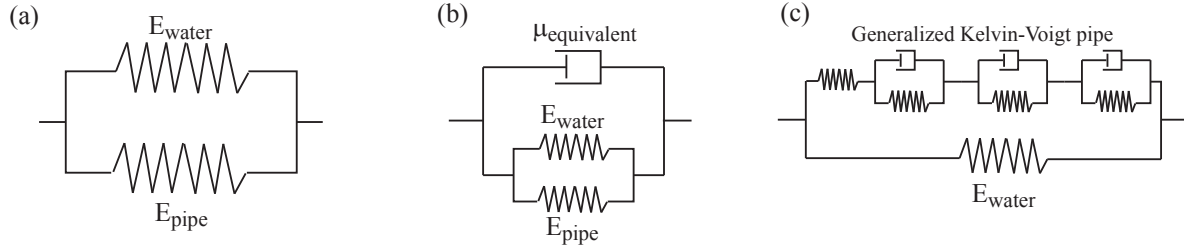


Figure B.1: Schematic representation of the rheological relation between the pressure and the mass per unit length; (a) elastic relation; (b) simple viscoelastic relation; (c) complex viscoelastic relation.

B.1 (b). Combining (B.1), (B.2) and (B.3), the following system of equation is obtained:

$$\frac{\partial(\rho A)}{\partial t} + \rho_0 A_0 \frac{\partial C}{\partial x} = 0 \quad (\text{B.4})$$

$$\rho_0 A_0 \frac{\partial C}{\partial t} + A_0 \frac{\partial p}{\partial x} + \frac{\lambda \rho_0 \sqrt{A_0} |C| C}{2} = 0 \quad (\text{B.5})$$

$$\frac{a_c^2}{A_0} \rho A + \frac{\mu}{\rho_0 A_0} \frac{\partial \rho A}{\partial t} = p \quad (\text{B.6})$$

Multiplying (B.6) by $\frac{\partial}{\partial x}$ and introducing the result into (B.5), we obtain:

$$\rho_0 A_0 \frac{\partial C}{\partial t} + A_0 \left(\frac{a_c^2}{A_0} \frac{\partial(\rho A)}{\partial x} + \frac{\mu}{\rho_0 A_0} \frac{\partial^2(\rho A)}{\partial x \partial t} \right) + \frac{\lambda \rho_0 \sqrt{A_0} |C| C}{2} = 0 \quad (\text{B.7})$$

On the other side, equation (B.4) is multiplied by $\frac{\partial}{\partial x}$ to obtain:

$$\frac{\partial^2(\rho A)}{\partial t \partial x} + \rho_0 A_0 \frac{\partial^2 C}{\partial x^2} = 0 \quad (\text{B.8})$$

Finally, before multiplying (B.7) by $\frac{\partial}{\partial t}$, the third term is replaced using (B.8) and similar substitution is applied to the second term after the time derivation. The following differential equation is obtained:

$$\frac{\partial^2 C}{\partial t^2} - a_c^2 \frac{\partial^2 C}{\partial x^2} - \frac{\mu}{\rho_0} \frac{\partial}{\partial t} \left(\frac{\partial^2 C}{\partial x^2} \right) + \frac{\lambda |C_0|}{\sqrt{A_0}} \frac{\partial C}{\partial t} = 0 \quad (\text{B.9})$$

Now we consider harmonic oscillation of the form $C(x, t) = \hat{C}(x) e^{i\omega t}$, where ω is the pulsation. From (B.9), the following relation is obtained [49, 70, 12]:

$$\frac{\partial^2 C}{\partial x^2} \simeq C \frac{\omega^2}{a_c^2} \left(\frac{-1 + i \frac{\lambda |C_0|}{\sqrt{A_0} \omega}}{1 - \frac{\mu}{\rho_0 a_c^2} i \omega} \right) \quad (\text{B.10})$$

For sufficiently small viscous damping $\frac{\omega \mu}{\rho_0 a_c^2} \ll 1$ and wall friction $\frac{\lambda |C_0|}{\sqrt{A_0} \omega} \ll 1$, the space derivative can be approximated as follow:

$$\frac{\partial^2 C}{\partial x^2} \simeq -C \frac{\omega^2}{a_c^2} \quad (\text{B.11})$$

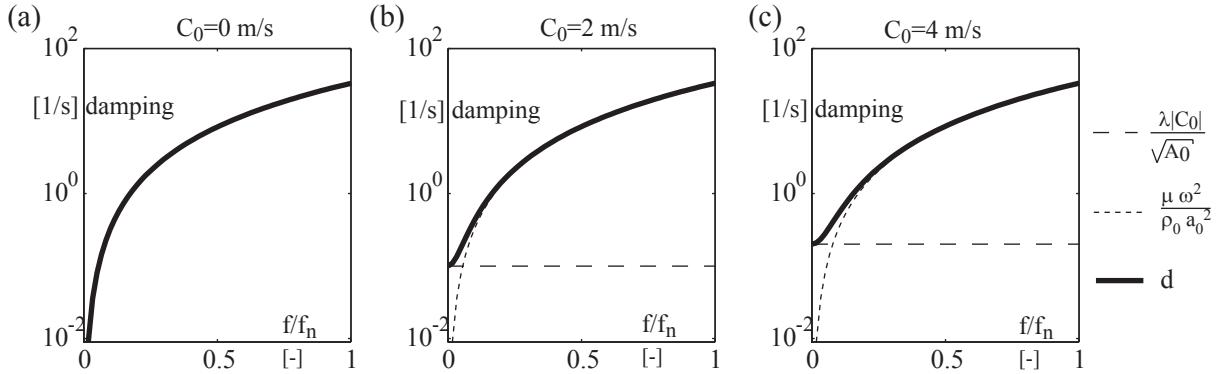


Figure B.2: Damping decomposed in the viscoelastic and friction part versus frequency with the reference velocity as parameter; numerical data are summarized in Table 6.1

For the PVC pipe under investigation, we have (considering $C_0 = 3$ m/s, $\lambda = 0.02$ and $\mu \simeq 3685$ kg·m⁻¹·s⁻¹) for the natural angular frequency of the pipe, $\omega_n = 2\pi f_n = 606$ s⁻¹:

$$\frac{\omega\mu}{\rho_0 a_c^2} \simeq 0.054 \quad (\text{B.12})$$

$$\frac{\lambda|C_0|}{\sqrt{A_0}\omega} \simeq 0.0025 \quad (\text{B.13})$$

Finally, equation (B.9) can be written:

$$a_c^2 \frac{\partial^2 \underline{C}}{\partial x^2} - \frac{\partial^2 \underline{C}}{\partial t^2} - d \frac{\partial \underline{C}}{\partial t} = 0 \quad (\text{B.14})$$

With

$$d = \frac{\lambda|C_0|}{\sqrt{A_0}} + \frac{\mu\omega^2}{\rho_0 a_c^2} \quad (\text{B.15})$$

This equation is known as the damped wave equation. Where a_c^2 is identified as the phase speed, and d as the damping coefficient. The damping is due to two elements:

- The frictional damping due to skin friction at the wall, $\frac{\lambda|C_0|}{\sqrt{A_0}}$. This damping mechanism is independent of the frequency and proportional to the reference velocity.
- The viscoelastic damping due to the wall deformation and fluid compression, $\frac{\mu\omega^2}{\rho_0 a_c^2}$. This damping mechanism is proportional to the frequency and is acting as a low-pass filter.

In Figure B.2, the damping is decomposed in the viscoelastic part and the frictional part for the pipe under investigation. Except for very low frequency fluctuation, the frictional damping is negligible with respect to the viscoelastic damping.

Analytical solution of the damped wave equation is known. The boundary conditions for zero velocity at both pipe ends is written:

$$\underline{C}(0, t) = 0 \quad (\text{B.16})$$

$$\underline{C}(L, t) = 0 \quad (\text{B.17})$$

The initial conditions are given by:

$$\underline{C}(x, 0) = f(x) \quad (\text{B.18})$$

$$\frac{\partial \underline{C}}{\partial t}(x, 0) = g(x) \quad (\text{B.19})$$

with the additional constraint:

$$0 < d < \frac{2\pi a_c}{L} \quad (\text{B.20})$$

The solution of (B.14) is:

$$\underline{C}(x, t) = \sum_{n=1}^{\infty} \sin\left(\frac{n\pi x}{L}\right) e^{-dt/2} [a_n \sin(\omega_n t) + b_n \cos(\omega_n t)] \quad (\text{B.21})$$

with

$$\omega_n = \frac{a_c \sqrt{4n^2\pi^2 - \frac{d^2 L^2}{a_c^2}}}{2L} \quad (\text{B.22})$$

$$b_n = \frac{2}{L} \int_0^L \sin\left(\frac{n\pi x}{L}\right) f(x) dx \quad (\text{B.23})$$

$$a_n = \frac{2}{L\mu_n} \left(\int_0^L \sin\left(\frac{n\pi x}{L}\right) \left[g(x) + \frac{d}{2} f(x) \right] dx \right) \quad (\text{B.24})$$

B.2 Experimental determination of the pipe viscoelastic response

To determine the viscoelastic damping of a pipe filled with water, a specific experiment has been set up. The pipe, closed at both ends, is hit at one end with a hammer, see Figure B.3(b). The shock generates compression wave over a large range of frequencies in the pipe. The pressure fluctuations are recorded using pressure sensors located at both ends of the pipe. The pressure signal is compared with the analytical solution, equation (B.21), to determine the propagation velocity and the viscoelastic damping, see Figure B.3(a). The dimensions of the PVC pipe are given in Table B.1. In contrast with the pipe used in the reference case study, this pipe is free of bluff body and plexiglass support. As shown in equation (B.21), the solution of the damped wave equation consists in a sum of eigenmodes fluctuating at the eigenfrequencies. As the damping is proportional to the frequency, see Figure B.2, all eigenfrequencies excepts the first eigenfrequency are rapidly damped. After the transition period, the equivalent in term of pressure for (B.21) as the following form:

$$\underline{p}(x, t) = \underline{\hat{p}}(x) e^{-dt/2} \sin(\omega_1 t) \quad (\text{B.25})$$

Where $\underline{\hat{p}}(x)$ is the fluctuation amplitude, $e^{-dt/2}$ the exponential decay and ω_1 the pulsation of the natural frequency. As the reference velocity is equal to zero, from (B.15) we have

Table B.1: Dimensions of the pipe.

Name	Description	Value	Unit
L	Pipe length	1	m
A	Cross section	$1.6 \cdot 10^{-3}$	m^2
H	Internal height	$4 \cdot 10^{-2}$	m
e	Pipe wall thickness	$2 \cdot 10^{-3}$	m

Table B.2: Curve fitting coefficients.

Coefficient	$C_3 = d/2$	$C_4 = \omega_1$
Unit	s^{-1}	s^{-1}
1	17.76	700.9
2	16.86	682.3
3	20.32	715
4	18.76	736.3
Mean	18.43 ± 1.28	708.63 ± 19.7

for the viscoelastic damping:

$$\mu = d \frac{\rho_0 a_c^2}{\omega^2} \quad (\text{B.26})$$

For small damping coefficient, we have for the natural frequency:

$$\omega_1 = \frac{a_c \sqrt{4\pi^2 - \frac{d^2 L^2}{a_c^2}}}{2L} \simeq 2\pi \frac{a_c}{2L} \quad (\text{B.27})$$

Curve fitting method is employed to compare the experimental results with the analytical solution of the damped wave equation, see equation (B.25).

$$p = C_1 + C_2 [e^{-C_3 t} + \sin(C_4 t + C_5)] \quad (\text{B.28})$$

An example is given in Figure B.3 (a). The process is iterated 4 times in order to quantify the error in the determination of the phase velocity and damping coefficient. The results are summarized in Table B.2. Introducing the average value and the standard deviation of d and ω_1 into (B.26) and (B.27), we have for the phase velocity and for the viscoelastic damping:

$$a_c = \frac{L}{2\pi} C_4 = 225.56 \pm 6.28 \text{ m/s} \quad (\text{B.29})$$

$$\mu = \frac{2\rho_0 L^2}{\pi^2} C_3 = 3685 \pm 256 \text{ kg} \cdot \text{m}^{-1} \cdot \text{s}^{-1} \quad (\text{B.30})$$

The phase velocity is lower than the predicted value using beam theory, see A.6. The difference is equal to 16.5 %.

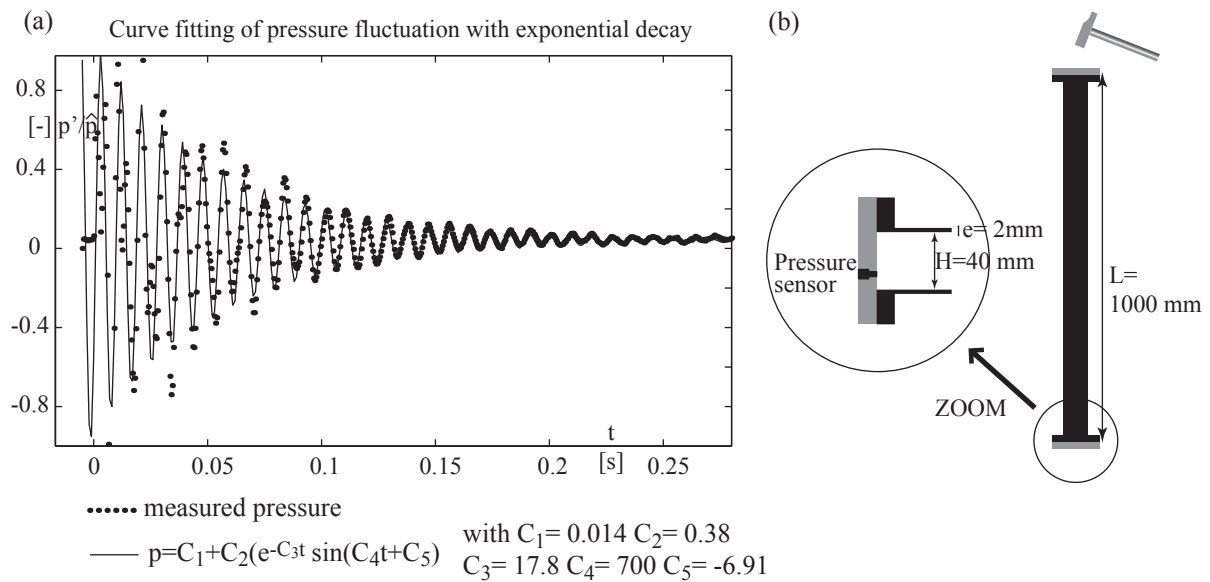


Figure B.3: (a) Curve fitting of pressure fluctuation to determine the phase velocity and the viscoelastic damping; (b) Dimensions of the pipe used for the experiment

Appendix C

Convergent and divergent pipe

For taper pipe, the HA model consists in the quasi-linear system of hyperbolic differential equation (6.23) and (6.24). The mass and momentum source terms can be included to correct the 1D approximation in the source regions.

$$\frac{1}{\rho_0 a_c^2} \left(\frac{\partial p}{\partial t} + \underline{C} \frac{\partial p}{\partial x} \right) + \frac{C}{A_0} \frac{\partial A_0}{\partial x} + \frac{\partial C}{\partial x} = \frac{1}{\rho_0 A_0} \frac{dm_s}{dt} \quad (\text{C.1})$$

$$\frac{\partial C}{\partial t} + \underline{C} \frac{\partial C}{\partial x} + \frac{1}{\rho_0} \frac{\partial p}{\partial x} + \frac{\lambda |C| C}{2\sqrt{A_0}} = \frac{1}{\rho_0 A_0} f_{x,s} \quad (\text{C.2})$$

The spatial discretization is performed on a staggered grid, see (C.3) and (C.4). In the momentum conservation (C.4) the velocity C_i is approximated using linear interpolation, $C_i = (C_{i+1/2} + C_{i-1/2})/2$.

$$\frac{1}{\rho_0 a_{ci}^2} \frac{dp_i}{dt} + \frac{C_i}{\rho_0 a_{ci}^2} \frac{p_{i+1} - p_{i-1}}{2\Delta x} + \frac{1}{A_{0i}} \left[\frac{dA_0}{dx} \right]_i C_i + \frac{C_{i+1/2} - C_{i-1/2}}{\Delta x} = \frac{1}{\rho_0 A_{0i}} \frac{dm_{si}}{dt} \quad (\text{C.3})$$

$$\begin{aligned} & \rho_0 \frac{dC_{i+1/2}}{dt} + \rho_0 C_{i+1/2} \frac{C_{i+3/2} - C_{i-1/2}}{2\Delta x} \\ & + \frac{p_{i+1} - p_i}{\Delta x} + \frac{\lambda \rho_0 |C_{i+1/2}|}{2\sqrt{A_{0i+1/2}}} C_{i+1/2} = \frac{1}{A_{0i+1/2}} f_{xsi+1/2} \quad (\text{C.4}) \end{aligned}$$

The system is quasi linear except for the convective terms (second terms in (C.3) (C.4)) and the friction term (fourth term in (C.4)). For those three terms, the time dependant velocity, C , is included in the coefficient matrix \mathbf{B} , the following system of linear differential equation is obtained:

$$\mathbf{A} \frac{d\mathbf{x}}{dt} = \mathbf{B}\mathbf{x} + \mathbf{s} \quad (\text{C.5})$$

For the sake of clarity, the source terms per unit length are replaced by the integral of the sources over the element, $\Delta x \frac{dm_{si}}{dt} = \frac{dM_{si}}{dt}$ and $\Delta x f_{xsi+1/2} = F_{xsi+1/2}$. The following notations are introduced to describe the elements of \mathbf{A} , \mathbf{B} and \mathbf{s} :

$$\begin{aligned} k_i &= \frac{\Delta x}{\rho_0 a_{ci}^2} & c_{Ai} &= \frac{C_i}{\rho_0 a_{ci}^2} & t_i &= \frac{\Delta x}{2A_{0i}} \left[\frac{\partial A_0}{\partial x} \right]_i & s_{Ai} &= \frac{1}{\rho_0 A_{0i}} \frac{dM_{si}}{dt} \\ l_{i+1/2} &= \rho_0 \Delta x & c_{Bi+1/2} &= \rho_0 C_{i+1/2} & r_{i+1/2} &= \frac{\lambda \rho_0 \Delta x |C_{i+1/2}|}{2\sqrt{A_{0i+1/2}}} & s_{Bi+1/2} &= \frac{1}{A_{0i+1/2}} F_{xsi+1/2} \end{aligned}$$

Where k is the compliance due to the liquid compressibility and pipe elasticity. The terms c_A and c_B are the convective terms due to the flow velocity. The pipe divergence or convergence is accounted for through the taper term, t . The term l is the fluid inertance and r is the friction term. Finally, the mass source term is written s_A and the momentum source s_B . In equation (C.5), the state variable vector \vec{x} for a five elements pipe is:

$$\mathbf{x} = [C_{1-1/2} \quad p_1 \quad C_{1+1/2} \quad p_2 \quad C_{2+1/2} \quad p_3 \quad C_{3+1/2}]^T$$

The source vector including the boundary conditions, constant pressure at inlet and outlet, is defined as:

$$\mathbf{s} = [p_{in} \quad (c_1 p_{in} + s_{B1}) \quad s_{A1+1/2} \quad s_{B2} \quad s_{A2+1/2} \quad (-c_3 p_{out} + s_{B3}) \quad -p_{out}]^T$$

The coefficient matrix \mathbf{A} is diagonal and the elements on the diagonal are the compliance and the inertance:

$$\mathbf{A} = \text{diag}(l_{1-1/2} , k_1 , l_{1+1/2} , k_2 , l_{2+1/2} , k_3 , l_{3+1/2})$$

Finally the coefficient matrix $[B]$ includes the convective, taper and friction terms:

$$\mathbf{B} = \begin{bmatrix} 2c_{B1-1/2} - r_{1-1/2} & -1 & -2c_{B1-1/2} & 0 & 0 & 0 & 0 & 0 \\ -t_1 + 1 & 0 & -t_1 - 1 & -c_{A1} & 0 & 0 & 0 & 0 \\ c_{B1+1/2} & 1 & -r_{1+1/2} & -1 & -c_{B1+1/2} & 0 & 0 & 0 \\ 0 & c_{A2} & -t_2 + 1 & 0 & -t_2 - 1 & -c_{A2} & 0 & 0 \\ 0 & 0 & c_{B2+1/2} & 1 & -r_{2+1/2} & -1 & -c_{B2+1/2} & 0 \\ 0 & 0 & 0 & c_{B3} & -t_3 + 1 & 0 & -t_3 - 1 & 0 \\ 0 & 0 & 0 & 0 & 2c_{A3+1/2} & 1 & r_{3+1/2} - 2c_{A3+1/2} & 0 \end{bmatrix}$$

For explicit time integration and pure wave equation, the maximal time step is limited by the CFL criteria defined by:

$$C_r = \frac{a_c \Delta t}{\Delta x} < 1 \quad (\text{C.6})$$

For quasi linear system the preceding constraints can still be used to give an estimate for the maximal time step, but a_c should be interpreted as an estimate of the maximum phase speed [20]. Due to the convective terms, the propagation velocity differs from the phase speed.

Appendix D

Computing resources

D.1 Hardware

The high performance computing capabilities used for this work are based on the IBM BladeCenter technology. At LMH, the cluster dedicated to parallel computing consists in 2 rakes of 4 and 12 blades respectively. Each blade consists in 2 Quad core processors. Gigabit Ethernet technology is used for the communication within the cluster. A single blade is affected to the communication with the standard 100 Mbits local network. One additional rake with 4 blades of 2 Quad core each is dedicated to serial solver. The computing capabilities are summarized in Table D.1.

D.2 Software

Two commercial software are employed for the coupling:

- The HD model simulations are performed using the CFD software ANSYS-CFX, Release 11. This programm allows the decomposition of the domain into partitions that are executed as separate processes that periodically exchange data to update the solution fields. The software architecture allow the user to access to the state variables in the different partitions with the help of FORTRAN subroutines [3].
- The HA model is implemented in the software SIMSEN. This object oriented software is based on a library of modules modeling the hydro-acoustic, the electrical and dynamics of hydro units. A specific module called DLL Link is dedicated to the communication with external software.
- The data exchange server is a very simple programm coded in Perl language. This server receive, store and distribute the data to the clients.

Table D.1: Computing capabilities at LMH.

Processor	Memory	OS
4 × 2×Quad Core Intel X5560	4 × 32 Mo	Linux SUSE
12 × 2×Quad Core Intel E5440	12 × 8 Mo	Linux SUSE
4 × 2×Quad Core Intel E5440	4 × 12 Mo	Windows

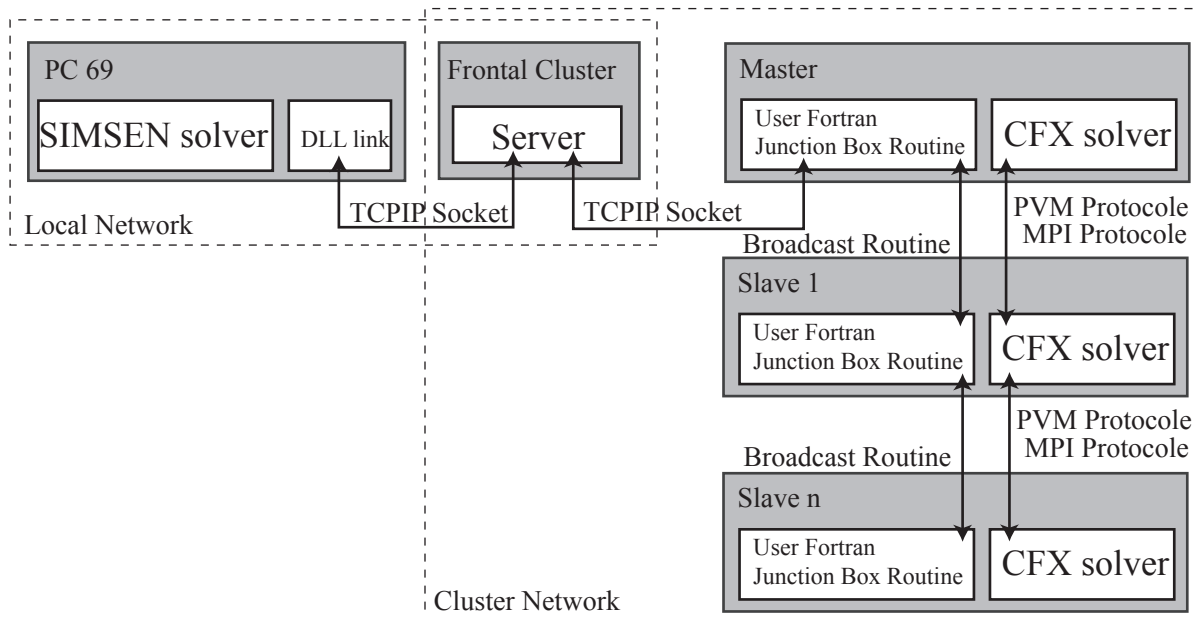


Figure D.1: Computational architecture for data exchange between local and HA model.

D.3 Communication

The communication procedure is presented in Figure D.1. The program SIMSEN (HA model) is executed on a laptop computer. In the framework of the program SIMSEN, the object DLL link is called at specific time step interval by the solver to execute the communication routine. This object has access to all variables \vec{x} and sources \vec{s} , see equation (8.21) of the solver. Specific routines are called to create TCPIP socket to transfer the necessary data between the client (DLL link) and the data exchange server. On the other side, the program ANSYS CFX (HD model) is executed in parallel mode with master and slaves nodes distributed on a cluster. The communication between the processes is handled by ANSYS-CFX itself using the MPI protocol. The FORTRAN subroutines are called by the solver at each time step to transfer data with the server. Those subroutines includes ANSYS-CFX specific functions to gather and dispatch the data among the partitions using MPI protocol. Finally the coupling information is exchanged between the master node and the data exchange server using TCPIP protocol.

Appendix E

Coupling algorithm

In partitioned procedure, the coupling between heterogeneous partition is performed at each time step during unsteady simulation. Depending on the level of coupling between the two partitions, various algorithm can be used for the coupling, see Figure E.1. Let's consider the arbitrary two partitions problem, where x is the state vector of partition 1 and y is the state vector of partition 2. The differential equations describing each partition are written:

$$\frac{dx}{dt} = \mathbf{B}_{11}\mathbf{x} + \mathbf{B}_{21}\mathbf{y} + \mathbf{s}_1(\mathbf{t}) \quad (\text{E.1})$$

$$\frac{dy}{dt} = \mathbf{B}_{22}\mathbf{y} + \mathbf{B}_{12}\mathbf{x} + \mathbf{s}_2(\mathbf{t}) \quad (\text{E.2})$$

Where \mathbf{B}_{12} and \mathbf{B}_{21} are the coupling terms, $\mathbf{s}_1(\mathbf{t})$ and $\mathbf{s}_2(\mathbf{t})$ are the time dependant source terms. The matrices \mathbf{B}_{11} , \mathbf{B}_{22} , \mathbf{B}_{21} and \mathbf{B}_{12} are time dependant for nonlinear problems such as fluid flow. Such system of equations is general, and may describe a wide range of coupled physical systems. It is used to present different coupling algorithms in the following simplified examples; euler time marching method is employed for the examples but the coupling algorithms are valid for a wide range of time integration methods.

E.1 One-way

For one-way coupling, the feedback of partition 2 on partition 1 doesn't exist or is neglected. the coupled system (E.1), (E.2) is solved as follow:

1. The partition 1 is advanced in time using explicit method.

$$\mathbf{x}^{t+1} = \mathbf{x}^t + dt(\mathbf{B}_{11}\mathbf{x}^t + \mathbf{s}_1^t) \quad (\text{E.3})$$

2. The partition 2 is advanced in time using implicit or explicit method.

$$\mathbf{y}^{t+1} = \mathbf{y}^t + dt(\mathbf{B}_{22}\mathbf{y}^{t+1} + \mathbf{B}_{12}\mathbf{x}^{t+1} + \mathbf{s}_2^t + \mathbf{1}) \quad (\text{E.4})$$

or

$$\mathbf{y}^{t+1} = \mathbf{y}^t + dt(\mathbf{B}_{22}\mathbf{y}^t + \mathbf{B}_{12}\mathbf{x}^t + \mathbf{s}_2^t) \quad (\text{E.5})$$

The procedure is reiterated at each time steps. The partitions are solved either simultaneously or sequentially. The partition 1 can be solved in a first step and used subsequently in the integration of the second partition.

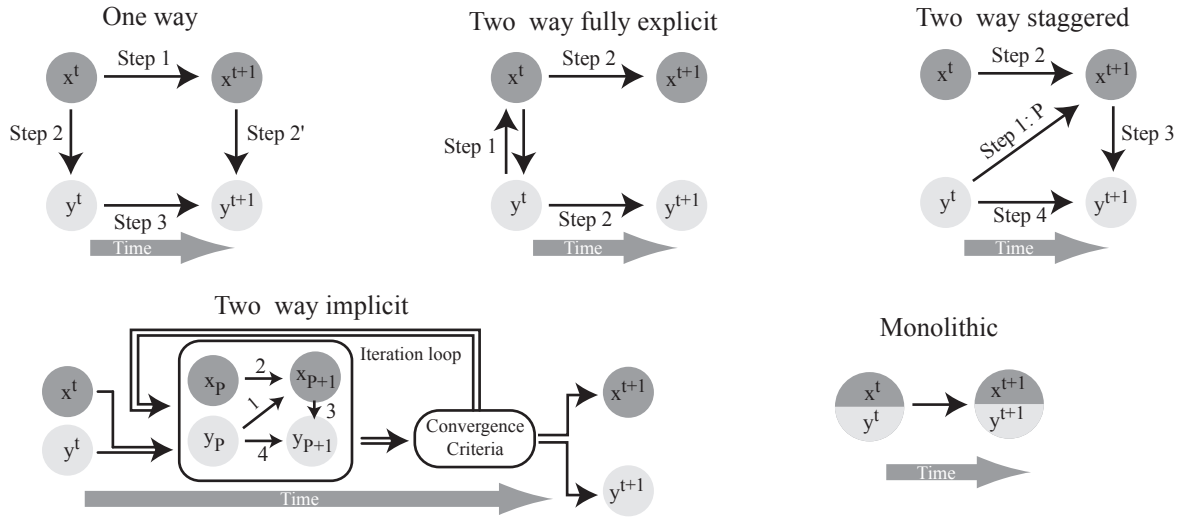


Figure E.1: Partitioned time marching methods.

E.2 Two-way fully explicit

For two-way fully explicit coupling, the coupled system is solved as follow:

1. Partition 1 and 2 are advanced in time using explicit information from the other partition.

$$\mathbf{x}^{t+1} = \mathbf{x}^t + \mathbf{dt}(\mathbf{B}_{11}\mathbf{x}^t + \mathbf{B}_{21}\mathbf{y}^t + \mathbf{s}_1^t) \quad (\text{E.6})$$

$$\mathbf{y}^{t+1} = \mathbf{y}^t + \mathbf{dt}(\mathbf{B}_{22}\mathbf{y}^t + \mathbf{B}_{12}\mathbf{x}^t + \mathbf{s}_2^t) \quad (\text{E.7})$$

Such method is straightforward but is valid only for loosely coupled systems. Such approach becomes unstable for strongly coupled system.

E.3 Two-way staggered

For two-way staggered explicit coupling, the action of partition 1 on partition 2 is taken into account in an implicit manner. The feedback of partition 2 on partition 1 is explicit. The coupled system is solved as follow:

1. The value of partition 2 is predicted using the information of the previous timestep.

$$\mathbf{y}_P^{t+1} = \mathbf{y}^t \quad (\text{E.8})$$

2. The partition 1 is advanced in time using predicted values from partition 2.

$$\mathbf{x}^{t+1} = \mathbf{x}^t + \mathbf{dt}(\mathbf{B}_{11}\mathbf{x}^t + \mathbf{y}_P^{t+1} + \mathbf{s}_1^{t+1}) \quad (\text{E.9})$$

3. The partition 2 is advanced in time using implicit method.

$$\mathbf{y}^{t+1} = \mathbf{y}^t + \mathbf{dt}(\mathbf{B}_{22}\mathbf{y}^{t+1} + \mathbf{B}_{12}\mathbf{x}^{t+1} + \mathbf{s}_2^{t+1}) \quad (\text{E.10})$$

Such method is conditionally stable for a certain range of problem but may fails for strongly coupled problems. Small time steps are necessary to conserve the stability.

E.4 Two-way iterative implicit

For two-way iterative implicit coupling, iteration loop is employed to guarantee a fully implicit coupling. This method is very attractive for none-linear systems. A convergence criteria e_{max} and a relaxation factor r are introduced. First the value of partition 2 is predicted using the information of the previous timestep:

$$\mathbf{y}_{P_1}^{t+1} = \mathbf{y}^t \quad (\text{E.11})$$

The iteration loop takes the following form:

1. The value of partition 1 is predicted using predicted values from partition 2.

$$\mathbf{x}_{P_i}^{t+1} = \mathbf{x}^t + dt(\mathbf{B}_{11}\mathbf{x}^{t+1} + \mathbf{y}_{P_i}^{t+1} + \mathbf{s}_1^{t+1}) \quad (\text{E.12})$$

2. The value of partition 2 is advanced using the predicted value of partition 1 multiplied by the relaxation factor.

$$\mathbf{y}_{P_{i+1}}^{t+1} = \mathbf{y}^t + dt(\mathbf{B}_{22}\mathbf{y}^{t+1} + \mathbf{B}_{12}[(1-r)\mathbf{x}^t + r\mathbf{x}_{P_i}^{t+1}] + \mathbf{s}_2^t + \mathbf{1}) \quad (\text{E.13})$$

3. The error is compared with the convergence criteria. If the error is more than the convergence criteria we go back to point 1 and we iterate until the convergence is fulfilled.

$$|\mathbf{x}_{P_{i+1}}^{t+1} - \mathbf{x}_{P_i}^{t+1}| = e_{max} \quad (\text{E.14})$$

$$|\mathbf{y}_{P_{i+1}}^{t+1} - \mathbf{y}_{P_i}^{t+1}| = e_{max} \quad (\text{E.15})$$

Using appropriate relaxation factor, this method is unconditionally stable but may necessitate a large number of iteration loops for strongly coupled problems. The modularity offered by the partitioned approach is a great advantage as specific software can be used for each partition.

E.5 Monolithic approach

In the monolithic approach both system of equation are solved simultaneously in a implicit manner:

$$\mathbf{x}^{t+1} = \mathbf{x}^t + dt(\mathbf{B}_{11}\mathbf{x}^{t+1} + \mathbf{B}_{21}\mathbf{y}^{t+1} + \mathbf{s}_1^{t+1}) \quad (\text{E.16})$$

$$\mathbf{y}^{t+1} = \mathbf{y}^t + dt(\mathbf{B}_{22}\mathbf{y}^{t+1} + \mathbf{B}_{12}\mathbf{x}^{t+1} + \mathbf{s}_2^{t+1}) \quad (\text{E.17})$$

Such method is unconditionally stable, but the monolithic approach is unrealistic for a large range of problems and the modularity offered by the partitioned approach is lost in the monolithic approach.

References

References

- [1] AIT BOUZIAD, Y. *physical modelling of leading edge cavitation: computational methodologies and application to hydraulic machinery*. PhD thesis, EPFL, 2006.
- [2] ALLIGNÉ, S. Influence of the vortex rope location of a francis turbine on the hydraulic system stability. In *IAHR 24th Symposium on Hydraulic Machinery and Systems* (2008).
- [3] ANSYS, I. *ANSYS CFX-Solver Theory Guide*, 2006.
- [4] ARCHIBALD, F. Self-excitation of an acoustic resonance by vortex shedding. *Journal of Sound and Vibration* 38 (1975), 81–103.
- [5] ARMSTRONG, B., BARNES, F., AND GRANT, I. The effect of a perturbation on the flow over a bluff cylinder. *Physics of Fluids* 29 (1986), 2095.
- [6] ARVESON, P., AND VENDITTIS, D. Radiated noise characteristics of a modern cargo ship. *The Journal of the Acoustical Society of America* 107 (2000), 118.
- [7] AURÉGAN, Y., PAGNEUX, V., AND PINTON, J. *Sound-flow interactions*. Springer Verlag, 2002.
- [8] AUSONI, P., FARHAT, M., ESCALER, X., EGUSQUIZA, E., AND AVELLAN, F. Cavitation influence on von Karman vortex shedding and induced hydrofoil vibrations. *Journal of Fluids Engineering* 129 (2007), 966.
- [9] BEARMAN, P. Vortex shedding from oscillating bluff bodies. *Annual Review of Fluid Mechanics* 16, 1 (1984), 195–222.
- [10] BELAHADJI, B., FRANC, J., AND MICHEL, J. Cavitation in the rotational structures of a turbulent wake. *Journal of Fluid Mechanics* 287 (1995), 383–403.
- [11] BERGER, E. WILLE, R. Periodic flow phenomena. *Annual Review of Fluid Mechanics* 4, 1 (1972), 313–340.
- [12] BLACKSTOCK, D. Transient solution for sound radiated into a viscous fluid. *The Journal of the Acoustical Society of America* 41 (1967), 1312.
- [13] BLAKE, W. *Mechanics of Flow-Induced Sound and Vibration, Volumes 1 & 2*. Orlando: Academic Press, 1986.
- [14] BRENNEN, C. *Cavitation and bubble dynamics*. Oxford University Press, USA, 1995.

- [15] BRENNEN, C., AND ACOSTA, A. Theoretical, quasi-static analysis of cavitation compliance in turbopumps. *Journal of Spacecraft and Rockets* 10, 3 (1973), 175–180.
- [16] BRENNEN, C., AND ACOSTA, A. The dynamic transfer function for a cavitating inducer. *American Society of Mechanical Engineers* 98 (1975), 182–191.
- [17] CHASSAING. *Turbulence en mécanique des fluides*. Institut National Polytechnique de Toulouse, 2000. (in french).
- [18] CHEN, C., NICOLET, C., YONEZAWA, K., FARHAT, M., AVELLAN, F., AND TSUJIMOTO, Y. One-Dimensional Analysis of Full Load Draft Tube Surge. *Journal of Fluids Engineering* 130 (2008), 041106.
- [19] CHEN, Y., AND HEISTER, S. A numerical treatment for attached cavitation. *Journal of Fluids Engineering* 116, 3 (1994), 613–618.
- [20] COLONIUS, T., AND LELE, S. Computational aeroacoustics: progress on nonlinear problems of sound generation. *Progress in Aerospace sciences* 40 (2004), 345–416.
- [21] COUSTON, M., AND PHILIBERT, R. Partial load modelling of gaseous francis turbine rope. In *Proc. of the III Conference on Modelling, Testing and Monitoring for Hydro Powerplants* (1998).
- [22] COVAS, D., STOIANOV, I., MANO, J., RAMOS, H., GRAHAM, N., AND MAKSIMOVIC, C. The dynamic effect of pipe-wall viscoelasticity in hydraulic transients. Part I-experimental analysis and creep characterization. *Journal of Hydraulic Research* 42 (2004), 516–530.
- [23] COVAS, D., STOIANOV, I., MANO, J., RAMOS, H., GRAHAM, N., AND MAKSIMOVIC, C. The dynamic effect of pipe-wall viscoelasticity in hydraulic transients. Part II-Model development, calibration and verification. *Journal of Hydraulic Research* 43, 1 (2005), 56–70.
- [24] CUMPSTY, N., AND WHITEHEAD, D. The excitation of acoustic resonances by vortex shedding. *Journal of Sound and Vibration* 18, 3 (1971), 353–369.
- [25] CURLE, N. The influence of solid boundaries upon aerodynamic sound. *Proceedings of the Royal Society of London. Series A, Mathematical and Physical Sciences* 231, 1187 (1955), 505–514.
- [26] DEL PEDRO, M., AND GMUR, T. *Eléments de mécanique des structures*. Presses polytechniques et universitaire romandes, 2001. (in french).
- [27] DELANNOY, Y., AND KUENY, J. Cavity flow predictions based on the Euler equations. In *ASME Cavitation and Multi-Phase Flow Forum* (1990), vol. 109, pp. 153–158.
- [28] DOERFLER, P. System dynamics of the Francis turbine half load surge. In *IAHR Symposium* (1982), vol. 39.
- [29] DOERFLER, P. Francis Turbine Surge Prediction and Prevention. In *Waerpower '85* (1985), pp. 952–961.

- [30] DOERFLER, P. Evaluating 1d models for vortex-induced pulsation in francis turbines. In *3rd IAHR International Meeting of the Workgroup on Cavitation and Dynamic Problems in Hydraulic Machinery and Systems* (2009).
- [31] DUTTWEILER, M., AND BRENNEN, C. Surge instability on a cavitating propeller. *Journal of Fluid Mechanics* 458 (2002), 133–152.
- [32] DYMOND, JH MALHOTRA, R. The Tait equation: 100 years on. *International Journal of Thermophysics* 9, 6 (1988), 941–951.
- [33] ESCUDIER, M. Confined vortices in flow machinery. *Annual Review of Fluid Mechanics* 19, 1 (1987), 27–52.
- [34] FARHAT, C., LESOINNE, M., AND MAMAN, N. Mixed explicit/implicit time integration of coupled aeroelastic problems: three-field formulation, geometric conservation and distributed solution. *International Journal for Numerical Methods in Fluids* 21, 10 (2005), 807–835.
- [35] FARHAT, M., NATAL, S., AVELLAN, F., PAQUET, F., LOWYS, P., AND COUSTON, M. Onboard measurements of pressure and strain fluctuations in a model of low head Francis turbine. Part 1: Instrumentation. In *Proceedings of the 21st IAHR Symposium on Hydraulic Machinery and Systems* (2002), pp. 9–12.
- [36] FAVRE, A., KOVASZNY, L., DUMAS, R., GAVIGLIO, J., AND COANTIC, M. *La Turbulence en Mécanique des Fluides*. CNRS, 1976. (in french).
- [37] FELIPPA, C., PARK, K., AND FARHAT, C. Partitioned analysis of coupled mechanical systems. *Computer methods in applied mechanics and engineering* 190, 24-25 (2001), 3247–3270.
- [38] FLEMMING, F., FOUST, J., KOUTNIK, J., AND FISHER, R. Overload surge investigation using CFD data. In *24th IAHR Symposium on Hydraulic Machinery and Systems, Foz Do Iguassu* (2008).
- [39] FORMAGGIA, L., GERBEAU, J., NOBILE, F., AND QUARTERONI, A. On the coupling of 3D and 1D Navier-Stokes equations for flow problems in compliant vessels. *Computer Methods in Applied Mechanics and Engineering* 191, 6-7 (2001), 561–582.
- [40] FRANC, J., AVELLAN, F., AND BELAHADJI, B. *La cavitation. Mécanismes physiques et aspects industriels*. EDP Sciences, 1995. (in french).
- [41] GHIDAOU, M., ZHAO, M., MCINNIS, D., AND AXWORTHY, D. A review of water hammer theory and practice. *Applied Mechanics Reviews* 58 (2005), 49.
- [42] HASSIS, H. Noise caused by cavitating butterfly and monovar valves. *Journal of Sound and Vibration* 225, 3 (1999), 515–526.
- [43] HÜBNER, B., WALHORN, E., AND DINKLER, D. A monolithic approach to fluid-structure interaction using space-time finite elements. *Computer methods in applied mechanics and engineering* 193, 23-26 (2004), 2087–2104.

- [44] HERRADA, M. A., AND FERNANDEZ-FERIA, R. On the development of three-dimensional vortex breakdown in cylindrical regions. *Physics of Fluids* 18, 8 (2006), 084105.
- [45] HIRSCHBERG, A. RIENSTRA, S. An introduction to aeroacoustics. Tech. rep., Eindhoven University of Technology, 2004.
- [46] HIRSCHI, R., DUPONT, P., AVELLAN, F., FAVRE, J., GUELICH, J., AND PARKINSON, E. Centrifugal pump performance drop due to leading edge cavitation: numerical predictions compared with model tests. *Journal of Fluids Engineering* 120 (1998), 705.
- [47] HOLL, J., AND YOUNG, J. Effects of cavitation on periodic wakes behind symmetric wedges. *ASME, Transactions, Series D-Journal of Basic Engineering* 88 (1966), 163–176.
- [48] INOUE, O., AND HATAKEYAMA, N. Sound generation by a two-dimensional circular cylinder in a uniform flow. *Journal of Fluid Mechanics* 471 (2002), 285–314.
- [49] JORDAN, P., MEYER, M., AND PURI, A. Causal implications of viscous damping in compressible fluid flows. *Physical Review E* 62, 6 (2000), 7918–7926.
- [50] JOST, AND LIPEJ. Numerical prediction of the vortex rope in the draft tube. In *3rd IAHR International Meeting of the Workgroup on Cavitation and Dynamic Problems in Hydraulic Machinery and Systems* (2009).
- [51] KORTEWEG, D. On the velocity of propagation of sound in elastic pipes. *Annalen der Physik und Chemie* 5 (1878), 525–542. (in german).
- [52] KOUTNIK, J., NICOLET, C., SCHOHL, G., AND AVELLAN, F. Overload Surge Event in a Pumped-Storage Power Plant. In *Proceedings of the 23rd IAHR Symposium* (2006).
- [53] KOUTNIK, J., AND PULPITEL, L. Modeling of the francis turbine full- load surge. In *Modeling, Testing and Monitoring for Hydro Power Plants* (1996).
- [54] KREYSZIG, E. *Advanced Engineering Mathematics*. John Wiley & Sons, 1999.
- [55] KÜTTLER, U., AND WALL, W. Fixed-point fluid–structure interaction solvers with dynamic relaxation. *Computational Mechanics* 43, 1 (2008), 61–72.
- [56] KUBOTA, A., KATO, H., AND YAMAGUCHI, H. A new modelling of cavitating flows: a numerical study of unsteady cavitation on a hydrofoil section. *Journal of Fluid Mechanics* 240 (2006), 59–96.
- [57] KUNZ, R., BOGER, D., CHYCZEWSKI, T., STINEBRING, D., GIBELING, H., AND GOVINDAN, T. Multi-phase CFD analysis of natural and ventilated cavitation about submerged bodies. In *3rd ASME/JSME Joint Fluids Engineering Conference* (1999).
- [58] LANGTHJEM, M., AND OLHOFF, N. A numerical study of flow-induced noise in a two-dimensional centrifugal pump. Part I. Hydrodynamics. *Journal of Fluids and Structures* 19, 3 (2004), 349–368.

- [59] LANGTHJEM, M., AND OLHOFF, N. A numerical study of flow-induced noise in a two-dimensional centrifugal pump. Part II. Hydroacoustics. *Journal of Fluids and Structures* 19, 3 (2004), 369–386.
- [60] LAUNDER, B., AND SPALDING, D. The numerical computation of turbulent flows. *Computer methods in applied mechanics and engineering* 3 (1974), 269–289.
- [61] LIÉNARD, P. FRANÇOIS, P. *Acoustique industrielle et environnement*. Eyrolles, 1983. (in french).
- [62] LIGHTHILL, M. On sound generated aerodynamically. I. General theory. *Proceedings of the Royal Society of London. Series A, Mathematical and Physical Sciences* 211, 1107 (1952), 564–587.
- [63] LIGHTHILL, M. On sound generated aerodynamically. II. Turbulence as a source of sound. *Proceedings of the Royal Society of London. Series A, Mathematical and Physical Sciences* 222, 1148 (1954), 1–32.
- [64] MAURI, S., KUENY, J., AND AVELLAN, F. Numerical prediction of the flow in a turbine draft tube, influence of the boundary conditions. In *FEDSM 00-11084, Proceedings of the ASME 2000 Fluids Engineering Division Summer Meeting, Boston, MA* (2000).
- [65] MENTER, F., AND EGOROV, Y. A Scale-Adaptive Simulation Model using Two-Equation Models. In *43 rd AIAA Aerospace Sciences Meeting and Exhibit* (2005), p. 2005.
- [66] MENTER, F., AND EGOROV, Y. SAS turbulence modelling of technical flows. *ER-COFTAC SERIES* 10 (2006), 687.
- [67] MOHAMMADI, B., AND PIRONNEAU, O. *Analysis of the k-epsilon turbulence model*. John Wiley & Sons, 1994.
- [68] NICOLET, C. *Hydroacoustic modeling and numerical simulation of unsteady operation of hydroelectric systems*. PhD thesis, EPFL, 2007.
- [69] NICOLET, C., ARPE, J., AND AVELLAN, F. Identification and modeling of pressure fluctuations of a Francis turbine scale model at part load operation. In *22nd Symposium of IAHR* (2004), vol. 7.
- [70] NORWOOD, F. Propagation of transient sound signals into a viscous fluid. *The Journal of the Acoustical Society of America* 44 (1968), 450.
- [71] OTA, T., OKAMOTO, Y., AND YOSHIKAWA, H. A correction formula for wall effects on unsteady forces of two-dimensional bluff bodies. *Journal of fluids engineering* 116, 3 (1994), 414–418.
- [72] PAIK, J., SOTIROPOULOS, F., SALE, M., ET AL. Numerical simulation of swirling flow in complex hydro-turbine draft tube using unsteady statistical turbulence models. *Journal of hydraulic engineering* 131 (2005), 441.

- [73] PARKER, R. Resonance effects in wake shedding from parallel plates: some experimental observations. *Journal of Sound and Vibration* 4, 1 (1966), 62–72.
- [74] PETERS, M., HIRSCHBERG, A., REIJNEN, A., AND WIJNANDS, A. Damping and reflection coefficient measurements for an open pipe at low Mach and low Helmholtz numbers. *Journal of Fluid Mechanics* 256 (1993), 499–534.
- [75] PEZZINGA, G. Evaluation of unsteady flow resistances by quasi-2 D or 1 D models. *Journal of Hydraulic Engineering* 126 (2000), 778–785.
- [76] PEZZINGA, G. Second viscosity in transient cavitating pipe flows. *Journal of Hydraulic Research* 41, 6 (2003), 656–665.
- [77] PHILIBERT, R., AND COUSTON, M. Francis turbines at part load, matrix simulating the gaseous rope. In *Hydraulic Machinery and Cavitation: Proceedings of the Nineteenth IAHR Symposium on Hydraulic Machinery and Cavitation* (1998).
- [78] RHEINGANS, W. Power swing in hydroelectric power plants. *Transaction, American Society of Mechanical Engineers* 62 (1940), 171–184.
- [79] RIBNER, H. The generation of sound by turbulent jets. *Advances in Applied Mechanics* 8 (1964), 103–182.
- [80] RUBIN, S. Longitudinal instability of liquid rockets due to propulsion feedback (pogo). *Journal of Spacecraft and Rockets* 3 (1966), 1188–1195.
- [81] RUPRECHT, A., HELMRICH, T., ASCHENBRENNER, T., AND SCHERER, T. Simulation of vortex rope in a turbine draft tube. In *Proceedings of the 21st IAHR Symposium on Hydraulic Machines and Systems*, (2002).
- [82] RYU, J., CHEONG, C., KIM, S., AND LEE, S. Computation of internal aerodynamic noise from a quick-opening throttle valve using frequency-domain acoustic analogy. *Applied Acoustics* 66, 11 (2005), 1278–1308.
- [83] SALVATORE, F., AND IANNIELLO, S. Preliminary results on acoustic modelling of cavitating propellers. *Computational Mechanics* 32, 4 (2003), 291–300.
- [84] SEOL, H., SUH, J., AND LEE, S. Development of hybrid method for the prediction of underwater propeller noise. *Journal of Sound and Vibration* 288, 1-2 (2005), 345–360.
- [85] SINGHAL, A., VAIDYA, N., AND LEONARD, A. Multi-dimensional simulation of cavitating flows using a PDF model for phase change. In *ASME Paper FEDSM97-3272* (1997).
- [86] SOARES, A., COVAS, D., AND REIS, L. Analysis of PVC Pipe-Wall Viscoelasticity during Water Hammer. *Journal of Hydraulic Engineering* 134 (2008), 1389.
- [87] SONG, C., AND YUAN, M. A weakly compressible flow model and rapid convergence methods. *Journal of Fluids Engineering* 110, 4 (1988), 441–455.

- [88] STEIN, P., SICK, M., DOERFLER, P., WHITE, P., AND BRAUNE, A. Numerical simulation of the cavitating draft tube vortex in a francis turbine. In *Proceedings of the 23rd IAHR Symposium on Hydraulic Machinery and Systems, Yokohama, Japan, Paper* (2006), vol. 228.
- [89] TESTUD, P., MOUSSOU, P., HIRSCHBERG, A., AND AURÉGAN, Y. Noise generated by cavitating single-hole and multi-hole orifices in a water pipe. *Journal of Fluids and Structures* 23, 2 (2007), 163–189.
- [90] THICKE, R. Practical solutions for draft tube instability. *Water Power & Dam Construction* 33, 2 (1981), 31–37.
- [91] TIJSSELING, A. . Fluid-structure interaction in liquid filled pipe system: a review. *Journal of Fluids and Structures* 10 (1996), 109–146.
- [92] VENTIKOS, Y., AND TZABIRAS, G. A numerical method for the simulation of steady and unsteady cavitating flows. *Computers & Fluids* 29, 1 (2000), 63–88.
- [93] WANG, G., SENOCAK, I., SHYY, W., IKOHAGI, T., AND CAO, S. Dynamics of attached turbulent cavitating flows. *Progress in Aerospace Sciences* 37, 6 (2001), 551–581.
- [94] WANG, M., FREUND, J., AND LELE, S. Computational prediction of flow-generated sound. *Annual Review of Fluid Mechanics* 38 (2005), 483–512.
- [95] WELCH, P. The use of fast Fourier transform for the estimation of power spectra: a method based on time averaging over short, modified periodograms. *IEEE Transactions on Audio and Electroacoustics* 15, 2 (1967), 70–73.
- [96] WILCOX, D. Multiscale model for turbulent flows. In *AIAA 24th Aerospace Sciences Meeting* (1986).
- [97] WILLIAMSON, C. Vortex dynamics in the cylinder wake. *Annual Review of Fluid Mechanics* 28, 1 (1996), 477–539.
- [98] WINEMAN, A., AND RAJAGOPAL, K. *Mechanical response of polymers: an introduction*. Cambridge Univ Pr, 2000.

Curriculum Vitae

Nicolas Ruchonnet

Plein-soleil
1071 Rivaz
Suisse
+41 78 644 86 27
nicolas.ruchonnet@a3.epfl.ch



Nationalité: Suisse
Né le 4 mars 1981

FORMATION

2006-2010 **Doctorat ès sciences**
Ecole Polytechnique Fédérale de Lausanne (EPFL), Suisse

2000-2005 **Master en Génie Mécanique, EPF**
Diplôme: Laboratoire de Machines Hydrauliques
Echange: IIT Delhi, Inde (1 année)

1997-2000 **Baccalauréat ès sciences**
Gymnase de Burier (VD)

EXPERIENCES PROFESSIONNELLES

2005-2010 **Ecole Polytechnique Fédérale de Lausanne (EPFL), Suisse**
Assistant doctorant au Laboratoire de Machines Hydrauliques (5 ans)

2005 **Heben Hezer, Lausanne**
Assistant éducateur en institution spécialisée (2 mois)

2002 **EOS, Martigny**
Stage d'usinage (1 mois)

2002 **BASPO, Yverdon**
Guide au pavillon des sports de l'exposition nationale (5 mois)

COMPÉTENCES INFORMATIQUES

Systemes: Windows, Linux
Program. : Matlab, Labview, C, Fortran
CFD: CFX, ICEM
Structure: Ansys
CAO: Ideas, Catia, AutoCAD
Bureautique: MS-Office
Multimédia: Suite Adobe, 3DS max

LANGUES

Français Langue maternelle
Anglais Avancé
Allemand Connaissances scolaires

List of Publications

Journal papers

- P. Maruzewski, S. Alligné, N. Ruchonnet, V. Hasmatuchi, H.-P. Mombelli, F. Avellan, B. Wang, T. Dinh, A. Fedorov, P. Finnegan, D. Burggraeve and J. Iosfin, Parametric Analysis of High Load Vortex Rope, *Journal of Fluids Engineering*, Submitted for publication

Conference papers

- C. Nicolet, N. Ruchonnet, J. Koutnick, F. Avellan; Hydroacoustic Simulation of Rotor-Stator Interaction in Resonance Conditions in Francis Pump-Turbine, *25rd IAHR Symposium on Hydraulic Machinery and Systems, Timisoara, September 2010, Submitted*
- S. Alligné, C. Nicolet, N. Ruchonnet, V. Hasmatuchi, P. Maruzewski, F. Avellan; Numerical Simulation of Nonlinear Self Oscillations of a Full Load Vortex Rope, *Proceedings of the 3rd IAHR International Meeting of the Workgroup on Cavitation and Dynamic Problems in Hydraulic Machinery and Systems, Brno, October 2009*
- N. Ruchonnet, C. Nicolet, S. Alligné, F. Avellan; Acoustic Resonance in Cavitation Free and Cavitating Flows, *Proceedings of the 3rd IAHR International Meeting of the Workgroup on Cavitation and Dynamic Problems in Hydraulic Machinery and Systems, Brno, October 2009*
- N. Ruchonnet, C. Nicolet, F. Avellan; One-Dimensional Modeling of Rotor Stator Interaction in Francis Pump-Turbine, *Proceedings of the 23rd IAHR Symposium on Hydraulic Machinery and Systems, Yokohama, October 2006*
- N. Ruchonnet, C. Nicolet, F. Avellan; Hydroacoustic Modeling of Rotor Stator Interaction in Francis Pump-Turbine, *Proceeding of the IAHR Int. Meeting of the Workgroup on Cavitation and Dynamic Problems in Hydraulic Machinery and Systems, Barcelona, Spain, June 2006*
- C. Nicolet, N. Ruchonnet, F. Avellan; One-Dimensional Modeling of Rotor Stator Interaction in Francis Pump-Turbine, *Proceedings of ISROMAC-11, February 2006*